Avilovas, Lukas (2021) *Micro electro-mechanical system design, fabrication and application for atomic force microscopy probe elasticity characterisation.* PhD thesis.

http://theses.gla.ac.uk/82287/

Copyright and moral rights for this work are retained by the author

A copy can be downloaded for personal non-commercial research or study, without prior permission or charge

This work cannot be reproduced or quoted extensively from without first obtaining permission in writing from the author

The content must not be changed in any way or sold commercially in any format or medium without the formal permission of the author

When referring to this work, full bibliographic details including the author, title, awarding institution and date of the thesis must be given

Enlighten: Theses
https://theses.gla.ac.uk/
research-enlighten@glasgow.ac.uk

University of Glasgow

Micro Electro-Mechanical System Design, Fabrication and Application for Atomic Force Microscopy Probe Elasticity Characterisation

Author: Lukas Avilovas

Supervisor: Dr. Phillip S. Dobson

A thesis submitted in fulfilment of the requirements for the Degree of Doctor of Philosophy

Division of Electronics and Nanoscale Engineering

James Watt School of Engineering

University of Glasgow

February 2021

Publications:

1. **Avilovas, L.**, Weaver J. M. R., Yin, H., Dobson, P. S. (2021): *"A simple MEMS device for non-linear AFM probe elasticity characterisation"* - article in review, publication in 2021.

2. Davaria S., Sriram Malladi V.V.N., **Avilovas L.**, Dobson P. S., Cammarano A., Tarazaga P.A. (2020): *"Study on Developing Micro-Scale Artificial Hair Cells"* - Dervilis N. (eds) Special Topics in Structural Dynamics & Experimental Techniques, Volume 5.

3. **Avilovas, L.**, Weaver J. M. R., Dobson, P. S. (2019): *"A facile method of direct elasticity measurement for AFM cantilevers"* - poster presentation at 45th Micro Nano Engineering Conference, Rhodes.

4. **Avilovas, L.**, Weaver J. M. R., Dobson, P. S. (2019): *"Method of direct stiffness measurement for AFM cantilevers"* - oral presentation at Microscience Microscopy Congress 2019, Manchester.

Abstract

The work in this thesis is focused on characterising elastic behaviour of micro-cantilever probes found at the core of Atomic Force Microscopy (AFM) tools. It is an essential property to AFM force measurements, since interpretation of the cantilever deflection is directly related to the measure of the tip-sample force via its elastic conduct. It was demonstrated that the conventional micro-cantilevers can be well characterised using analytical and FE methods, together with the ready developed tools and experimental techniques, which formed the insights for the design practices used in further and more complex structure development efforts. However, this project's emphasis was placed on assessment of non-traditional AFM cantilever structures that are not supported by the said methods, and hence necessitated in the conceptualisation and development of a dedicated micro electro-mechanical system (MEMS) solution. The sensitive force and elasticity measurement device, based on metal film resistive strain sensing, was realised using semiconductor and MEMS fabrication approaches in the James Watt Nanofabrication Centre, allowing the desired performance to be achieved with an in-house process optimisation. The functional MEMS tool paired with bespoke instrumentation was then employed to characterise a range of commercial cantilevers as well as non-standard probes consisting of complex composition multi-structures and non-linear elasticity, providing novel insights into their elastic character.

Sesei, Tėvams, Tėvų Tėvams ir Krikštatėviams.

Acknowledgments

My gratitude goes to The University of Glasgow for the opportunity, James Watt Nanofabrication Centre for the means and Engineering and Physical Sciences Research Council for the funding that enabled this research to be undertaken.

I will forever cherish this adventure, which is to blame on my supervisors' contagious excitement for research and discovery. To my first supervisor - Phillip S. Dobson - the gratitude should be expressed in each and every page. I am immensely grateful for Phil's leap of faith in accepting me to his research group, allowing this journey to commence and progress with the provision of crucial insights, resources, and plain old optimism that ensured the tough times could be endured and good ones - celebrated. My second supervisor, Jonathan M. R. Weaver entertained this thesis with the yet unsurpassed comprehension of the field, supporting this work with intuition, deductions and recollections that often left me questioning limits of human cognition. His mastery of making sand count was instrumental to this thesis progressing beyond Chapter 4.

Ravish, Rory, Yuan, Lesley, Huabing - I am thankful for your input and patience in all things related to fabrication and microscopy, which allowed the truly fun parts of this thesis to materialise.

Chris, Hao, David, Francesca, Rory, Ravish, Anton, Zarina and Jamie - thank you to the incredibly bright members of AFM group for the companionship during the research trials and tribulations - I will never forget working alongside you and wish the utmost success in your coming feats!

Vitalija P., Lyczezar I., Yavor G, Graham F., Callum M., Ed P., Colin R., Jeb M., Jim B. - thank you for being my early teachers and mentors, whose educational generosity and encouragement allowed me to absorb some of the witnessed creativity and ethic.

Thank you to Douglas, Hristo, Justas, Kester, Matthew and the remainder of the University of Glasgow Racing team for making my university experience much more varied and engaging. Additional thank you goes to GUU and Bank St establishments for supplying the wet solutions, 568 ml at a time.

Finally, I am mostly grateful for my partner Milda, whose love, support and unexplainable dedication to improve my existence was, without contest, the main motive allowing this thesis to come to completion.

Table of Contents

Abstract 1

Acknowledgments 3

Chapter 1 - Introduction 9

1.1 Introduction 9

1.2 Scanning Probe Microscopy (SPM) 10

1.3 Atomic Force Microscopy (AFM) 12

1.4 AFM operation 16

1.5 AFM scale force measurement 20

1.6 Thesis direction 23

Chapter 2 - Review of the AFM probe elasticity characterisation techniques 25

2.1 AFM probe elasticity characterisation literature overview 25

2.2 Technique review through a case study 31

2.3 Elasticity characterisation via thermal fluctuation interpretation 36

2.4 Elasticity characterisation via comparison to elastic reference 43

2.5 Elasticity characterisation by a nanoindenter 49

2.6 Conclusion 57

Chapter 3 - MEMS sensing theory 59

3.1 Structural mechanics theory 60

3.1.1 Analytical methods for MEMS characterisation 69

3.1.2 Finite Element methods for MEMS characterisation 75

3.2 Electrical sensing theory 80

3.2.1 Capacitive deformation sensing 80

3.2.2 Resistive deformation sensing 83

3.3 Signal interpretation and instrumentation 86

Chapter 4 - MEMS Fabrication 90

4.1 Fabrication concept and starter substrate 90

4.2 Step 1 - metal film lift off, marker layer 94

4.3 Step 2 - metal film lift off, sensor layer 97

4.3.1 Metal film strain sensor fabrication trial 99

4.4 Step 3 - plasma etching, elastic structure definition 104

4.5 Step 4 - selective chemical etching, elastic structure release 107

4.5.1 Elastic structure geometry optimisation 112

4.5.2 Stress concentration reduction 116

4.5.3 Metal thin-film stress reduction 118

4.6 Result - fabrication of the MEMS calibration device 126

Chapter 5 - MEMS device characterisation 129

5.1 Mechanical characterisation 130

5.1.1 Silicon nitride elastic modulus assessment 131

5.1.2 Direct MEMS elastic modulus assessment failure 136

5.1.3 Indirect MEMS spring constant assessment 139

5.2 Electrical characterisation 144

5.2.1 Strain sensor resistive properties 146

5.2.2 MEMS device electrical noise spectrum analysis 149

5.3 Thermal behaviour characterisation 152

5.3.1 Thermal Coefficient of Resistance (TCR) and Coefficient of Thermal Bending (CTE) 152

5.3.2 MEMS device thermal behaviour in AFM environment 157

5.4 In-situ AFM elasticity characterisation...161

5.4.1 MEMS contact point elasticity characterisation with a calibrated

AFM cantilever 161

5.4.2 MEMS strain signal correlation to an externally determined

interaction force 165

5.5 Conclusion 172

Chapter 6 - MEMS tool application for AFM probe elasticity characterisation..175

6.1 Complex composition batch produced AFM cantilever elasticity

characterisation 176

6.1.1 Visual inspection..178

6.1.2 Elasticity assessment with the MEMS tool....................................183

6.1.3 Indirect elasticity assessment via dynamic behaviour observation.188

6.1.4 Elasticity assessment with a calibrated reference spring 191

6.1.5 Experimentally obtained elasticity modulus comparison 194

6.2 MEMS tool application for AFM probe structural modification

characterisation 197

6.3 Complex AFM probe characterisation...201

6.3.1 Non-linear elasticity AFM probe characterisation..........................201

6.3.2 Additional complex composition probe characterisation 206

Chapter 7 - Conclusions and future work 209

7.1 Conclusions...209

7.2 Future work...213

Appendix A - MEMS Instrumentation Schematic 218

Appendix B - MEMS Device Fabrication Process Details 221

List of Figures 224

List of Tables 237

References 240

Chapter 1 - Introduction

1.1 Introduction

The work outlined in this thesis is concerned with the mechanical characterisation of Atomic Force Microscope cantilever probes. Atomic Force Microscopy (AFM) is a fundamental technique for many branches of science operating at the nano-scale that rely on the imaging, interaction and manipulation ability offered by the tool. The force measuring ability in the force-distance domain is particularly sought after by cutting edge fields - e.g., bio-science and cancer research where it enables live soft tissue mechanical characterisation [1], with precise force measurements allowing for differentiation between healthy and cancerous cells [2]; chemistry and material science, where the unprecedented resolution load mapping permits single molecule structure [3] and intra-bond strength [4] characterisation as well as accelerating the graphene [5] and carbon nanotube [6] development through their mechanical understanding and self-serving employment [7]; and recently the AFM force capacity is utilised in the early stages of SARS-CoV-2 understanding beyond surface level visualisation [8].

The maturing yet still expanding field has produced many derivative techniques tailored for application-specific sensing performance, which have been achieved through functionalisation and optimisation of the AFM cantilever - a component instrumental to relate force and displacement. Such developments are increasing the complexity of this key component’s mechanical behaviour, necessitating the parallel development of tools and techniques required to characterise and maintain its function. The following chapter will

introduce the key work in the field of AFM interaction measurement methods, followed by AFM probe elasticity characterisation in chapter 2, which is fundamental to the thesis progression in subsequent chapters, where conceptualisation, realisation and application demonstration of the novel MEMS based solution is presented.

1.2 Scanning Probe Microscopy (SPM)

The field of microscopy provides the gift of sight and observation of samples which are beyond our natural means. The conception of the optical microscope had a disruptive impact on our understanding of the micro-world, eventually morphing into the paradoxical appreciation of the tremendous amount of sense hiding in the infinitesimal universe [9]. The relentless development of the natural sciences created a constant demand for better microscopy tools and techniques, which the optical microscope eventually could not satisfy. The ongoing developments in super-resolution microscopy continue challenging the constraints of visible light diffraction limit [10] [11], while electron-beam based imaging (EM) solutions had already beaten the optical resolution several-fold as early as 1933 - Ruska with the Transmission Electron Microscope (TEM) [12]. This further developing field had extended imaging from raster-like single point observation to continuous surface imaging of samples by introduction of the Scanning Electron Microscope (SEM) by Ardenne [13] in 1938, drastically expanding the EM technique’s practicality and applicability.

The extended limit of understanding smaller and smaller measurements facilitated the next ground-breaking development in the microscopy field - the emergence of scanning probe

microscopy (SPM). This technique's ability to measure physical interactions between a scanning probe and sample at previously unchartered scale was first demonstrated by Binnig and Rohrer in 1983 [14] with the scanning tunnelling microscope (STM). The limitations stemming from the use of tunnelling current, such as restriction to solid and conductive samples, were soon addressed by Binnig and Gerber [15] in 1986 with the introduction of the Atomic Force Microscope (AFM), enabling the acquisition of three dimensional surface topography of (virtually) any solid sample. The presented AFM tool design was expanded further to form many derivative niches of thermal [16], electrostatic [17], magnetic [18], electrochemical [19] and near field optical [20] applications. The development of SPM techniques beyond imaging applications made a claim that microscopy is now more than just a topography graphing tool, since the availability and volume of acquired data had organically prompted the development of a wide range signal interpretation instrumentation and data processing methodologies. These approaches can be applied to extract quantitative information from the observed spectrum - e.g. bandwidth narrowing (lock-in reliance [21] [22]), statistical (Scanning Noise Microscope [23]) and spectroscopic (Current Imaging Tunnelling Spectroscopy [24]) measures. Given the unprecedented versatility and resolution these tools offer, it is no great surprise that SPM and further AFM derivatives have established themselves as essential metrology tools enabling new and already developed branches of science to operate at the nanoscale.

1.3 Atomic Force Microscopy (AFM)

The AFM forms images of surfaces using a mechanical probe that scans the specimen. The interaction forces between a sharp tip mounted at the end of a cantilever and the surface being scanned are measured by monitoring either the static or dynamic deflection of the cantilever. Fundamental modes associated with general AFM applications are contact, non-contact or hybrid (tapping or intermittent contact) and are characteristically achieved with an *xyz* scanner stage, cantilever deflection sensor and dedicated control and drive systems (Figure 1 and Figure 2). In addition, modern tools often utilise additional sensing devices for improved operational guidance, usability and performance in conjunction with the base setup - e.g. optical microscope live-view, closed-loop displacement and positioning elements, anti-collision safety features, etc.

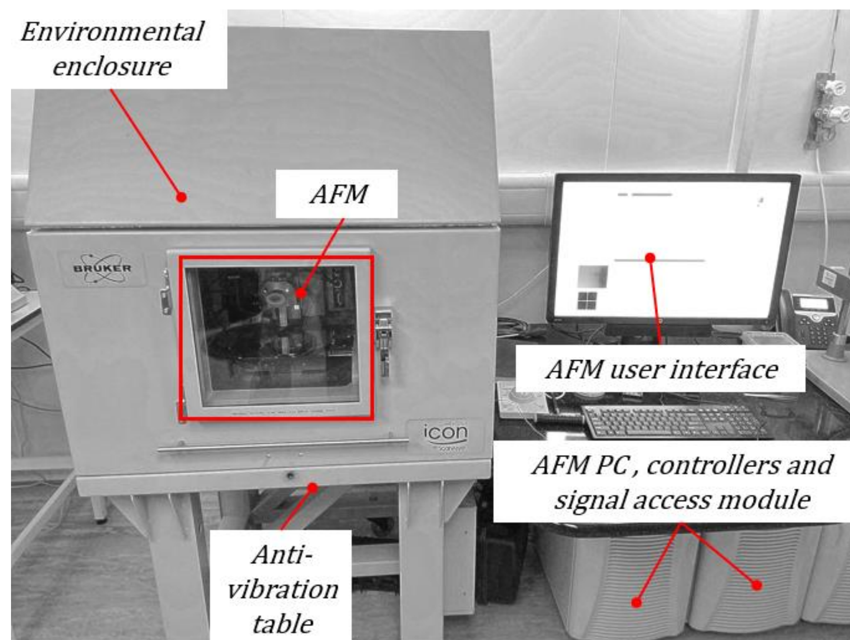

Figure 1. AFM system photograph, highlighting external composition, Bruker Dimension Icon AFM [25].

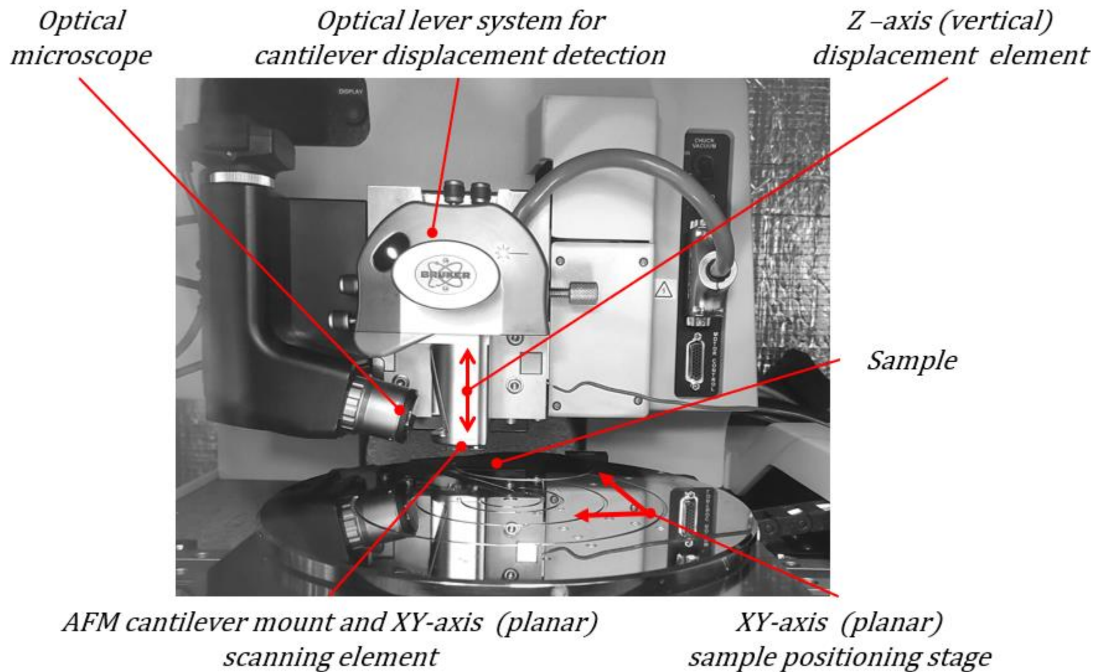

Figure 2. Photograph highlighting components composing the core of the AFM system, Bruker Dimension Icon AFM [25].

The most fundamental AFM scanning mode, traceable back to its creation, is termed contact mode [15]. This method closely resembles the principle workings of a conventional surface profiler [26] – the cantilever deflection is regulated to be maintained at constant value of deflection and hence – force, whilst the tip is continuously interacting with the topography of the sample. The resultant *z*-axis correction error required to maintain constant deflection is logged as a proportional value to the vertical displacement, providing vertical imaging in relation to the planar scanning field. The requirement to maintain constant deflection does mean that scanning speed is limited to that of the cantilever dynamics and drive electronics, meaning a typical scan rate of a few Hz per line, as determined by the system eigenfrequency limitations [27]. Therefore, the slow scanning contact mode is nowadays almost exclusively reserved for functionalised imaging where direct tip-sample contact is required or physical sample manipulation is undertaken [28].

If constant scanning force is not prerequisite, high-speed in-contact scanning is possible at some cost of the topography caused displacement artefacts and increased tip-wear due to topography determined engagement force [29].

In non-contact or dynamic modes [30] – the tip is oscillated above the sample whilst the topographic image is constructed from the change in cantilever oscillation (phase, amplitude or frequency) in response to sample's property variation. Unlike the quasi-static contact mode tip-sample interaction, the dynamic force mechanics of such interaction are complex and need to be interpreted indirectly through an oscillator model that is processed within the built in AFM software. Such scanning modes contain numerous advantages - their non-destructive nature due to a lack of rigid contact, a reduction in tip artefacts and their increased speed - which is now limited by the mechanical structure and surrounding fluid interaction dynamics, reaching scanning rates of tens of Hz per line [31]. However, the practical application of these modes do pose limitations on the AFM cantilever dynamic properties (high quality factor structures required), complexity and cost of the necessary high-speed feedback loop hardware.

Tapping mode combines aspects of both techniques, meaning that as the probe oscillates, it makes intermittent contact with the sample. Advances in mechanically optimised cantilever dynamics, rapid feedback loop control and signal processing allow for simultaneous mapping of tip-sample physical interactions and the oscillated cantilever's own dynamic changes, permitting a compromise of speed and information quantifiability from the coupled dynamic and static cantilever response. The latest advancements in hybrid techniques are best illustrated by academic and commercial efforts through patents and newly setup ventures [32] [33] [34] [35] that aim to deliver wafer scale, 'video rate' (up to

25 Hz per frame) imaging speeds compatible with use at temperature extremes [36] [37] and under various environmental media [38] [39].

The AFM software employed for data interpretation and processing is instrumental to making use of the recorded information, with proprietary [40] [41] as well as open-source solutions [42] [43] available to end-users. All scanning methods offer their advantages and applications, some of which rely critically on the ability to determine force via knowledge of the scanning probe elasticity - a key property which is the focus of further described work.

1.4 AFM operation

Contact mode AFM operation is driven by the repulsive force between the sample and scanning tip, which is measured via the deflection of the spring (cantilever) upon which the scanning tip is attached (Figure 3). Other interatomic forces (i.e., Van der Waals, capillary, electrostatic, long-range etc.) are present and can be identified explicitly by appropriate interpretation methodologies [44]. In order to measure and maintain the tip to sample separation via a feedback loop, the AFM's predecessor, scanning tunnelling microscopy (STM), related this distance to tunnelling current magnitude – a method which allowed for vertical resolution of up to 2×10^{-11} m [45]. The later-developed AFM designs were focused on adapting the similar application of feedback loop control to non-conductive samples, therefore alternative solutions, such as mechanical cantilever deflection sensing via an optical interferometer [46], a laser optical lever system [47] or self-sensing cantilever probes [48] were introduced (Figure 3). All methods have found their application as decided by the offered compromises between accuracy, cost and speed. The modern, general purpose AFM systems which are of interest to this thesis have mostly settled for the optical lever solution [49], which is a monument to the ingenious simplicity and reliability of this height determination method over the accuracy potential of alternatives, as judged by the community preference and subsequent adaptation. Unsurprisingly, the versatility of optical levers does come with its own set of notable shortcomings. These include thermal irradiation effects [50], errors compounded in signal hysteresis, non-linearities in rotational bend to vertical displacement transformation [51] and inferior accuracy when compared to interferometry sensing (prompting a development of hybrid methods, e.g. [52]) - as will be discussed in upcoming chapters 5 and 6.

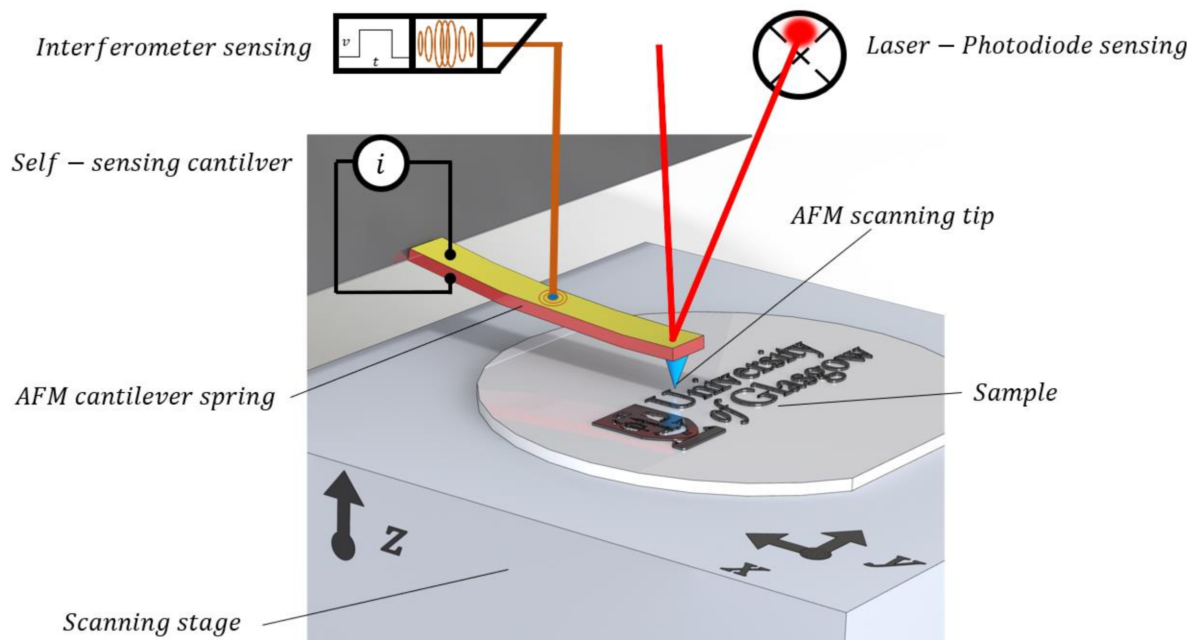

Figure 3. Representation of the AFM tip and sample interaction arrangement, highlighting the common AFM cantilever displacement detection options and interacting components.

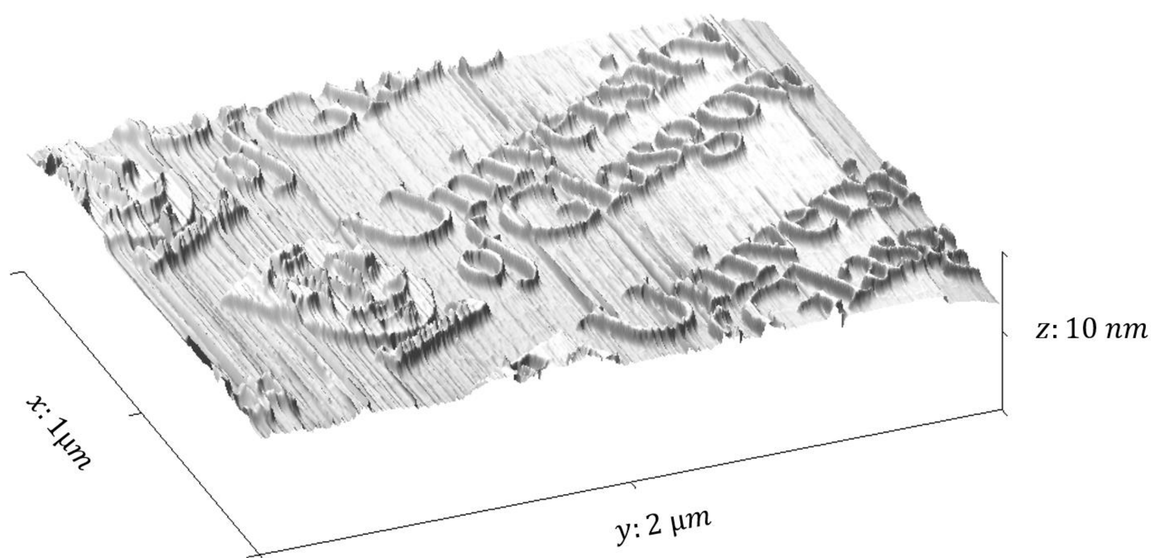

Figure 4. Software reconstructed plot of the scanned topography. The z-axis is proportional to cantilever deflection. Topography data courtesy of Hao Xu [53] of AFM and Hyperlithography Group, University of Glasgow.

The optical lever detection system integrates a laser-photodiode height sensor, *xyz* stage as well as built in control electronics. In this setup, the surface is scanned by moving the piezo driven *xy* stage. The sample is brought in contact with the tip by a combined piezo and stepper-motor actuated *z*-axis. During the scan, the laser deflection induced by the cantilever bend is monitored. This value is input into a feedback loop that maintains constant engagement by adjusting the probe or sample vertical height, which in turn maintains a constant cantilever bend that is proportional to the tip-sample force. A plot of the constant force *z* position at each *xy* point is then used as a 3-dimensional map of the surface (Figure 4).

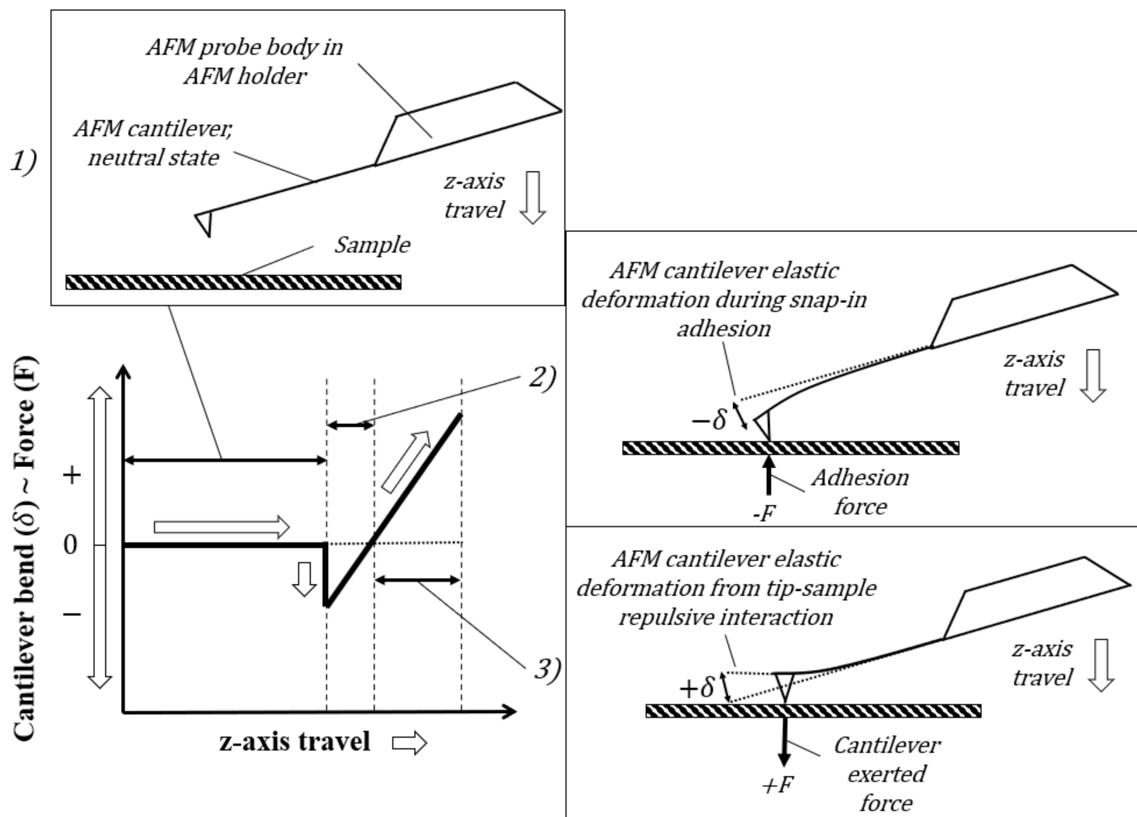

Figure 5. Force-distance curve obtained by optical lever AFM plotting retracting cantilever bend versus its z-axis displacement, noting the distinct probe-sample interaction and force exchange regions.

The force-distance ramp (Figure 5) - a type of contact mode subroutine - is tailored to observe the tip-sample force at various z positions. In such a routine, a cantilever is driven into the sample until a pre-set deflection or force is reached and then the motion is reversed - resulting in a controlled cyclic indentation a.k.a. ramping. This point interaction can then be analysed by relating vertical stage displacement (z) to the measured cantilever mechanical response in the form of its vertical deformation - deflection (δ). A plethora of techniques exist to identify and interpret these repulsive interaction forces (e.g. environmental [54], Van der Waals [55], material specific attraction and repulsion [56]) and adhesion force parameters (e.g. Hertz [57], DMT [58] and JKR [59]).

Techniques used to resolve the force component in the z-direction require the ability to accurately relate the normal force and the AFM measured cantilever displacement, which necessitates characterisation of the cantilever elasticity. The default model is the linear spring approximation per Hooke's Law (Eq. 1) - which relates the interaction elasticity (k) to the force (F) and measured cantilever displacement (δ). This linear proportionality constant, conventionally called an elasticity modulus or a spring constant, is expressed in units of N m^{-1}. Its characterisation is critical if accurate force magnitudes are required, hence the methods used to determine AFM probe elasticity are of particular interest to this work and are explored in detail in chapter 2.

$$k = F\delta^{-1}; \qquad \textit{Eq. 1}$$

1.5 AFM scale force measurement

Force measurement at the microscale is not a trivial task even with the latest metrological tools and techniques. To obtain a metrologically significant force measurand two co-dependent steps are undertaken – interaction sensing and sensed information interpretation. Quantification of the measurand, in this setting – quantitative measurement of force component, is expressed as a most likely value with a stated degree of confidence (certainty) that it is assessed to carry. If the measurement is conducted using a traceable measurement system, the measurand can be expressed in absolute terms that allows individually obtained measurements to be compared. Per SI, the considered unit of measurement is the Newton (N), which is composed of three base units - kg m s^{-2} [60] - as force is derived from mass through Newtons second law ($F=ma$). The current metrologically recognised and industry adopted small-scale force measurement standard is a characterised deadweight balance (CMCs [61]). Whilst it may provide direct measurement traceability to the SI, it is limited in application by the $>10^{-1}$ N range measurement ability, as it lies some orders of magnitude away from the typical AFM range of 10^{-10} to 10^{-6} N. Alternatively, a standard mass application may be employed, allowing for an indirect traceability to SI in the range of 10^{-1} N to 10^{-6} N [62]. Therefore, by national metrology institute's own recognition (EURAMET [63]), the AFM scale force measurements are not directly supported by the conventional metrological standard and calibration chains. Although efforts to establish a suitable tool (e.g., a precision compensation balance and nano-positioner [64]) with required accessibility are in development, for the absolute majority of users - i.e., those not involved in the force

balance tool adaptation and development, this means that the 10^{-10} to 10^{-6} Newton force range encountered in AFM interactions cannot be traced to SI.

Non-traceable force interpretation options rely on dimensional metrology methods (based on optical and electrical detection) that do not suffer from scaled solid-body manufacturing challenges and can be used in tandem with mechanical structures to assess the degree of deformation, permitting a transformation of displacement into force. The sensory choices for force measurements are extensive - e.g., mechanical balancing, acoustic sensing, resistive, inductive, capacitive, and magnetic - meaning the force transduction may be achieved via a mechanical, electrical or hybrid response [65]. The detected signal is then transformed into SI defined force measurand via means of comparison to a known force reference. The combination of these principles into an electro-mechanical transducer with control and drive instrumentation is the technological basis of the current micro-scale force measurement solutions, to which the Atomic Force Microscope - an optical detection system employing a mechanically responsive structure - falls under.

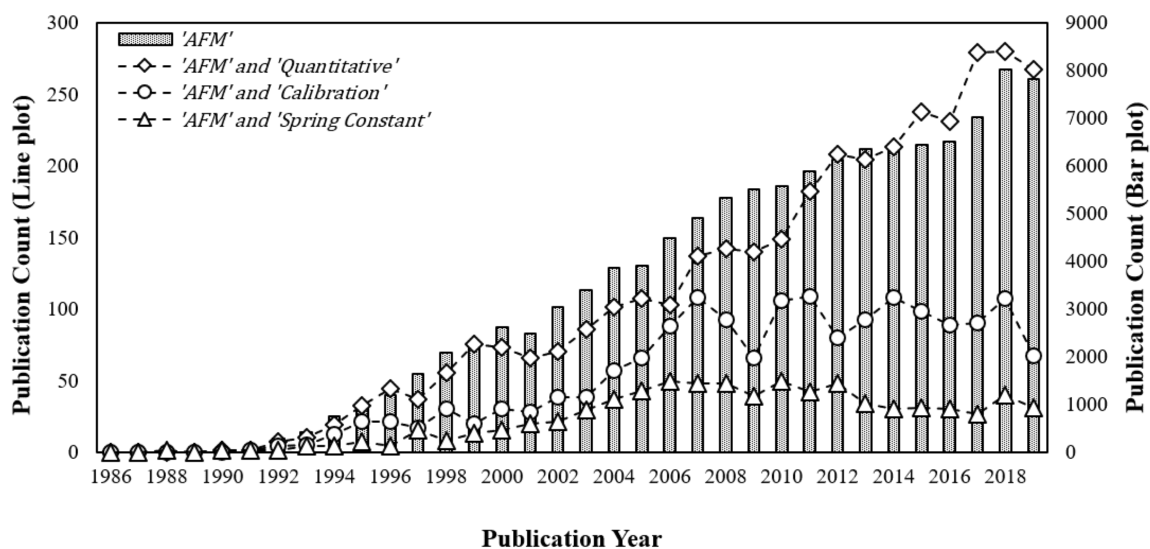

Figure 6. Publication volume of the AFM sub-fields by keyword phrases, according to Web of Science index [66].

The general use of AFM and particularly its deployment in quantitative measurements are progressively growing fields, which is illustrated by the keyword specific annual publication volume (Figure 6). This growth rate is however unmatched by the publications focusing on cantilever elastic constant quantification, typically classed under ‘spring constant’ and ‘calibration’ keywords. The apparent stagnation in calibration focused publications since 2005 may indicate that the field has adopted a separate standard for elasticity determination, since interest in quantitative measurements had continued to increase. A review of calibration techniques [67] released the same year included developments in critical dimension force microscopy (CD-AFM) and the NIST force-balance calibration project [68], destined to become the traceable metrological standard, which may suggest that the quantitative AFM community had settled on the status quo method. However, whilst this established a pathway to traceable measurements [69] and found repeated success in adoptions as a force transfer standard [70], the solution remained incompatible with in-situ operation, and as a result, it did not find wide adoption within wider AFM circles. This highlights the continued metrological interest in establishing an SI-traceable, small force measurement standard that will achieve wide acceptance, which hinges on a practical and logistically convenient procedure [71] [72].

Other solutions do claim the desired accuracy and traceability potential. These are further adaptations of electrostatic [73] and electromagnetic [74] force balances as well as photo-elastic sensing miniaturisations [75], although they too have yet to find their way to AFM laboratories for similar practical application limitations. Instead, a typical AFM force measurement calibration is conducted via separate deflection and elasticity determinations by indirect observation, resulting in the widespread acceptance that ‘quantitative’ force

measurements in the context of AFM are only able to define relative rather than absolute force magnitudes [76].

1.6 Thesis direction

The atomic force microscope is often offered as the de-facto solution for nanoscale force measurements, yet due to the limited accuracy of the available elasticity characterisation techniques necessary for this function, AFM validity as a force referencing tool is often debated [77]. These practical, rather than technological limitations mean that users have adopted indirect elasticity estimation methods that are of limited applicability to increasingly complex AFM cantilever structures. The presented work describes a novel MEMS device that allows for detailed elasticity characterisation of AFM cantilevers of 'unknown' mechanical properties. The research and development of this candidate solution is described in the following work, focusing on addressing these key areas:

- Current AFM probe elasticity characterisation technique review and practical exploration through a case study in chapter 2.
- Introduction of necessary theory and concepts behind structural mechanics, electrical sensing and instrumentation considerations required for device development in chapter 3.
- Description of the adaptation and targeted optimisation of state-of-the cleanroom-based processing and development of the micro electro-mechanical sensor in chapter 4.

- Addressing metal thinfilm sensing accuracy coupled with practical usability challenges in post-fabrication characterisation and demonstration in chapter 5.
- Operational demonstration by in-situ cantilever elasticity characterisation of complex AFM probes in chapter 6.

Chapter 2 - Review of the AFM probe elasticity characterisation techniques

The case study conducted in this chapter will investigate a range of techniques, each relying on differing philosophies of elasticity characterisation, that are compatible with the investigated cantilever - an off-the-shelf reference calibration structure, thermal fluctuation interpretation and nano-indentation based bend profile characterisation.

2.1 AFM probe elasticity characterisation literature overview

In the optical deflection detection employed in most AFM systems, force measurement is obtained through the elastic response of the interacting structure. This structure is simply referred to as 'the cantilever' due to its geometric characteristic of single fixed and single free end. As a result, the quality of its elastic characterisation is transferred to the accuracy of force measurement. Early designs of hand-crafted laboratory-unique cantilevers [78] have long since been replaced by commercial adaptations of consistent, batch produced microfabricated structures [79]. These now have a well-established record performing metrologically reliable measurements at the nanoscale. Whereas even hand fabricated probes could obtain the unprecedented topographical scanning of nanometre structures, the increasing structural complexity of microfabricated probes, compounded by the increasing use of functionalisation [80] [81] [82] quickly rendered the most basic elasticity characterisation methods inadequate. As will be discussed in chapter 6, these methods are generally not valid for cantilevers with complex geometries, or those functionalised with sensing and actuating features. However, the demands for increased accessibility, even with a penalty to accuracy or lack of direct traceability, have spawned development of

numerous solutions for calibration - reference structures, sensors, theoretical static and dynamic property-based descriptions [83] [84]. Some of these methods have found commercial success and user approval based on cost and ease of use, confirming an acceptance of relative over absolute measurement.

The first calibration solution concerned with practicality and ease of use was published in 1992 by Cleveland et al. [85]. This demonstrated the dynamic quantification of cantilever natural resonance shift caused by attaching a known mass to the AFM cantilever. The principal measurement of cantilever resonance amplitude versus its frequency could now be done in-situ without knowledge of the cantilever elastic constant value and with hardware already present in many optical-lever equipped AFM systems. The method employs a simplistic harmonic oscillation model with estimated or measured mass and velocity change to quantify the elastic dampening component, from which a cantilever elasticity can be expressed. Alternatively, an appropriately setup laser-doppler vibrometer system (LDV) can be used for the same purpose ex-situ, as preferred in cantilever mechanical quality assessment of probe batches [86] (as demonstrated further in section 5.1.3). No external driving force is necessary to excite the cantilever, since it is possible to capture the angstrom[1] level thermal vibration amplitudes using the optical lever or LDV. The magnitude of background noise caused by Brownian motion is related to the cantilever and its surrounding fluid temperature, which is particularly challenging to determine locally at this scale - an attractive solution for this challenge is demonstrated with the newly developed MEMS device in section 5.3.2. The major technical and accuracy disadvantages of this approach are caused by the uncertainties associated with the mass quantification via

---

[1] 1 $A = 10^{-1}$ m, sometimes against convention noted as $\mathring{A}$ [79].

a partial dimensional assessment and simplified dynamic expressions that are not straightforwardly transferable to complex structures. The practical challenge of reliable mass attachment and detachment ex-situ is also not a risk-free exercise – a handling step which users can avoid with later-developed solutions, suggesting why the technique is not commonly used today.

In 1993 Hutler et al. [87] introduced a further dynamic observation based method, now known as as 'thermal tune calibration'. Similar to Cleveland's solution, it involved analysis of an acquired resonance spectrum, but with a critical distinction in the data interpretation method. The technique relates the total thermal energy in the system to the observed motion velocity and displacement of the cantilever through a dissipated elastic energy model. For the first time, no additional metrological tools outside conventional AFM hardware were required. As a consequence, a software enabled spectrum analyser and mathematical processing are now shipped with most commercial AFM systems as the technique has since established itself to be a default 'push of a button' calibration solution. The wealth of published geometry and fluid specific correction factors [88] [89] [90] illustrate an often-ignored aspect of the technique's idealised motion interpretation – whilst it is excellently descriptive in straight-cut cases of linear rectangular and 'V' cantilevers when compared to a traceable standard [91], it is of limited applicability to more complex cantilever structures exhibiting nonlinear behaviour that are increasingly popular in quantitative AFM measurements. An experimental demonstration and discussion through a case study is described in detail in further work (section 2.3).

In direct response to Cleveland's added mass method, another practical and thus highly popular approach in relating dynamic behaviour to the elasticity constant was introduced

by Sader et al. in 1995 [92]. The newly formulated interpretation did not rely on a physical modification to harmonic properties (an anticipated improvement by the community), but instead mathematically related the observed geometry and resonant mechanical behaviour to a form of hydrodynamic transfer function, which could also be applied under liquid environments [93]. The publication itself recognised the vast uncertainty budgets associated with AFM cantilever elasticity characterisation techniques and extended the discussion to overall AFM-specific measurement difficulties arising due to the lack of standardisation. Two decades later, the same author introduced a 'virtual' standard transfer tool [94] via an online database in an attempt to observe cantilever variations and to create a statistical transfer platform through individual observed thermal resonance data, mitigating the laboratory-specific cantilever elasticity determination uncertainties. Here, the uncertainty reduction relies on the size of the statistical set, naturally benefiting data acquired with commonly used cantilevers. As a consequence, experimental and prototype cantilever designs are not supported, requiring dedicated modelling and statistical study efforts from the interested parties.

Recognising the difficulties in dynamic behaviour interpretations, in 1995 Torii published a reference cantilever elasticity relation method [95]. This demonstration employed a reference elastic structure of increased scale when compared to a typical cantilever, improving the accuracy of dimensional characterisation. The analytically obtained load-deflection characterisation of the reference cantilever in turn could be transferred to the 'unknown' property of a cantilever via comparison of force-displacement curves obtained using the cantilever under test during interaction with the known elasticity (reference) cantilevers. This direct physical interaction method, received further development and

application improvements by Gates and Reitsma [96], and has since become established as a direct static elastic property characterisation technique. A detailed discussion and application examples employing an off-shelf product are presented in - section 2.4. The demonstrated potential of the method to be scaled to different force ranges also meant that previously unsuitable techniques, such as instrumented indentation, could be used to characterise the reference structure, in turn transferring the elasticity projection to AFM cantilever measurements.

Tortonese et al. [97] showcased a philosophically different approach in 1992, focusing on direct elasticity interpretation via a dedicated MEMS sensor. Whilst this is not a method for cantilever calibration per-se, it is a technique that can resolve Force interactions in an AFM setting, the demonstration of which inspired numerous other force and elasticity measurement solutions. The introduced stiffness and deflection measurement was conducted using a strain sensor placed on the AFM cantilever paving way for the development of dedicated MEMS sensing, that can be integrated in parallel with the conventional AFM composition, demonstrating unprecedented accuracy [98]. The method allowed for an attractive simplification of the AFM deflection measurement hardware, at the cost of a complex and purpose-built active cantilever system. The following year (1993) Jarvis introduced another example of a self-sensing cantilever, this time via integrated magnet-coil sensing system [99]. The method brought a novelty of bypassing the cantilever elasticity component altogether and directly inferred interaction forces from the AFM tip. In the subsequent year, Scholl [100] introduced a capacitively sensed cantilever, now the third electro-mechanical transduction solution - all of which have since been adapted into potential calibration tools, but not as work-horse probes in general purpose AFM systems.

As AFM probes are consumables, outside of the niche applications where the integrated detection and actuation functions are essential (e.g. [101]), most users and manufacturers have preferred to invest in permanent deflection sensing hardware in the microscope, allowing the use of a wide range of low-cost probes differentiated by their suitability for scanning a particular type of sample, rather than by their suitability for scanning within a particular instrument.

The current EURAMET recommendation [63] regarding traceable elasticity determination at the nanoscale is to use a dedicated tool comprising of a precision compensation balance and nano-positioner [64]. Access to such a tool, as well as the complexity involved in obtaining a measurement within the AFM, is prohibitive to most AFM users, therefore it is not surprising that to-date neither industry nor the AFM research community widely rely on this tool. The demand for accessibility and ease of use, even at the cost of accuracy or lack of traceability, has therefore driven development of the indirect experimental techniques introduced, some of which have found commercial success and user approval thanks to their favourable economic and practical characteristics - enabling the experimental review demonstration described next. It should be noted that some popular and well recognised methods were not investigated in the following practical review due to their intrusive and potentially destructive nature (added mass in static [102] and dynamic [85] characterisation), resulting in them being closely supplanted by other techniques already being considered (e.g. resonance in air interpretation through Sader method [93]) or accessibility - unavailable due to their developmental or cost prohibitive nature (instrumented elasticity reference samples [103] and dedicated force balancing structures [63] [104] [105]).

2.2 Technique review through a case study

A case study on some of the most prominent AFM probe elasticity assessment techniques is conducted next, serving as a supplement to the earlier literature overview. By investigating a single AFM cantilever, the study aims to highlight technique related strengths and weaknesses, focusing on inputs and processing steps involved when defining the experimental output as an elasticity value. The absolute or true elasticity figure for the investigated structure cannot be determined or traced to a standardisation instruction due to the lack of established access to an international standard. Therefore, it is not possible to comment on measurement accuracy for the investigated techniques and the use of *calibration* term throughout the text is suggestive of its user adopted meaning - elasticity scalar value determination - and not an international standard or procedure. The summarised findings will be used to identify and attribute preferred qualities and possible improvements to the considered methods, which will outline a basis for the proposed elasticity characterisation method described in further chapters.

By convention, the force component in AFM experimental routines treat cantilever elastic bending as the linear compression of a spring. This allows Hooke's law (Eq. 1) to be employed, relating AFM registered cantilever displacements to forces experienced between the AFM tip and substrate. In order to describe an AFM cantilever as linear it is required that the displacement component in Hooke's law is constant throughout the deformation range of the cantilever, ranging from sub-nanometre up to tens of micrometres. The key (but non-exhaustive) requirements for a near-linear cantilever spring undergoing quasi-static displacement in its elastic region are:

- a single clamped (fixed) end and opposing end unconstrained (free),
- uniform cross-section and internal stress distribution,
- length of the beam is much larger than the free end displacement and the width of the beam is much smaller than its length - per slender beam requirements of an Euler-Bernoulli beam definition [106].

These requirements are often not met in the most abundant modern-day cantilever designs – e.g. film coated and sensing (functionalised) cantilever probes. Therefore, in order to introduce the least obscurity into the intra-technique comparison case study, the most basic composition contact mode cantilever was chosen – whilst acknowledging that this is not necessarily representative of the most common and/or technically challenging probes employed in the community. The studied cantilever, available off-the-shelf as Veeco MPP-21100-W (currently superseded by Bruker RFESPW-75 [107]), was taken from a wafer with production number 2149 [108] (Table 1 and Figure 7).

Table 1. Veeco MPP-21100-W Cantilever manufacturer provided specifications.

	Nominal	Min	Max
Length, µm	225	215	235
Width, µm	35	30	40
Thickness, µm	4	3.5	4.5
k - Spring Constant, N m^{-1}	3	1.5	6
Resonant Frequency, Hz	87.5	80	95

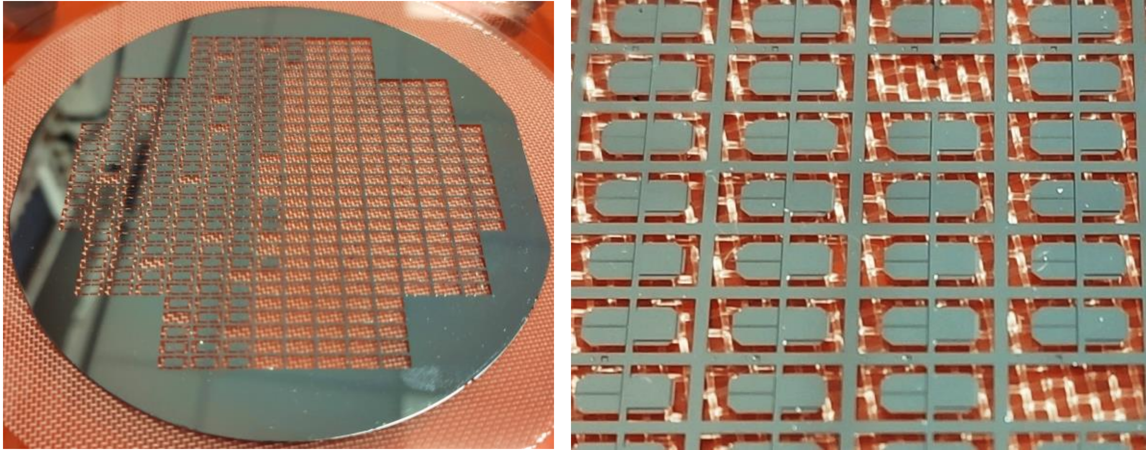

Figure 7. Batch produced Veeco MPP-21100-W probes, wafer no 2149 (left) and close-up, highlighting of the 'pop-out' style probe retention and release features on the microfabricated probe wafer (right).

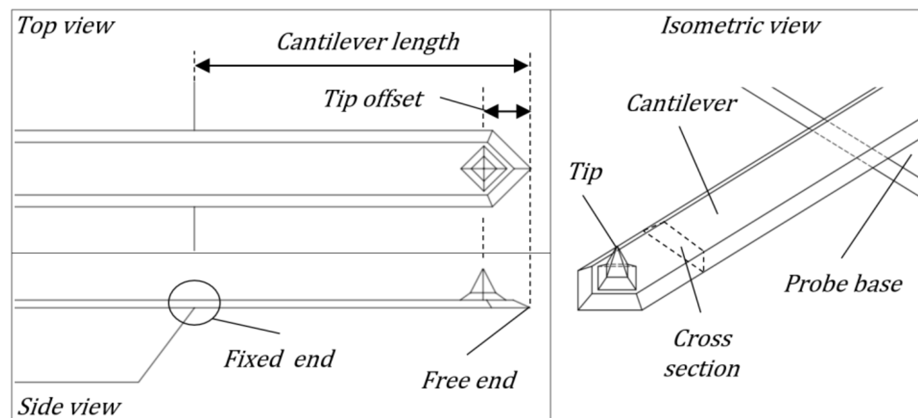

Figure 8. The schematic representation of the investigated AFM cantilever geometrical composition.

The probe is an uncoated, uniform cross-section, plain silicon cantilever (Figure 8), that is well suited to be described with minimal simplifications and corrections using common elasticity estimation methods. The most notable exceptions are the cross-section non-uniformities present at the free end, non-rectangular (trapezoid) cross section, presence of end mass in the form of a tip pyramid and the offset tip, meaning that any tip force applied

will also be distributed and offset. This deviates the structure from some technique specific simplifications, which will be discussed further where appropriate.

The starting point of this investigation was the most trivial way of obtaining an elasticity estimate – by referring to manufacturer specified geometrical and mechanical properties (Table 1). The manufacturer provided nominal cantilever spring constant was 3 N m^{-1}, covering a large range of extremities - 1.5 to 6 N m^{-1}, meaning the tremendous 400% variability is also transferred to any AFM force measurements conducted with the provided guidelines. What is clear from the supplied data sheet is that tolerance control is difficult during batch fabrication and variance wafer to wafer is anticipated by the manufacturer. It may be stipulated that the major contributor to this elasticity variance is due to the difficult process control of the microfabricated cantilever thickness definition - a component which is related to the cantilever elasticity by an inverse cubic relationship (to be introduced in 3.1 and eq. 22). The process specific limitations on achieving the resultant cantilever thickness is challenging to manufacturers due to the time-sensitive nature of anisotropic etching (akin to the process described in 4.5) and is typical to most batch produced silicon AFM cantilevers (ref. to 3.1.1 for supporting dimensional characterisation). This manufacturer provided elasticity is unlikely to be sufficient for any quantitative force measurement within an AFM setting, however at the very least it indicates an initial (expected) elasticity magnitude from which compatible calibration experiments and techniques may be identified. Whilst adopting the nominal elasticity specification is infinitely better than ignoring cantilever spring constant altogether, any user intending to employ the force component of AFM is well advised to look further into experimental characterisation techniques - for example, the thermal tune, reference spring and nano-

indentation equipment, and conduct an individual investigation of their probes. Whether a casual end user chooses to utilise manufacturer suggested nominal values or decides to conduct their own assessment based on quoted cantilever dimensions, it is important they appreciate the variance natively present in most micro-fabricated probes.

2.3 Elasticity characterisation via thermal fluctuation interpretation

Thermal tuning, as introduced by Hutter and Bechhoefer [87], is a technique that aims to experimentally characterise the elasticity of AFM cantilevers by interpreting their energy dissipation from thermally induced oscillation. Its popularity is unprecedented, with many AFM users making use of its accessibility, setup simplicity and non-destructive nature. It is generally regarded and presented as a ‘single button’ solution to AFM cantilever elasticity calibration, and is thus highly automated, requiring little user input or appreciation of its heavy reliance on various assumptions and simplifications. However, according to literature best practices and not relying on the tested AFM system built-in processing algorithm, the work presented here will analyse this data ‘by hand’.

The required acquisition tools are built-in and setup with most modern AFM systems and consist of conducting a power spectrum analysis of cantilever oscillation near its resonance frequency whilst it is excited thermally by a surrounding fluid. The technique relates the system thermodynamic energy scale “k_BT” (where k_B is Boltzmann constant and T is temperature) to the observed oscillation velocity and displacement spectral density ($<z^2>$) in order to solve for the elasticity constant (k), as expressed in Eq. 2:

$$k = \frac{k_B T}{< z^2 >}; \qquad \textit{Eq. 2}$$

All experimental data was obtained using a Bruker Dimension Icon AFM [25] system utilising its environmental enclosure (previously shown in Figure 2). First, the sensitivity of the system was determined, relating the optical lever registered cantilever displacement to piezo-element measured vertical axis travel - procedure explained in detail in section 2.4 and Figure 14. This was subsequently used to obtain the deflection velocity of the thermally

excited cantilever by measuring its displacement amplitude and frequency. Using the AFM's built in spectrum analysis hardware/software the deflection power spectrum density was recorded (Figure 9). The peak of the first resonance frequency was observed to be at 86229 Hz, which is within the manufacturer provided range of resonances (80-95 kHz, Table 1), obtaining a first experimental agreement that the structure performs in line with manufacturer characterisation. The spectrum plot allows for a Lorentzian fit to be obtained in the ± 3000 Hz region around it (Figure 10, Eq. 3), which sufficiently encapsulates the area of the observed peak above the noise line. The area under the noise baseline was excluded due to the assumption that it is a background signal and does not contribute to the power dissipation of the cantilever, hence only the positive area was considered in the numerical integration, which obtained the $\langle z^2 \rangle$ value (Eq. 4).

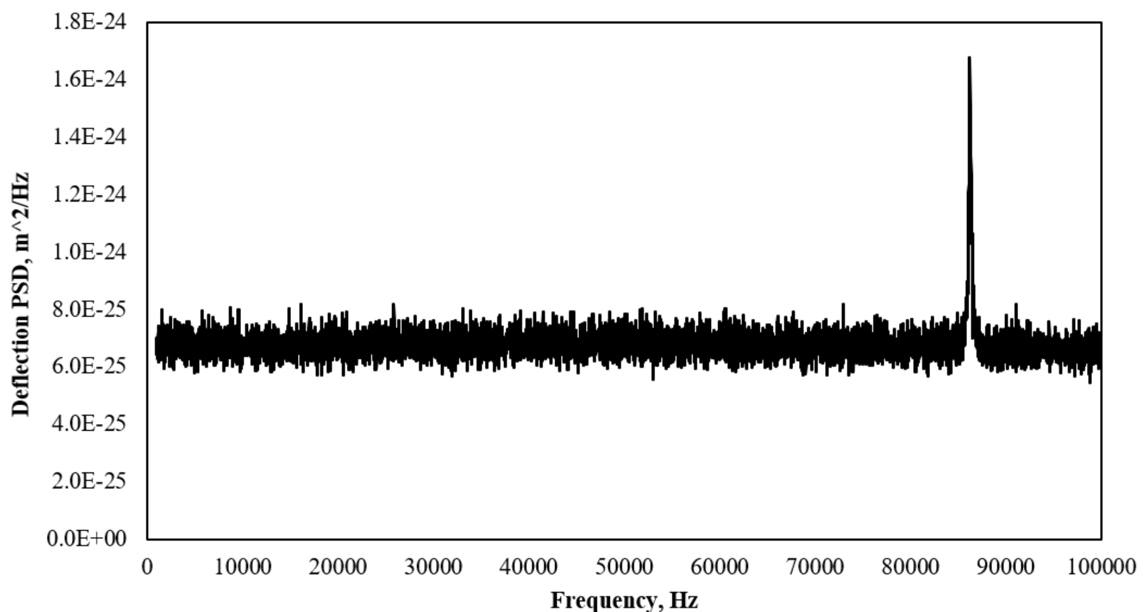

Figure 9. The full range (1-100 kHz, bandwidth - 7.63 Hz) acquired Thermal Tune Power Spectrum Density capture for the Veeco MPP-21100-W cantilever.

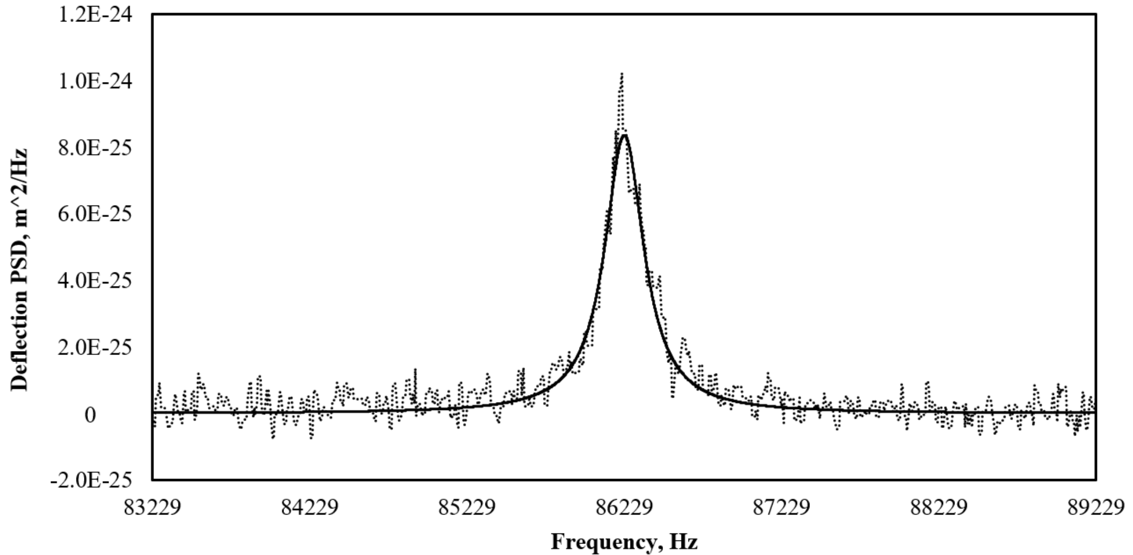

Figure 10. Lorentzian fit (solid line) over the raw signal (dotted line) of the cantilever natural resonance shape over the investigated frequency span.

$$F(x) = \frac{y_0 + a}{b^2 + (x - x_0)^2} = \frac{664.8 \times 10^{-27} + 19.312 \times 10^{-21}}{(x - 86229)^2 + 23088.8} \qquad \textit{Eq. 3}$$

$$< z^2 >= \int_{x_0}^{x_1} F(x) \qquad \textit{Eq. 4}$$

$$= \int_{83229}^{89229} \frac{664.8 \times 10^{-27} + 19.312 \times 10^{-21}}{(x - 86229)^2 + 23088.8} dx = 3.8643 \times 10^{-22}\ m^2;$$

The measurement was repeated 50 times at one-minute intervals, emphasising the technique's speed and more importantly - the extremely small degree of variation between the obtained $<z^2>$ values (Table 2). The attributed natural distribution is also implied from the measurement spread density (Figure 11), allowing the statistical confidence limits of the measurand to be expressed. It should be emphasised, that this statistical expression focuses on the practical repeatability and thus the statistical confidence of the measurement, and not the measurement uncertainty in the conventional metrological definition, as it does not include the experimental setup unique uncertainty contributors

(e.g. the thermometer, AFM calibration detection and displacement calibration data), which are laboratory specific.

Table 2. Thermal tune <z²> statistical component summary.

Mean, $\langle z^2 \rangle$	$3.8663 \times 10^{-22}, m^2$
Number of observations	50
Standard deviation, $s(\langle z^2 \rangle)$	$5.7032 \times 10^{-24}, m^2$
Margin of error, $e(\langle z^2 \rangle)$	$8.0656 \times 10^{-25}, m^2$
95% confidence limit coverage (1.96e)	± 0.41 %

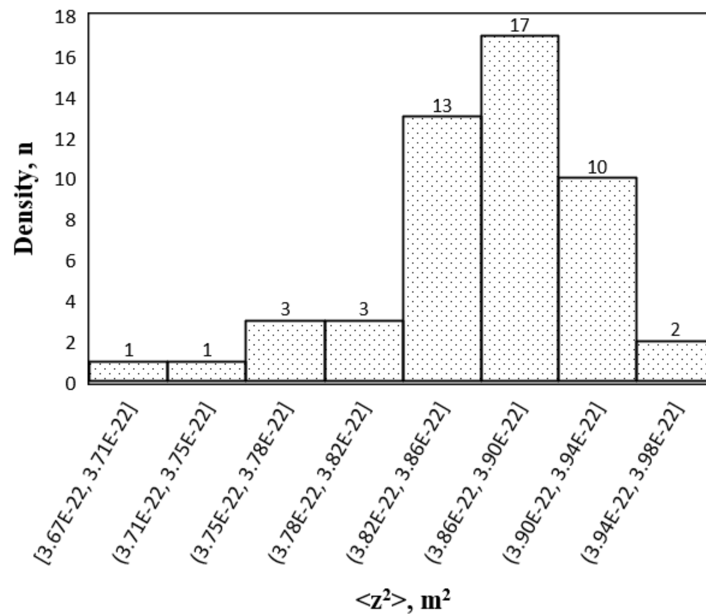

Figure 11. Thermal tune obtained $\langle z^2 \rangle$ integral variation density, indicating a natural distribution.

Since exact local thermal conditions surrounding the cantilever are not possible to determine with a conventional AFM system alone (a solution to be discussed in 5.3.2), an estimate temperature reading of 294 Kelvin is taken from a few cm proximity by a K-type thermocouple, which is then employed in the final expression allowing for the elasticity constant to be calculated using Eq. 2:

$$k = \frac{k_B T}{< z^2 >}$$

$$= \frac{1.38064852 \times 10^{-23}\, m^2 \times kg \times s^{-2} \times K^{-1} \times 294\, K}{3.8643 \times 10^{-22}\ m^2}$$

$$= 10.51\, kg\, s^{-2} = 10.5\, N\, m^{-1};$$

Due to the widespread use of this calibration technique, it receives constant attention from users and developers who have introduced additional improvements and corrections to this fundamental expression, allowing for further data interpretation steps to be explored. For example, an inclusion of a correction factor of 0.971 addresses the afore-mentioned fact that only the energy stored in the first bending mode is considered [109], proportionally trimming the elasticity estimation, as shown in Eq. 5. The validity of this approach has been experimentally confirmed in [88] and is generally accepted by the community and manufacturers as the default for thermal fluctuation elasticity determination of reasonably high Q factor rectangular cantilevers, even though it only contributes a comparatively small (2.9%) adjustment.

$$k = 0.971 \frac{k_\beta T}{< z^2 >} = 10.2\, N\, m^{-1}; \qquad \textit{Eq. 5}$$

Another common correction is the correlation of cantilever displacement amplitude to the angular change interpretation provided by an optical lever system - since the measured thermal noise correlates strongly to the spot size, due to the nature of photodiode operation which is based on laser reflection intensity change interpretation [90]. To achieve this, knowledge of the cantilever's planar shape is required as well as certainty about the cantilever's total length relation to laser spot size in order to apply an appropriate correction constant, that the user is required to identify from literature [109]. For the investigated

cantilever, the manufacturer provided planar dimensions and knowledge of the laser spot size (shown in further studies, e.g. Figure 85), the appropriate correction factor was identified to be 1.09, per [110] and [111]. This squared factor is integrated in most commercially available AFM thermal tune processing tools that employ optical lever detection systems, adding another correction factor to the fundamental expression - as shown in Eq. 6.

$$k = \frac{0.971}{1.09^2} \frac{k_\beta T}{< z^2 >} = 8.6\, N\, m^{-1}; \qquad \textit{Eq. 6}$$

Finally, a mounting angle correction is addressed, relating the in-situ observed cantilever elasticity to its mechanical structure property. Such a correction is necessary due to the fact that AFM cantilevers are typically mounted at an angle α (typ. 10° - 15° from parallel to surface and 13° in the tested AFM system), allowing the final thermal tune expression for the described setup in Eq. 7 to be obtained.

$$k = \frac{0.971}{1.09^2} \frac{k_\beta T}{< z^2 >} \times cos^2 13° = 8.2\, N\, m^{-1}; \qquad \textit{Eq. 7}$$

This final elasticity figure of 8.16 N m^{-1} exceeds the manufacturer identified nominal elasticity figure nearly three-fold. Whilst a dedicated uncertainty analysis was not conducted in this instance, the literature reports the method measurement uncertainties in the 10-20% range [112] [113] [114]. This means that even accounting for the measurement uncertainty, the obtained elasticity expression is outside the maximal indicated elasticity modulus of 6 N m^{-1}, illustrating that the elasticity variation in AFM structures is often even more excessive than the already broad range provided by probe manufacturers (to be expanded upon in section 3.1.1 and 3.1.2).

It can be seen why thermal tuning is an attractive technique that can obtain an elasticity modulus for simplistic composition AFM cantilevers thanks to its high speed, conventional instrumentation (often integrated in AFM) and non-destructive operation. The technique's application is challenged by the indirect nature of the elasticity characterisation, which for confident results require user caution when applying appropriate output correction factors. Cantilevers with complex geometry thus exhibiting complex dynamic behaviour, outside the idealised harmonic oscillation expectations, are not represented by the ready-developed literature descriptions, limiting the technique's applicability for structures beyond the most basic composition - as will be demonstrated in chapter 6.

2.4 Elasticity characterisation via comparison to elastic reference

A common way of understanding forces at the nano/micro scale involves relative or proportionality-based comparisons between observed elastic deformations. In Atomic Force Microscopy such interpretation may employ a reference structure of a known elasticity structure such as cantilevers [84] [96] or beams (e.g. glass fibres [115] or torsional springs [103]). One common elastic reference configuration is a cantilever spring, much like the AFM cantilever, but with minimal geometrical complexities - e.g., a lack of coatings or sensing enabling features such as tips or sensors. The calibrated (reference) cantilevers themselves are characterised using external calibration tools e.g., dynamic methods that deliver a good relation between elasticity and frequency thanks to the appropriately simple cantilever shapes. Ultimately, the elastic reference structure allows 'transfer' of a chosen elasticity characterisation method to the AFM cantilever context via the two elastic spring interaction analogy (Eq. 8), which has been arranged into an expression that accommodates an AFM force-distance curve gradient by the technique's developers, Gates and Reitsma [96] (as shown further in Eq. 10 and Figure 12).

$$k_{combined} = \left(\frac{1}{k_{reference}} + \frac{1}{k_{AFM}}\right)^{-1}; \qquad \textit{Eq. 8}$$

In order to explore the practical application of this static elasticity characterisation method, a commercially available reference grid - Bruker CLFC [116], Wafer No: A002/01 box 5 - Probe 5, was used to determine the elasticity of the subject cantilever (Veeco MPP-21100-W), following manufacturer instructions [117]. The manufacturer advises users to stay within the $0.3k_{reference} < k_{AFM} < 3k_{reference}$ range whilst conducting a spring-on-spring measurement [111], meaning the stiffest spring of 9.3 N m^{-1} was used, as informed by the probes estimated spring constant obtained in previous elasticity assessment.

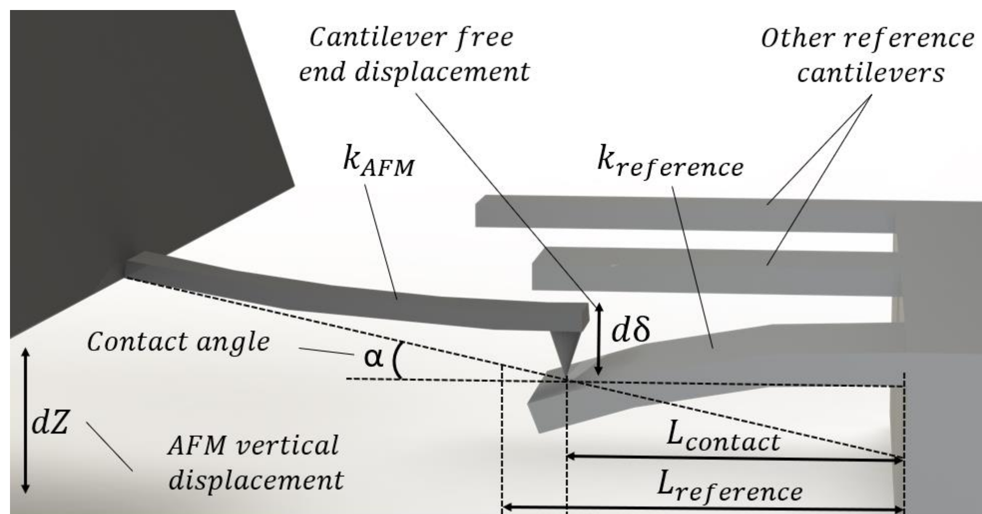

Figure 12. Spring on spring experimental schematic, depicting the soft interaction (S_{soft}) force-distance ramp and variable, figure inspired by Gates et al. [96] description.

The calibration or relative elasticity value transfer from structure to structure was conducted in two steps – by hard and soft contact force-distance ramp interactions (Figure 13). First this involved displacing the unknown spring constant AFM cantilever on an infinitely stiff spring (e.g. a bulk sapphire or silicon sample) employing the AFM's built in force-distance ramp routine, ensuring the only compliant component - the cantilever bend (dδ) was related directly to the observed vertical displacement (dZ). This provided the hard contact ratio S_{hard}, also known as sensitivity (Eq. 9). In this way, the cantilever bend displacement registered by the optical lever system could be related to the driven

displacement of the Z axis, plotted in Figure 14 and expressed in Eq. 10. Such a procedure is a prerequisite in many AFM experiments and is commonly referred to as sensitivity determination. Then in the second step, the AFM cantilever k_{AFM} was brought into contact with the cantilever of known stiffness ($k_{reference}$) and length ($L_{reference}$) at a determined contact point ($L_{contact}$). A force distance ramp routine was performed by the AFM system, where the vertical displacement (dZ) and resultant cantilever bend (dδ) was related to the ratio S_{soft}. A squared cosine component (α) is present in the equation to relate the normal elasticity component to the absolute elasticity of the cantilever, which arises from the contact angle between the interacting structures.

$$S = \frac{d\delta}{dZ}; \qquad \text{Eq. 9}$$

$$k_{AFM} = k_{reference} \left(\frac{L_{reference}}{L_{contact}}\right)^3 \left(\frac{S_{hard}}{S_{soft}} - 1\right) \cos^2\alpha; \qquad \text{Eq. 10}$$

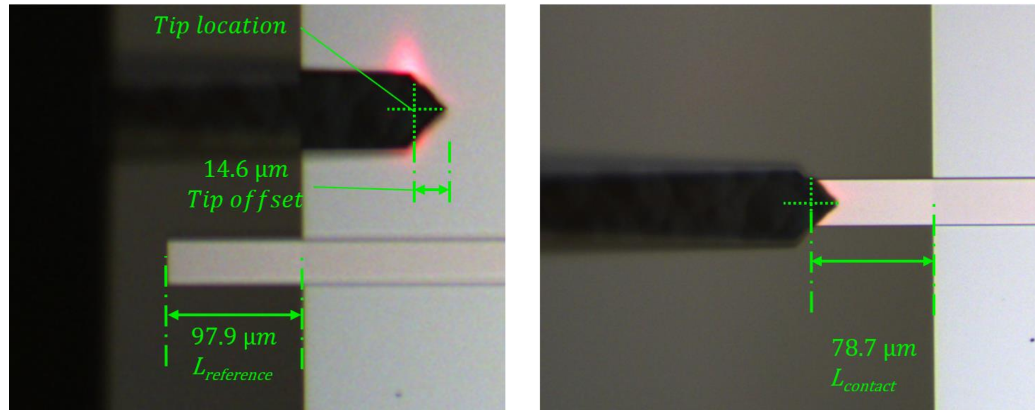

Figure 13. Tested cantilever positioned to interact in ramp mode with the bulk silicon surface (left) and reference spring (right), obtaining the S_{soft} and S_{hard} values.

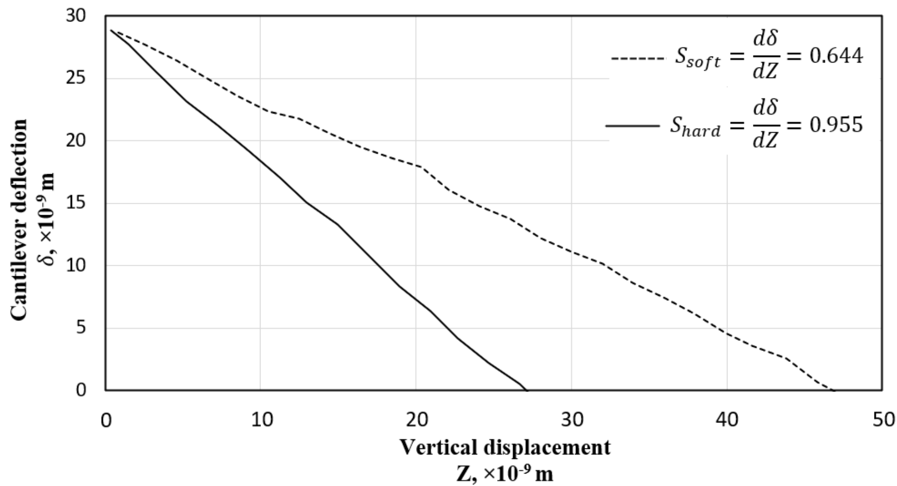

Figure 14. Veeco RFESPW probe f-d ramp engagement approach region on solid (S_{hard}) and CLFC calibrated spring (S_{soft}). The difference in curve steepness allows to relate curve gradient ratios to the known interaction elasticity of the calibrated spring.

The uncertainty analysis for this approach is non-trivial since a major contribution to uncertainty and error in the experiment rises from interpretation of the force-distance gradient linear region, the calibration certainty of the reference springs as well as the determination of the spring-on-spring interaction (or offset) point. Evidence from other reference grid studies indicate that uncertainty from 2 - 20% can be expected, depending on the chosen calibration transfer method [64] [112]. The bend gradients from 10 repeats (Table 3) were obtained by finding the best linear fit to the data points in the positive bend region using the method of least squares. Due to the low sample count, the distribution shape was assumed to be natural, in order to express the measurement 95% confidence interval.

Table 3. Spring on spring measurement interaction gradient summary.

Observation no.	S_{hard}, average	S_{soft}, average
1	0.9951	0.6444
2	1.0232	0.6638
3	0.9565	0.6332
4	0.9397	0.6108
5	1.1118	0.6181
6	1.0315	0.6289
7	1.0417	0.6185
8	1.0711	0.6069
9	1.0677	0.6026
10	1.0798	0.64887
Mean, S	1.03181	0.62761
Standard deviation, s(S)	0.05498	0.01996
Margin of error, e(S)	0.01739	0.006313
95% confidence limit coverage (1.96e)	±3.30%	±1.97%

Finally, the nominal elasticity figure for the investigated cantilever was obtained by applying the obtained variables to Eq. 10.

$$k_{AFM} = k_{reference}\left(\frac{L_{reference}}{L_{contact}}\right)^3\left(\frac{S_{hard}}{S_{soft}} - 1\right)cos^2\alpha \qquad \textit{Eq. 11}$$

$$= 9.3\ \mathrm{N\ m^{-1}}\left(\frac{97.9\times10^{-6}\ \mathrm{m}}{78.7\times10^{-6}\ \mathrm{m}}\right)^3\left(\frac{1.303181}{0.62761} - 1\right)\cos^2 13° = 10.9\mathrm{N\ m^{-1}}\ ;$$

It should be noted that the obtained figure of 10.9 N m^{-1} is noticeably higher (+34 %) than the value obtained using thermal tune, indicating the structural elasticity was interpreted differently. Since there is no absolute point of reference to aid in accuracy judgement, the practical conclusion is that the method is worthy of employment just by virtue of its approach to characterising elasticity. Specifically, this method loads the AFM cantilever being characterised through the tip and is therefore highly (if not completely) representative of the in-use load scenario. In addition, the technique requires minimal

mechanical or geometrical knowledge of the cantilever being characterised and is compatible with use within a standard AFM system - the tip offset being one notable exception for some cantilevers. However, the results do suffer from the limited positional placement ability of many AFM's navigation stages and camera systems, as well as inaccuracies in optical levers over large displacement ranges and non-standardised calibration reference samples, meaning users are likely to suffer from locally variable inaccuracies. Finally, the obtained force is not measured at the tip, but extrapolated from deflection much further down the structure - somewhere on the mid-point of the cantilever. Therefore, any possible bend compliance in the region between the cantilever tip and laser reflection point is not accounted by this method.

2.5 Elasticity characterisation by a nanoindenter

Nanoindenters are versatile tools employed in a broad variety of micro-scale material studies. Their high sensitivity load cell transducers combined with high resolution data logging, provide a sought-after ability to resolve nano/micro phenomena from direct interaction observation [118]. Aside from plastic deformation studies, nanoindenters can also be employed non-destructively to study elastic structural behaviour - such as AFM cantilever deformation. The following measurements made use of a commercially available indentation system - Hysitron PI85 Nano Indenter [119], mounted inside a ZEISS Sigma SEM [120] system (Figure 15) at the Henry Royce Institute facilities in Manchester[2]. Nano indentation is an attractive approach for elastic structure characterisation, although its application to AFM cantilevers is limited due to the fact that commercial nanoindenters are typically only just sensitive enough to directly measure interaction forces relevant to the stiffer AFM cantilevers - 1 N m^{-1} and above. Whilst their displacement sensing is capable of sub-nanometre resolution, their load transducers are noise limited at the bottom end, resulting in a practical detection floor of 0.5 to 1 $\times$ 10^{-6} N. In practical terms this means that a typical contact mode cantilever of 0.1 N m^{-1} will need to be displaced between 5 and 10 μm just to reliably register a force on the load transducer. This large deflection is not only potentially destructive to such cantilevers, but also means that the elasticity is characterised in a deformation range that may be far beyond its operating range. In addition, the fact that this measurement is made ex-situ of the AFM, requires a comparatively complex measurement setup and employs specialist equipment means that this approach

[2] Accessed through the Henry Royce PhD student access scheme, EPSRC grant EP/R00661X/1.

sees little use by AFM users, despite its promise for measurement accuracy. Having said this, the relatively stiff cantilever employed in this study is fully compatible with the limitations of this technique. The anticipated high stiffness (> 1.5 N m^{-1}, per manufacturer instructions, Table 1) of the cantilever combined with its deformation compliance, as indicated by its dimensions, suggest that it will be able to tolerate micro-Newton forces without exceeding its structural elastic limit. As an ex-situ assessment technique, the approach is slower and has higher costs than the previous methods investigated, however it benefits from the accuracy of the externally calibrated load cell and SEM derived positioning accuracy when compared to the deflection interpretation and optical microscope aided positioning offered by AFM hardware.

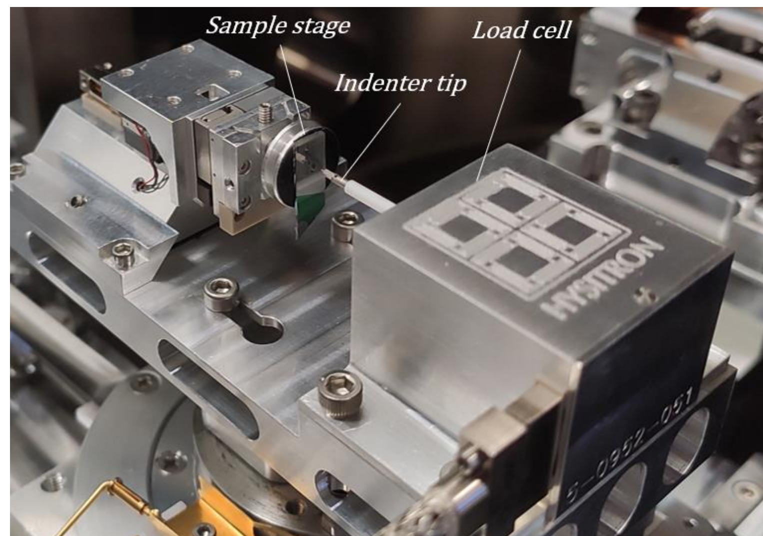

Figure 15. The nanoindenter with mounted sample (AFM probe not pictured).

The concept behind this characterisation is inspired by Clifford and Seah [121] as well as Z. Ying [122], who conducted a multi-point load study across the cantilever length and then extrapolated the data to find the tip point elasticity. In this way, the nanoindenter can

be used to mechanically displace a cantilever and define its elasticity at the contact point via interpretation of the force-distance plot generated.

In this case study, displacements were performed using a spherical end diamond cone tip, originally employed for bulk material indentation (Figure 16). Although a load case most resembling a real-life cantilever load condition would be a direct tip apex displacement by a flat 'landing pad' style tip attached to the nanoindenter load cell, such a configuration was not available in the instrument employed. Due to the practical positioning limitations, potential for cantilever damage or slippage of the diamond sphere and tip apex during interaction with each other, it was deemed unfeasible to attempt to load the AFM tip directly with the conical indenter tip. Another consideration was the orientation of the cantilever relative to the indenter. If the AFM tip apex was facing away from the indenter, it would be possible to perform an indentation at the back side of the AFM tip, emulating a load at an offset equivalent to a real AFM use scenario. However, this would result in the loading direction being opposite to the real-life AFM mounted orientation. In a scenario of a linear elasticity cantilever this should not have any negative affect, but more specialist AFM cantilevers that have non-uniform stress conditions or complex neutral axes can exhibit direction unique elastic behaviour, depending on whether the bend is positive or negative. Therefore, it was decided to collect the multi-point bend data along the cantilever length in the positive bend orientation as this retains the orientation of a real-life AFM load, allowing a multi-point experimental assessment of the bend shape to be conducted, from which the tip offset equivalent elasticity could be projected.

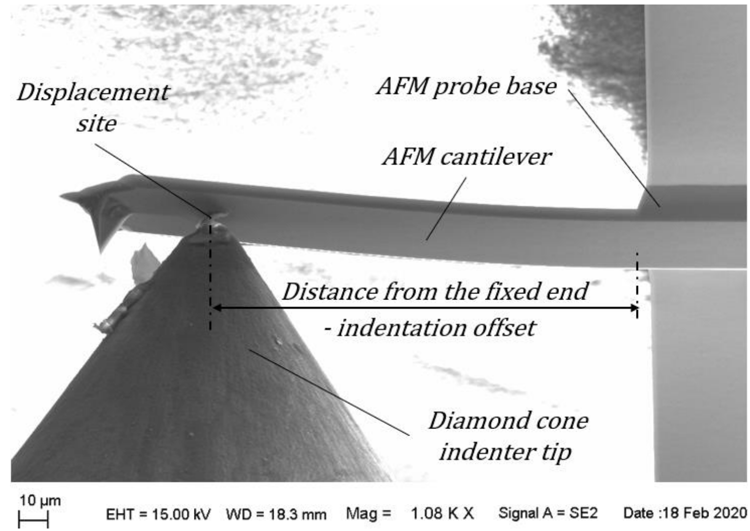

Figure 16. The nanoindenter tip displacing the AFM cantilever, captured at maximal indenter displacement.

The AFM cantilever was mounted perpendicular to the spherical diamond indenter tip at a shallow angle to the scanning electron beam. This allowed the nanoindenter displacement and load cell signal to be recorded and related to the captured SEM images. The AFM cantilever was displaced at nine points along its length (distance from fixed end indicated by k subscript), as shown in Figure 17. As desired, no plastic indentation upon spring back point and contact point was visible. This fact was confirmed by the overlapping load-unload curves indicating the indenter tip was displacing the compliant beam in near-perfect elastic interaction [123].

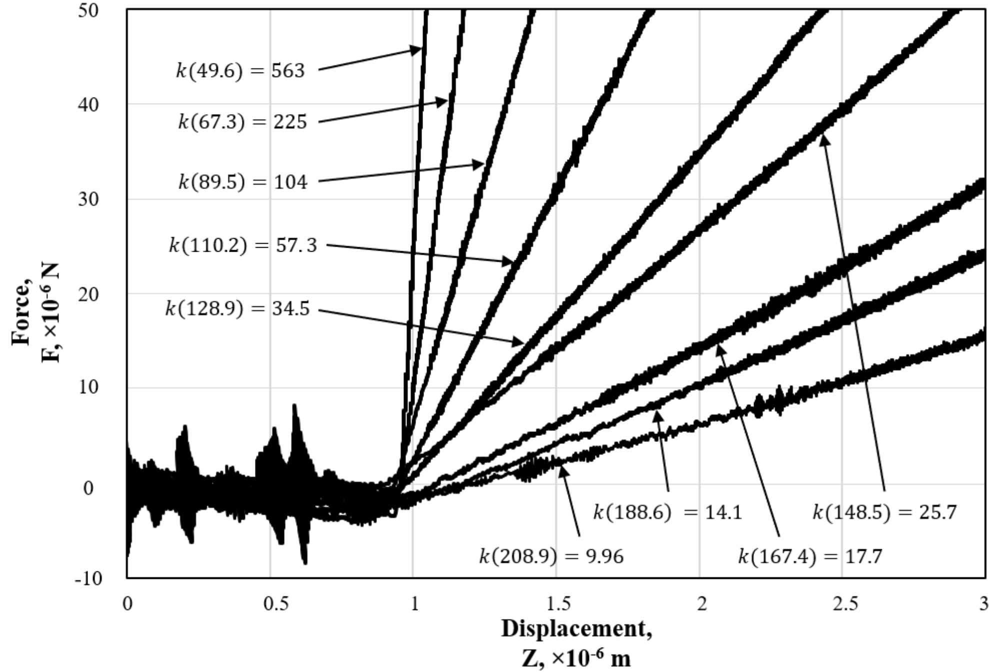

Figure 17. Indenter registered force-distance signals for the 9 tested contact positions. The offset specific elasticities (indicated in microns in k bracket value) resolved by derivation of the linear fit of the interaction region in N m^{-1} units.

The data was logged as the force experienced by the load cell versus the closed loop measured displacement, resulting in data analogous to an atomic force microscopy force-distance experiment, allowing the same interpretation and gradient extraction. In order to define the elasticity, the gradient needed to be resolved into the rate of change scalar ($\frac{dy}{dx} \sim \frac{dF}{dZ}$ = k in N m^{-1}) that could subsequently be used in the calculation. The gradient of the curve was distinct in all the tested positions and straightforward to define by a linear as visible in the plotted representation. It is worth noting that the experiment was setup as displacement-controlled ramp, with the AFM cantilever undergoing a maximum supported extension by the indenter (5 μm) in order to maximise the information sensed from the interaction. To ensure the engagement point was captured, the indenter was retracted from the contact point by visual aid only. The displacement ramp was then started before the contact point (equivalent to out of contact region in AFM), therefore the practical limit of

displacement became 1 or 2 μm smaller than the maximum permitted indentation range, limiting displacement at positions 1 to 4. A pre-set force limit of 50 μN was also applied in order prevent permanent plastic indentation (penetration) of the AFM cantilever, meaning that positions were force (rather than displacement) limited.

Knowledge of the offset specific elasticity properties allowed a bend profile to be defined for this beam by plotting the load proportional vertical displacement ($k^{-1} = \frac{dZ}{dF}$) versus the distance from fixed end (Figure 18). This provided a useful visual representation, proportionally resembling the cantilever bend profile shape, but also permitted a curve fit to be obtained that could then be used to project beam elasticity at a chosen offset. The bend profile was obtained by fitting a third-degree polynomial fit (per cubed length to stiffness relationship of a cantilever beam [124]) to the data points obtained by the offset specific indentation elasticity, allowing interpolation to give load proportional vertical displacement values at any chosen offset.

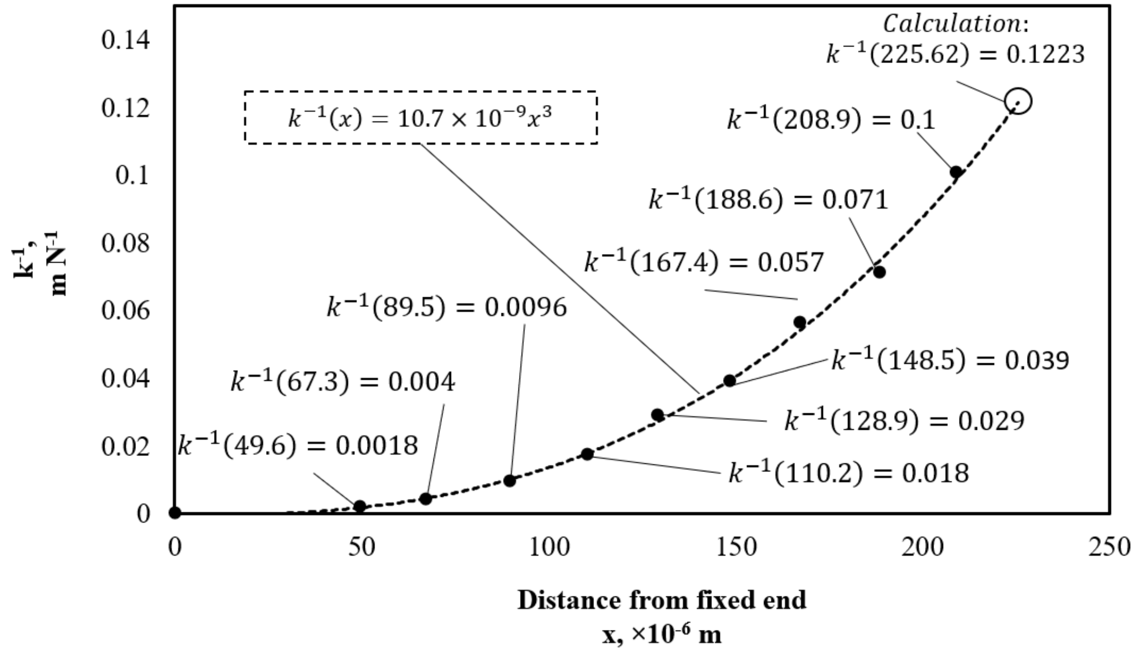

Figure 18. Offset to inverse elasticity, indicating the resistance to bend relationship plot, showing the third power fit line and the extrapolated calculation point at the tip offset value (k^{-1} expressed in units of m N^{-1}).

$$k = \frac{F}{[dZ]} = \frac{1}{\frac{dZ}{F}} = \frac{1}{0.1223} = 8.2\ N\ m^{-1}; \qquad \textit{Eq. 12}$$

The obtained $k^{-1}(x)$ function could then be solved for the point of interest - the tip location (225.6 µm), allowing the load proportional vertical displacement at the tip equivalent offset to be identified as 0.1223 m N^{-1}, per Eq. 12. In order to obtain the elasticity at the offset, the inverse of this value was taken giving a projected elasticity of 8.2 N m^{-1} at the probe tip. The major contributors to the errors with this measurement are associated with the offset estimation and load cell calibration. The calibration certificate for this equipment was not available at the time, therefore literature was employed to estimate a representative accuracy associated with this method. A guidance uncertainty was determined for an equivalent load transducer at a load similar to this work - 4 µN. The identified source [125] defines a load resolution (dZ) to load (F) ratio of 1.1% for conventional systems in this

loading range. The positional error was determined by SEM calibration and at the given scale (~1000 times magnification) was established at $\pm 10^{-6}$ m, (both x and y error bars are not visible in Figure 18 due to being eclipsed by the marker dot). It should be emphasised that the physical load-cell interaction allowed for much more in-depth characterisation of this beam's elastic profile without geometrical (exception of tip and indentation offsets from fixed end) or mechanical knowledge off the cantilever properties. It is also a significant advantage that the AFM tip was not touched at any point, reducing potential opportunities for contamination and damage. Obtaining and characterising cantilevers bend profiles is not available using rest of the other experimental methods investigated and can be immensely useful in structure characterisation - defining structural non-uniformity throughout the beam as well as operational corrections - e.g., compensation for optical lever reflection spot deviation from the tip-sample contact point.

The lack of reliance on extensive external dimensional characterisation or angular corrections native to in-situ methods, as well as knowledge of material properties required for analytical or modelling based approaches, appears to justify the use of such a complex instrument, albeit at the cost of practical inconvenience and limited application for softer AFM cantilevers.

2.6 Conclusion

The common techniques of experimental characterisation overviewed above highlighted the broad and varied approaches which have been taken towards the singular task of AFM cantilever elasticity (spring constant) determination. Since it has been established that as far as the public is concerned - no measurements at the considered scale can be directly traced to the SI, only a relative comparison between each techniques output could be conducted. When applied to the single structure characterisation, two of the three methods returned almost identical elasticity figures visible when additional significant figure is included - 8.16 vs. 8.18 N m^{-1}, thermal tune and multi-point indentation respectively. However, neither of these techniques physically assessed the elasticity property exerted through the cantilever tip, which in other cases, may be a significant contributor to the elastic behaviour characteristic. The in-situ reference spring method returned a value of 10.9 N m^{-1} - overestimating the other methods by a third. However, this method did involve observation of an operationally relevant behaviour - elastic deformation through tip, meaning that regardless of the structural composition, the complete cantilever elastic character was observed. The convenience of conducting this experiment in-situ is also suspected to be its major contributor to the witnessed disagreement with other methods. The necessary reliance on optical lever detection and the associated limited positioning accuracy of the interrogating laser leads to lack of reproducibility in force measurement due to alignment and displacement non-linearities. This is paralleled by the thermal tune method's reliance on single point optical lever detection, which is not appropriate for AFM structures with complex composition, that are of interest to this work (to be demonstrated in further detail in chapter 6).

A process of elimination thus leads to the conclusion that an independent form of tip load sensing, uncoupled from the AFM built-in optical lever (similar to the load cell used in the nanoindenter) and integrated with the convenience of operation in-situ within an AFM setting (similar to the reference spring setup), could be a far better solution to the problem of characterising and calibrating AFM response to applied forces. Such a system would provide high speed and a low complexity of setup for cantilever behaviour characterisation (akin to the 'push-button' operation of thermal tune). Work on micromachined force sensors for applications (such as pressure sensing and integrated AFM force sensing cantilevers) has demonstrated the stability and accuracy of such technology. Whilst the direct use of integrated force sensing within an AFM cantilever increases the cost of the consumable AFM probe and precludes the use of many advanced probe types and materials, the use of such a technology as a non-consumable calibration sample would fulfil the requirements identified above. The theory of such sensors is introduced next, in chapter 3.

Chapter 3 - MEMS sensing theory

A sensor (from the Latin 'sentire' - meaning 'to perceive') translates an encountered physical magnitude into another, often electrical value, corresponding to the investigated measurand. The process of conversion is called transduction and the term transducer typically refers to the complete sensing device assembly - mechanical structure, electrical sensor (or actuator), wiring and instrumentation involved in the process [126]. Conventional, macro-scale force sensors are often categorised as load cells, which are assembled with the separate components necessary for the complete transduction function. These assemblies compose force and displacement transducers that are based on capacitive, resistive, electromagnetic or piezoelectric sensors integrated with deformable mechanical structures, such as membranes or beams. The advent of semiconductor microfabrication technology allowed for the development of highly miniaturised and integrated sensor solutions, often classed as micro electro-mechanical systems (MEMS), a term introduced in 1986 [127] by a proposal to DARPA [128]. These micro-devices can offer an accurate, low-cost solution with minimal additional hardware and easy integration within commercially available AFM systems, which is often not practical with conventional macro-scale load cell setups. Some of the numerous unique mechanical and sensing compositions that have been developed for AFM cantilever characterisation are introduced in this chapter, together with the relevant MEMS theory serving as a conceptual definition of the device presented in this thesis. First, the theory concerning the mechanical structure is described, introducing the relevant continuum mechanics concepts, which allow the analytical and Finite Element modelling theory of structures to be utilised. Then, the

relevant methods of microfabrication supported sensing are reviewed, while a description of the chosen strain sensing instrumentation technology is introduced.

3.1 Structural mechanics theory

MEMS (including AFM) cantilever elasticity can be understood using classical mechanics theory, which forms the fundamental physical descriptions behind the analytical and finite element modelling methods employed in the field. In solid body mechanics, convention dictates that the body (e.g. surface of area A, m^2) responds to applied external load (e.g. load force F, N) by internally opposing forces and deformations (changes) in shape [129] (Figure 19 and Eq. 13). In continuum mechanics, these interactions are understood in stress (σ) and strain (ε) terms respectively, which are ordered to the chosen coordinate convention. The directionally and spatially categorised elements can then be attributed their own individual strain and stress values, which allows the structure to be considered not only as a continuous mass body, but also a composition of elements related to each other in stress relationships - conventionally expressed as tensors (Figure 20).

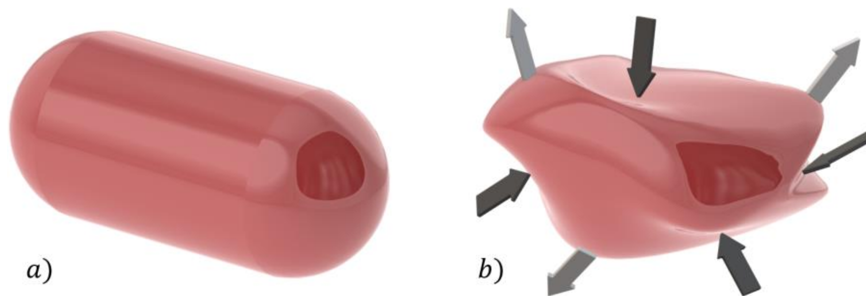

Figure 19. An ellipse shaped solid body (a) subjected to external loads (b) that result in body deformations.

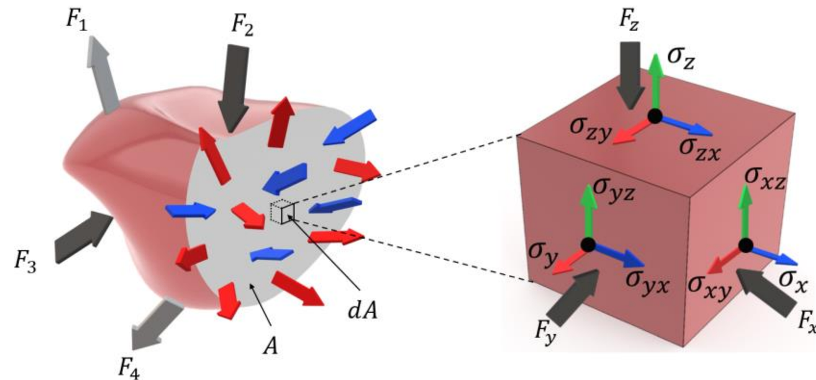

Figure 20. External forces applied on a solid body are distributed internally as normal and shear stress vectors (σ), marked with their indicated directions, which form the tensor element description.

$$\sigma = \frac{F}{A}; \qquad \textit{Eq. 13}$$

The tensor can thus be used to understand stress and strain relationships in the elastic region of three dimensional objects, summarising the relevant mechanical expressions to the further considered elastic structures (Eq. 14 in support of the naming convention of Figure 20). Strain (ε) is the relative or fractional change in structure length in the direction of applied load (Figure 21 and Eq. 15). The relationship between lateral and longitudinal strains is defined by a material property called Poisson's ratio (v), which defines the magnitude of change in the directions perpendicular to the load (Eq. 16), a property that is essential in understanding not only the mechanical component, but also the operation of strained electrical conductors (further expanded upon in section 3.2.2).

$$\varepsilon_x = \frac{\sigma_x}{E} - \nu\frac{\sigma_y}{E} - \nu\frac{\sigma_z}{E} = \frac{1}{E}\left[\sigma_x - \nu(\sigma_y + \sigma_z)\right],$$
$$\varepsilon_y = \frac{\sigma_y}{E} - \nu\frac{\sigma_x}{E} - \nu\frac{\sigma_z}{E} = \frac{1}{E}\left[\sigma_y - \nu(\sigma_x + \sigma_z)\right], \quad \textit{Eq. 14}$$
$$\varepsilon_z = \frac{\sigma_z}{E} - \nu\frac{\sigma_x}{E} - \nu\frac{\sigma_y}{E} = \frac{1}{E}\left[\sigma_z - \nu(\sigma_x + \sigma_y)\right];$$

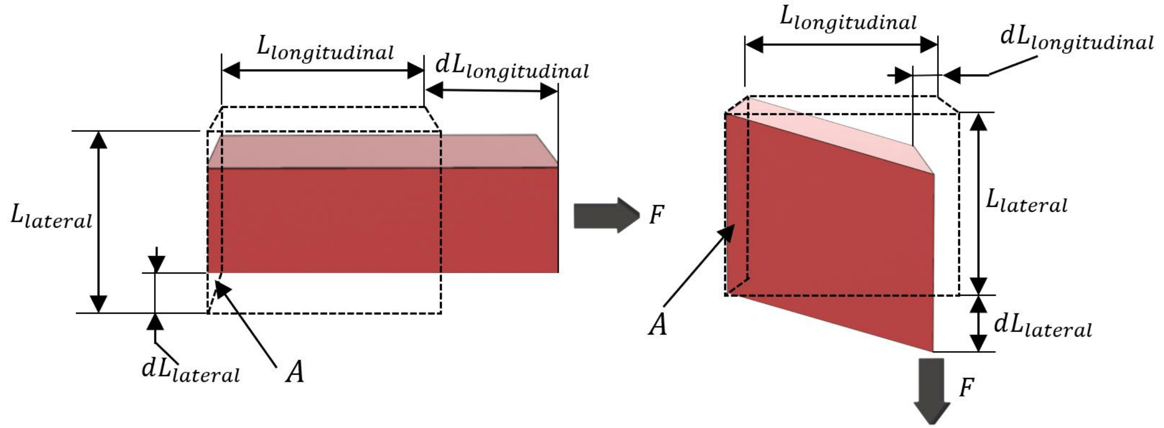

Figure 21. Force induced elastic uniaxial deformation of a solid structure allowing for the corresponding lateral and longitudinal strain resolution.

$$\varepsilon = \frac{dL}{L}; \quad \textit{Eq. 15}$$

$$\nu = \frac{-\varepsilon_{lateral}}{\varepsilon_{longitudinal}}; \quad \textit{Eq. 16}$$

Whilst the tensor describes the stress relationships at the element level, the strain is also understood from this multilinear relationship via the knowledge of elastic modulus (Eq. 17). The gradient of the elastic region describes material compliance in uniaxial loading (Figure 21) and is called elastic (or Young's) modulus (E, Eq. 17). However, in the load case concerning elastic deformations, the elastic compliance also involves a shear modulus (G) component since beam bending involves shear stress arising from the perpendicularly applied load. This can be accounted for by expressing the shear modulus in elasticity

modulus terms (Eq. 14), allowing for further expression simplifications, eliminating the need to refer to the shear modulus value explicitly.

$$E = \frac{\sigma}{\varepsilon}; \qquad \textit{Eq. 17}$$

$$G = \frac{E}{2(1+\nu)}; \qquad \textit{Eq. 18}$$

In a given material, the relation between stress and strain is dictated by an experimentally obtained stress and strain plot (illustrative example shown in Figure 22), which is split into three distinct regions:

- elastic deformation region (0-1), where the stresses and strains manifest as elastic (reversible) deformations, that are defined by the elastic modulus defined linear proportionality.
- plastic deformation region (1-2), where deformations become non-linear and non-reversible.
- failure region where fracture limit or yield strength (2) value indicates the material failure point.

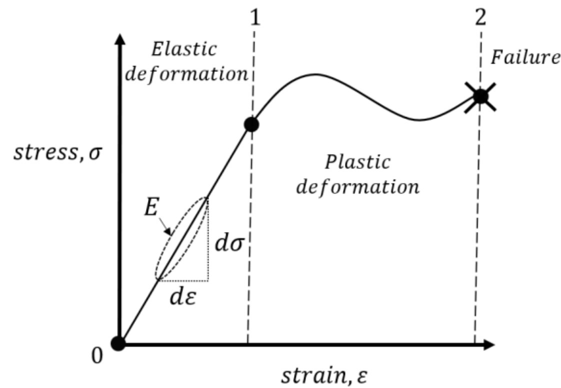

Figure 22. Stress and strain relationship example. For isotropic, elastically deforming structure, the relationship between directional stress and strain is described in elastic deformation region governed by the proportionality limit.

As the vast majority of MEMS structures are required to undergo repeat operation, it is necessary to ensure that their operational load stays inside their elastic deformation limit, allowing the load induced strain to reverse back to the neutral position once the load is removed (Figure 23).

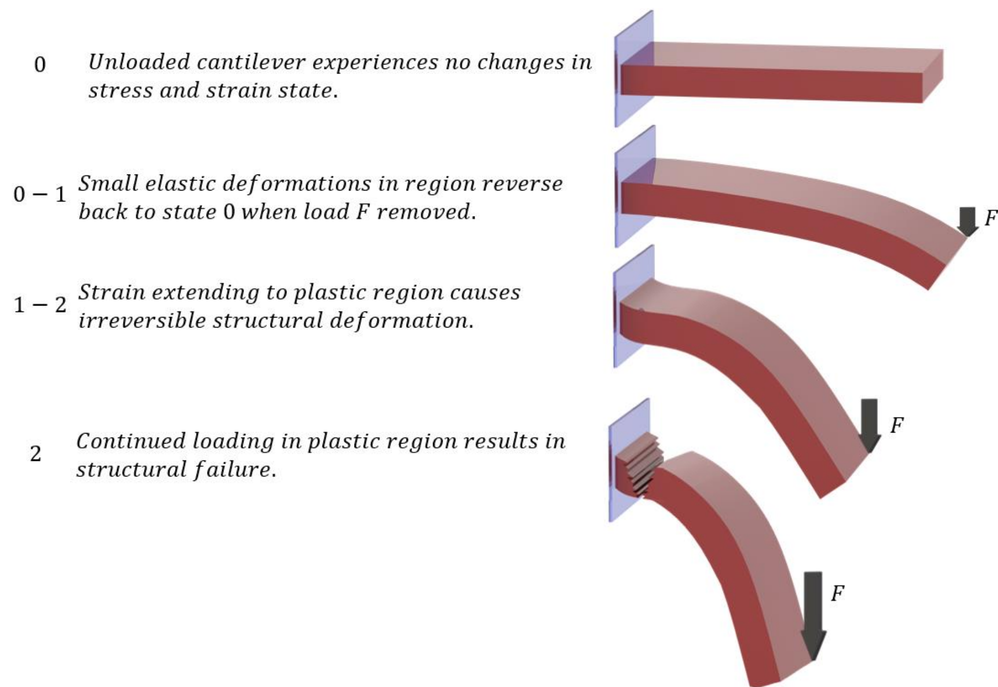

Figure 23. Perpendicular load induced deformation of a cantilever beam.

Mechanical sensors are typically designed in a geometrically simplistic manner where load induced stress and strain relationships are as straightforward as possible, with any additional geometrical complexity only included for well-considered reasons - e.g. manufacturing constraints or sensing enabling features. In force sensing applications, such structures most often take shape of deformable beams with a range of constraints as illustrated in Figure 24.

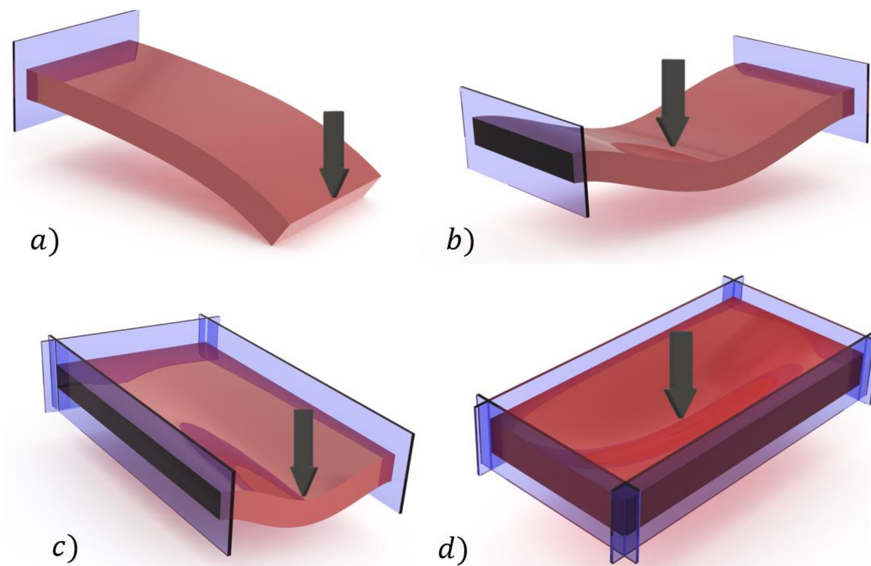

Figure 24. Deformable mechanical structures in red and displayed fixed planes in blue. The load point (black arrow) is responsible for the induced deformation response of the showcased structures: a) single fixed end beam (cantilever); b) double fixed end beam; c) three end fixed beam; d) four end fixed beam (membrane).

The primary optimisation area of a load sensitive structure, requires maximising stress or strain response (illustrated by an FE study in Figure 25, methods of which are introduced in 3.1.2), therefore the least constrained arrangement – a single end clamped cantilever beam must be considered as the preferential design option. Such a structure, when displaced using a normal load, experiences a bending action which results in polar direction strain and stress in the structure. If this stress or strain is measured by a dedicated strain gauge this information can be combined with knowledge of the type of loading to resolve

the normal magnitude of this load. For most materials, it can be straightforward to identify tensile-compression and shear values from representative cases presented in the literature. However, for microfabrication materials such as polymers, metals and silicon based thin-films this can be particularly challenging since their material composition and form can vary to a significant extent, as dictated by their deposition parameters. For this reason, testing of each individual structure or material deposition is necessary if an accurate value is required. This limited material property knowledge leads to an early design decision – utilizing a structure with the largest magnitude specific surface strain, which can be relatively determined using continuum mechanics concepts and finite element analysis tools.

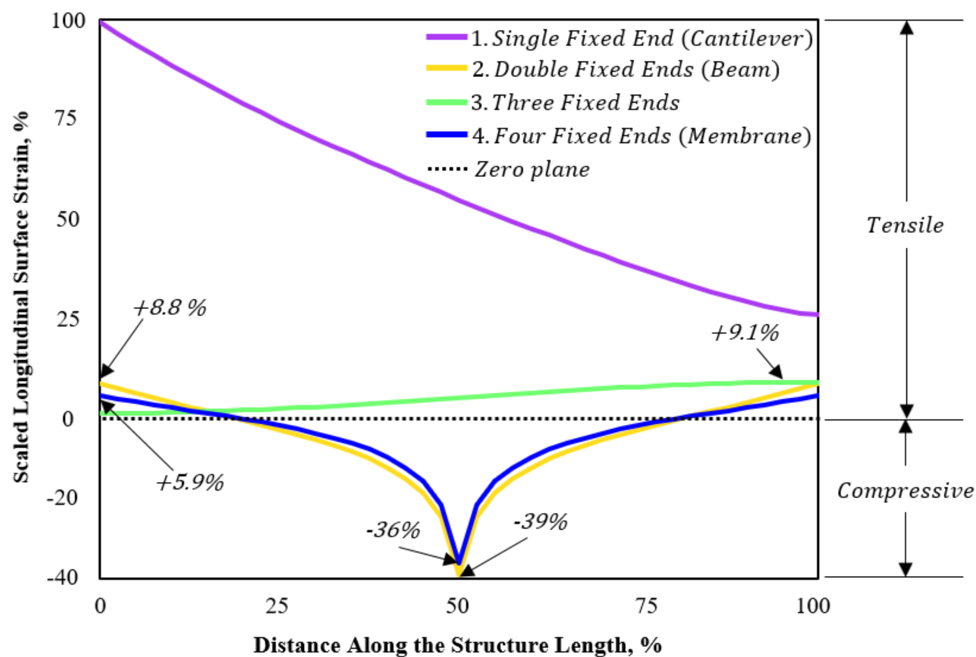

Figure 25. Unit load applied at maximal strain inducing locations (see Figure 24) comparing the surface strains of different degree of freedom beams (FEA, Abaqus). The structures have a width and length ratio of 1:1, and length to thickness ratio of 100:1. Graph scaled to 100% in vertical axis – as determined by value of maximal strain on a single clamped cantilever under unit load. The arrow values indicate comparative percentage of maximal surface strain, as compared to single end clamped beam - cantilever.

Once the load effects on deformation are understood, it is necessary to consider the structural description relevant to the further considered geometries - the second moment of inertia (I, m^4). This describes the phenomenon where the further material is located from the bend axis, the more resistant the structure is to deflecting under a given load. The scalar value for I is obtained through integration of the material cross-sectional area (dA) and its squared vertical displacement during bending (z^2) orthogonal to load bend axis (Eq. 19). For a rectangular beam (Figure 26), as considered in this case, the integral reveals that resistance to mechanical deformation is related to thickness cubed but is linear in relation to width (Eq. 20) – an important design consideration for fabrication control and optimisation.

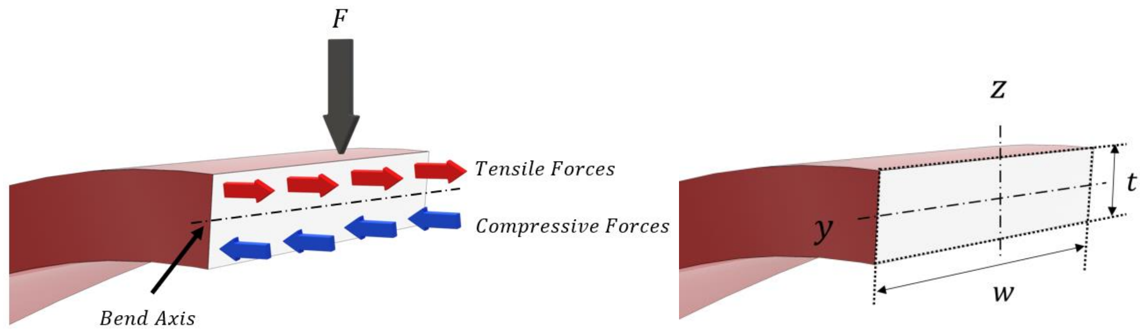

Figure 26. Cross-sectional representation of force directions as induced by orthogonal concentrated force in a rectangular cantilever (left) and of second moment of inertia defining variables and neutral axes y and z (right).

$$I = \int z^2 dA\,; \qquad \textit{Eq. 19}$$

$$I = \int_{-\frac{t}{2}}^{\frac{t}{2}} wz^2 dz = w\left[\frac{z^3}{3}\right]_{-\frac{t}{2}}^{\frac{t}{2}} = \frac{wt^3}{12}\,; \qquad \textit{Eq. 20}$$

For a concentrated force on a single fixed end beam, elastic deformations resulting from small deflections and lateral only loads, Euler-Bernoulli beam theory [130] can be

employed. Therefore, if an offset point load is considered (per Figure 27 configuration), in relevance to the loading type concerned with AFM cantilever and substrate interaction, the mathematical relationship between force and deflection is expressed in Eq. 21.

$$\delta = \frac{FL^3}{3EI}; \qquad \textit{Eq. 21}$$

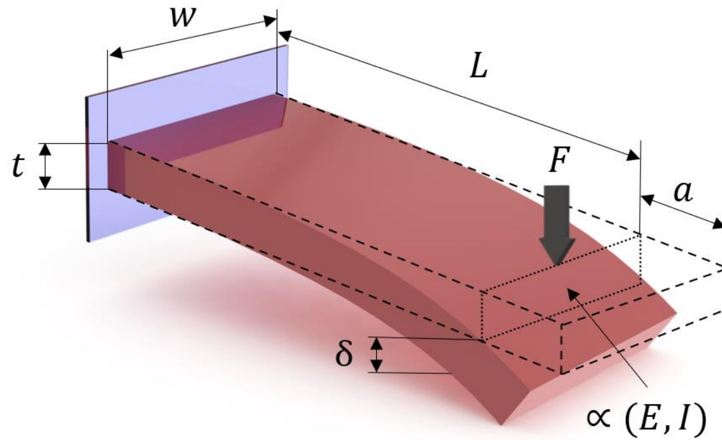

Figure 27. Depiction of cantilever beam structural variables.

Finally, by combining the above expression (Eq. 21) with the Hooke's law (Eq. 1) elasticity expression relating deflection (δ) and force (F) relationship in a linear elastic system, the elasticity value for the cantilever beam can be expressed solely based on in its external dimensions (I, L) and material property (E) terms. This expression (Eq. 22) concludes the fundamental relationships relevant to the mechanical behaviour descriptions used in future work, allowing the cantilever based MEMS device development to be discussed using appropriate terminology.

$$k = \frac{3EI}{L^3}; \qquad \textit{Eq. 22}$$

3.1.1 Analytical methods for MEMS characterisation

The validity of the analytically modelled cantilever elasticity characterisation was investigated by comparing the analytical results to the previously experimentally evaluated MEMS structure - the Veeco MPP-21100-W AFM probe (introduced in section 2.2). Clearly, analytically obtained spring constant reliability is dependent on the accuracy of its inputs, therefore a dedicated structural geometry study of the investigated cantilever was carried out. Both optical and scanning electron microscopy (SEM) were used to geometrically characterise the AFM cantilever with good resolution, capturing the major length and cross-section dimensions - as summarised in Table 4. SEM's higher resolution comes at higher cost, but the approach may prove preferable, when compared to optical techniques, particularly if more complex geometries or sub-micrometre features are present – e.g., the exact tip shape or cantilever shape non-uniformities. SEMs also offer improved depth of field over conventional optical microscopy, making acute angle images, such as looking at the thickness profile, easier to interpret. Additionally, some common AFM cantilevers can have a thickness component of tens or hundreds of nanometres, making thickness characterisation impossible with conventional optical microscopy and tricky even when using an SEM. In these instances, more specialised approaches, such as thin film characterising techniques (e.g., ellipsometry [131] and spectral reflectance [132]) can be employed. The thickness of the cantilever was measured to vary from 3.38-3.42 μm along its length using SEM. Therefore, for use in the expressions introduced in the previous section, the mean figure of these two values was employed. The fixed end point (where the cantilever meets the silicon probe body) was also somewhat difficult to define due to the etch plane forming an outward draft angle, hence the origin was chosen at the cantilever

and etch draft intersection. Young's modulus uncertainty was not experimentally obtained in this study, with the value 176 GPa being employed as described in the literature (obtained by indentation) [133]. The probe manufacturer's website provided a pictorial cantilever description from which it can be seen the cantilever has a tapered cross-section. This edge profile is distinct, indicating an anisotropic silicon etch, necessitating a trapezoid geometry moment of inertia evaluation. To obtain the values described above, a calibrated SEM (FEI Nova NanoSEM 630 [134]) was used to obtain the cantilever length, tip offset and thickness figures, whilst planar dimensions were obtained using an optical microscope (Nikon Eclipse L200N/DS-U3 [135]) as illustrated in Figure 28 and Figure 29. The obtained result differences clearly illustrate the previously speculated manufacturing tolerance control difficulties (section 2.2) and highlights the expense required to confidently build a representative analytical model of a mechanical system at this scale.

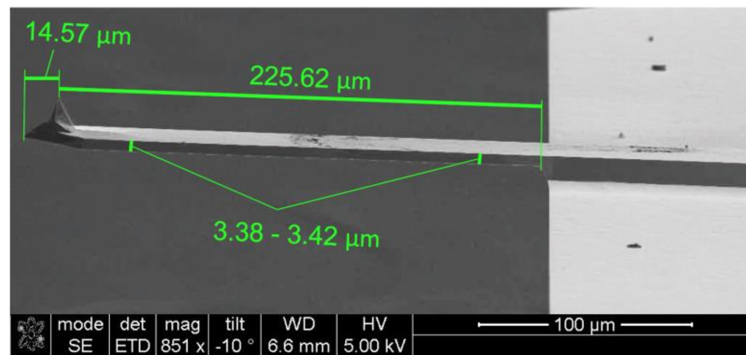

Figure 28. Cantilever dimensions summarised on an isometric capture of the investigated AFM cantilever (dimensions are angle compensated, SEM).

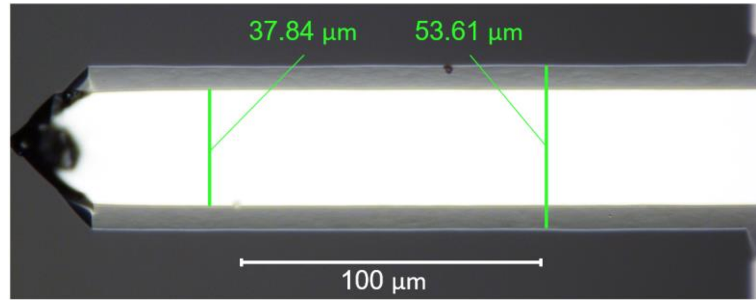

Figure 29. Planar image showing the two distinct width boundaries resulting from the tapered cross-section (optical microscope).

Table 4. Veeco MPP-21100-W, mechanical property assessment necessary for analytical and FE modelling exercises.

Property	Manufacturer Nominal	Measured, Nominal	Source
Length (to tip peak), L, µm	225	225.62	SEM, Figure 28
Top width, w_{top}, µm	35	37.84	Optical microscope, Figure 29
Bottom width, w_{bottom}, µm	35	53.61	Optical microscope, Figure 29
Thickness, t, µm	4	3.40	SEM, Figure 28
Natural resonant frequency, f_0, kHz	87.5	86.2	Air thermal fluctuation spectrum, Figure 9
Elastic modulus, E, GPa	176		Literature, Silicon undoped [133]
Density, ρ, kg m^{-3}	2330		Literature, Silicon undoped, [136]
Poisson's ratio	0.279		Literature, [137] (100) plane

Using this in formation, an analogous assessment using the Euler-Bernoulli expression mentioned in the previous section could then be carried out (Eq. 19). Firstly, a moment of inertia was calculated for the evidently trapezoidal (where measured top and bottom widths are expressed separately) cross-section of the cantilever:

$$I_{trapezoid} = \frac{t^3\left(w_{top}^2 + 4w_{top}w_{bottom} + w_{bottom}^2\right)}{36\left(w_{top} + w_{bottom}\right)} = 1.48 \times 10^{-22}\ m^4; \quad \textit{Eq. 23}$$

Then, using the Euler-Bernoulli equation (Eq. 22) an analytical elasticity solution was obtained by employing the measured variables as shown in Eq. 24.

$$k = \frac{3EI}{L^3} = \frac{3 \times 176\ GPa \times 1.48 \times 10^{-22}\ m^4}{(225.62 \times 10^{-6}\ m)^3} = 6.8\ N\ m^{-1}; \qquad \textit{Eq. 24}$$

This result, based on real life measurements in combination with a literature value for material elasticity modulus, agrees approximately with the experimentally obtained values - underestimating the elasticity by 16 % when compared to thermal tune, 17 % to indentation and 38 % to reference spring. This variation may be attributed to a non-experimentally obtained elasticity modulus value and the idealised uniformity and simplified geometric variables involved in the Eulerian bend equation, which are not completely valid in real-life structures. Having said this, it can be concluded that static analytical modelling based on accurate dimensions is a reasonable technique for MEMS structural behaviour description, although it poses limitations on the complexity of the geometry which can be represented, reducing the design freedom or its potential accuracy.

Another analytical modelling method, also heavily reliant on dimensional characterisation should be introduced for completeness. It is one of the earliest AFM specific elasticity characterisation techniques based on dynamic behaviour - natural resonance value, related to mass and elasticity, as described by Cleveland [85] and formulated in its presented equivalence form by Clifford [112] (for simplicity the 2π term is used instead of the effective mass accounting coefficient). In this approach, resonance is analytically derived from a simple cantilever harmonic oscillator model, which relates elasticity to the oscillator mass or expresses the mass in density terms, per Eq. 25. The developed harmonic oscillator equation can be rearranged for MEMS (and AFM cantilevers) in a convenient manner,

equating it with the Eulerian cantilever expression (Eq. 22), allowing the often-complicated thickness component to be exchanged for a dynamic resonance measurement (Eq. 26). Appealingly, obtaining the resonance frequency is trivial in practice for MEMS structures due to their ability to oscillate through Brownian motion in the surrounding medium (e.g. air), therefore not requiring forced excitation. In this case study, the oscillation spectrum for the cantilever was obtained by employing the previously described tools (section 2.3), allowing this technique to be employed.

$$f_0 = \frac{1}{2\pi}\sqrt{\frac{k}{M}} \approx \frac{1}{2\pi L^2}\sqrt{\frac{E}{\rho}}; \qquad \textit{Eq. 25}$$

In this case, the expression also requires knowledge of the planar dimensions (w, L), cantilever resonance frequency (f_0), elastic modulus (E) and density (ρ). The density of n-type silicon was found from the literature and unlike Young's modulus, is reported consistently as 2330 kg m^{-3} [136], allowing for the part-dimensional and part-experimental elasticity expression:

$$k = 2\pi^3 w \frac{\left(f_0 L\sqrt{\rho}\right)^3}{\sqrt{E}} \qquad \textit{Eq. 26}$$

$$= \frac{2\pi^3(45.7 \times 10^{-6}\, m)(86229\, s^{-1} \times 225.62 \times 10^{-6}\, m \times \sqrt{2330\, kg\, m^{-3}}\,)^3}{\sqrt{176\, GPa}} = 5.6\, N\, m^{-1};$$

The obtained elasticity of 5.6 N m^{-1} is 17.9 % less than the previously obtained value employing Eulerian beam theory, resulting in a value that falls below the experimentally obtained figures, an outcome that is also attributed to the highly idealised and simplified geometric representation - e.g. the trapezoid cross-section is not accounted for (average width used) by the resonance model as well as the presence of the tip-mass which acts against the uniformity of the spring-mass oscillator analogy the theory is based on.

From these results, it is possible to say that the analytical beam elasticity characterisation methods were able to determine the elasticity modulus with reasonable agreement with the established experimental methods. This adds further weight to the conclusion that the structure's true spring constant deviates significantly from the manufacturer's figures. Overall, it is reasonable to say that analytical methods can be extremely useful in the characterisation of cantilever-like MEMS designs as they provide clarity in the influence of individual variables. For example, the third order length (Eq. 24) and frequency (Eq. 26) relationship to elasticity is an extremely useful indicator of the elasticity behaviour via simplistic (e.g. optical microscope) and indirect (vibrometer) observation means, as exploited in the further developments (described in section 5.1). On the other hand, as described, they are limited to simplistic structures, which may not always be realistic due to multi-layer microfabrication processing and added complexity present in some probes and MEMS devices.

3.1.2 Finite Element methods for MEMS characterisation

In addition to the analytical modelling, a finite element study was carried out to further explore commonly used methodologies. FE methods offer the ability to apply the established mathematical descriptions of physical behaviour (e.g., thermal, structural, magnetic, or fluid or a combination of them in a hybrid-physics modelling exercise) to individual elements, from which a complex structure can be represented. FE methods for structural analysis can therefore be employed for a geometrically unrestricted MEMS component. The validity and usefulness of the finite element method was investigated by employing an FE analysis software tool (Simulia Abaqus FEA, Dassault Systemes [138]) to determine elasticity of the Veeco MPP-21100-W and compare it to the experimental and analytical solutions. All inputs into the model were based on the previously conducted dimensional characterisation of the cantilever structure (Table 4).

Firstly, an analysis of the effect of three-dimensional mesh types and element quantity on accuracy was conducted on an arbitrary structure, of similar dimensions to the AFM cantilever being studied – specifically, a rectangular cantilever of width and length ratio of 1 to 1 and thickness to length of 1 to 100. The elements available in Abaqus suitable for such modelling consist of three-dimensional hexahedral continuum bricks (C3D) of two node counts (8 and 20), and varied solution types (full or reduced integration and hybrid pressure). Since the available computing power is not a restriction for the straightforward bend cases of cantilever structures, the computationally ‘cheaper’ element types - truss, membrane, shell and beam, were not investigated, as they suffer from restrictions similar to the analytical methods. It was assumed that the analytical solutions would give a

'perfect' answer for such an idealised and simple cantilever, so the resulting FE derived values were compared to the analytical solutions as an error percentage in Table 5.

Table 5. Study of Abaqus 3D continuum hexahedral element mesh configuration and quantity effect in comparison to the analytical solution.

Element Type / Element Count	Error to numerical solution, %				Average error to numerical solution, %
	180 elements	360 elements	720 elements	2880 elements	
C3D8	99.6	99.6	99.6	98.4	99.3
C3D8H	99.6	99.6	99.6	98.4	99.3
C3D8R	8518	26.16	1.28	1.45	2136
C3D8IH	2.53	2.85	2.93	1.23	2.38
C3D20	1.35	1.15	1.10	0.75	1.09
C3D20R	1.08	0.75	0.65	0.60	0.77
C3D20H	1.20	1.08	1.05	0.73	1.01
C3D20RH	0.70	0.65	0.63	0.60	0.64

The mesh element type and quantity comparison revealed that the 20-node quadratic brick hexagonal element with hybrid formulation and reduced integration (C3D20RH) provided the smallest deviation from the theoretical model used, with an average error of 0.64%. As expected due to larger node count and the quadratic, as opposed to linear, integration along the cross-section, the twenty node (C3D20) brick elements represented the variable elastic shear in much better detail - and thus accuracy than the eight node (C3D8) elements. The hybrid linear pressure (H) element, which is recommended for incompressible materials - such as the considered solid silicon, also improved simulation accuracy. Interestingly, the lesser order of integration solving element (R) showed a marginally closer match to the analytical solution compared to full integration in the considered case. Whilst this may be just a coincidence of the chosen geometry, nevertheless it can be concluded that this element should be considered due to its result's closeness to the full integration at cheaper computational cost. Conceivably, the study also demonstrated that increasing the element count does increase the modelling accuracy. Whilst the effect may not be as significant for

the simplified structure considered here - e.g., a 0.1% accuracy increase for 16-fold element increase for the chosen C3D20RH type, if more detailed geometries are considered the impact should be more pronounced. The broad element specific accuracy variance - from 0.6% to 8000% illustrates the necessary precautions that need to be taken into account when using FE methods. For instance, the 8-node version of the reduced integration element (C3D8R) displayed a pronounced hour-glassing effect, making it completely unsuitable for this study, reaching a near three orders of magnitude overestimation. The importance of correct element type identification and the positive relationship between element type and accuracy is therefore considered in the further studies, where much more complex geometry devices are explored.

To employ the finite element method on the Veeco MPP-21100-W cantilever the cantilever dimensions described in the previous section were used. This then allowed a CAD model of the cantilever to be created in FE software (Figure 30). The solid pyramid shape tip geometry was not included, due to the assumption that it is significantly more rigid than the cantilever and does not contribute to the overall structure elasticity. The point load (F) of 1 μN magnitude was applied at the planar projection where the tip peak would be – 225.62 μm offset from fixed end. The simulation returned a displacement (δ) of 0.137 μm at the corresponding node. Utilizing Hooke's law (Eq. 1) the node specific spring constant was derived per Eq. 27.

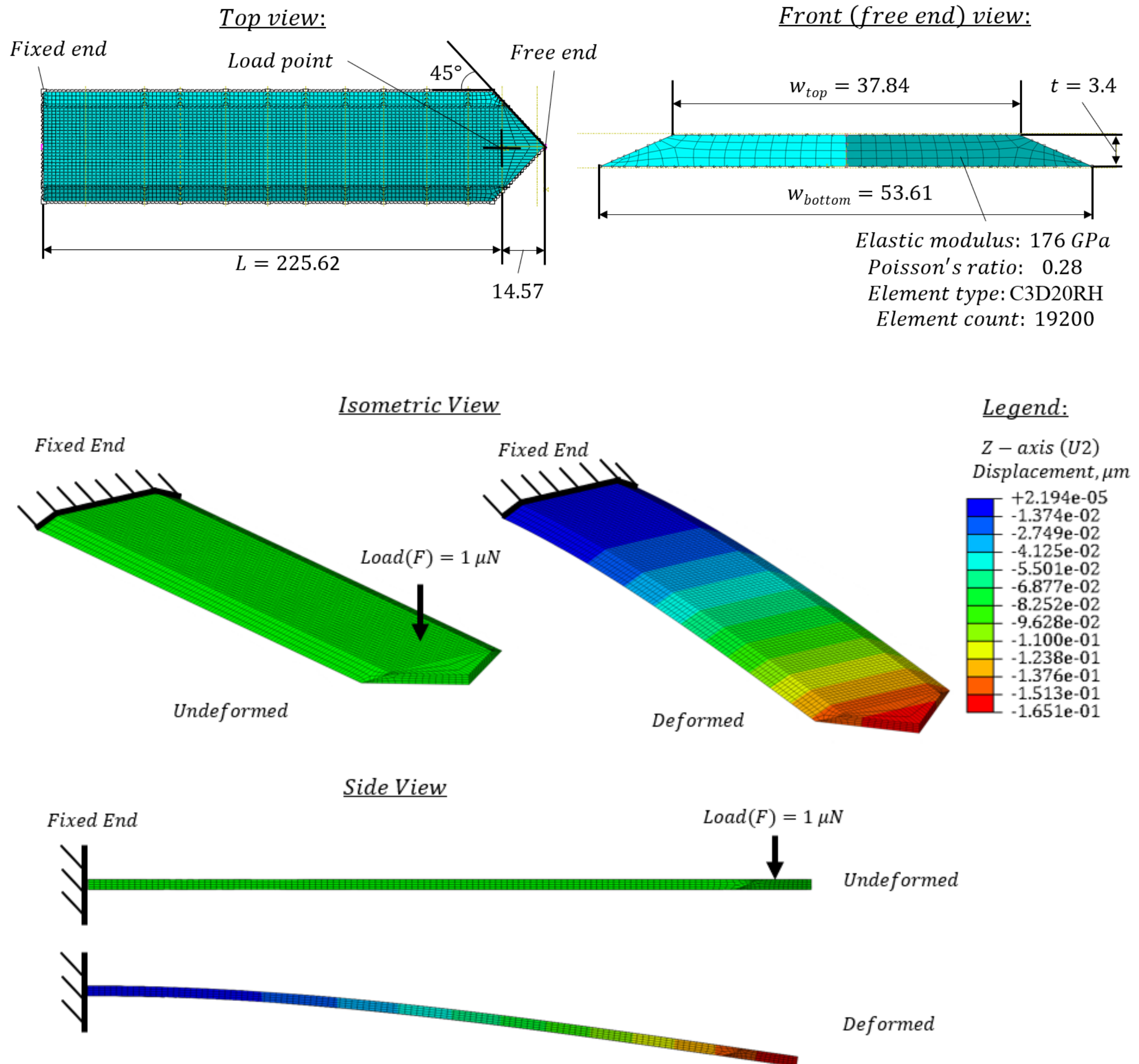

Figure 30. Finite Element Analysis representation of the loaded AFM cantilever. NB: 1) Geometry dimensions in micrometres. 2) Part symmetrical along its length. 3) The deformed model visualization scale is hyperbolized by a factor of 150.

$$k = F\delta^{-1} = \frac{10^{-6}\,N}{1.37 \times 10^{-7}\,m} = 7.3\;N\,m^{-1}; \qquad \text{Eq. 27}$$

The resultant figure of 7.3 N m^{-1} overestimates the elasticity by 7 % when compared to the analytically acquired static beam displacement result (6.8 N m^{-1}). The disagreement between the two can be attributed to more a complete geometrical representation of the structure in the FE model, including the structure past the load point as well as the

accounted directional strain changes by accounting for the Poisson's ratio. The obtained elasticity figure is also closer to the experimental characterisation values - e.g., 11 % underestimation compared to nano-indentation and thermal tune, and 33% less than the reference spring. It may be suggested that the added complexity involved in conducting an FE study through a dedicated simulation package may not be justified for such a simple cantilever, due to the result being so close to the straightforward analytical solution. However, it should be noted that the FE model, if needed, could provide a much more in-depth and complex simulation of loading and interaction cases, displaying stress concentrations and surface strains that are of interest to the more complex structures used later in this work. These studies are introduced in the appropriate sections concerning the MEMS device development in chapters 4 and 5.

3.2 Electrical sensing theory

The ultimate intention of this work was the design, fabrication and characterisation of a MEMS device to be employed in the characterisation of AFM cantilevers. With this in mind, the two MEMS sensing approaches available for fabrication wholly within the James Watt Nanofabrication Centre (JWNC) were judged to be resistive and capacitive based. Therefore, these two fundamental electrical sensing approaches are introduced next.

3.2.1 Capacitive deformation sensing

Capacitive sensing relies on monitoring change in a capacitance (C) resulting from the deformation or displacement in the separation (Z) of two conducting surfaces or in their overlapping area (A), separated by a vacuum or dielectric material having a permittivity (ϵ), per relationship in Eq. 28 [139]. This technology is commonly employed in microfabricated load sensing applications – static and dynamic pressure sensing [140] and acceleration [141] with example configurations of which are shown in Figure 31 - an arrangement that is equivalent to its use in AFM elasticity calibration tools [73] [103] [142].

$$C = \epsilon \left(\frac{A}{Z + dZ} \right); \qquad \textit{Eq. 28}$$

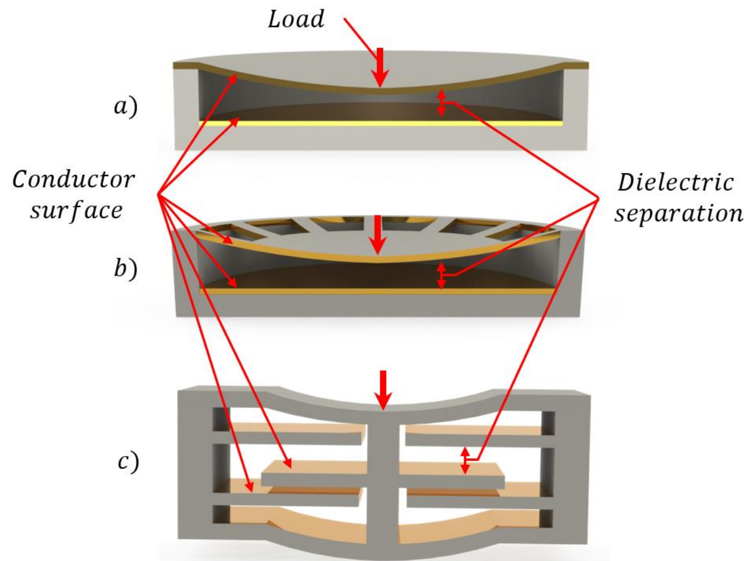

Figure 31. Capacitive MEMS load sensor cross-sectioned examples – a) pressure sensors (diaphragm configuration), b) microphone acoustic structures (open surfaces) and c) accelerometers (suspended stages).

Unlike the linear Hookean spring (Eq. 1) relation between force and elasticity in cantilever structures, capacitive signals based on changes in separation of dZ do not exhibit a linear relation to displacement [143]. This complicates the calibration methodology and necessitates an external calibration that maps all relevant force-displacement relationship ranges. On the other hand, the nature of charge measurements lends itself to traceable and repeatable measurements, since a direct quantification of charge value can be related through the SI definitions of mole and elementary charge - a method metrological institutes employ for AFM calibration balance solutions [70].

Material selection is relatively straightforward and requires a suitable elastic carrier structure and conductor. Typical choices of material for the elastic structure are silicon, silicon nitride or silicon oxide, allowing for fabrication using common wafer processing procedures. The capacitor conductor material is only limited to those that can be accommodated in cleanroom tools - physical vapour deposition or sputtering and includes

materials such as nichrome, gold, aluminium and platinum. One advantage of microfabrication is the flexibility it possesses in planar geometry, although there are rigid constraints in vertical axis and resolution of patterns. With this in mind, an opportunity lies in maximising the charge coupled area. The closed membrane design (shown in Figure 31 a) is attractive for its encapsulated conductor and dielectric configuration that are then inert to environmental effects (except changes in air pressure). However, sensitivity would be limited by the size of the planar charge area (A). In addition, the complexity in Z required by the encapsulation would make it expensive and complex to fabricate. A more efficient design has been described in the literature that offers sensitivity in the nano-Newton range [144]. This design (Figure 31, b) increases the sensing surface area by utilising a comb-like packaging for an interdigitated surface configuration [145], thus returning a higher magnitude signal contrast in response to the changed separation displacement. A similar solution could further simplify the design by employing planar lithographical definition of the capacitive elastic and anchored surfaces. However, even this simplified design places substantial challenges on the fabrication process (surface micro-machining, also known as MUMPs processing), requiring extremely close tolerance in pattern definition and transfer and may require extensive optimisation of surface adhesion and curling properties [146]. Therefore, it can be anticipated that a capacitive sensing solution would be potentially accurate and sensitive, yet complex and expensive to produce.

3.2.2 Resistive deformation sensing

Metal conductor strain gauges (e.g. nichrome, gold, aluminium, constantan) are widely used in macro and micro scale environments due to their relative simplicity and reliability. As a result they can be encountered in precision surface strain measuring applications - e.g. bone [147] and micro-beam [148] deformation. Extending or compressing an electrical conductor of absolute resistivity (R_{abs}) has an impact on its cross sectional area (A) and length (L), meaning that its resistance changes (dR) in response to the geometry changes, per Figure 32 and relationship in Eq. 29. This makes it possible to relate resistance change (dR) to the strain experienced by the carrier surface (ε). The ratio relating the electrical resistance change to the experienced mechanical strain is called the gauge factor (GF) and is used to express the resistive strain gauge sensitivity to mechanical load, per Eq. 30.

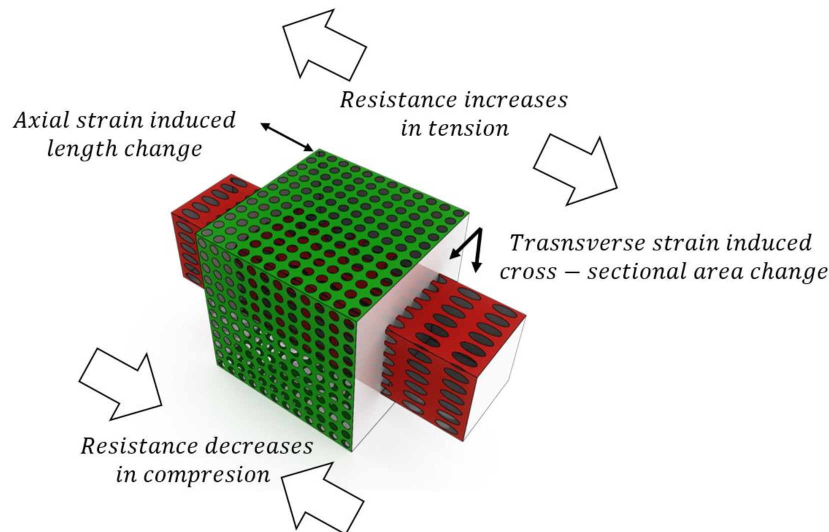

Figure 32. Strained conductor geometry affecting electrical resistance.

$$R_{abs} = \rho \frac{L}{A}; \quad \text{Eq. 29}$$

$$dR/R_{abs} = GF\varepsilon; \quad \text{Eq. 30}$$

Whilst the term strain-gauge is often reserved for metallic conductors, semiconductor-based strain sensing techniques are frequently found in micro-structures - a method referred to as piezo-resistive sensing. In these devices resistive response to strain is the result of material bandgap changes [149] [150] rather than cross section modulation. This phenomenon is limited to materials that exhibit the piezo-resistive effect such as polycrystalline diamond or doped silicon. This is attractive in MEMS as both functions - electrical strain sensing and mechanical deformation are integrated into a single structure. Furthermore, semi-conductor strain gauges offer the advantage of upto 50 times higher specific sensitivity to strain (or gauge factor, as defined in Eq. 30) than conventional conductors e.g. - $GF_{Silicon} = 120$ [151], versus a metal resistor value of $GF_{Nichrome} = 2$ to 2.5 [152]. However, piezoresistive materials are much more sensitive to thermal effects and also exhibit photo-conductive properties [153], meaning any device is sensitive to local illumination (e.g. microscope light, optical lever laser overspill and surrounding laboratory lighting), all of which challenge the implementation of piezo-resistive technology in reliable calibration approaches for AFM cantilever stiffness characterisation. For example, the thermal coefficient of resistance TCR for Silicon is over an order of magnitude higher compared to metals (e.g., $TCR_{Silicon} = 1000+$ ppm [154], when $TCR_{Nichrome} = 85$ ppm [155]), a phenomenon of significance to this work, hence described in further detail in section 5.3.1.

As a consequence, metallic resistors were considered preferably due to their relative fabrication simplicity as well as additional degree of material choice and manipulation that can compensate for their lower gauge factor. In addition, their strain induced resistance change can be simply interpreted due to its linear nature and lesser dependency on local

environment thermal effects. The anticipated TCR behaviour should be much lower than conventional silicon sensors, as highlighted in the literature [140]. It was expected that the most significant shortcoming of this sensing composition would be observed at the system level – e.g., the bi-material bend originating at the interface between the different coefficients of thermal bending [156] of the complex composition structure. However, the advantages, such as a potential force sensing capability down to 10^{-8} N sensitivity (demonstrated by [157]) made resistive sensing an appealing configuration to develop with in-house controlled processes and simplistic instrumentation setup, to be described in sections 5.2 and 5.3.

3.3 Signal interpretation and instrumentation

Instrumentation is an umbrella term referring to an assembly of electronic components, necessary for sensor the signal acquisition and conditioning. In this work, the instrumentation required for the resistive strain sensor was required to output a potential change (or voltage, dV_{sensor}) corresponding to changes in its resistance (dR_{sensor}) as a response to the offset force (F(L)) induced strain on conductor (ε):

$$F(L) \leftrightarrow \varepsilon \leftrightarrow dR_{sensor} \leftrightarrow dV_{sensor}$$

For such precision measurements it is common to employ a Wheatstone bridge configuration which works in tandem with additional amplification and filtration before ultimately logging the data (e.g. by employing an oscilloscope). The Wheatstone bridge circuit (Figure 33) was originally conceived by Samuel Cristie, but popularised by, and hence now referred after Charles Wheatstone [158]. This type of sensing method is commonly used in applications where there is a change of equilibrium [159] and the change to the baseline resistance is converted to a voltage by an externally supplied current. Having a single strained element allows for quarter bridge circuit implementation, which produces a non-linear, thermally sensitive signal. The more complex half bridge configuration, where there is an additional instrumented strain gauge isolated from the load induced strain, could be used for thermal compensation although this does not compensate for the bridge nonlinearity. Beyond this, a full-bridge configuration involving a total of four strain gauges, placed in unstrained and opposing strain directions (opposing surface from the one in quarter bridge configuration) offers additional advantages, by compensating for the non-linear strain behaviour of the signal.

However, the placement of additional strain gauges in these nanofabricated structures can be challenging and impractical. Therefore, employing a quarter bridge together with characterisation of the thermal resistance dependence and calibrating non-linearity effects inherent in such configuration is a worthwhile price to pay to reduce device complexity. In this configuration, by plotting the V_{sensor} reading (Eq. 31) versus the AFM registered displacement, a calibrated system could obtain not only the cantilever exerted force (V_{sensor}~F), but also the elasticity profile of the interaction (k) if the rate of change is monitored - e.g. by the instrument clock, as demonstrated in section 5.4.2.

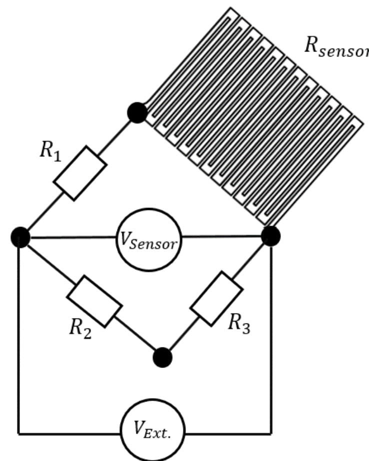

Figure 33. Composition of a quarter Wheatstone bridge where one of the resistors is sensitive to strain R_{sensor} and passive resistors ($R_{1\text{-}3}$) are not.

$$V_{Sensor} = \left[\frac{R_3}{R_{sensor} + R_3} - \frac{R_2}{R_1 + R_2}\right] V_{Ext.} \qquad \text{Eq. 31}$$

Moreover, in order to prevent other resistive variables from affecting the reading, a four terminal measurement method can be employed (Figure 34). This makes the measurement insensitive to the resistance of the signal carrying wires from instrumentation leads to the device level connections, thus allowing the system to only record the resistance between the strain sensor junction points. Insensitivity to signal wire resistance allows for simpler

instrumentation and a less complex device level fabrication approach that does not focus on lead wire resistance or stability.

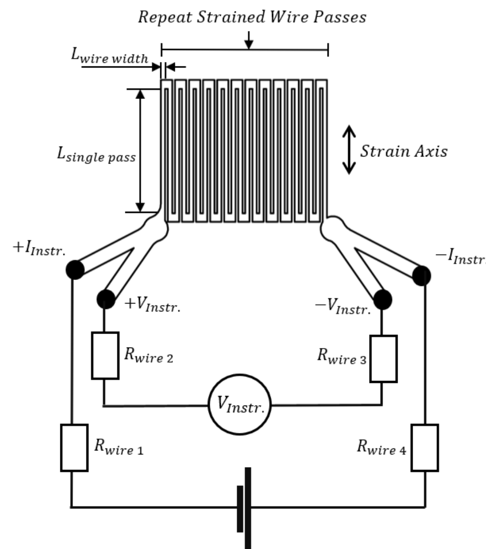

Figure 34. Resistive strain resistor connected by a four-terminal arrangement, where current is passed through two wires and instrumentation measures the voltage across two terminals, negating the total wire resistances up to the terminal junction. The strain gauge arrangement contains multiple wire passes in-line with the strain direction, increasing the strained wire length and thus the relative change in resistance, for increased sensitivity.

Appropriate filtration should also be considered in order to reduce interference present in laboratory environment, a major source of which is the AFM high-voltage piezo-element drive. Contact mode AFM force-distance interactions, required for force ramp measurements, are typically carried out between 0.1-50 Hz - e.g., the tested Dimension D3100 AFM system is hardware limited to 0.1-14 Hz range. Therefore, the MEMS instrument was destined for operation above 0.1 Hz and below 50 Hz, posing no particular requirements on the mechanical hardware as the mechanical resonance frequencies for these structures are in the kHz domain (expanded upon 5.2.2). To minimise external noise pickup, the instrumentation should be appropriately grounded and ideally be enclosed in a Faraday cage, where it would be isolated from electromagnetic interference. An example

noise spectrum of the laboratory is shown in Figure 35, as an indicative illustration of the ambient noise and signal presence. This was measured using a spectrum analyser with a connected open-end coaxial cable acting as antenna and high input impedance input. This power spectral density plot indicates that in the 0-50 Hz range the environmental noise is proportional to f^{-1}, indicating that the fastest permissible ramp speed will increase the signal to noise ratio. It is also evident that there are noise spikes at 50, 150, 200, 250 and 350 Hz, resulting from the. mains frequency of 50 Hz and its harmonics, which could be eliminated through appropriate filtration as they sit beyond the maximum operation frequencies intended for the MEMS instrument and AFM.

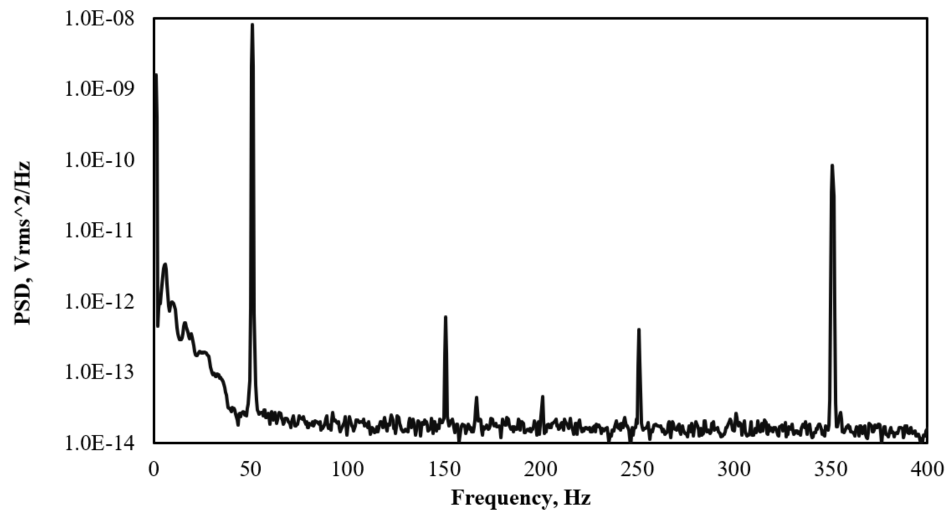

Figure 35. Power spectral density analysis of the AFM Group Laboratory (Rankine Building, School of Engineering, University of Glasgow) where an AFM system was being run (capture by Agilent 35670A spectrum analyser, bandwidth - 0.5 Hz).

This section concludes the necessary theory and terminology overview, which is utilised throughout the device conceptualisation, development, final product characterisation and application demonstration in the forthcoming chapters 4, 5 and 6 respectively.

Chapter 4 - MEMS Fabrication

The following section focuses on the fabrication process carried out within the James Watt Nanofabrication Centre at the University of Glasgow. Developments in micro and nano fabrication methods now allow unprecedented accuracy in lithographical definition, permitting nanometre scale tolerance controls across micrometre scaled structures. The materials and fabrication methods are greatly inspired by previous work carried out at Glasgow producing novel scanning probes [160] [161] [162] [163] [164] and related thin film MEMS sensing devices [165] [166] [167], expanding upon it with novel process choices and improvements permitting the production of a functional MEMS tool.

4.1 Fabrication concept and starter substrate

The discussion in this chapter forms the underlying basis for the new MEMS component that was designed, fabricated and characterised in the rest of the discussed work. For practical reasons aimed at development time reduction, the starter wafer substrate is outsourced as it posed no limitations on design and processing freedom - hence an off-shelf picked silicon wafer[3]. Due to local limitations in insulator deposition, the substrate received a low stress silicon nitride LPCVD coating[4] at the Chalmers Nanofabrication Laboratory (Gothenburg, Sweden [168]) - which will serve as the structural layer for the mechanical sensor component as well as insulating carrier for the conductive strain gauge.

[3] Single side polished *3*-inch and phosphor (*n*-type) doped 380 μm thick silicon wafer, <100> lattice orientation by PI-KEM Limited [155], UK.
[4] Proprietary composition, described in part in S. Tönnberg's work [170].

The further processing is to be conducted fully in house. The concept behind the proposed MEMS tool is that it can be realised using standard cleanroom fabrication approaches, resulting in batch produced devices of high reproducibility, spreading unit cost and offering a competitive alternative to the previously mentioned probe calibration instruments and techniques. The idea is that a suitably small tool could be permanently integrated within an AFM system - e.g., on the positioning stage, in a similar way to the existing alignment assistance stage on a Brucker Dimension Icon AFM, providing the user with a push-button solution which is no harder to use than a conventional thermal tuning measurement. A top-down fabrication is chosen in order to produce the device in robust batch production friendly manner with the least complex processing - as visualised in Figure 37, with the undertaken process developments and optimisations in metallisation and surface machining are detailed in the upcoming sections.

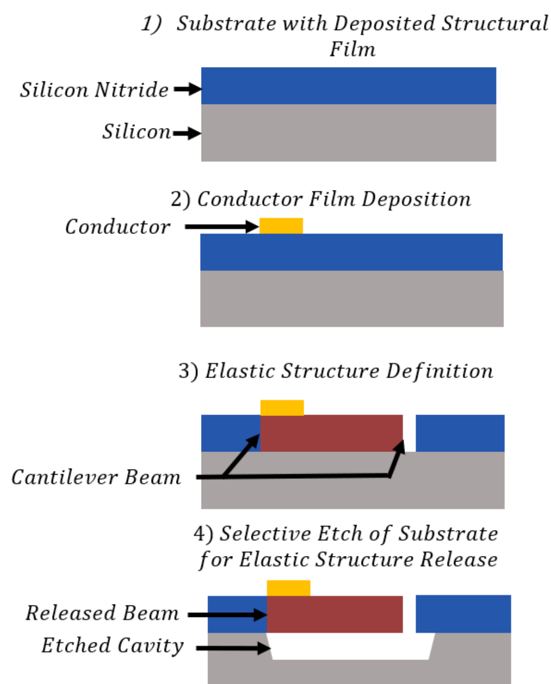

Figure 36. Fabrication sequence and material choice outline for the conceptualised strained resistor equipped cantilever force sensor.

This necessitated for scalable functional design choices during the prototyping and development stages. Firstly, the electrical sensitivity needs to be considered. It relies on one key parameter - load strained wire length. Its sufficient length is difficult to define without a test involving a complete integration with instrumentation and AFM system, therefore efforts from the get-go were focused on choosing a flexible manufacturing method providing maximal flexibility in scaling strain gauge design packaging - electron beam lithography. This enabled easy prototyping by means of a simple CAD mask modification, allowing for the desired serpentine wire packaging to be iteratively achieved (as showcased in 4.3). Secondly, a high mechanical compliance (low stiffness) of the carrier cantilever means larger deflection per load unit, which results in higher sensitivity due to increased strain experienced by the sensing wire. Minimising the MEMS device spring constant is therefore another key goal that was enabled by the easily scalable electron beam lithography defined planar dimensions. Similar thickness (~400 nm) silicon nitride cantilevers are consistently available in the sub 0.1 N m^{-1} range [169] [170] [171], therefore producing a MEMS device with elasticity at this or lower range is a reasonable expectation (achieved successfully per assessment in 5.1.3). Combining both electro-mechanical requirements meant that the key features relied on parametrically driven packaging dice sizes, scalable on-chip connectors, flexible alignment marker positioning and finally - intra-dependent etch and beam boundary geometries. The conceptualised MEMS device is shown in Figure 37 with its fabrication explored in-sequence throughout this chapter. However, the MEMS device shape has evolved significantly throughout the process development stages, with the final successfully fabricated designs showcased in 4.6 and Figure 62 and 64.

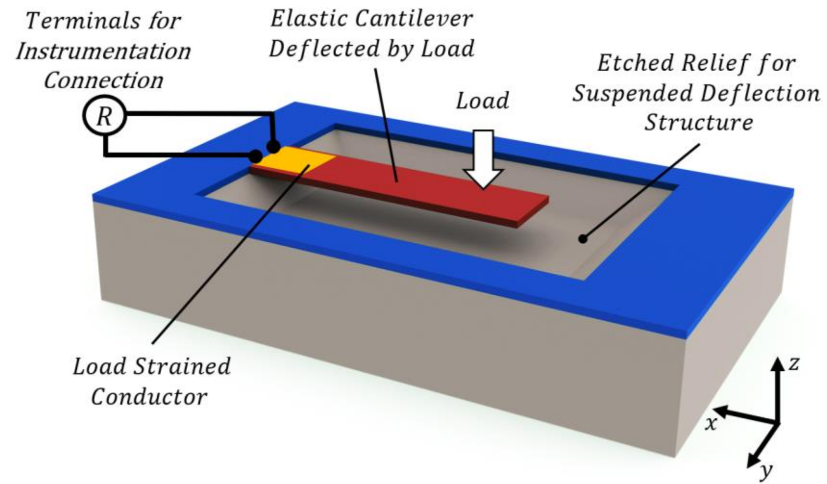

Figure 37. Visualisation of an elastic cantilever with integrated resistive strain sensor near the fixed end.

4.2 Step 1 - metal film lift off, marker layer

The MEMS device fabrication aimed to achieve geometrically and functionally consistent devices that could be reliably fabricated with high success rate, hence the considered microfabrication processes are based on robust batch production practices. A key consideration to achieve this in a multi-layer fabrication process is the successful realisation of inter-layer registration, allowing alignment of different lithographic layers. This can be done by employing a permanent coordinate system on the substrate – colloquially referred to as a 'marker layer'. 'Markers' can be produced using lithography followed by pattern transfer through additive (metal deposition) or subtractive (etching) techniques, forming recognisable contrast with the background substrate. In this work, an additive technique based on physical vapour deposition (PVD) was chosen to form this feature, with a commercially available electron beam evaporator (Plassys MEB 550S, France [172]). This employed a combination of gold top layer and adhesive nickel-chromium underlayer patterned using a process called metal lift-off, shown in Figure 38. The combination of gold and nichrome was chosen as the marker material due to the following practical considerations. Gold on silicon nitride provides a high contrast signal when imaged using a secondary electron emission detector as employed in the e-beam tool used in this work (Vistek VB6 by Raith, Germany). Gold is also inert to the remainder of the microfabrication processes employed, retaining its form and function throughout the device fabrication cycle. Nickel-chromium was used as the adhesion layer between gold and silicon nitride, since a direct gold to silicon nitride interface exhibits poor adhesion and can result in delamination or poor edge definition, affecting subsequent registration

accuracy [173]. The initial feature enabling further fabrication layer alignment is shown in Figure 39 and the fabrication process is detailed in Appendix B, process table 1.

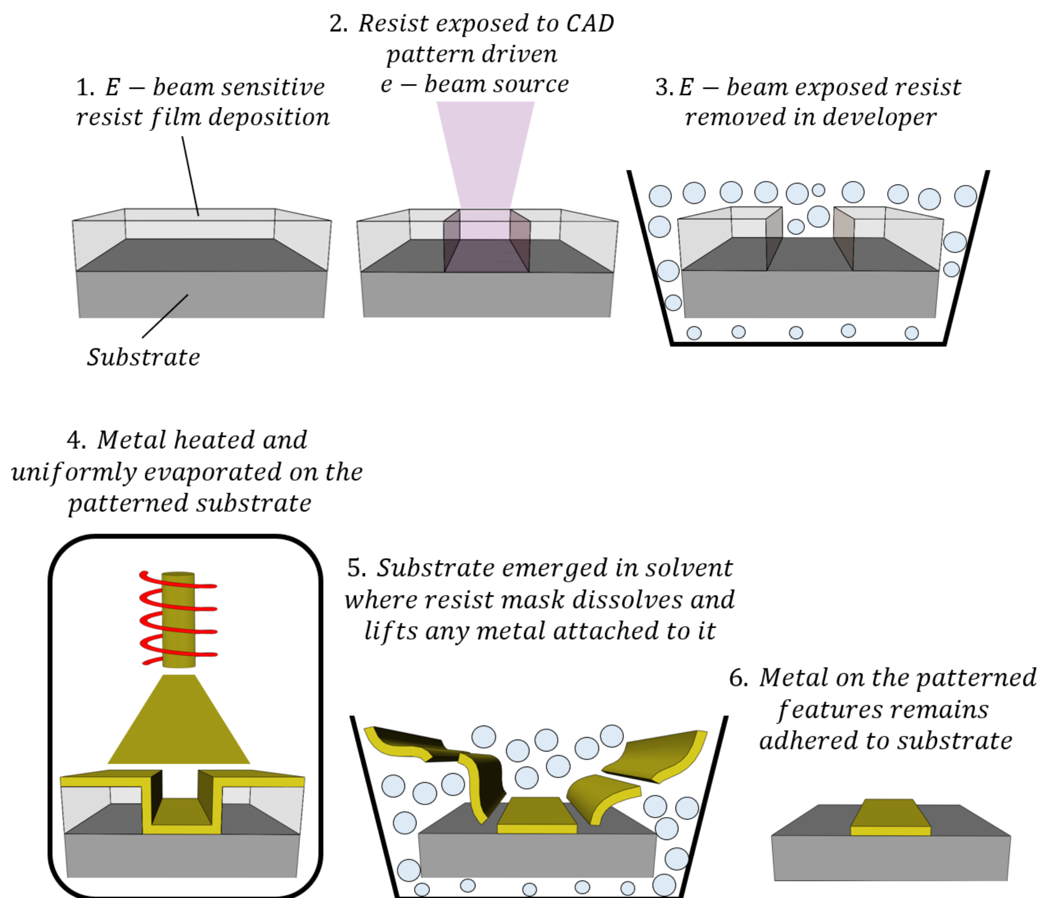

Figure 38. 1-2) The marker layer mask pattern is written by CAD data driven electron beam machine on a layer of sacrificial polymer resist layer applied on the substrate by a spin-coat method. 3) Changes in polymer cross-linking under exposure to the electron beam allows a suitable developer liquid to selectively remove material exposed to it. 4) The substrate with the revealed pattern is then uniformly coated by evaporated metal in a physical vapour deposition apparatus, where the metal layer sticks to the revealed silicon nitride surface and the surrounding resist mask. 5-6) The mask is then dissolved in a suitable solvent (e.g. acetone), causing a separation or lifting of the metal from the substrate that is adhered to it and thus only the mask formed features remain coated in the chosen metal.

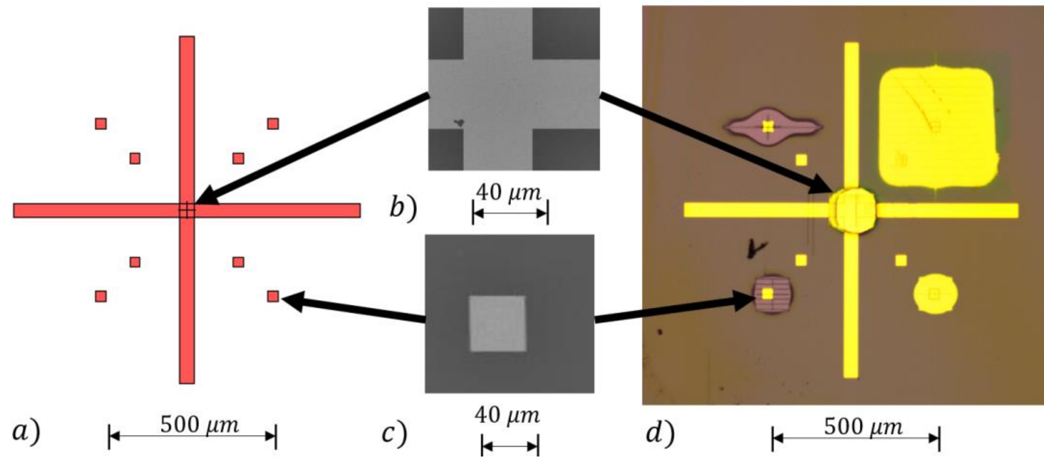

Figure 39. Registration feature with origin cross and square location markers: a) CAD file for pattern; b-c) Secondary electron scanned origin points and cell marker; d) Optical image after final metalisation steps, indicating the previously exposed areas.

4.3 Step 2 - metal film lift off, sensor layer

Once alignment marks were available on the substrate, the second fabrication step, also a metallisation layer, was patterned through an analogous metal lift off method. In this layer electron beam lithography was used to define a complex metal pattern which included the strain resistor pattern, Vernier marks, text containing device identification information, large area connection pads for instrumentation and four leads joining the strained resistor ends and the corresponding four pads - per sequence detailed in Appendix B, process table 2 and graphical representation in Figure 40.

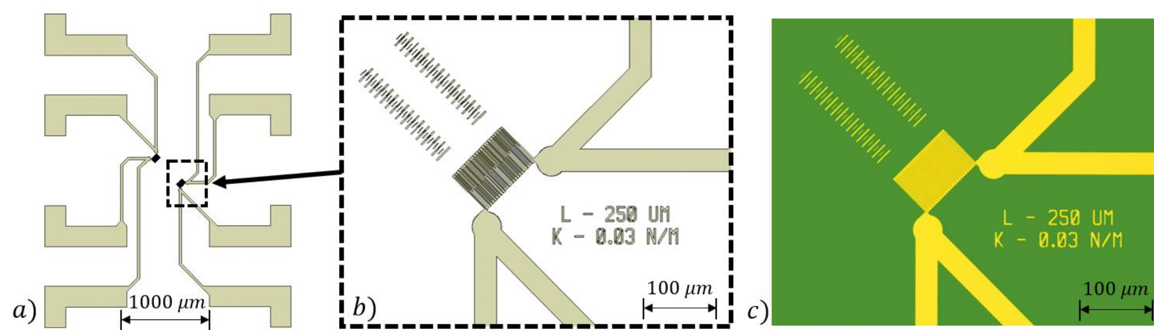

Figure 40. a) and b) metallisation layer pattern pictured in CAD and c) optical image of the fabricated metal layer.

The material chosen for this layer was a nickel chromium alloy with a nickel:chromium ratio of 3:2, (commonly referred to as nichrome). Nichrome was selected over the other available materials for a number of reasons. Firstly, it exhibits the highest specific resistivity of the available PVD metals, meaning that the strain induced changes in resistance would have the highest magnitude for the given geometry. Secondly, nichrome has the lowest thermal coefficient of resistance, reducing environmental temperature effects during the device operation. An in-depth characterisation and literature overview supporting this can be found in characterisation section 5.3. Finally, as mentioned in the

first step, nichrome is compatible with the remainder of the fabrication process - particularly the aggressive KOH etch which damages aluminium films. However, nichrome is not a perfect material as it exhibits an undesirably high elastic strength when compared to other options such as gold or aluminium. It can also suffer from high internal stress in deposited film form which may result in layer wide delamination or cracking. In the end, it was felt that its advantages outweighed these negative features, which may also be remedied by a certain degree through having full in-house process control over the nichrome deposition.

4.3.1 Metal film strain sensor fabrication trial

Test structures covering a range of strain sensor geometries were produced in order to assess lithography and lift-off quality, as judged by visual inspection. The fabrication and technological limits of the chosen lift-off method were tested by modulating the conductor wire width, length and offset to achieve a range of conductor packaging densities in the chosen planar envelope, while the film thickness was fixed at the determined minimal value. Summary of the trailed metal film sensor geometries - variable location and fabricated sensor variations pictured in the images below (Figure 41 - 43), while the corresponding variables are listed in Table 6.

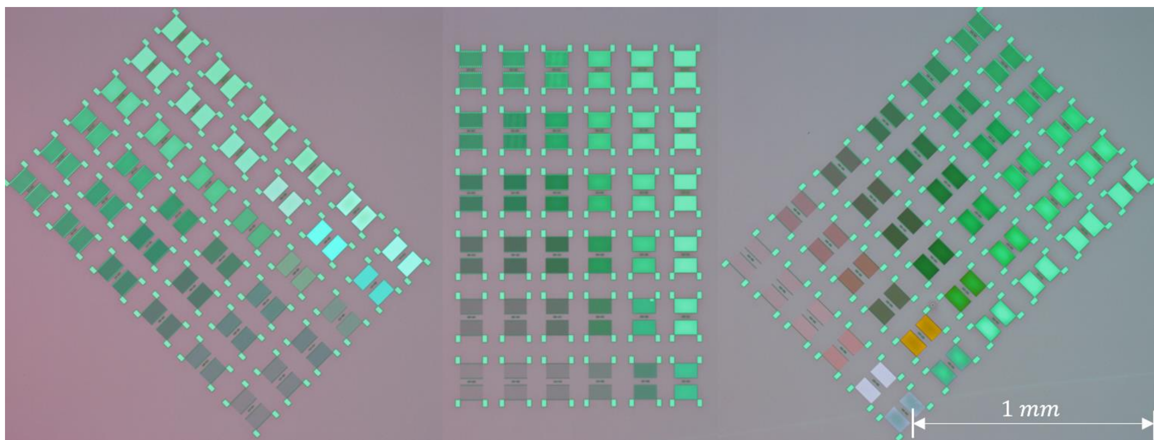

Figure 41. Showcase of the variation of tested devices described in Table 6, where lift-off quality, directionality variations and repeatability were assessed.

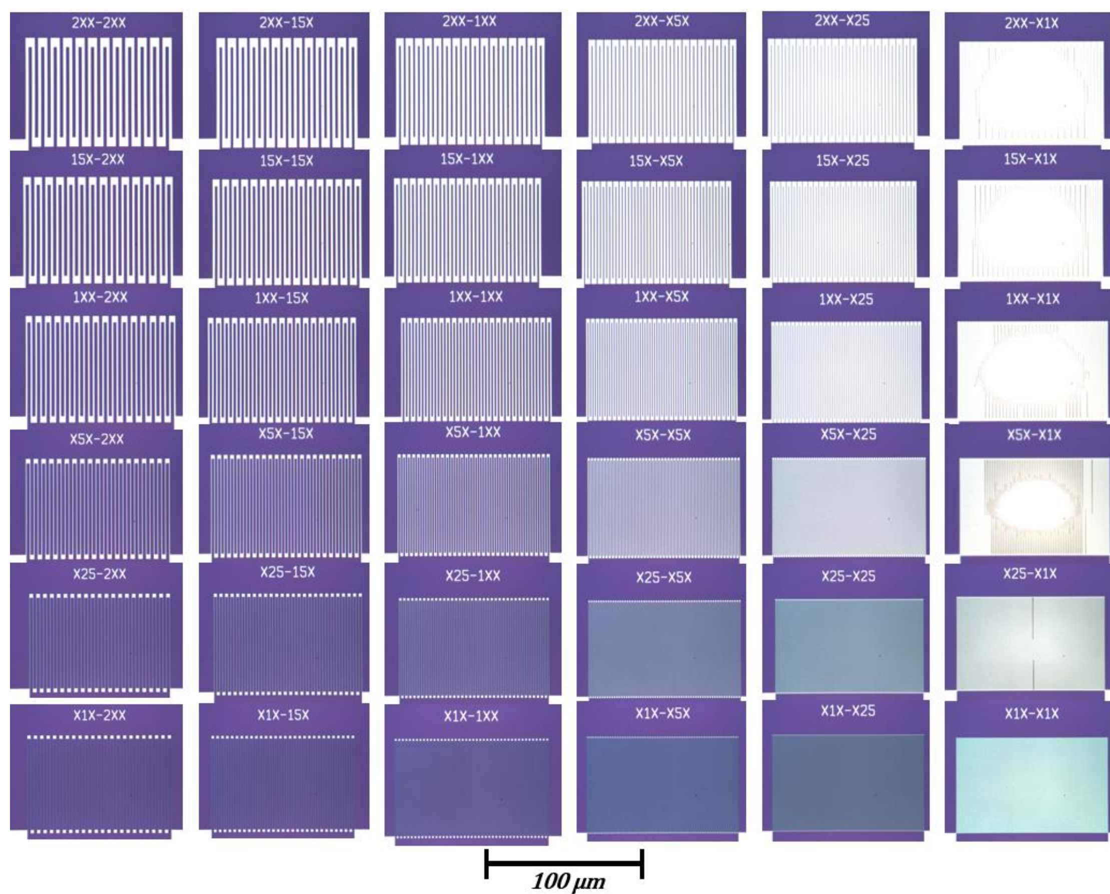

Figure 42. Fabricated sensors stitched into a single scale image.

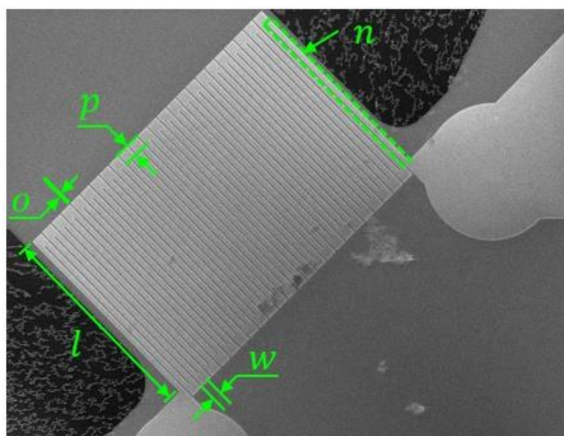

Figure 43. Strained sensor (serpentine)geometry parameters.

Table 6. The 36 trialled strain gauge configurations design to fit a 100 by 60 µm envelope, representing the strain sensor occupied region on the MEMS cantilever. NB: Strike-out numbers had not been successfully fabricated.

No	Conf. Name	Wire width, w, (µm)	Offset, o, (µm)	Pass-over, (2w + o), p, (µm)	Repeat passes, n	Total wire length, (60 × n), (µm)
1	200-200	2	2	6	24	1440
2	200-150	2	1.5	5.5	26	1560
3	200-100	2	1	5	32	1920
4	200-050	2	0.5	4.5	38	2280
5	200-025	2	0.25	4.25	42	2520
~~6~~	200-010	2	0.1	4.1	44	2640
7	150-200	1.5	2	5	26	1560
8	150-150	1.5	1.5	4.5	32	1920
9	150-100	1.5	1	4	38	2280
10	150-050	1.5	0.5	3.5	48	2880
11	150-025	1.5	0.25	3.25	54	3240
~~12~~	150-010	1.5	0.1	3.1	60	3600
13	100-200	1	2	4	32	1920
14	100-150	1	1.5	3.5	38	2280
15	100-100	1	1	3	48	2880
16	100-050	1	0.5	2.5	64	3840
17	100-025	1	0.25	2.25	76	4560
~~18~~	100-010	1	0.1	2.1	86	5160
19	050-200	0.5	2	3	38	2280
20	050-150	0.5	1.5	2.5	48	2880
21	050-100	0.5	1	2	64	3840
22	050-050	0.5	0.5	1.5	96	5760
23	050-025	0.5	0.25	1.25	128	7680
~~24~~	050-010	0.5	0.1	1.1	160	9600
25	025-200	0.25	2	2.5	42	2520
26	025-150	0.25	1.5	2	54	3240
27	025-100	0.25	1	1.5	76	4560
28	025-050	0.25	0.5	1	128	7680
29	025-025	0.25	0.25	0.75	192	11520
~~30~~	025-010	0.25	0.1	0.6	274	16440
31	010-200	0.1	2	2.2	44	2640
32	010-150	0.1	1.5	1.7	60	3600
33	010-100	0.1	1	1.2	86	5160
34	010-050	0.1	0.5	0.7	160	9600
35	010-025	0.1	0.25	0.45	274	16440
36	010-010	0.1	0.1	0.3	480	28800

The minimum film thickness that could sustain a given current was determined by assessing the maximum current density (Eq. 32). The anticipated instrumentation employed a sensor current of I_{max}=10^{-7} to 10^{-5} A, resulting in a current density between 10^{7} and 10^{9} Am^{-2} for the proposed designs. This maximum sustainable value for a device is dependent upon the material, substrate and environment, and for the options considered was expected to fall in the J_{max}=10^{6} - 10^{10} Am^{-2} range, as presented by Ho and Kwok [174]. This was also demonstrated in palladium with a comparable geometry (cross section A=6.6×10^{-14} m^{-2}) by Y.Ge [166] at Glasgow. Therefore, the resistors were designed to be of 30 nm thickness in order to maintain a cross-section within the range deemed 'safe' [166], preventing any detrimental instability (e.g. melting) or electron migration.

$$J_{max} = I_{max}A^{-1}; \qquad \textit{Eq. 32}$$

The produced and tested strain geometries ranged in strained wire lengths from 1.8 mm to 28.8 mm[5]. This wide range was permitted by the broad scaling capabilities of the electron beam mask and lift-off deposition technique. Some of the serpentine designs were observed to suffer from poor metal lift-off, most likely caused by over-exposure of the pattern during electron beam definition (Figure 45, a), where the high feature density resulted in indirect exposure of the background resist - a phenomenon known by lithography users as the proximity effect. Although these effects can be corrected for by modifying the electron beam dose of selected areas, it was felt that the successful strain sensors were sufficient for the expected strain magnitude sensing and so development moved on to sensor integration with the free-standing thin-film carrier structure.

---

[5] Length is proportional to the expected operational strain sensitivity, per:
$R_{abs} = \rho\frac{L}{A}$ and $dR/R_{abs} = GF\varepsilon$;

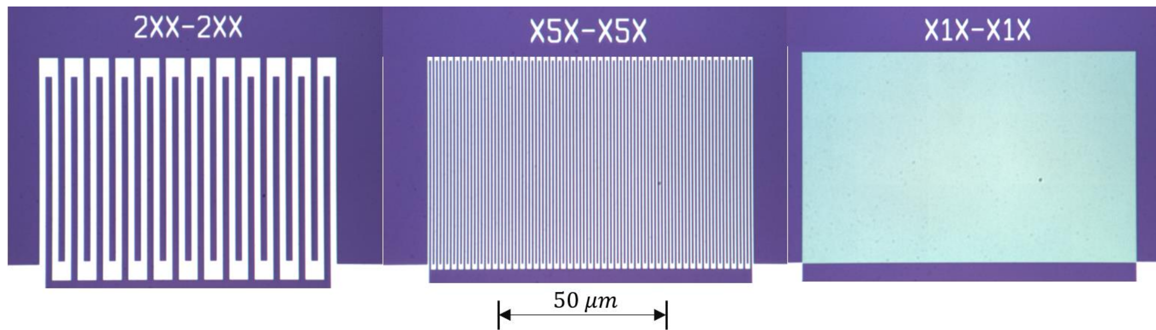

Figure 44. Highlights of the strained wire packaging density variation in the chosen envelope – e.g. the 1.8 mm achieved by the least miniaturised '2XX-2XX' serpentine geometry, versus the highest density successfully fabricated 'X1X-X1X' design with a total length of 28.8 mm. N.B. the 'X' symbol replaces '0' in order to remove closed contours and aid lift-off clarity.

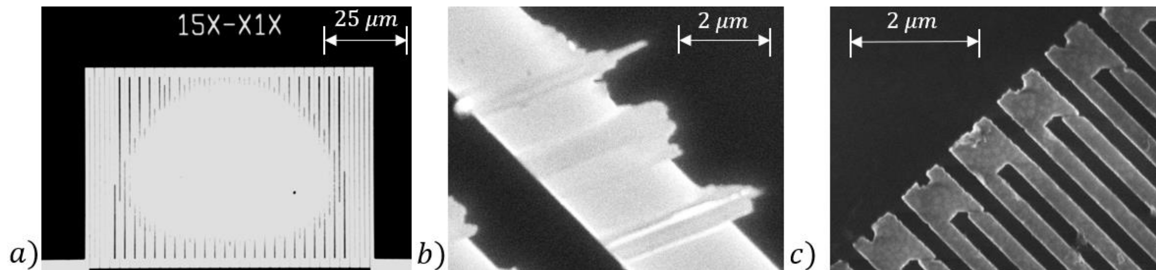

Figure 45. Common failure modes: a) a poorly developed (overexposed) pattern containing thick wires and small offset gaps, illustrating a lift-off failure mode and the chosen additive deposition limitations. b) poor lift-off mask quality, resulting in excess metal not 'lifting' from the substrate. c) failed strain sensor geometry definition caused by insufficient mask exposure resulting in localised undercuts at the overpass – common failure for sub 250 nm width wires.

4.4 Step 3 - plasma etching, elastic structure definition

The outline of the silicon nitride cantilever was defined using an e-beam lithography PMMA resist pattern, that was subsequently used as a dry etch mask. Once transferred into the silicon nitride, this pattern formed the structural cantilever as well as the etch boundary that defined the extent of the anisotropic etch pit in the silicon substrate. Much like metal lift off, reactive etching is a standard process in micro/nano fabrication - parameters of which are dictated by the substrate, mask and pattern material choice as well as the desired etch profile, rate and depth. In this instance, the process specific parameters were adopted from silicon nitride etching described in previous work by the group (e.g. [163]) using commercial reactive ion etching tools - BP80 RIE and RIE 80 Plus by Oxford Instruments, Bristol, UK [175].

The patterned mask was exposed to an RF energised plasma based on the fluorine containing gas (halocarbon R116 or C_2F_6). Plasma etching not only erodes the silicon nitride but also the polymer mask at a significant rate, therefore it is commonplace to transfer the resist pattern into a metal mask, which is then employed in the etch. However, it was felt that this addition and removal of metal could introduce contamination to the strain sensor geometry and, together with the added process cost, was felt to be an undesired addition. Therefore, the PMMA resist mask was exposed to the plasma's physical bombardment resulting in its steady consumption, as well as chemical attachment of fluorine, breaking its carbon-carbon and carbon-fluorine bonds (mechanism explained in [176]). This potentially marginal use of a highly sacrificial masking method for the prolonged and aggressive etch was demonstrated to be reliable when used as described in

the device fabrication procedure (Figure 46). Due to the relatively large feature size of the etch mask (smallest feature, stress relief corner radius of 10^{-6} m) a 10 % spot size (10^{-7} m) resolution achieved with the thickest available single layer PMMA (Allresist PMMA AR-P 642.15) resist was deemed sufficient in the test pattern geometries (Figure 47). A C_2F_6 resist to Si_3N_4 etch ratio was experimentally determined to be at around 2 to 1. This meant that a mask of thickness exceeding the nitride thickness by 2.5-3 (to allow for some fabrication variation and process tolerances) would survive the process without requiring the use of a metal mask (Figure 46) whilst still producing adequate definition features. The fabrication sequence was followed by a conventional clean in solvents to remove the remaining polymer mask, per process parameters detailed in Appendix B, process table 3.

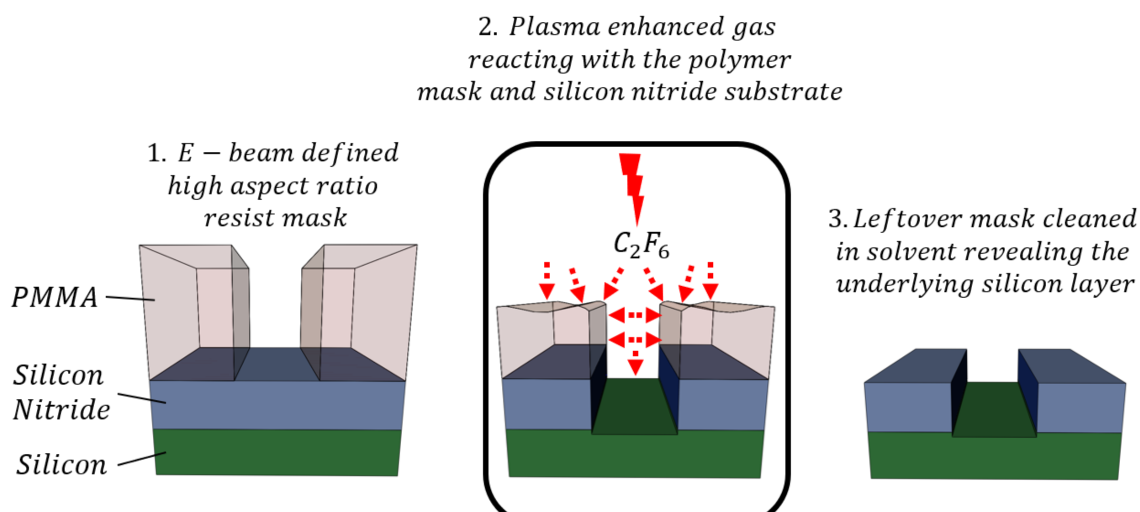

Figure 46. 1) A thick mask is patterned by an e-beam., 2) Substrate is bombarded by a charged halocarbon gas that reacts and removes the silicon nitride, as well as the patterned resist layer. 3) Leftover resist is cleaned in solvent, revealing the mask pattern on the silicon nitride and exposing the underlying silicon substrate.

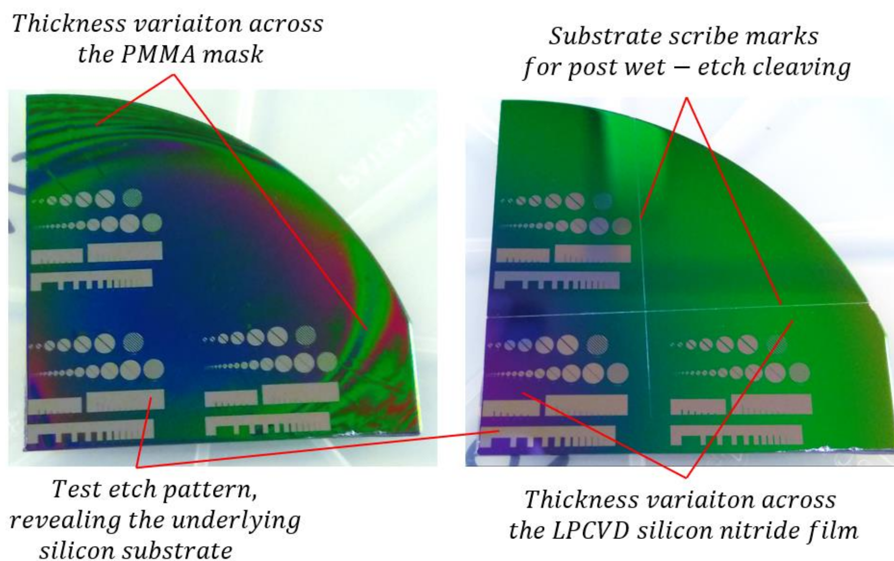

Figure 47. The etch pattern on the test substrate (quarter of the LPCVD nitride coated 3" wafer) showcasing the (left) post-plasma etch revealed etched features on silicon and the non-uniform PMMA thickness caused by the plasma base etch. Right - the cleaned and scribed wafer with the desired silicon nitride features. The colour gradient non-uniformity is due to the LPCVD film variation and not related to dry etch.

4.5 Step 4 - selective chemical etching, elastic structure release

Following definition of the silicon nitride cantilever, the underlying silicon was removed to form a free-standing cantilever structure. Silicon etching can be achieved in two distinct ways - isotropically, in a directionally independent manner (by employing a solution an acetic acid, nitric acid and hydrofluoric acid solution), or anisotropically, at geometrically varied etch rates (e.g. by employing a potassium hydroxide solution). This liquid anisotropic etching technique is often employed in MEMS component formation, due to the geometrical control provided that allows complex feature formation, necessary for the mechanical device designs - e.g. of microfluidic apertures [177] and thin film SPM cantilever undercuts [162]. The etching solution continuously reacts with any exposed silicon, generating by-products that move away from the surface, exposing fresh silicon thus removing (or 'machining') away the material. Etch rates are defined by solution concentration and temperature, allowing a fine level of control over the process described in Figure 48.

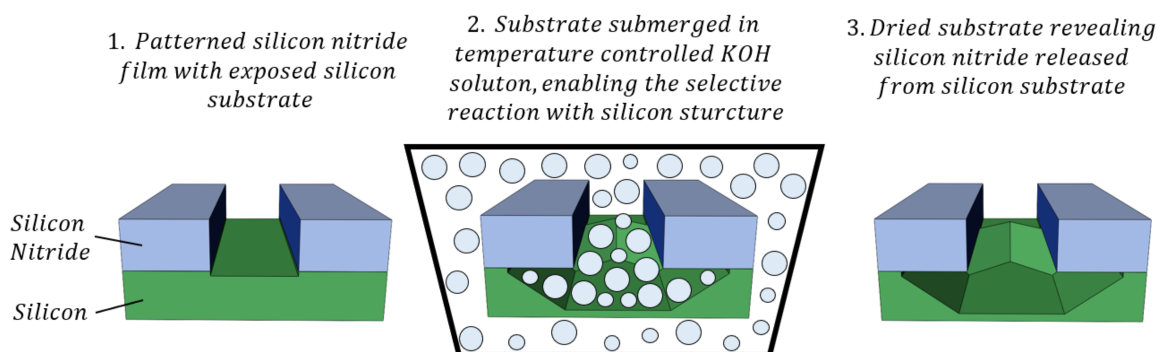

Figure 48. Wet etching process showcasing how the silicon nitride structure can be released by under etching silicon substrate through taking advantage of the selective etch planes.

The anisotropic nature of some etches, a hereby desired feature, is a result of the fact most silicon substrates are single crystals. In a crystalline solid, atom placement and proximity defines the direction of the individual atom bonds and are conventionally described in terms of Miller index naming convention. When exposed to a hydroxide containing etchant, e.g. potassium hydroxide (KOH), the varied number of inter Si atomic bonds at the surface undergo the chemical reaction outlined in Eq. 33 [178] at different rates, thus allowing for intricate geometric feature formation (e.g. [179]), not offered by other surface machining methods. This allows for selective positive or negative three-dimensional feature (pyramid or pit) formation, from the planar (two-dimensional) mask. Conveniently, simulation software is available to aid in predicting more complex topography etches (e.g. Anisotropic Crystalline Etch Simulation ACES by UIUC MASS Group, hosted at [180]). The achieved feature (negative pyramid pit) required for the cantilever structure release is shown in Figure 49, using the Miller index convention - e.g. {100} is the 'fast' etch plane (parallel to the plane of the mask if a <100> oriented Si wafer is used) and {111} is the 'slow' etch plane that is at 54.7° angle to the {100} plane, as dictated by the silicon substrate atomic lattice formation.

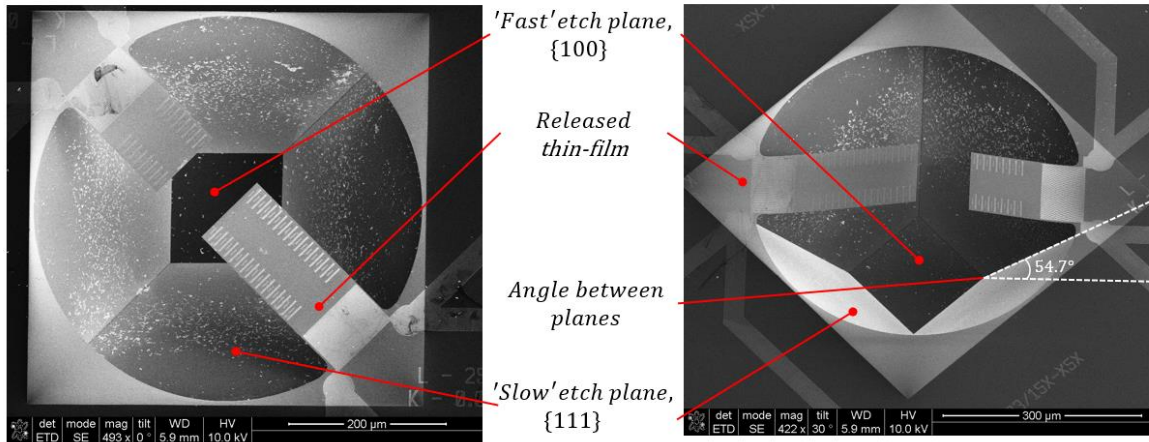

Figure 49. The MEMS device a) planar and b) tilted views highlighting the anisotropic removed pyramid. Silicon etch planes named per Miller Index convention. The selective etch method allows for different plane etch rates along the crystal planes - ratios of 1:100 are achieved in slow:fast planes with selected KOH concentration [181], enabling consistent regular pyramid feature formation.

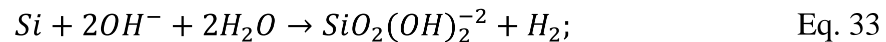

$$Si + 2OH^{-} + 2H_2O \rightarrow SiO_2(OH)_2^{-2} + H_2; \qquad \text{Eq. 33}$$

The released structures were extremely fragile to any submersion and drying induced forces. Several methods of drying were tested on the substrates, allowing a sequence enabling the fabrication of the highly deformable structures to be identified. A full base neutralisation (e.g. in sulphuric acid) and native silicon oxide removal in (hydrofluoric acid), that are often used in such processes, were eliminated due to consistent cantilever failures (Figure 50) suspected to be caused by the additional agitation and submersion/drying mechanics.

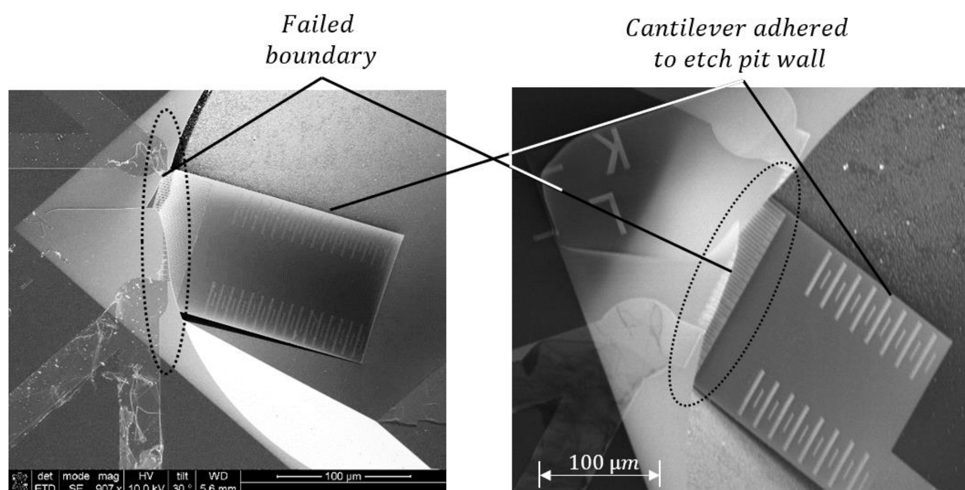

Figure 50. Post wet-etch failure mode where cantilever adheres to the nearby underlying etch pit. The consistently downward direction and lack displacement form the failure site suggest a common interaction between the wall and cantilever - e.g. a drying liquid presence.

To mitigate the agitation and drying steps, a pipet wetted transfer from the etch solution to a non-agitated water was conducted first, where the potassium hydroxide dilution takes place - leaving salt deposits behind (Figure 51). A straight drying from water to air took a significant amount of time (assisted with nitrogen flow 30-45 minutes, non-assisted 60-90 minutes) and resulted in failures indistinguishable from the, now eliminated, acid submersion cycles. The cantilever breakage and stiction to nearby sites was attributed to the liquid pooling at the bottom of the etch pits and gradually pulling the compliant structures together during the drying process. Therefore, an additional wetted transfer to a methanol solution was introduced, to take advantage of the methanol's significantly lower surface tension (γ=22.5×10^{-3} N m^{-1} for methanol-air compared to γ=72×10^{-3} N m^{-1} for water-air [182], and γ=70-80×10^{-3} N m^{-1} for the aqueous potassium hydroxide to air [183]) and accelerated methanol evaporation (5-minute nitrogen gun assisted drying).

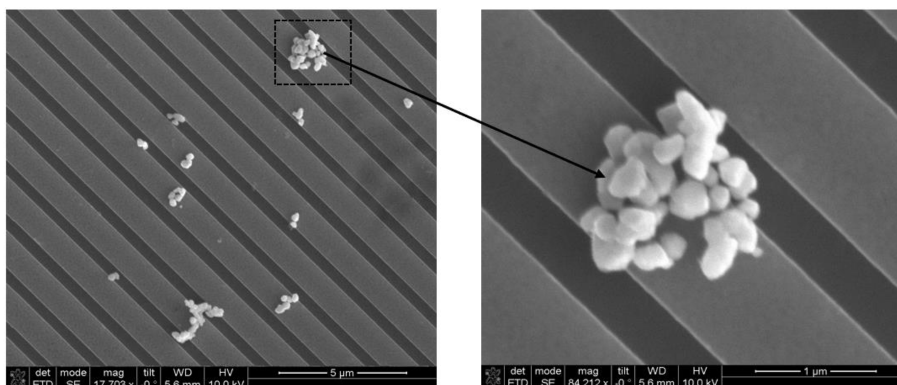

Figure 51. The presence of crystal-like particles - believed to be potassium salts, after a non-complete post wet-etch solution neutralisation in water.

The remaining failure modes witnessed after introduction of this step were attributed to the film quality as well as cracking and shock damage during cleaving process, therefore for maximum yield, the devices were cleaved before the wet etch step, so no purposeful shock induction was necessary post release. The fabrication specifics are described in Appendix B, process table 4 and illustrated in Figure 52. The following section focuses on the device level results and function related parameter development.

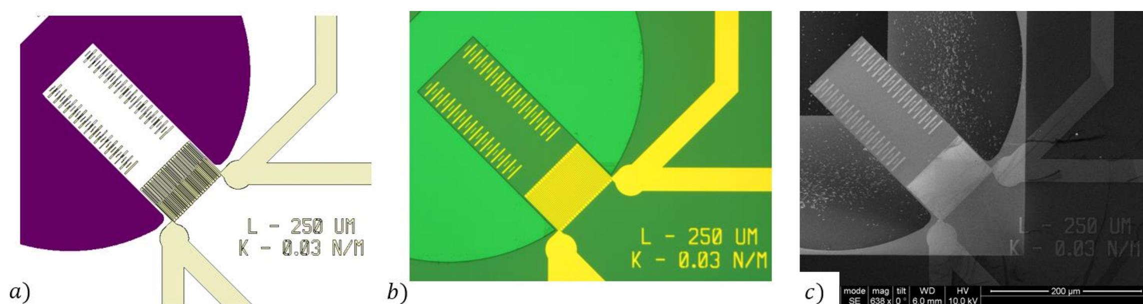

Figure 52. MEMS wet etch pattern in a) CAD file, b) optical image before submersion and c) SEM image the after selective KOH etch, releasing the device with a directionally formed boundary in the underlying silicon substrate.

4.5.1 Elastic structure geometry optimisation

The pattern defined in the silicon nitride was designed and oriented to take advantage of anisotropic silicon etching to form a consistent boundary from the 'slow' etch plane. To test the fabrication method, cantilever arrays of varied length were formed from the silicon nitride film (Figure 54). This design was inspired by Petersen's work [184], but resized to an appropriate scale relevant for this task. The detailed geometries and dimensions are discussed in the characterisation chapter (section 5.1) whilst the focus here remains on the fabrication feasibility with the available methods. It was desirable for the calibration structure to be planar and sized so that each cantilever could be located within a typical AFM - i.e., length of ~10^{-4} m and width ~10^{-5} m. This was intended to permit straightforward alignment using the AFM's own positioning stage. The rectangular cantilevers, chosen due to their ease of fabrication and excellent description using analytical models [112], also allowed for straightforward performance prediction. However, the use of the rectangular boundary structures aligned along the {100} planes often resulted in incomplete cantilever release and inconsistent edge definition (e.g., Figure 53), undermining the structural correlation to analytical descriptions.

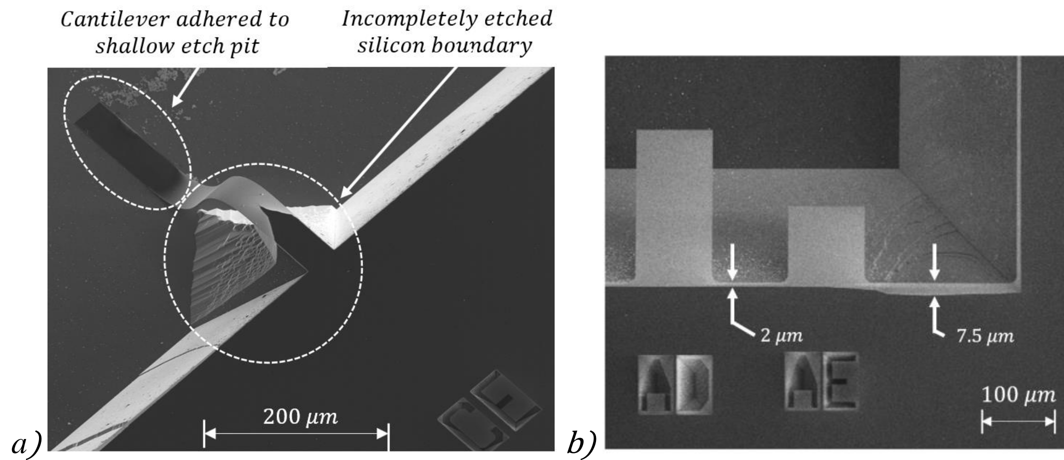

Figure 53. a) Test beam structure experiencing two failure modes simultaneously under-etch failure caused incomplete edge formation and long cantilever stiction to the shallow etch pit (SEM). b) Inconsistent cantilever boundary revealing a shifted silicon plane during release, due to possible deposition and/or masking contamination.

Additionally, it was observed that long cantilevers were prone to adhering to the bottom of the etch pit. It was speculated that the mechanism for this was the liquid solution droplets vacating the etch pit progressively pulling the compliant structure to the bottom surface during the drying process (described in 4.5). The practical implication of this was that such geometries had limits to the maximum cantilever length and thus compliance, with the wet processing preventing the production of cantilevers that exceed the etch pit depth with ratio of roughly 1.5:1 (Figure 54). This placed a practical maximum cantilever length at 400 µm, as dictated by the 380 µm thick wafer used, if at least 100 µm of the thickness was to remain at the base of the pit in order to retain its structural integrity.

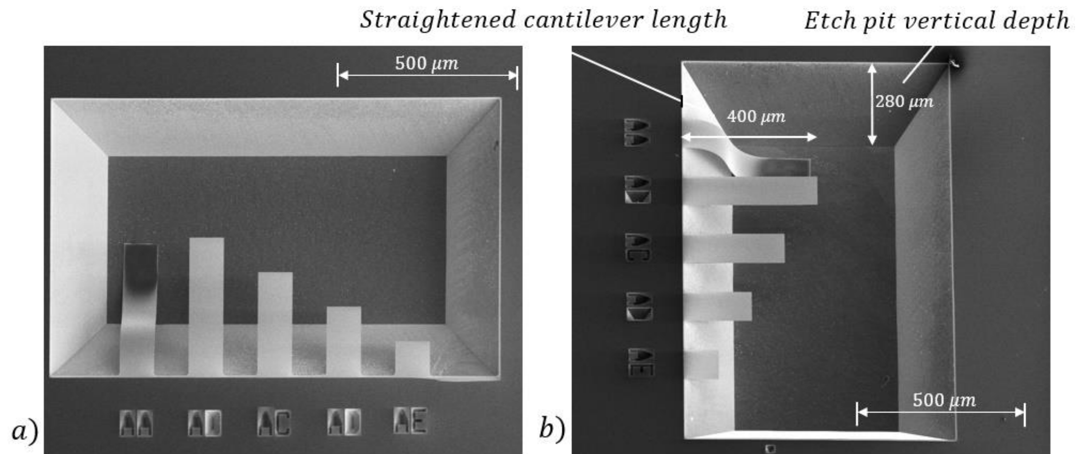

Figure 54. a) planar and b) isometric SEM images of the microfabricated test cantilevers, showcasing the formed free-standing features. Post release cantilever adhesion to etch pit, if etch pit to cantilever length ratio exceeds ~ 1.5:1.

In an attempt to mitigate the fabrication irregularities at the design stage, a circular boundary was proposed. Orientating the fixed end to be at a 45° angle to the fast silicon etch plane (Figure 55) allowed for a consistent and scalable boundary that was significantly less sensitive to imperfections in alignment and etching. There was a risk of such a cantilever boundary condition being less rigid (no underlying substrate support), therefore reducing agreement with established analytical descriptions. However, in light of the advantages offered to the fabrication procedure, this solution was implemented in the full-scale device fabrication by a successful trial.

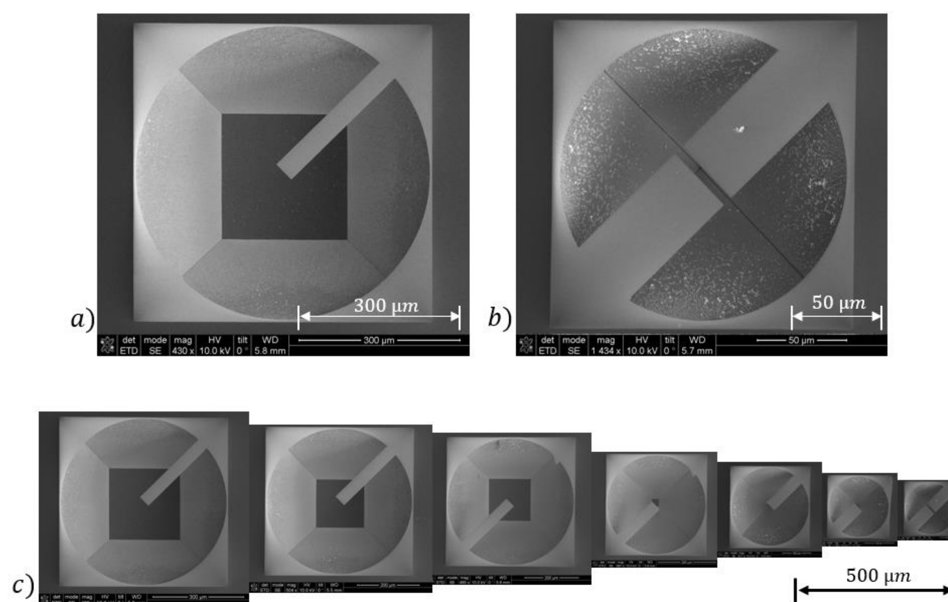

Figure 55. Circular boundary cantilevers form a consistent and scalable boundary formation as well as increased cantilever length before stiction to bottom pit.

4.5.2 Stress concentration reduction

The decision to include a metal film feature on top of a compliant insulator introduced additional fabrication failure modes unique to the complex structures - excessive beam bending and cracking. The analogous geometry, but monolithic structures (nitride-only cantilevers detailed in Figure 55) did not experience such failures, therefore the cause was attributed to the surface of the PVD metal film.

The drying process optimisation (section 4.5) allowed a reduction in the failure rate and provide some further insight into the in-progress failure mechanisms, where cracks had not fully propagated. A partially developed crack was captured (Figure 56 a and b) allowing identification of the corner as the crack initiation point. Therefore, a stress relief radius was incorporated to mitigate this stress concentration. Finite element analysis was employed to determine the relief geometry, suggesting that the inclusion of a 10 μm radius would reduce the maximum operational load stress (10^{-6} N free-end point load) experienced at the structure by 2.65 times - from 220 MPa down to 83 MPa. The radius was minimised in order to mitigate the resultant stiffness increase, which allowed it to remain effectively unchanged - a 2.4% increase, from 0.058 to 0.0594 Nm^{-1} at the end-point of the showcased structure.

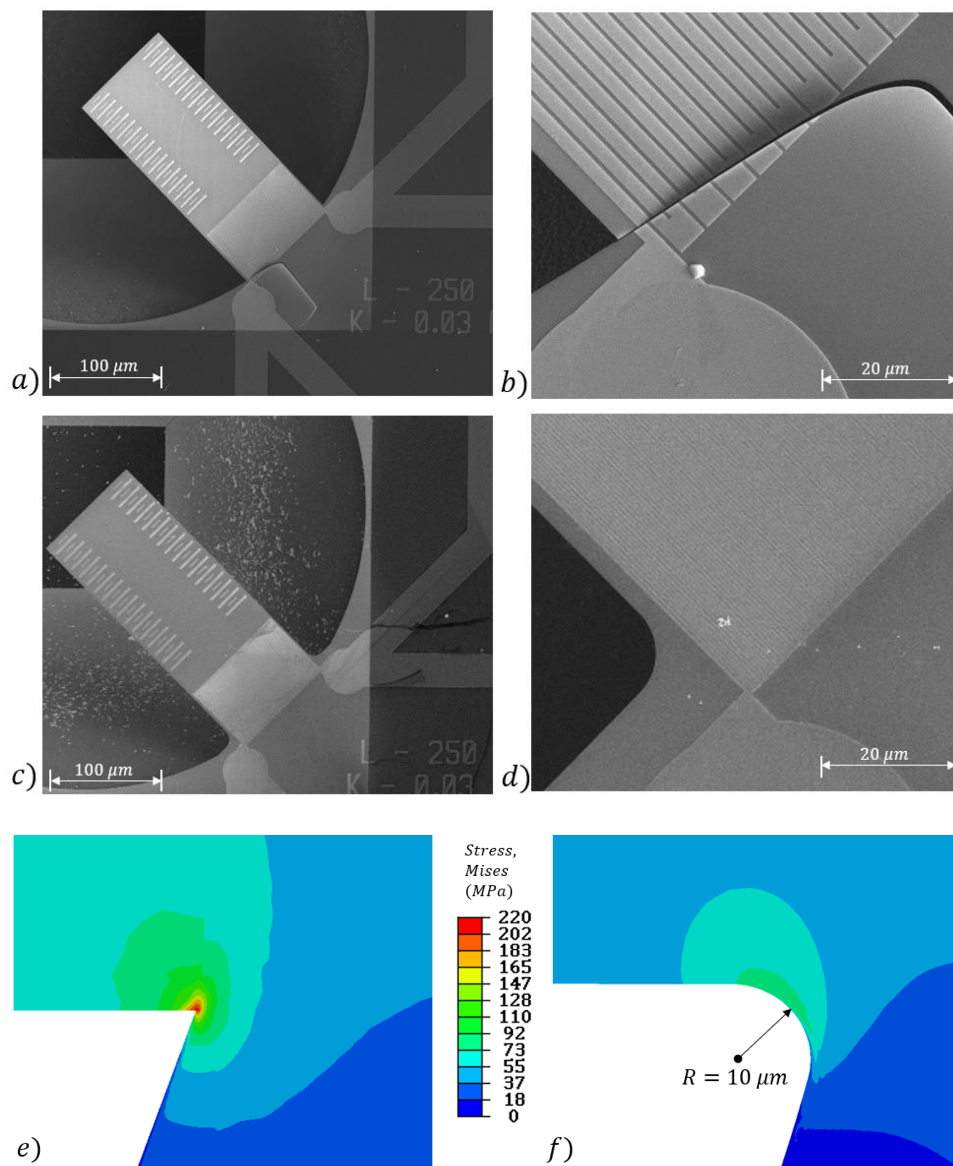

Figure 56. a) and b) SEM images of failed devices and stress raiser induced crack in silicon nitride; c) and d) SEM images of the devices with stress relieving fillet at the stress raiser point; e) and f) FEA stress analysis of surface stress magnitude at the cantilever corner.

Whilst the yield had improved drastically (85-95% depending on feature size) the released structures still retained a pronounced upward bend – a suspected manifestation of bi-material surface stress, a phenomenon that required additional exploration.

4.5.3 Metal thin-film stress reduction

In order to minimise the cantilever bend and allow structures with the highest possible compliance, efforts were taken to reduce the deposition stress in the nichrome conductor film. To confirm the bending root cause, the NiCr film was removed from one of the devices using chromium etchant [185] (Transene, USA) which effectively dissolves nickel chromium (Figure 57). The arched cantilever straightened out upon removal of the strain gauge, confirming that it was the source of the problem. This indicated two possible approaches to resolve the problem: either increasing the silicon nitride stiffness and making the structure less prone to bending and/or reducing the metallisation induced stress. The former option would reduce the sensitivity to strain and require access to externally procured process modification - the LPCVD film deposition. Therefore, the latter was explored in-depth.

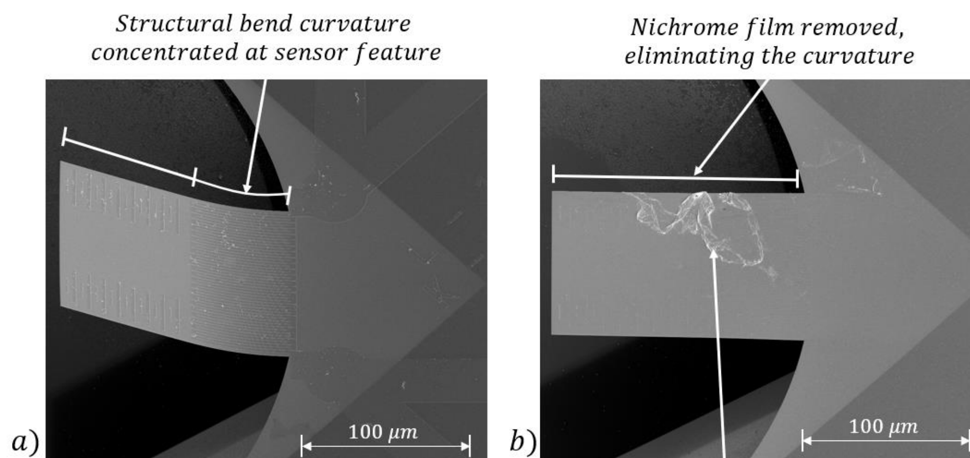

Figure 57. Images taken at angle to the device planar surface, showcasing the a) presence of bend on the complex structure and b) absence of curvature with the metal layer removed.

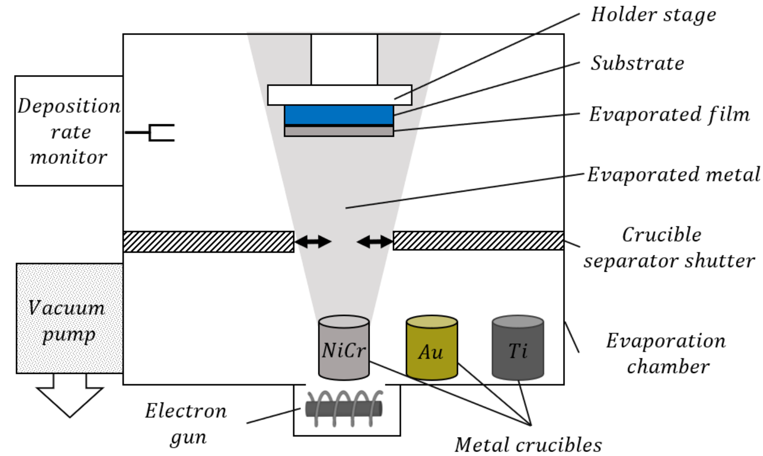

Figure 58. Physical vapour deposition tool (Plassys Bestek) schematic.

The stress present in a deposited nickel chromium film is a product of material formation during the physical vapour deposition process [186] (Figure 58). A first principle approach in understanding the molecular adsorption and deposition thermal expansion parameters is beyond the scope of this work. However, the added film stress can be estimated in practice by quantifying cantilever curvature magnitude. The most straightforward expression relating thin-film stress effect on a substrate in force terms (F_f) was introduced by Stoney [156] and has been reformulated for a simplified bi-material cantilever expression in width (w), curvature (r), substrate elastic modulus (E), film elastic modulus (E_f) substrate thickness (t) and film thickness (t_f) terms [187], per Eq. 34:

$$F_f \times \frac{t + t_f}{2} = \frac{Et^3 w}{12r} + \frac{E_f {t_f}^3 w}{12r}; \qquad \textit{Eq. 34}$$

This expression is useful for illustrating the relationships of conveniently quantifiable variables - curvature magnitude and thickness, that can be determined by optical surface profiling (Figure 60) and physical surface profiling. However, the expression's application is limited to slender beams (w:L<50) with low film to substrate thickness ratios ($t:t_f<0.01$). These conditions are unsupported by the MEMS device geometry employed here - w:L of

1.3-2.5 and t:t_f =0.075, as well as the non-orthogonal fixed end boundary geometry. This meant that the assessment could only be used for a relative stress magnitude quantification, although it was decided that this was still sufficient for process optimisation.

Several test structures replicating the MEMS geometry were fabricated from a single wafer to minimise any substrate thickness variation. The samples were individually cleaved, and the NiCr was deposited on each sample uniformly, resulting in the detectable curvature (Figure 59). The choice to conduct experiments on separate samples rather than adding and dissolving nichrome film away (Figure 57) was motivated by the structural fragility post release and high chance of sample breakage during the etching and cleaning process as well as unintended surface contamination.

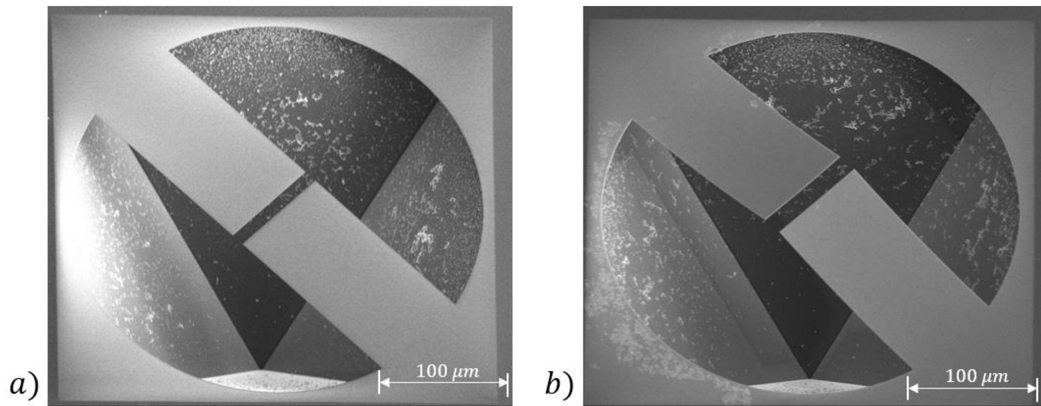

Figure 59. Planar images of the (a) non-metallised beams with no visible bend and (b) metallised structures, portraying a pronounced upward arch.

Nickel chromium is often used as an adhesion promoter for metals that have poor adhesion properties of their own (e.g., gold and platinum). As this layer is typically under 10 nm and deposited on solid substrates, the resultant surface stress is not of concern to most tool users. A reduction below the safe electrical current-density thickness of 30 nm (section

4.3.1) was therefore not explored due to the anticipated electrical fragility and the process development focused on manipulating other available parameters.

The avenues explored were concentrated in four major process iterations employing previously introduced metal evaporator system [172], returning notable improvement steps, further referred to as Recipes 1 to 4. The baseline configuration, employed in the previous runs (e.g. Figure 56 and Figure 57), now called Recipe 1, was set to a target thickness of 30 nm and the evaporation rate of 0.4 nm s^{-1} per tool pre-set standard. Literature indicates [188] that a reduced deposition rate reduces the deposited metal grain boundary size, which results in lower metal film stress. This theory was tested by altering the rate of evaporation, which was configured by controlling the crucible evaporating electron gun voltage, with the resultant deposition rate being measured by the built-in quartz resonator. An initial reduction of the rate to 0.1 nm s^{-1} for Recipe 2 was introduced, yielding a significant bend reduction. Therefore, another iteration (Recipe 3) at the lowest permissible rate (0.04 nm s^{-1}) was conducted and resulted in further, although less significant beam relaxation. A final process development improvement was introduced in Recipe 4 per in-person suggestion [189], focusing on chamber and crucible conditioning. This step isolated the sample from the evaporation by keeping the sample shutter closed, preventing deposition on the sample. This process was conducted for one minute in order to remove any nichrome crucible oxidation and/or other contaminant build up present. Furthermore, with the shutter separation lid still closed, titanium was also evaporated for an additional minute, in order to reduce any oxygen present in chamber - a forced reaction to titanium oxide, resembling ion pump operation [190]. These conditioning improvements again resulted in detectable curvature reduction (Figure 60 and Figure 61).

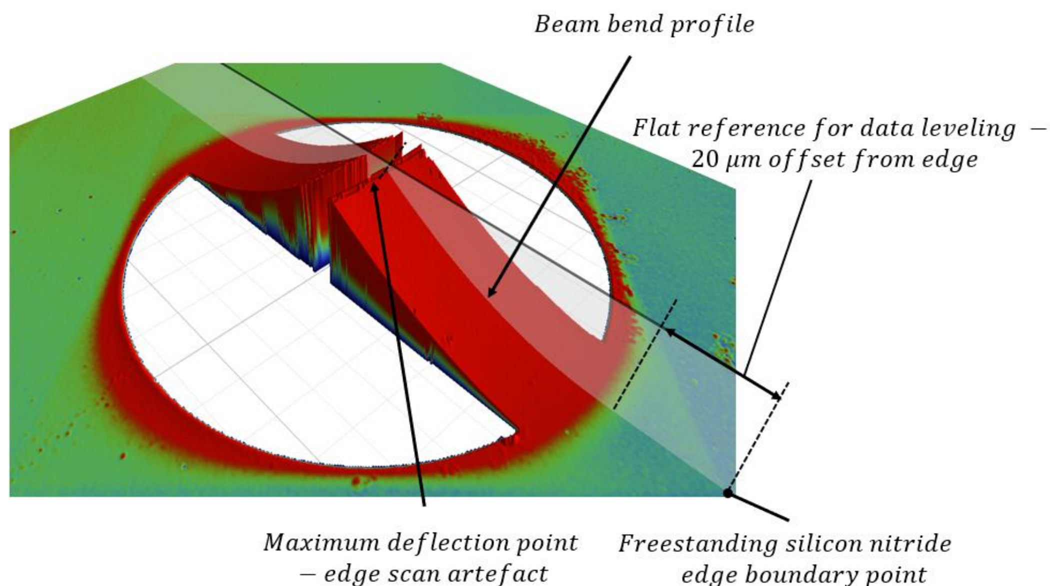

Figure 60. Reconstructed 3D image and profile cross-sectioning line (Optical Profiler - Contour XT, Bruker) from which the deflection profiles are obtained.

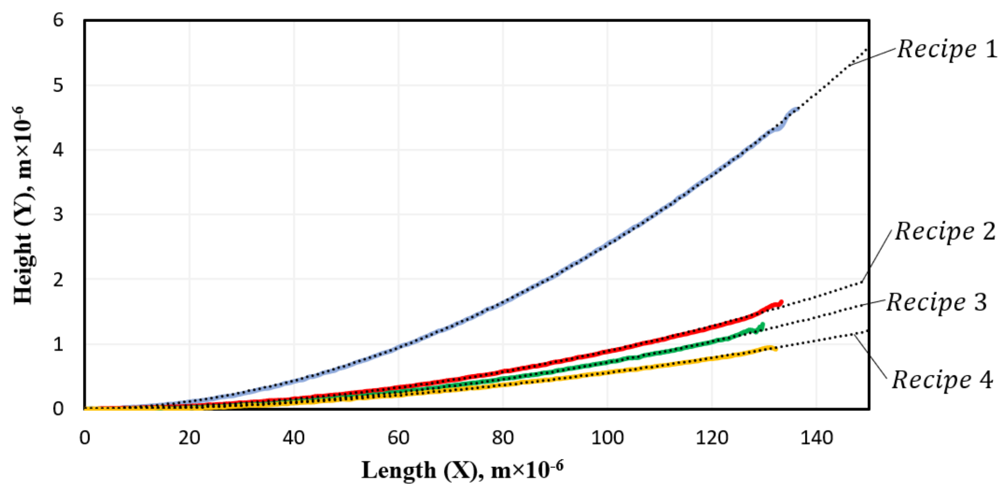

Figure 61. Overlaid bend profiles deflection towards the free cantilever end captured by the optical profiler system (Contour XT, Bruker). Dotted line represents polynomial fit line. NB. The near end non uniformities are due to edge reflection artefacts displayed by the optical profiling technique.

Table 7. Recipe iteration dependant cantilever profile polynomial curve fit variables, $y(x) = c_1x^2 + c_2x + c_3$.

Curve Fit Value	Recipe 1	Recipe 2	Recipe 3	Recipe 4
c_1	2.362×10^{2}	8.766×10^{1}	7.227×10^{1}	4.759×10^{1}
c_2	1.852×10^{-6}	5.105×10^{-8}	8.955×10^{-8}	1.019×10^{-6}
c_3	-1.431×10^{-2}	1.106×10^{-2}	-1.054×10^{-2}	-1.932×10^{-2}
$\frac{d^2y}{d^2x} = 2c_1$	4.724×10^{2}	1.753×10^{2}	1.445×10^{2}	9.518×10^{1}

The assessment criteria thus focused on reducing the second term in Eq. 34 ($\frac{E_f t_f{}^3 w}{12r}$) - wrelating the cubed film thickness relationship to the observed curvature, in order to determine the relative film stress magnitude. Polynomial expressions were fitted to to optical profiler date were used to obtain the curvature magnitude. This approach was used as the deposition target thickness varied between each of the recipes and needed to be compensated for (variation of up to 20%, as shown further in Table 8). Therefore, the investigated bend curvature could be expressed by the Eq. 35, per description provided by [187].

$$r = \frac{\left(1 + \frac{dy}{dx}^2\right)^{3/2}}{\frac{d^2y}{d^2x}}; \qquad \textit{Eq. 35}$$

Since the first derivative ($\frac{dy}{dx}$) is much smaller than 1 (in the 10^{-5} range), the expression could be simplified to Eq. 36. This allowed for complete assessment of the criteria from

the observed curvature (Figure 61) and resultant polynomial fits (Table 7) with a summary of the findings shown in Table 8.

$$r = \left(\frac{d^2y}{d^2x}\right)^{-1}; \qquad \textit{Eq. 36}$$

Table 8. Metallisation run summary, highlighting the process parameters and resultant film thickness (AFM, Bruker Dimension Icon) and curvature (Optical Profiler, Contour XT).

Recipe no.	Change purpose	Targeted deposition rate, $\times 10^{-9}$ ms^{-1}	Measured deposition thickness, t, $\times 10^{-9}$ m	Curvature, r, $\times 10^{-3}$ m	t^3r^{-1} $\times 10^{-21}$ m
1	Original recipe	0.4	30.8	2.12	13.8
2	Intermediate rate	0.1	35.2	5.71	7.64
3	Lowest rate	0.04	36.3	6.92	6.91
4	Pressure reduction	0.04	32.8	10.5	3.36

Nickel chromium deposited using this final recipe exhibited a fourfold improvement in the chosen criteria in thickness and curvature ratio (t^3r^{-1}) and was therefore included in the MEMS device fabrication procedure. This optimised deposition process resulted in a significant reduction of the MEMS device bend - the root cause of witnessed failures, subsequently enabling a much longer (from 130 µm to 250 µm, Figure 62) and therefore more strain sensitive cantilever to be fabricated. This metal stress optimisation was therefore a key factor in enabling densely nichrome strain sensors to be employed.

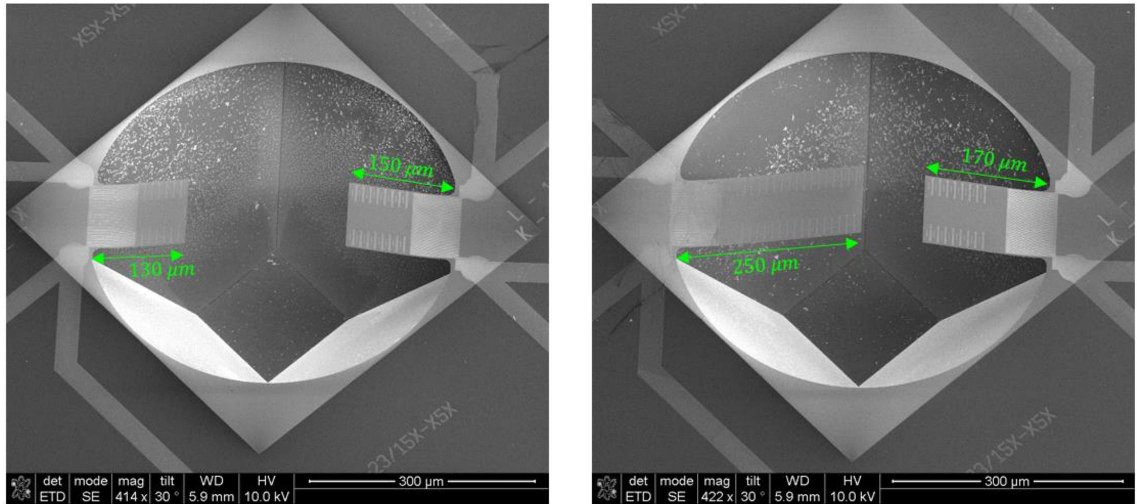

Figure 62. MEMS devices with varied length elastic structures, providing a range of mechanical compliances. The isometric view displays the presence of nichrome film resistor caused bend.

4.6 Result - fabrication of the MEMS calibration device

The compliant beam fabrication combined with the chosen metal film proved to be a highly challenging task, requiring four generations of design cycles in order to produce the final device iteration shown in Figure 63 and Figure 64.

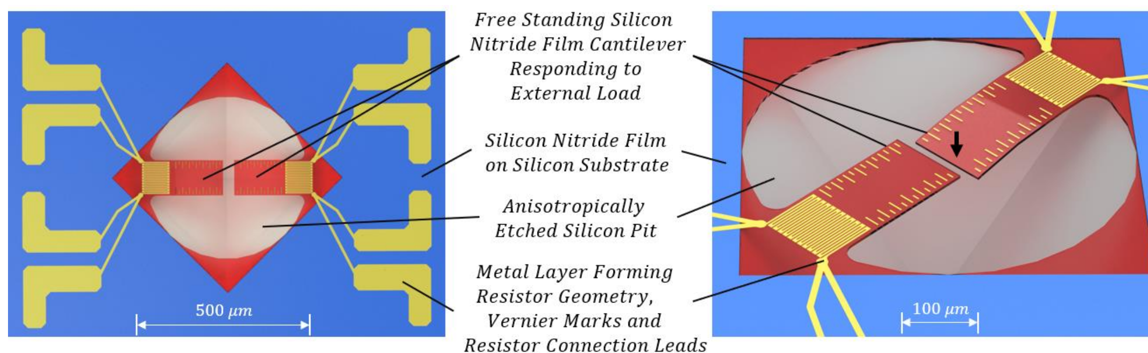

Figure 63. Top (left) and isometric (right) view of the MEMS device, highlighting the key components and composition (CAD visualisation).

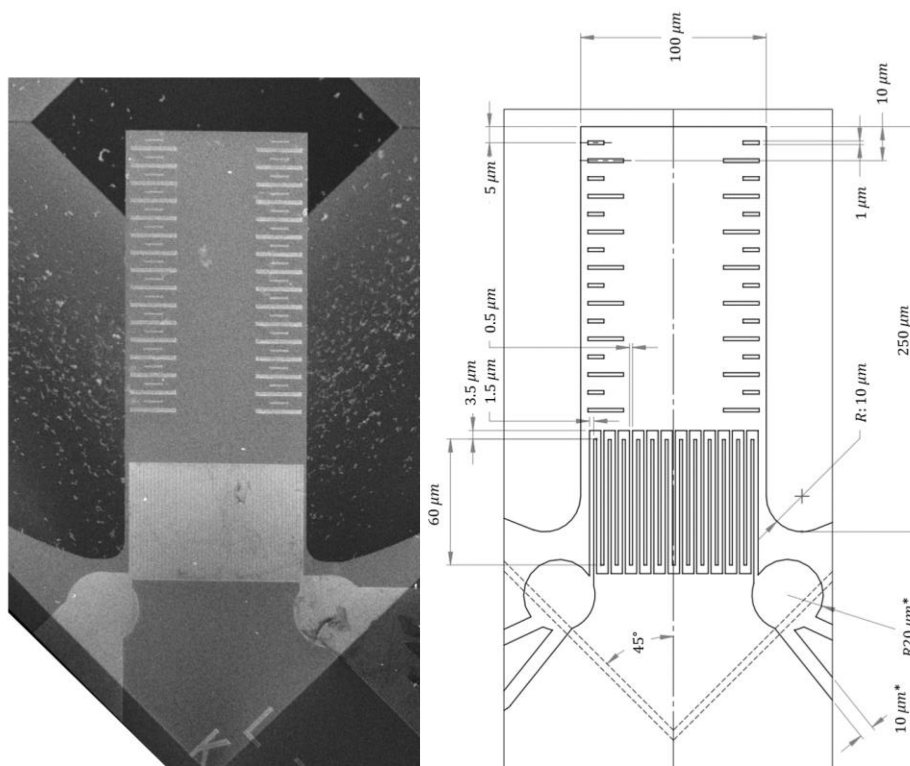

Figure 64. SEM picture (left) and CAD drawing (right) of the prototype MEMS device, highlighting cantilever structure and strained resistor dimensions.
N.B.: '' indicates features that are pictured not to scale.*

Numerous geometrical and process optimisation decisions shaped the device into its final form. The final version requires just three lithographic steps, making it a straightforward product to batch fabricate at wafer scale (Figure 65). The fabrication step count is lower than that of a commercial functionalised AFM probe, but the device units (dices) occupy a relatively large area so that only 88 MEMS devices versus 200-300 units of conventional AFM probes may be fitted on a single 3″ wafer. This suggests that such a device may have similar production costs to instrumented AFM probes such as the SThM probe (to be introduced in Chapter 6 [191]), currently retailing in the 200-300 EUR per unit range in mounted and bonded form. The finalised process could be developed for further cost reduction if cheaper lithography options were employed - e.g., photolithography may replace the electron beam patterning in marker, contact pad and cantilever definition steps (1 and 3). The higher resolution and better alignment of electron beam nanolithography is necessary however for the fabrication of high resistance meander metallic resistors with high yield.

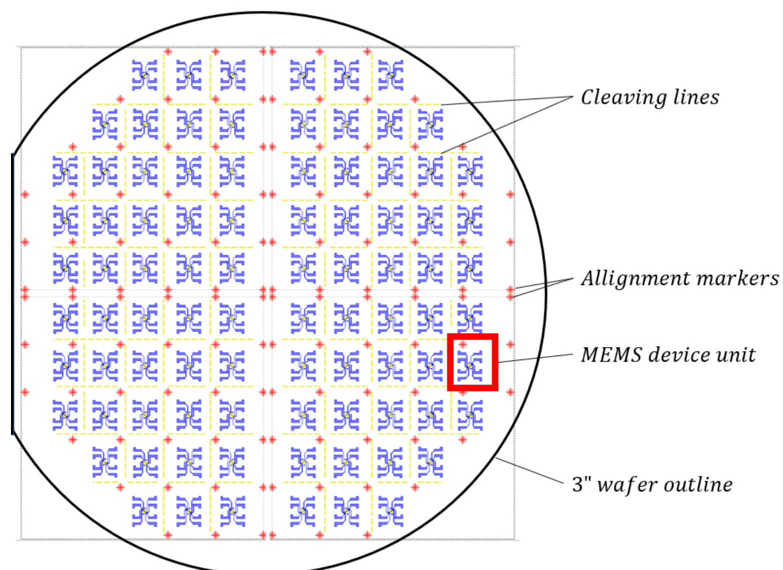

Figure 65. The complete fabrication mask design for the wafer scale production of the MEMS device, packaging 88 unit dices on a 3-inch (diameter) fabrication wafer.

The fabricated devices may now be characterised and instrumented for their primary purpose - in-situ AFM load and interaction elasticity measurement, as described in the next chapter.

Chapter 5 - MEMS device characterisation

The MEMS calibration device presented in the previous chapter consists of materials that are challenging to ascribe properties using literature values due to their composition dependence on local microfabrication processing. Therefore, the practice of acquiring property defining constants from the literature is not sufficient in most cases. [192]. For that reason, their experimental characterisation was undertaken, in order to understand the mechanical and electrical behaviour of the system. Where possible, direct characterisation was carried out – e.g., carrier structure elasticity modulus, sensor electrical properties and measurement noise, signal sensitivity to temperature, and MEMS tool response to environmental thermal effects. Where direct characterisation was not possible due to equipment limitations, routes for indirect property assessment were explored and applied – e.g., the MEMS tool elasticity and contact point offset relationship established via dynamic methods and MEMS tool calibration conducted with an externally characterised elastic structure.

5.1 Mechanical characterisation

Ensuring the MEMS tool responded to mechanical loads as a linear spring was crucial to the device's function. This premise was investigated by ensuring the structure complied with the load and deflection behaviour correlated by analytical descriptions. As demonstrated earlier in section 2.5 - nano indentation is a highly accurate characterisation method, however the system employed had sensitivity and application specific limitations that restricted its use for fabricated structure assessment. These practical limitations prompted exploitation of an alternative method for elastic behaviour assessment - resonant frequency correlation to stiffness, as introduced in mechanical theory section 3.1. This allowed a quality assurance test of the fabricated devices to be conducted, whilst the contact point specific elasticity was characterised directly using AFM.

5.1.1 Silicon nitride elastic modulus assessment

Initially, monolithic silicon nitride cantilevers were characterised using nano indentation displacement, analogous to the setup introduced in 2.5, allowing their analytically derived elastic modulus to be obtained (Figure 66 and Figure 67). To achieve this, the Euler–Bernoulli rectangular beam expression Eq. 22 (introduced in 3.1.1 and repeated below, was rearranged to solve for rectangular cross-section (Eq. 20, repeated below) cantilever elastic modulus - as shown in Eq. 37.

$$k = \frac{3EI}{L^3}; \qquad \textit{Eq. 22}$$

$$I = \int_{-\frac{t}{2}}^{\frac{t}{2}} wz^2 dz = w\left[\frac{z^3}{3}\right]_{-\frac{t}{2}}^{\frac{t}{2}} = \frac{wt^3}{12}; \qquad \textit{Eq. 20}$$

$$E = \frac{4kL^3}{wt^3}; \qquad \textit{Eq. 37}$$

Whilst carrying out the indentation, only four successful force-displacement measurements could be obtained near the cantilever fixed end where the structure is least compliant. Failure of some measurements was attributed to restrictions in the instrument setup (bottom end sensitivity) and material specific limitations related to low cantilever stiffness and charging effects (Figure 68). A significant aspect of the measurements made near the cantilever fixed end was due the fact that errors associated with contact position determination had the greatest effect on the measurement. Combined with the low number of indentations this resulted in a poor quality quantification. This situation could not be improved by additional data points as any measurements obtained with a contact point further than 60 μm offset from the cantilever fixed end, resulted in extremely low

confidence linear fits (e.g. Figure 69). With this in mind, the data presented below highlights the shortcomings associated with the available experimental setup when applied to characterising highly compliant, silicon nitride structures in SEM.

Initially, it proved impossible to obtain measurements on the silicon nitride structures, with strange deflection behaviour appearing to be dependent on SEM acceleration voltage which caused upward bend of the cantilever (Figure 68 and Table 9). Two repeats at different acceleration voltages were attempted before the cantilever failed through attraction and stiction to the indenter diamond tip. These measurements produced widely differing values, further diminishing confidence in the experimental setup due to the apparent severe electrostatic interaction. This highlighted sensitivity to SEM acceleration voltage, even though the linearity of the fitted gradient for individual experimental data sets was high - showing R^2 >0.97, per Figure 67. Ultimately, the artefacts were attributed to a phenomenon commonly referred to as ‘charging’. This is seen in insulators (such as hereby shown silicon nitride thinfilm) exposed to high static potential fields and can be mitigated by coating them in a conductive metal film as is commonplace in SEM imaging. However, addition of such a film would negate the efforts of obtaining the base silicon nitride stiffness as the measured cantilever would have become a complex (bi-material) structure.

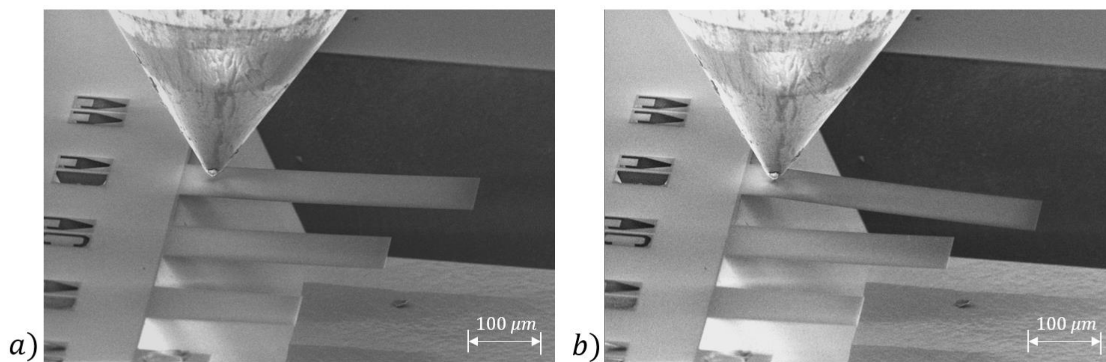

Figure 66. Silicon nitride cantilever t=0.389 µm, w=100 µm indented by the Hysitron PI85. The indentations can only be performed near the fixed end (L< 60 µm), where the structure is most resilient to static charging effects.

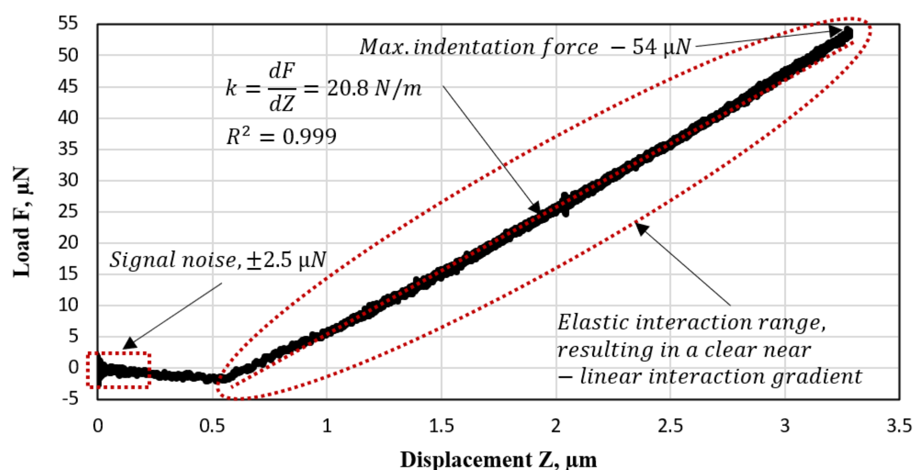

Figure 67. Silicon nitride cantilever indentation near the fixed end position 1, 23.94 µm, highlighting the clear engagement region, the near-linear force and displacement relationship and high measurement signal to baseline noise ratio. N.B.: The initial downward slope before engagement is likely caused by the repulsive interaction between indenter tip and nitride cantilever.

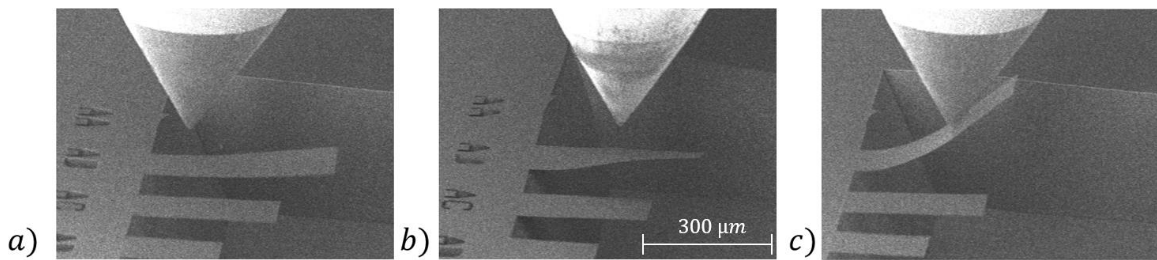

Figure 68. SEM captures of the scanning beam static charging affecting the cantilever mechanical behaviour - by a) bending, b) twisting and c) sticking to the indenter probe, thus preventing its free-state property characterisation. An example of the captured interaction is provided in Figure 69.

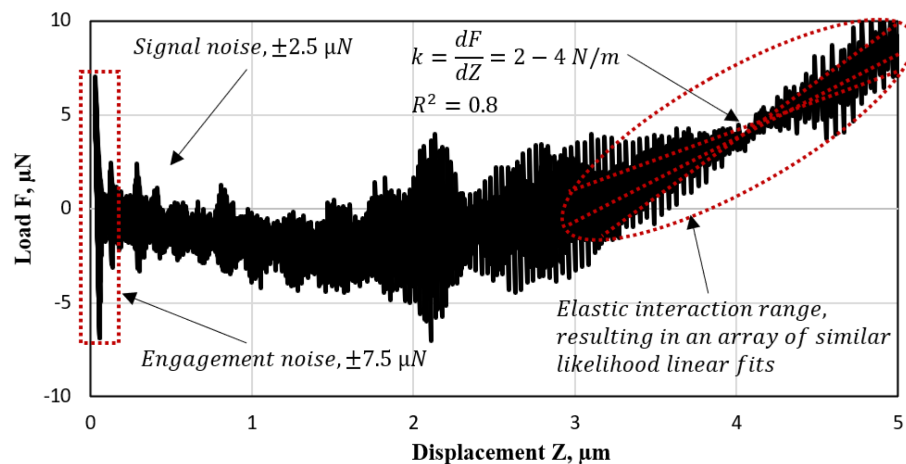

Figure 69. Load-displacement curve of an interaction at a 60 μm, offset, where the low stiffness results in high engagement noise and low measurement to noise ratio due to the small magnitude forces measured during the interaction.

As a consequence, the limited number of samples and an unquantified static interaction prevented any meaningful definition of uncertainty since neither a distribution shape, nor the individual measurement budgets could be confidently determined due to the unquantified systematic errors present. Therefore, only the mean and statistical standard error were calculated for the determined elastic modulus. An argument may be made that, if enough instrument time had been available, optimal SEM imaging conditions could have been identified, reducing the charging effect and thus allowing a more behaviourally representative measurement to be made. However, since the magnitude of charging is also

influenced by several other variables (e.g., exposure area and time, underlying substrate, proximity of the indenter cone) an averaged figure, obtained from a larger number of samples was preferred.

Table 9. Indentation obtained position specific interactions allowing for analytical solution for elastic modulus (E). Note the relationship to SEM beam voltage.

Indentation position	Distance from fixed end,L $\times 10^{-6}$ m	SEM accel-eration voltage, (kV)	Indenter measured elasticity, k, N m^{-1}	Linear fit, R^2	Indenter obtained position specific elastic modulus Eq. 37, (GPa)
1	23.94	5	20.83	0.999	194
2	22.47	20	36.25	0.999	279
3	36.76	5	4.789	0.966	162
4	37.81	20	7.299	0.976	268

Table 10. SEM beam acceleration voltage dependant experimental elastic modulus (E) figures for the Silicon Nitride film used as the structural layer for the MEMS device.

	5 kV	20 kV	Combined
E, Mean, (GPa)	178	273.5	225.8
Number of observations, n	2	2	4
e(E), standard deviation, (GPa)	3.89	11.3	24.6

With this in mind, the all-observation averaged silicon nitride cantilever elastic modulus and standard deviation was found to be 225.8±24.6 GPa, expressed as the mean and standard deviation (Table 9). However, this should not be referred to as the silicon nitride Young's modulus due to the potentially complex interactions between the structure and measurement system witnessed here. A comparison to literature reported values may be drawn – with the figure laying within the 217 [193] - 370 GPa [194] range reported elsewhere. These sources attribute the wide variation in this value to dependence on film thickness and atomic structure, as well as fabrication specific internal and surface stresses

[195]. Having considered the above, the measurement of an absolute elastic modulus value, despite its shortcomings, still has merit as it aids the structural behaviour prediction when analytical and FE modelling is conducted in the forthcoming work.

5.1.2 Direct MEMS elastic modulus assessment failure

A nano-indentation characterisation experiment was then setup to determine the elastic modulus of the fabricated MEMS device (Figure 70) per experimental setup described in section above. Unfortunately, limitations in the equipment prevented direct characterisation when using the multi-point nano-indentation method - as illustrated through the data described next.

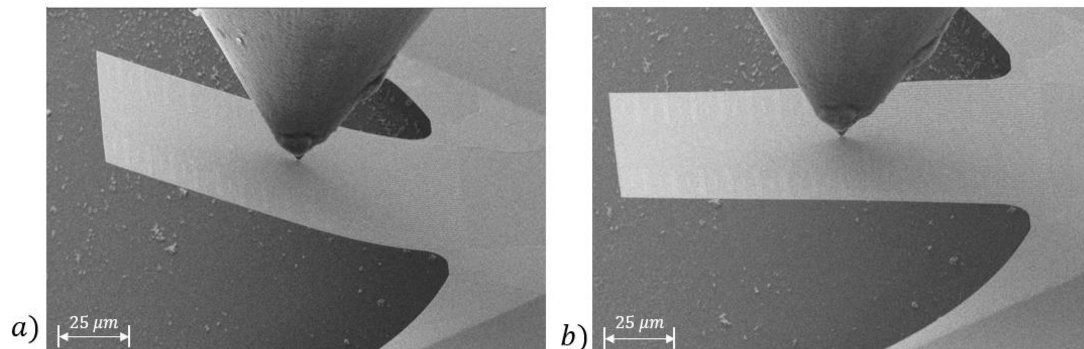

Figure 70. MEMS device characterised by the Hysitron PI85 [119] Nano Indenter – a) pre-indentation live capture, b) end indentation, live capture (SEM at 5 kV).

Five interactions were registered for their force and displacement relations obtained at the most compliant area still producing a reading on the indenter loadcell - immediately after the strain gauge, towards the cantilever free end. Following this approach, the measured interaction plots produced spring constant figures (k) that did not agree with the previously presented analytical Eulerian beam relationships, where $k \sim L^{-3}$ as introduced in section

3.1.1. The elastic moduli (E) values analytically obtained exceed the previously quoted literature figures by 2 to 6 times (up to 1282 GPa) making them comparable to carbon nanotubes [196], but not silicon nitride based structures. These values obtained through the SEM-based measurements may still have been affected by charging effects, however the significantly less noisy interaction gradient (Figure 71) suggests the effect was less pronounced. This reduced charging can be attributed to the proximity of the metal film resistor, which partially helped dissipate the built-up charge.

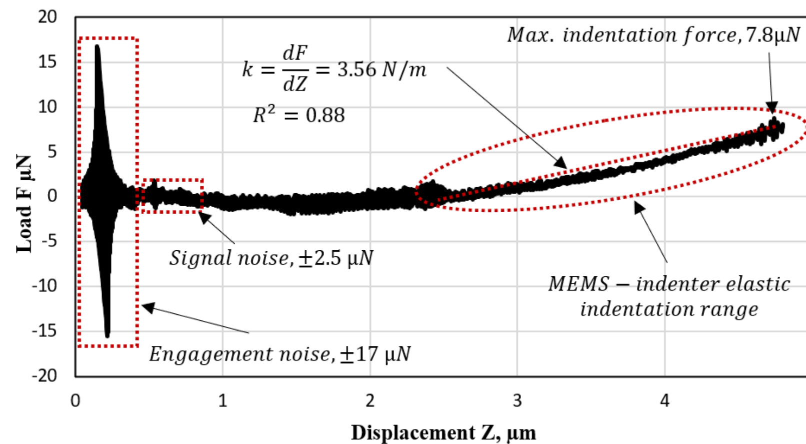

Figure 71. MEMS indentation data at position 1, showcasing the poor linearity of the force measurement during the engagement – downsides associated with low mechanical resistance in the structure causing the maximal force registered to be at 7.8 μN at the maximal displacement range, value - which is below the engagement noise. The lack of post-engagement linearity in this region concludes that a reliable spring consant approximation (from the rate of change dy/dx fit) may not be obtained.

Therefore, the major cause of error was attributed to the low instrument accuracy of the indenter due to it operating near the bottom of its force sensing limit. An attempt to interpret the spring constant through the linear derivative of the measured force and displacement plot (Figure 71, Table 10) resulted in a poor linear fit, with the coefficient of determination (R^2) ranging between the 0.65-0.88, rather than the previously observed >0.96 (Table 9). From this figure it can be seen that the measured forces during contact are below those

registered during the pre-engagement area of the indentation (±17 µN) while the indenter instrument is subject to no external force. The exact source of this non-contact signal is open to interpretation (although external factors were suspected due to construction works on campus during experiments), however it may indicate that the reliability of these measurements are highly dependent upon laboratory specific experimental setup and sample choice. It should also be noted that this signal severalfold exceeds the manufacturers claimed noise floor for the Hysitron PI85 [119] of 0.4 µN, indicating that the noise is may not be an artefact of the instrument itself. These findings can further be extended to allude that the contact mode AFM cantilevers (in the sub 1 N m^{-1} range) are at the limit of the capacitive force transducer-based nano-indenter's characterisation ability and are thus generally unsuitable but may be in reach for the experimental MEMS based solutions introduced in section 2.5.

Table 11. The 5 indentations at different offsets returning similar spring constant (k) values instead of following the third order analytical relationship – a product of poor measurement.

Indentation position	Distance from fixed end, L (µm)	Indenter measured spring const., k linear fit, $(\mathrm{N\ m^{-1}})$	Linear fit, R^2 value	Indenter obtained position specific elastic modulus Eq. 37, (GPa)
1	58	3.56	0.878	471
2	62.75	3.65	0.879	612
3	63	4.98	0.653	846
4	73.5	3.31	0.774	892
5	84	3.18	0.724	1282

5.1.3 Indirect MEMS spring constant assessment

Failure of the direct MEMS device calibration via nano-indentation necessitated an alternative method to be employed. Therefore, dynamic behaviour was explored in order to confirm the third order length/offset to spring constant relationship of the MEMS structure – a key cantilever-like quality allowing point load force to be related to elastic response. It is important not to take uniform elastic behaviour of the microfabricated structure for granted, since the previously discussed structural inconsistencies and feature definition can be challenging to assess using dimensional techniques. Some structural flaws are simply not detectable by conventional inspection methods - e.g., micro cracks below the imaging resolution or conventionally 'invisible' internal material stresses generated during deposition. Therefore, it is common to conduct post-fabrication quality assurance by measurement of the structure's resonance behaviour. As established by the number of references introduced in the literature review and calibration case study sections - simple mechanical structures exhibit a reliable relationship between end-point spring constant and fundamental resonance [112], therefore a study was conducted to determine the analytically determined cantilever spring constant (k) to fundamental resonance frequency relationship (f_0).

An indirect stiffness (k) to resonance frequency relationship was confirmed by exploring the measured resonant frequency and theoretically estimated equivalence, agreement of which was to confirm the $k{\sim}f_0$ (Eq. 26) power correlation. An experimental assessment based on this assumption was conducted on four different MEMS devices (Figure 72, a), representing the varied absolute end point stiffness, alongside the uniform composition

structures employed in the previous fabrication trials (Figure 72, b) – summarised in Table 12. The stiffness of the simplistic rectangular structure was estimated using analytical methods, described in 3.1.1, while the complex boundary structures were characterised by FEA methods, analogous to methodology described in section 3.1.2. The elastic modulus determination enabling the theoretical estimates used was described in section 5.1.1. The resonance profile was characterised non-destructively using a Laser Doppler Vibrometer system (MSA-100-3D, Polytec GmbH, Germany - Figure 73). This measurement system registers the Brownian motion excited cantilever velocity providing a resonance profile from which the fundamental (natural) resonance frequency f_0 can be extracted.

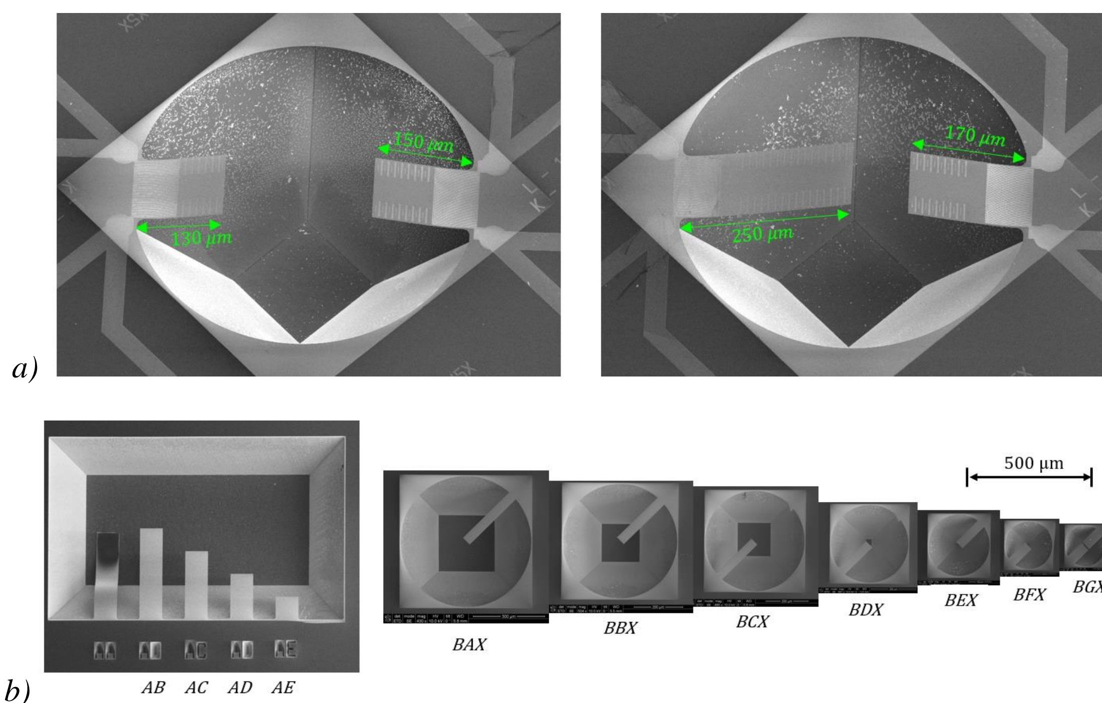

Figure 72. Dynamically assessed free standing structures spanning a range of geometrical variations, summarised in Table 12 - a) full scale MEMS devices of varied lengths and resultant end point stiffness and b) stitched and scaled SEM images of the fabricated test structures.

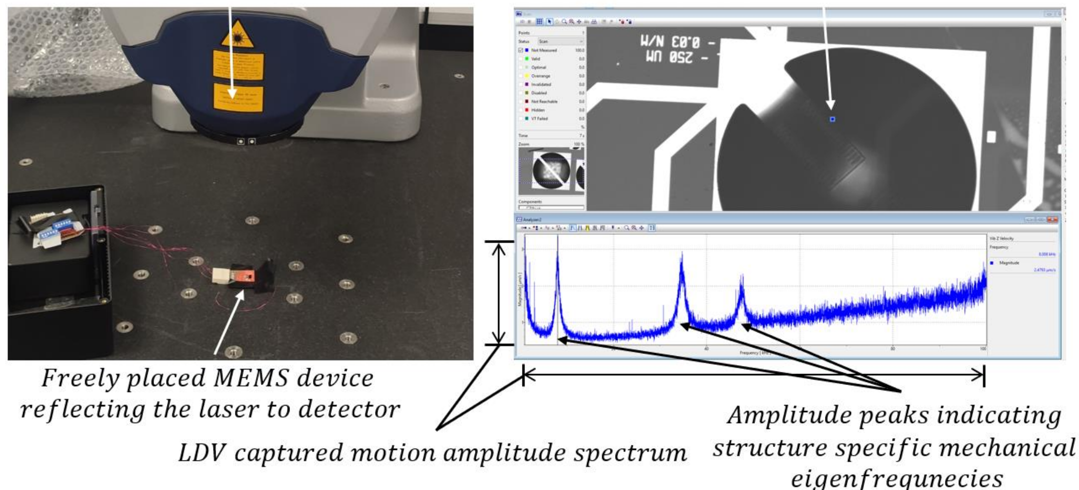

Figure 73. The Laser Doppler Vibrometer system - Polytec MSA-100-3D, for analysing the MEMS cantilever frequency and motion spectrum.

Table 12. Tested cantilever structures, summarising the dimensions, estimated spring constant and measured natural resonance values.

No	Name	Boundary type, cross-section composition	Beam length, L, μm	Beam width, w, μm	Spring constant approximation, $\mathrm{N\ m^{-1}}$	Natural resonance frequency, LDV f_0, Hz
1	AB	Square, uniform	400	100	0.0057 (Eq. 22)	2008
2	AC	Square, uniform	300	100	0.014 (Eq. 22)	3641
3	AD	Square, uniform	200	100	0.046 (Eq. 22)	8086
4	AE	Square, uniform	100	100	0.37 (Eq. 22)	32977
5	BAX	Circular, uniform	271	40	0.0074 (FEA)	7382
6	BBX	Circular, uniform	231	40	0.012 (FEA)	9164
7	BCX	Circular, uniform	208	40	0.016 (FEA)	10648
8	BDX	Circular, uniform	166	40	0.032 (FEA)	16414
9	BEX	Circular, uniform	132	40	0.064 (FEA)	23500
10	BFX	Circular, uniform	96	40	0.17 (FEA)	27055
11	BGX	Circular, uniform	74	40	0.36 (FEA)	45063
12	MEMS1	Circular, complex	250	100	0.023 (FEA)	8008
13	MEMS2	Circular, complex	170	100	0.075 (FEA)	17133
14	MEMS3	Circular, complex	150	100	0.11 (FEA)	21148
15	MEMS4	Circular, complex	130	100	0.17 (FEA)	27719

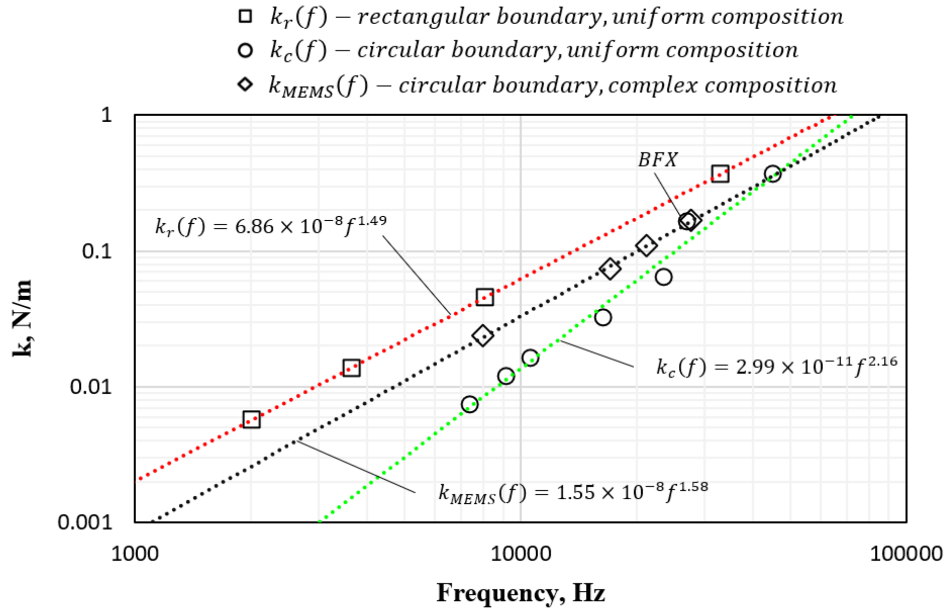

Figure 74. Measured natural resonance frequency to estimated end-point stiffness (k) relationship following the power law fit, distinguished by planar geometry and boundary fixation type. NB. The BFX circular boundary fit has an outlier structure at 27 kHz, with stiffness twice as high as the one expected – possible cause of an otherwise undetected structural defect.

Using the experimentally obtained natural frequency plot an analytically derived relationship was created - showing the power relationship between the properties in the three distinct trendlines (Figure 74). Without further processing, such a figure does not reveal absolute stiffness information in N m^{-1} (only a correlation to theoretically estimated elasticity shown in this example), however, it is immensely useful in identifying structures that do not exhibit expected elastic behaviour. For example, an outlier circular boundary cantilever (BFX measured at 27 kHz instead of the expected ~35 kHz) is indicated as not following the cubic relationship trend, suggesting a structural defect is present in the structure - although neither cursory SEM or optical profiler inspection techniques revealed any obvious deviations. On the other hand, the four MEMS structures tested do demonstrate consistent compliance with the expected relationship, indicating that all MEMS structures maintain the Eulerian stiffness (k) and length (L) inverse cubed

relationship (as introduced in section 3.1.1). Understanding it for each structure type allowed for further development work focusing on related geometry cantilever modification and rapid assessment using the non-destructive method.

5.2 Electrical characterisation

To characterise the electrical behaviour of the MEMS strain sensor, a fabricated device (Figure 75) was cleaved into individual units that were bonded on to a copper PCB, connecting the four terminals to a macroscale plug (Figure 76) allowing for convenient integration with laboratory measurement instruments.

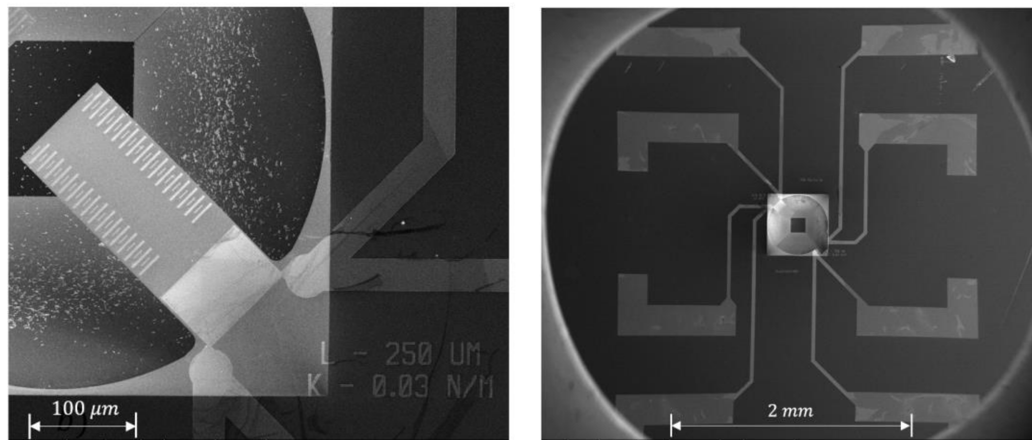

Figure 75. Left - capture of the 250 μm long MEMS device cantilever used in the electrical characterisation sequence; Right - the device envelope, mostly occupied by the millimetre sized four terminal connection leads required for handling.

The primary device function - strain induced resistance change should be detectable by employing conventional electrical instrumentation e.g. - high-quality ohmmeter. However, anticipating the small resistance changes and overall low signal amplitude, a purpose-built instrument was preferred for conditioning the sensor output. Therefore, in order to quantify the device resistance change (dR) from the instrumentation output voltage (dV) a conversion constant (dV/dR) was required. This could be determined theoretically from the specific component values employed in the instrumentation (described in Appendix A - MEMS Instrumentation Schematic), or, as used here, experimentally by introducing a known resistance change and measuring the corresponding change in output signal voltage.

This allowed MEMS device measurements to be reported as change in sensor resistance rather than voltage by employing the conversion constant shown Table 13, enabling the forthcoming sensor signal output to be presented as relative strain resistance change - dR/R_{abs}.

Table 13. Instrumentation conversion constant.

Symbol	*Value*	*Unit*
dV/dR	0.00095586	V/Ω

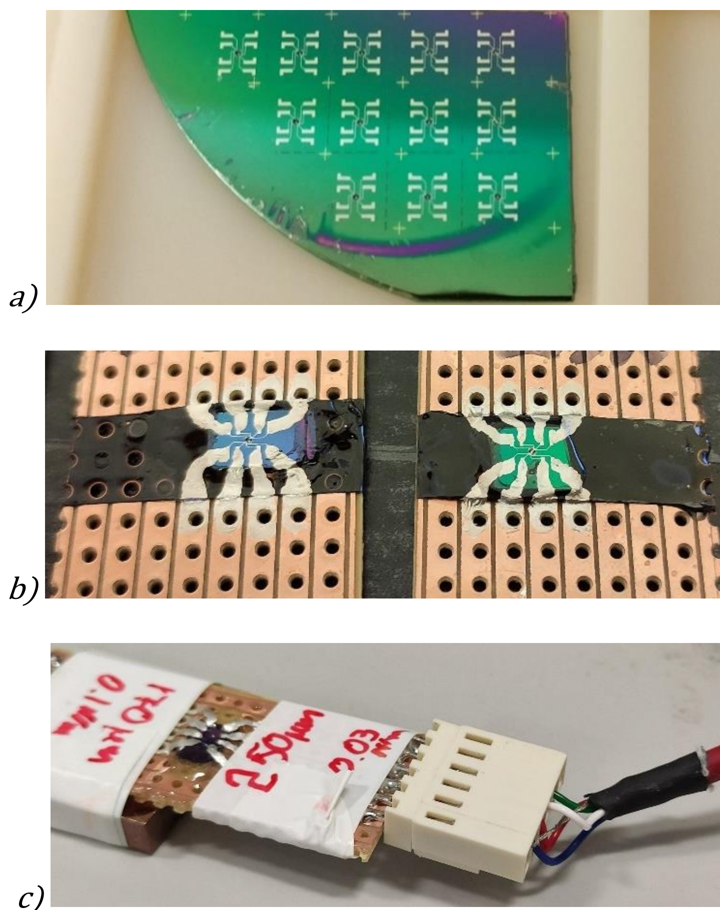

Figure 76. a) batch fabricated MEMS devices on a substrate quarter wafer, b) individually cleaved, bonded and connected to copper film PCB tracks with conductive paint, to allow for c) soldering a handling-friendly MOLEX type connector for connection to instrumentation.

5.2.1 Strain sensor resistive properties

The strained resistor formed the sensing component of the MEMS structure, characterised by its electrical response to applied strain. The material specific resistivity of the nichrome film used was estimated by measuring the conductor absolute resistance and relating it to the area and length ratio (Eq. 29). In this measurement, the strain gauge resistance measurement was conducted using a four-terminal ohmmeter (GW Instek GDM-8251A, Taiwan) and the conductor geometry was assessed using an SEM (FEI Nova Nanosem 630, USA) to measure planar length and width values, while the conductor thickness was measured using a surface profiler (Bruker Dektak XT, USA) due to its large scanning area capability, capturing a full strain sensor cross-section. Several (36) strain resistor geometries were fabricated, however the further showcased characterisation efforts focus on a single resistor, which was used throughout the device real-world application trials - the ‘150-050’ strain gauge is shown in Figure 75, table 14 (as described back in section 4.3.1).

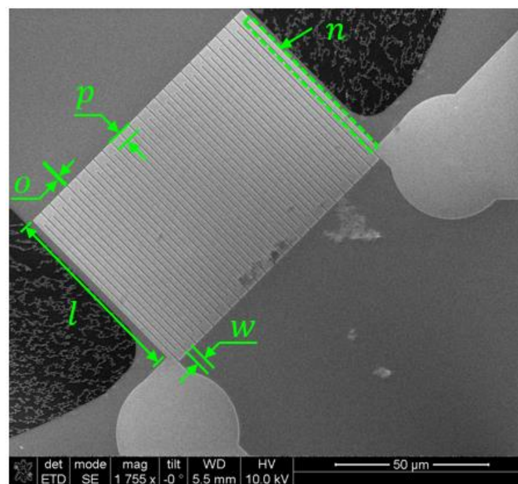

Figure 77. The ‘150-050’ strain resistor with geometrical property describing symbols.

The obtained measurements (Table 14) allow the determination of the fabricated device nichrome resistivity ($\rho_{MEMS}=2.62\times10^{-6}\ \Omega$ m), and it should be observed that this does not agree with typical nichrome bulk resistivity values reported in literature by a notable margin (e.g. $\rho_{nichrome}=1.5\times10^{-6}\ \Omega$ m [197]). However, when the device resistance was measured prior to the final MEMS wet etch step in potassium hydroxide solution, nichrome resistivity was found to be much closer to the bulk value figure ($\rho_{Strain\ gauge}=1.3\times10^{-6}\ \Omega$ m, Table 14). This change is not surprising given the extremely aggressive environment produced by high KOH concentration and temperature solutions. The reaction between nichrome alloys and potassium hydroxide is highly complex and dependent upon the exact alloy composition [198]. Additionally, conductor thickness in the sub-micron range has a significant impact on specific resistivity, as described by Kazi[6] [199]. Whilst both of these findings are interesting and further illustrate the challenges in thin film device design and fabrication, the exact investigation of the precise processes occurring in these instances would require considerable work beyond the scope of this thesis. The afore mentioned effects have no direct relevance to the device function, since the strain gauge operates as a relative resistance change device, meaning the change in resistivity, rather than its absolute value defines the relationship between the perceived change in strain.

[6] NB: the publication investigates a Ni/Cr composition of 80/20, rather than 60/40 used in this work.

Table 14. The '150-050' configuration strain sensor geometry and measured resistivity.

Property	Symbol	Value	Source
Length (single pass), µm	l	59	Nominal
Width, µm	w	1.5	Nominal
Offset spacing, µm	o	0.5	Nominal
Overpass height (2×w+o), µm	p	3.5	Nominal
Number of repeat passes, 'n'	n	48	Nominal
Thickness, nm	t	32.7	Measured: AFM
Strained cross-section, µm^2	A	0.0491	Calculation: ($w \times t$)
Total strained wire length, µm	L	2832	Calculation: ($l \times n$)
Strain gauge resistance (before wet etch), Ω	$R_{\text{Strain gauge}}$	75224	Measured: four-terminal ohmmeter
Material resistivity (before wet etch), ×10^{-6} Ω m	$\rho_{\text{Strain gauge}}$	1.30	Calculation: ($R_{\text{Strain gauge}} \times A/L$)
Strain gauge resistance (post wet etch), Ω	R_{MEMS}	151000	Measured: four-terminal ohmmeter
Material resistivity (post wet etch), ×10^{-6} Ω m	ρ_{MEMS}	2.62	Calculation: ($R_{\text{MEMS}} \times A/L$)

5.2.2 MEMS device electrical noise spectrum analysis

Analysis of the signal spectrum was also carried out on the completed device. The purpose of this was primarily to establish the device signal to noise performance. However, it additionally allowed sources of environmental interference to be visualised. The 1-100 Hz frequency range was first scrutinised as this easily covered the relevant frequencies of the experiment as dictated by the experiment ramp speed (max. 14 Hz for the Digital Instruments Dimension D3100 system used throughout the investigation). This relatively high speed of Z motion was employed in order to minimise any signal drift due to thermal and mechanical instabilities present in laboratory environment.

The spectral analysis was conducted on the instrumentation output for four scenarios (Figure 78). First, the AFM cantilever was positioned on the MEMS beam and continuous force-distance ramps were conducted, representative of device operation. Second, an identical indentation routine was performed on the substrate, but at a site 1 millimetre away from the MEMS beam, in order to identify any noise generated by the AFM system control and drive sources. Thirdly, the output of the idle AFM was captured whilst the probe was positioned at the top of the ramp engagement position, which corresponds to the background noise of the instrumentation. Finally, the instrumentation was disconnected from the spectrum analyser and analysis of the laboratory background was conducted through the open end co-axial cable, now acting as an antenna. This provided the PSD profile of the laboratory and contrasted that to the measured instrumentation output signal magnitudes.

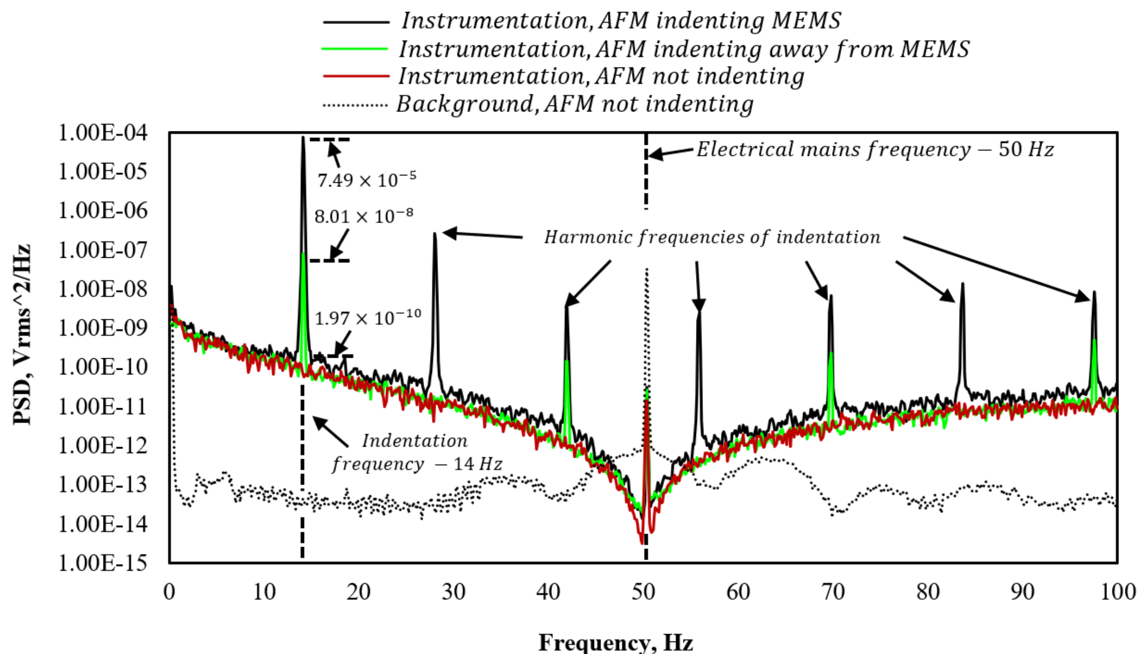

Figure 78. Power spectrum analysis of the MEMS device signal and environment in the 1-100 Hz range (Agilent 35670A, bandwidth - 0.125 Hz).

The spectral analysis revealed that the primary MEMS signal had a signal to noise ratio[7] of 218:1 or 47 dB. The harmonics of the indentation, induced by the compliant beam and AFM drive and control system, were also visible and of significant magnitude (comparable to mains interference), however they were easily distinguished from the main measurement signal at 14 Hz which is 1000 times (or 30 dB) larger. The inclusion of a passive twin-T notch filter [200] and electronic screening also resulted in a quantifiable reduction in the mains interference at 50 Hz of some 40 dB.

An investigation of the broader frequency spectrum (1.2-51.2 kHz) was also conducted. This was carried out with the MEMS device idle (powered on, but not in contact with external bodies) and thus subject to thermal vibrations, as described in the thermal tune

[7] Signal to noise ratio in unit bandwidth is determined by the square root ratio of frequency of interest peak (7.49×10^{-5}) to base (1.97×10^{-10}) multiplied by the square root of measurement bandwidth (1/8 Hz): $\left(\frac{\sqrt{7.49\times10^{-5}/1.97\times10^{-10}}}{\sqrt{8}}\right)$ = 218 - for a linear ratio expression, or $20\log_{10}\left(\frac{\sqrt{7.49\times10^{-5}/1.97\times10^{-10}}}{\sqrt{8}}\right)$ = 47 dB for a logarithmic scale expression.

calibration routine in chapter 2. The Brownian motion excitation of an AFM cantilever, which this structure is very similar to, manifests as vibrational amplitudes in the nanometre range [109]. The lack of unique signal peaks that match the mechanical vibration frequency range (Figure 79) demonstrated that the strain gauge was not sensitive enough to pick up strains of that magnitude in the kHz range. This eliminated the opportunity to investigate a 'self-calibrating' beam concept, that could measure variations in its frequency and refer that to an anticipated change in elasticity (as discussed in 3.1.1).

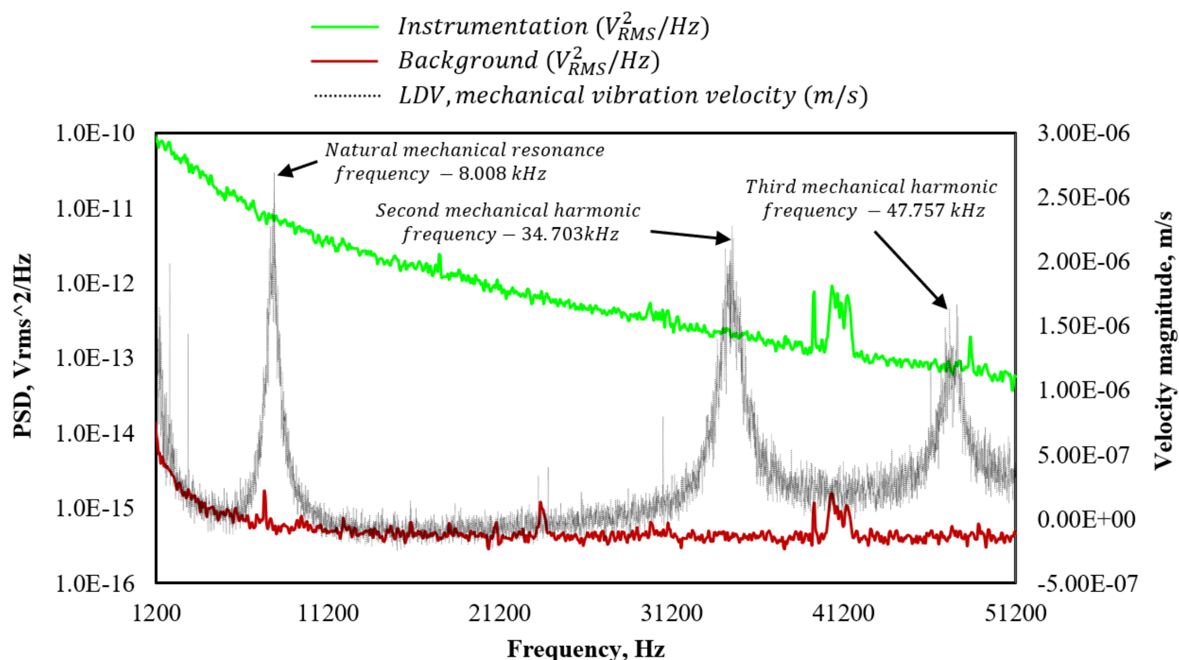

Figure 79. Frequency and signal amplitude comparison of the background and MEMS signal spectrum analysis (Agilent 35670A, bandwidth - 62.5 Hz) contrasted with mechanical (Brownian) motion spectrum of the MEMS beam, captured by laser doppler vibrometer system (Polytec MSA-100-3D, bandwidth ~ 100 Hz).

5.3 Thermal behaviour characterisation

Since the MEMS tool was implemented as part of the quarter-bridge circuit, as highlighted in section 3.3, it was important to understand its relationship to temperature changes, particularly as the device may be used for transferable or comparative force measurements in non temperature-controlled environments.

5.3.1 Thermal Coefficient of Resistance (TCR) and Coefficient of Thermal Bending (CTE)

The metric employed to understand the signal relationship to temperature is called the thermal coefficient of resistance (TCR). This relates the conductor's sensitivity to temperature in relative change terms, per degree of temperature change (Eq. 38). TCR is both a material property - unique to the deposited nichrome conductive pattern, and a system property once the conductor is incorporated on a temperature-sensitive structure - released MEMS beam (Figure 80).

$$TCR = \frac{1}{R_{abs}} \times \frac{R(T) - R(T_0)}{T - T_0} = \frac{d[dR/R_{abs}]}{dT}; \qquad \text{Eq. 38}$$

To achieve this, the complete MEMS device TCR constant was determined experimentally. The MEMS device was submerged in a fluid medium (here: chemically inert liquid - Flutec PP3 [201] with high thermal and low electrical conductivity), which was uniformly heated in the insulated copper enclosure attached to a controlled Peltier heater element, as shown in Figure 81.

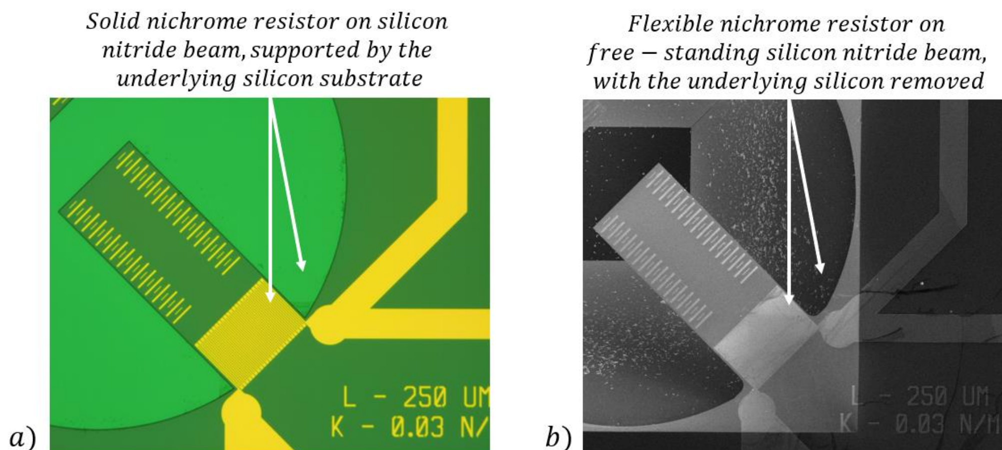

Figure 80. Two MEMS configurations used to determine mechanically de-coupled strain gauge TCR (a) and a released MEMS system TCR that contains a product of bi-material beam mechanical behaviour (b).

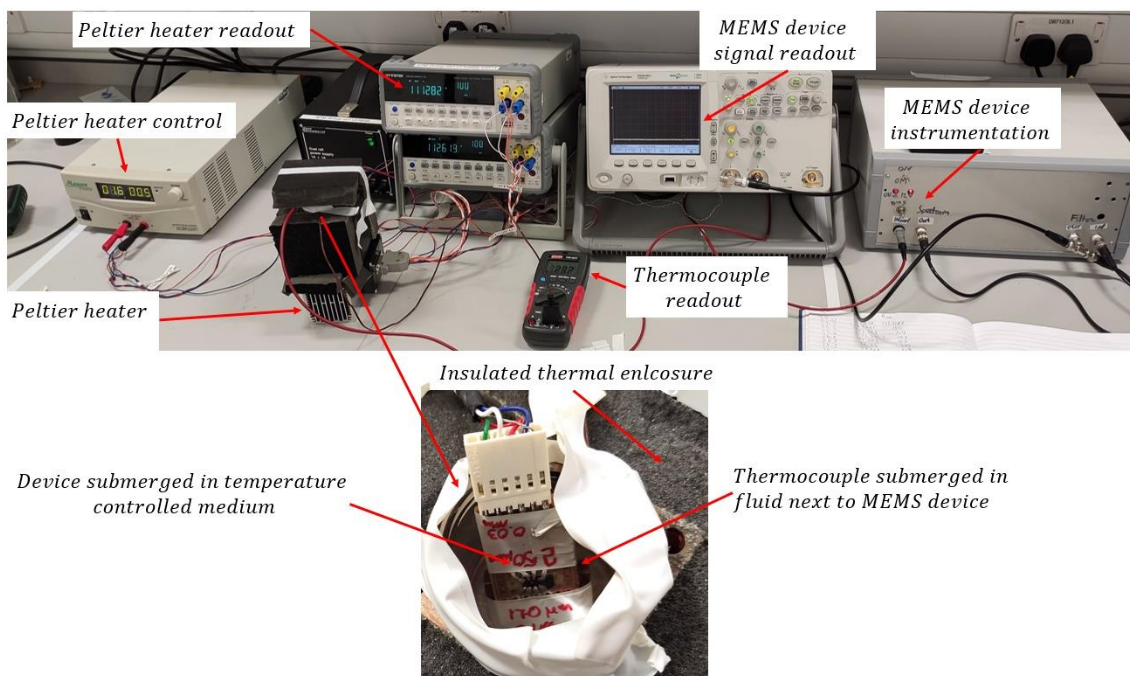

Figure 81. TCR experiment setup with a temperature-controlled enclosure.

The MEMS device signal was recorded against the settled fluid temperature over a range of temperatures, defining the coefficient of temperature and resistance relationship. This method allowed the TCR to be defined by translating the recorded temperature (T) specific device resistance (R(T)) to the absolute device resistance at ambient temperature (R_{abs}).

Plotting the recorded data points against absolute temperature or relative temperature change allowed a TCR to be defined from the slope of the linear fit - per Figure 82 and Table 15. In order to separate nichrome TCR from other thermal sensitivities within the system, including the bi-material bend of the cantilever, measurements were taken on a device pre-release (strain gauge) and post release (MEMS) over the 18 to 36 °C temperature range.

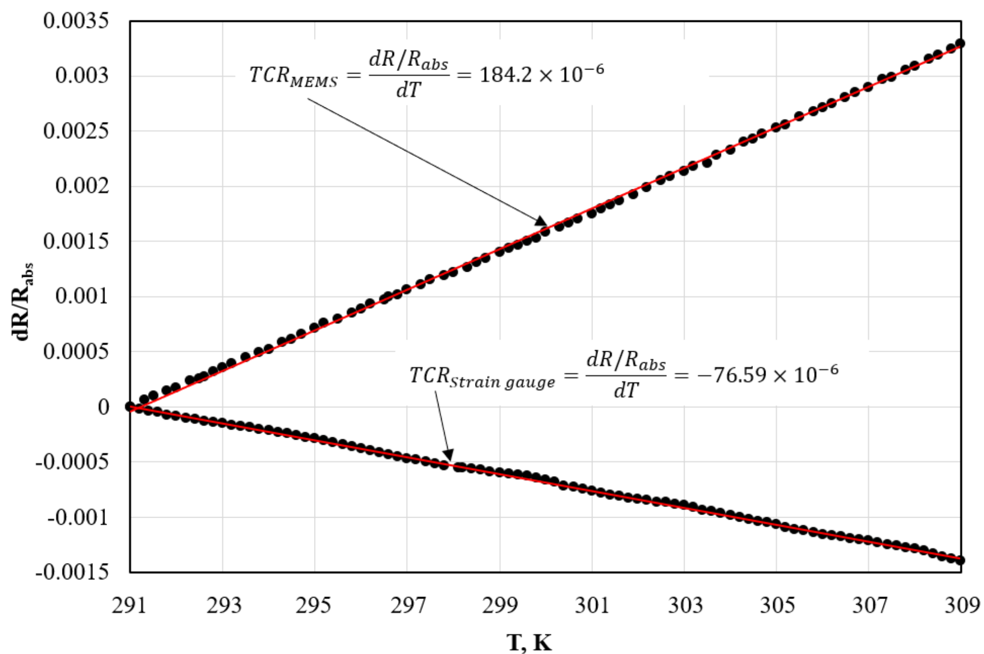

Figure 82. Experimentally obtained data points showcasing the TCR relationships for the strain gauge and MEMS device, highlighting the radical change in slope gradient once the mechanical response to thermal effects is included. Linear fit gradient shown in red.

Table 15. Statistical summary of the TCR experimental determination.

	Strain gauge	MEMS
TCR, Mean, K^{-1}	-7.659×10^{-5}	1.842×10^{-4}
e(TCR), standard error	2.261×10^{-7}	3.269×10^{-7}
Number of observations, n	80	77

This data emphasises the importance of considering the differences in device behaviour on a component and system level. Firstly, the obtained thermal coefficient for the nichrome strain gauge supported on a solid silicon substrate revealed a $TCR_{Strain\ gauge}$ = -76.59 ppm

K^{-1} (Figure 82). This figure indicates that the resistance drops as the temperature increases, which is characteristic to nichrome alloys [202]. The magnitude is also comparable to that of constantan alloys ($TCR_{Constantan}$ = ±50 ppm K^{-1}, [203]) that are purpose engineered for high thermal stability[8], confirming the excellent thermal performance of nichrome and justifying its use in this application. Studies conducted by Chuang et al. [202] on comparable thickness nichrome films suggest that the strain gauge TCR performance could be further improved by annealing, resulting in thermal coefficients as low as ±5 ppm K^{-1}, establishing nichrome as the metal of choice for high thermal stability resistive films, especially when compared to non-metal strain gauge options such as silicon[9].

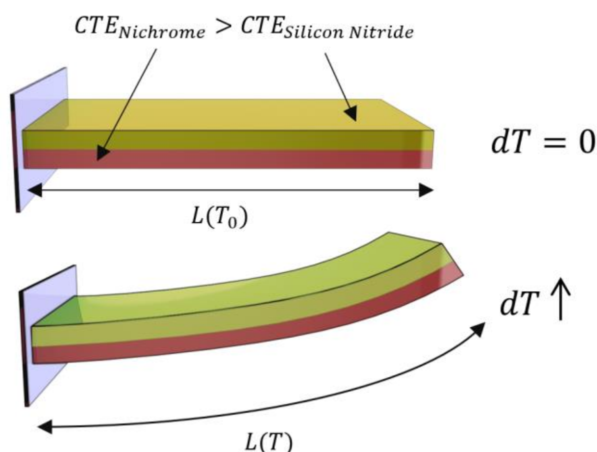

Figure 83. A single fixed end cantilever of bi-material composition - containing two different CTE values, will respond to temperature change in different rates of expansion that cause non-uniform stress the cross section that manifest in a curvature.

However, once the resistor was incorporated on top of a mechanically compliant beam, the device TCR performance needs to be considered at a whole-device level where the thermal behaviour changes fundamentally. The observed TCR_{MEMS} relationship for this configuration was 184.2 ppm K^{-1} (Figure 82) – meaning its direction had reversed and its

[8] Yet intrinsically incompatible with the chosen fabrication procedures, per chapter 4.
[9] N.B.: $TCR_{Silicon}$=1000's ppm K^{-1} [146].

magnitude doubled when compared to the mechanically rigid system, highlighting the downsides of nichrome as a strain gauge material choice in this arrangement. Here, the bi-material structure experienced different changes in length with temperature change, resulting in different thermal expansion coefficients or CTE's [204]. The thermal expansion coefficient of nichrome exceeds that of its silicon nitride carrier structure by 5-6 times ($CTE_{Nichrome} = 14\times10^{-6}\ K^{-1}$ [205] while $CTE_{Silicon\ nitride} = 2\text{-}3\times10^{-6}\ K^{-1}$ [206]), which resulted in the interface originating strains. The high elastic strength of the metal film ($E_{Nichrome}$=100-200 GPa, depending on composition and geometry, e.g. [207] and [208] respectively) exaggerated the effect further meaning that stress manifest as a large magnitude force on the surface (Figure 83), causing the strain sensor to stretch and respond in resistance change, which in operation, was indistinguishable from the strain induced by a mechanical load. Little could be done to mitigate this effect due to the microfabrication material choice limitations, where matching or achieving a lesser contrasting expansion coefficient ratio was not possible. Therefore, the solution lay in the understanding of how the MEMS device reacted to thermal sources in operation - the AFM environment, exploration of which is described next.

5.3.2 MEMS device thermal behaviour in AFM environment

The TCR experiment characterised a uniformly heated device response to temperature, whereas in practice a typical AFM substrate is subject to multitude of localised thermal sources. Having established that the MEMS device was sensitive to thermal effects, it was therefore necessary to investigate the possible magnitude of these effects during device operation in a real-life scenario. The characterised TCR figure allowed the MEMS resistance reading to be used as a temperature measurement, provided no mechanical loading was applied. This provided the ability to isolate thermal effects from sources present in the AFM system, which are not typically accessible using external measurement methods. These thermal sources were unique to the experimental setup and understanding them can aid experimental consistency and allow thermal mitigation practices to be employed as necessary.

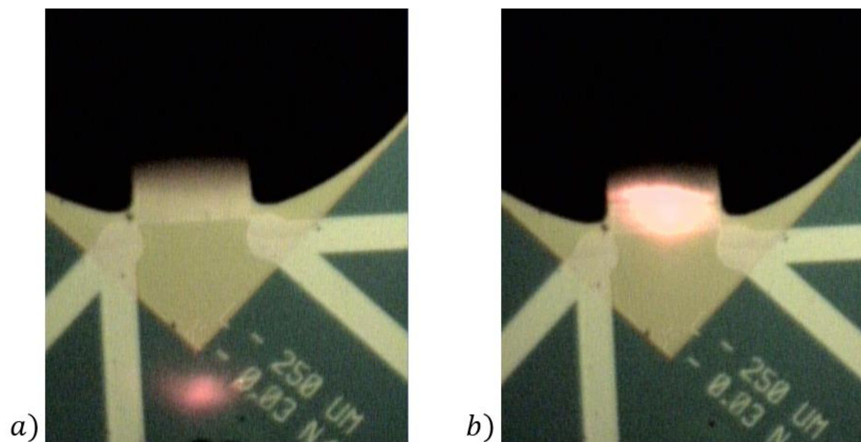

Figure 84. (a) AFM optical lever laser spot aimed away and (b) aimed at the MEMS device strain gauge, introducing localised heating to the low thermal mass cantilever. N.B.: MEMS device not visible completely in the capture due to the curvature falling outside the AFM camera depth of field range.

Localised heating due to the laser light required for AFM optical lever systems is a common issue in scanning probe microscopy, being particularly significant in methods such as scanning thermal microscopy (SThM), where pronounced effects on substrate and cantilever heating have been widely investigated [209]. Using the MEMS sensor as a thermometer, it was observed that when aiming the AFM (Digital Instruments Dimension D3100) laser directly at the strain sensor a large resistance increase occurred - dR=715 Ω averaged over ten positioning cycles as shown in Figure 84. This is equivalent to a temperature jump of dT=26.5 K (295 K to 321.5 K), suggesting significant localised heating is manifesting as mechanical bending – as previously witnessed in the uniformly heated TCR investigation. The thermal effect caused by camera illumination was also measured - dR=0.4 Ω averaged over ten toggle on/off cycles, equivalent to temperature change of dT=0.02 K. Whilst this was far less significant than the laser overspill in this AFM setup due to the non-locally focused illumination, it was still considered good practice to pay attention to surrounding light and heat sources as they may have posed a detectable effect on the final measurements.

To further investigate optical lever laser thermal effects that could be expected during normal device operation the 1 mW laser from the AFM optical lever system was aligned onto an AFM cantilever (Bruker Scanasyst Air HPI [210], Figure 85) which was then lowered into proximity with the MEMS substrate surface without making contact. The location of the probe above the MEMS structure was moved around 200 x-y datapoints in the 300 by 300 µm area around the device and the measurements linearly interpolated to create the 3-axis map shown in Figure 86.

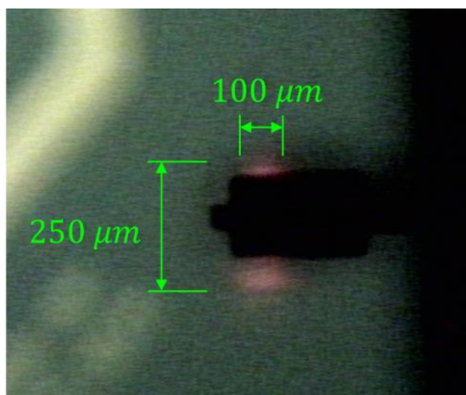

Figure 85. AFM camera capture of the laser aimed at the reflective cantilever surface and the visible laser overspill.

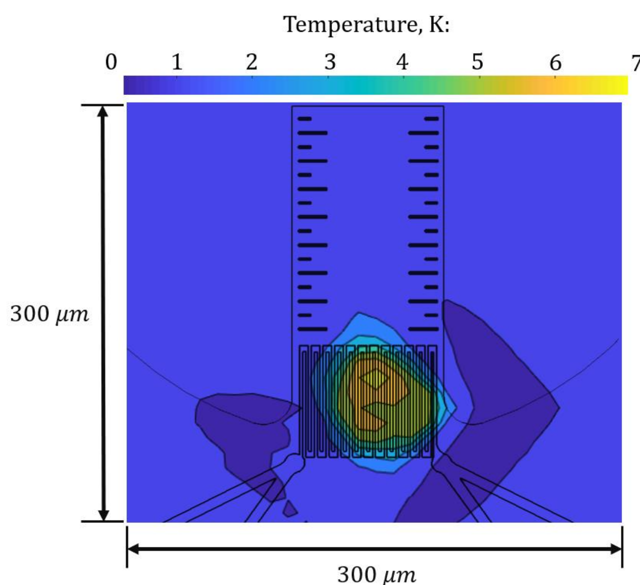

Figure 86. Thermal intensity heatmap overlaid with the MEMS device contour, highlighting the intensity and location from the optical lever cantilever laser overspill.

Unsurprisingly, this revealed that the nichrome strain gauge was the most sensitive zone to laser overspill heating, resulting in a temperature increase equivalent to dT=6.7 K from ambient (room) temperature. As expected, this was much lower than the heating observed previously where the AFM probe was removed, and the laser spot aligned directly onto the MEMS device. It was also clear that the magnitude of laser heating reduced rapidly as the cantilever was planarly distanced from the strain sensor proximity, stabilising around 1 K. This is not an insignificant effect, and the uncertainty it introduced affected each

measurement, possibly proving to be the limiting factor of device measurement sensitivity. For illustration, the 1 K temperature change induces thermal strain that registers a relative resistance change of 0.006% (8.4 Ω)[10], which, as demonstrated further in the force measurement experiments, is equivalent to the mechanical strain caused by a ~1 nN operational load (at 20 µm offset from free end) for this device - indicating the real-life measurement floor. Compensating for this localised heating was very challenging as the localised overspill is unique to each AFM probe type and optical lever alignment. What is more, compensation of the effect - e.g., with a half-bridge employing a resistor placed on the opposite surface of the beam, would make device fabrication impractical, therefore the ability to employ the MEMS device as a thermal environment assessment tool is particularly useful, especially if intra-laboratory measurements are considered.

---

[10] The resistance values vary in response to the instrumentation configuration - bias current, amplification magnitude and bridge imbalance, therefore the early characterisation stage measurement magnitudes are not comparable directly in bridge resistance terms. The instrumentation configuration is set in the calibration stage described next, allowing for the further measurements to be contrasted directly.

5.4 In-situ AFM elasticity characterisation

The demonstration of the device operating in an AFM environment was investigated next. This was done through MEMS elasticity measurement against a known elasticity AFM cantilever - completing the mechanical characterisation of the intended load site in-situ. Then, interpretation of the instrumentation output signal was assessed as a calibration procedure, correlating the sensor resistance change to the AFM-MEMS interaction force as well as determining the rate of the force application. The latter metric - the first order derivative of the force application in time domain, further referred to as force rate, was then interpreted as the elasticity property determining metric – elasticity or spring constant profile, forming a demonstration of the key purpose of the conceived device.

5.4.1 MEMS contact point elasticity characterisation with a calibrated AFM cantilever

A procedure was selected to serve as a showcase for the MEMS device relating measured strain to a known interaction force and displacement. This application focused on demonstrating the ability to detect loads exerted by an AFM cantilever when interacting with the MEMS device. To achieve this, elasticity of the MEMS device (at a selected loading site) was determined using a calibrated AFM cantilever and conventional force-distance ramp setup (schematic in Figure 87 and Figure 89). A springs in series analogy was used to determine the unknown MEMS device elasticity (k_{MEMS}) from the obtained interaction elasticity ($k_{interaction}$) and known AFM elasticity (k_{AFM}) via the relationships described in Figure 88 and Eq. 39 - Eq. 41.

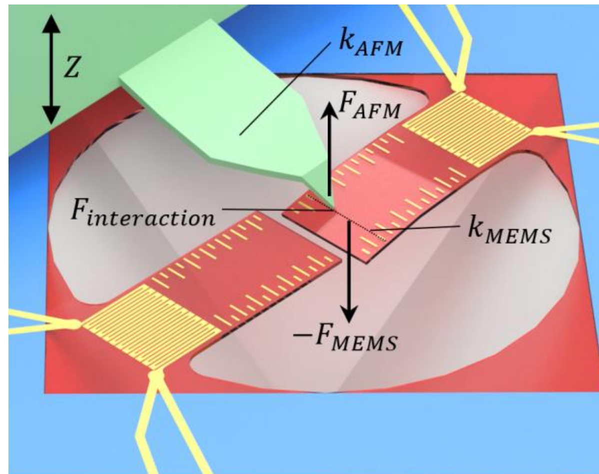

Figure 87. Illustration (CAD) of the different elasticity AFM and MEMS device interaction, resulting in an equal opposite direction force exchange at a contact point.

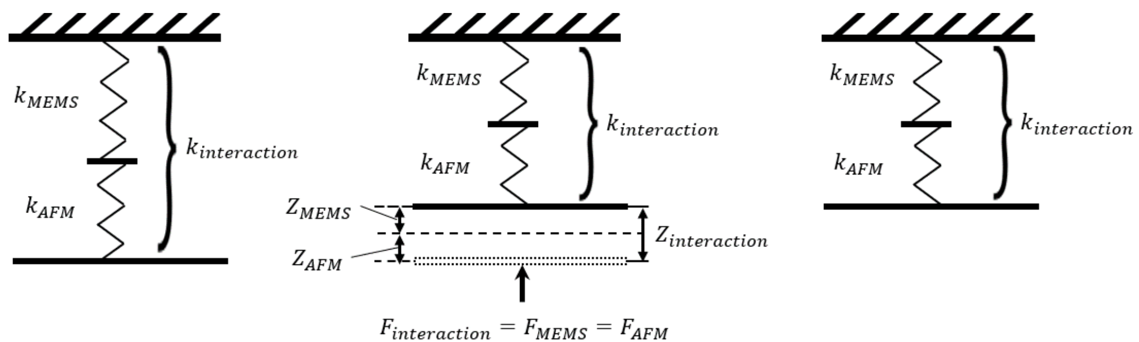

Figure 88. Springs in series analogy used to represent the two distinct elasticity structures (k_{MEMS} and k_{AFM} cantilevers), which act as a compound system with its own resistance to acting force (F), expressed as common elasticity constant ($k_{interaction}$) and displacement (Z).

$$F_{interaction} = F_{MEMS} = F_{AFM}\,; \qquad \textit{Eq. 39}$$

$$Z_{interaction} = Z_{MEMS} + Z_{AFM}; \qquad \textit{Eq. 40}$$

$$k_{interaction} = \left(\frac{1}{k_{MEMS}} + \frac{1}{k_{AFM}}\right)^{-1}; \qquad \textit{Eq. 41}$$

Determining the MEMS elasticity (k_{MEMS}) at the chosen contact point was a non-trivial but crucial exercise. Much like the AFM system, the MEMS device was used to measure interaction elasticity, from which the compounded AFM elasticity (k_{AFM}) was decoupled by employing knowledge of the experimentally determined shared interaction elasticity value ($k_{interaction}$).

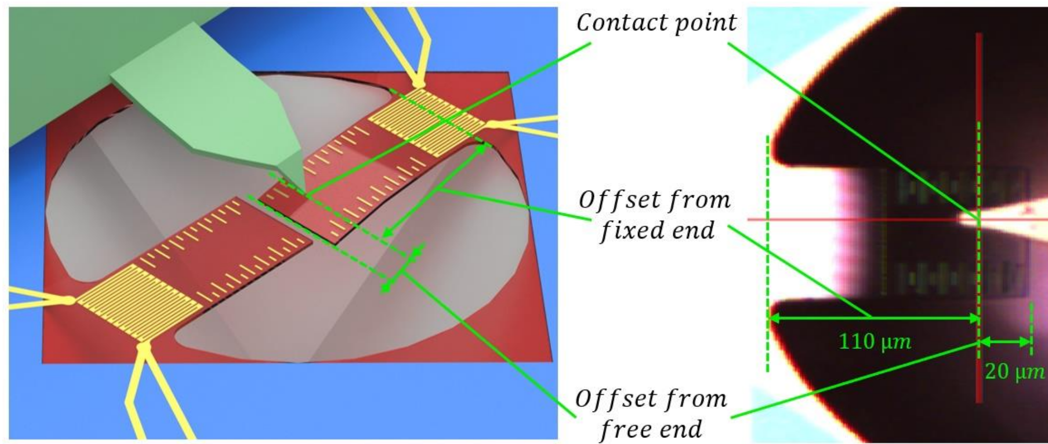

Figure 89. MEMS-AFM probe interaction at the elasticity characterised loading point illustration (left) and the AFM camera capture of the interaction (right).

The MEMS device used in this exercise was the 130 µm long cantilever structure with 1.5 µm width, 2.832 mm long thin film nichrome wire forming the strain gauge and all indentations were conducted at the 110 µm site (Figure 89). Whilst this was not the highest compliance and thus not the most sensitive of all of the fabricated MEMS structures, it was the first device to be successfully fabricated, therefore receiving the most experimental time and attention.

The AFM cantilever employed was the Veeco MPP-21100-W (Figure 16), with known elasticity (k_{AFM}=8.18 N m^{-1}), as determined by the multi-point cantilever profile elasticity study carried out using the nano-indentation system described in 2.5. By carrying out a force ramp on the MEMS cantilever the AFM produced a force-distance plot from which the loading gradient could be interpreted to extract the elasticity constant from two spring interaction ($k_{interaction}$=0.24 N m^{-1}) as a first order derivative ($dF/dZ=k_{interaction}$, per Eq. 1) from the rising curve - loading region, shown in Figure 90.

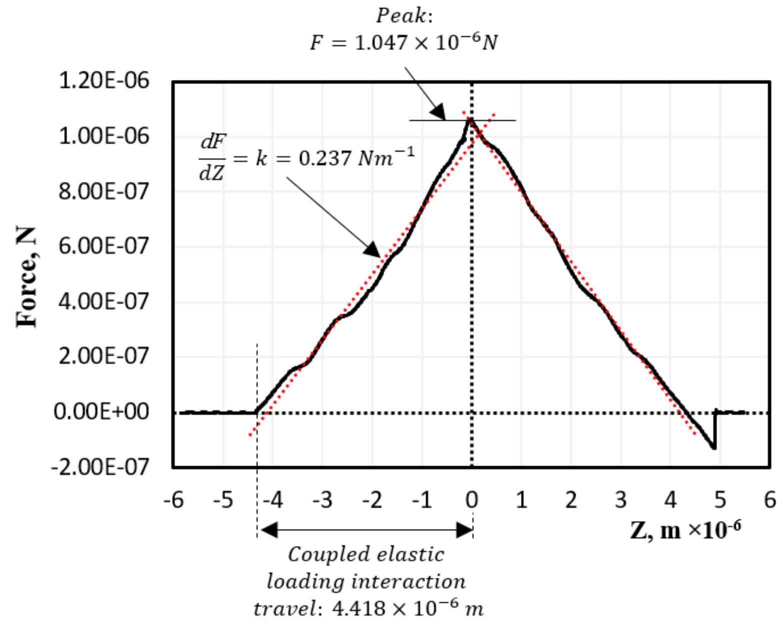

Figure 90. The AFM obtained indentation data from the known elasticity AFM cantilever indentation of the MEMS device, allowing to express the resultant loading and unloading region gradients in elasticity terms by fitting a linear gradient.

The elasticity relationship of springs acting in series could now be resolved in order to determine the MEMS device elasticity at the interaction point - giving k_{MEMS} = 0.24 N m^{-1}, per Eq. 42:

$$k_{MEMS} = \left(\frac{1}{k_{AFM}} - \frac{1}{k_{interaction}}\right)^{-1} = \left(\frac{1}{8.18} - \frac{1}{0.237}\right)^{-1} = 0.24\ Nm^{-1}; \qquad \textit{Eq. 42}$$

5.4.2 MEMS strain signal correlation to an externally determined interaction force

In order to relate the instrumentation output to the magnitude and rate of the induced mechanical strain - the device was exposed to a known force or displacement at a known rate. It would be possible to employ traceable sources as part of this calibration procedure e.g. a dead-weight application [62], characterisation by a metrological institute developed force balancing tool [70] or a sufficiently sensitive and appropriately calibrated nano-indentation system [119]. However, access to such methods is non-trivial, resulting in use of a non-traceable strain to force quantification solution described here. On the other hand, it should be considered that either the MEMS device or AFM cantilever employed to characterise it could be calibrated using a traceable standard in the future. In recognition of this, the datasets obtained are presented in the native instrumentation output units of relative strain change (dR/R_{abs} - unitless as a measurement of relative resistance change) and strain rate ($d[dR/R_{abs}]/dt$, s^{-1}), with the resultant force magnitude (F, N) and related elasticity expression (k, N m^{-1}) noted as secondary values where applicable.

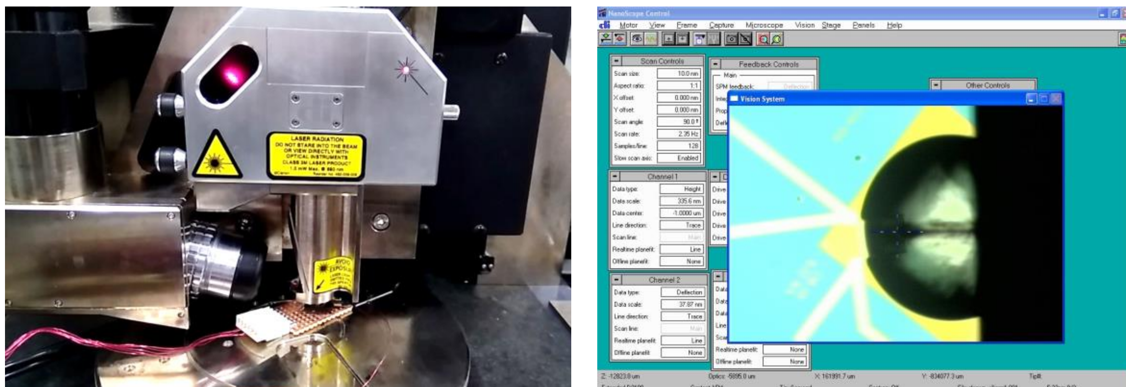

Figure 91. The MEMS sensor positioned in the AFM system (Left), permitting user control of the interaction parameters through the AFM ramping mode interface (Right).

The force applied by the AFM during the interaction showcased in the previous section (schematic setup in Figure 89 and experimental setup in Figure 91) was simultaneously recorded by the MEMS instrumentation (Figure 93). The AFM-MEMS experimental parameters were fixed during the AFM ramps - the location of the loading site, ramp rate and ramp amplitude (per summary in Table 16), meaning all further experiments were conducted with the same settings, allowing application of the force rate to be directly referenceable to this particular calibration. The data was presented as an interaction plot, enabling direct comparison and the extraction of the necessary parameters, described in the following text.

The analogue output signal of the instrument was recorded using an oscilloscope (Agilent DSO6102A, Figure 92) permitting capture of the interaction data in the form of a two-variable matrix - relative voltage change (dV, Volts) and time (t, seconds). A single cycle of this interaction is shown on a shared area plot (to be shown in Figure 94) – illustrating the measured interaction equivalence and subsequently devised scalar expressions for the relationships.

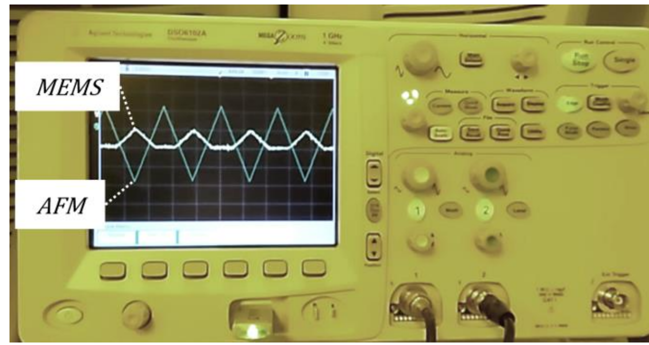

Figure 92. Snapshot of the two-channel oscilloscope interface showcasing the MEMS signal (yellow) and the low voltage Z axis piezo (green). Both channels synchronised (triggered) on the rising AFM Z-signal sawtooth wave allowing for obtaining multiple samples through averaging function.

This could be directly related to the load induced strain gauge resistance change (dR, Ohm) by employing the known instrumentation constant (c_i), that defines the Wheatstone bridge resistance imbalance to the measured voltage change. The MEMS voltage signal could then be displayed as a relative resistance change (dR/R_{abs}) by dividing the relative resistance change by the known free-state strain gauge resistance (R_{abs}). The obtained strain signal amplitude (dR/R_{abs} peak, Figure 93) was related to the previously measured force magnitude (F peak) via ratio expressing the strain to force calibration coefficient - c_f (N). Similarly, the recorded data enabled the coupled interaction first order parameter to be scalarly equated between the AFM measured interaction elasticity (dF/dZ) and the MEMS device recorded strain rate ($d[dR/R_{abs}]/dt$, Figure 93), resulting in the strain rate calibration constant – $c_{k,}$ (N s m^{-1}), Eq. 44.

$$c_f = \frac{dF}{d[dR/R_{abs}]} = \frac{1.047 \times 10^{-6}}{3.208 \times 10^{-10}} = 3.264 \times 10^{3}\ N; \qquad Eq.\ 43$$

$$c_k = \frac{dF/dZ}{d[dR/R_{abs}]/dt} = \frac{0.24}{1.711 \times 10^{-9}} = 1.385 \times 10^{8}\ N\ s\ m^{-1}; \qquad Eq.\ 44$$

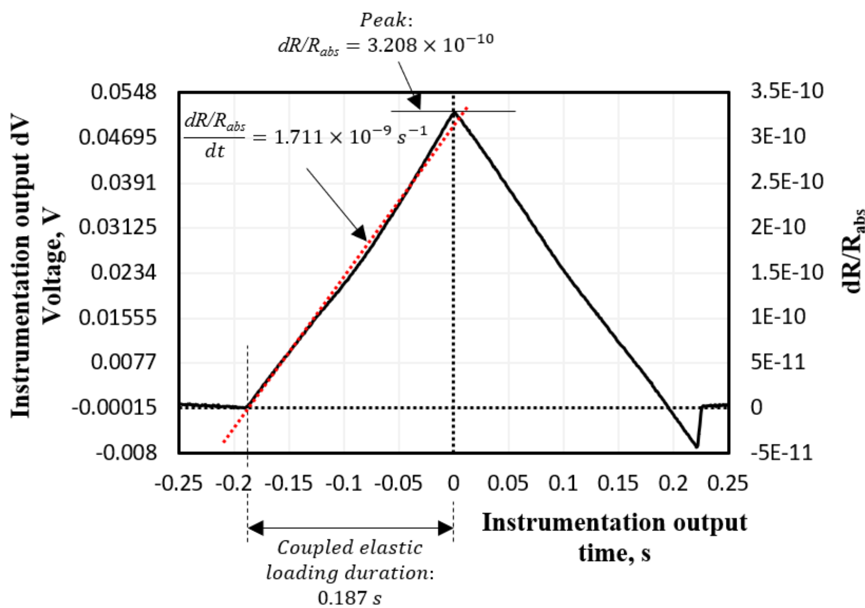

Figure 93. The MEMS instrumentation output from the AFM indentation, displaying a single cycle of the load and unload displacement, centred at the direction change point. The secondary axis displays the relative resistance change value, as obtained by the linear mathematical conversion described in Figure 95.

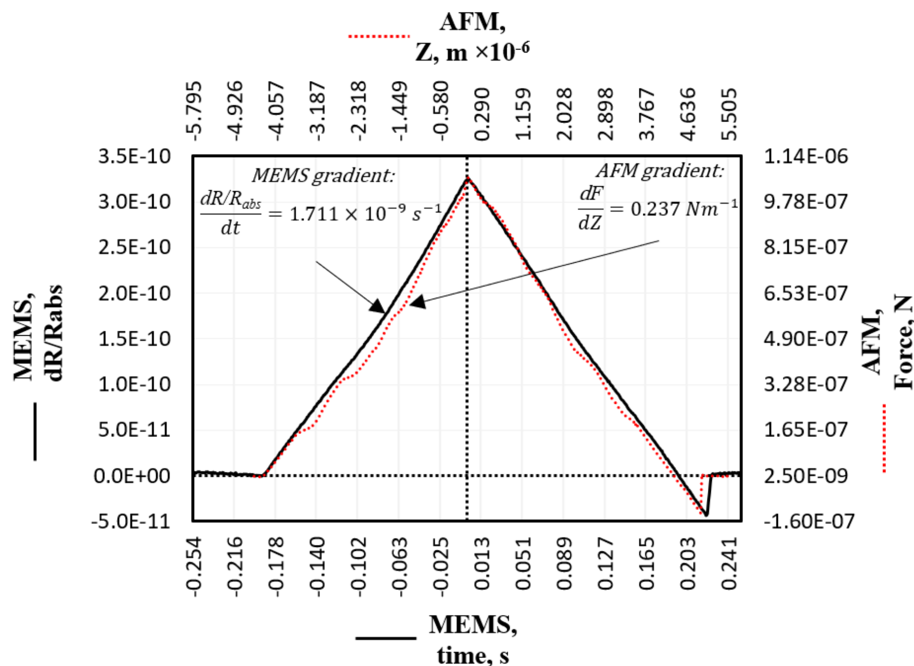

Figure 94. The independently and simultaneously captured AFM-MEMS interaction plots, highlighting the relationship between the vertical amplitude axis and the shared displacement capture.

It is worth highlighting that the coupled interaction duration may also be used to relate the AFM displacement (dZ, Figure 90) to the time of the capture as recorded by the oscilloscope (dt, Figure 93) by correlating ramp-velocity, allowing ramp frequency and amplitude to be altered between the calibration events. However, translation from the measured time domain to AFM ramp displacement was explicitly avoided in this work to circumvent untested assumptions regarding AFM system ramp control and drive linearity behaviour of the tested calibration conditions. Furthermore, it avoids possible confusion about the device operation as independent load and displacement detection may be inferred if displaying in these units. Utilising the raw MEMS device output of strain amplitude in time domain avoids this implication and remains transparent about the fundamentally simple, single sensor enabled functionality.

Table 16. Strain to force determination by a measured force exchange with an AFM probe.

Ramping rate, Hz	1.99	AFM control parameter
Ramping amplitude, µm	5.795	AFM control parameter
Instrumentation constant, c_i	0.00095586	Measurement, ohmmeter, Table 13.
Absolute device resistance, R_{abs}, Ω	151000	Measurement, ohmmeter (four-terminal), Table 14
Strain signal amplitude in response to exerted force by AFM cantilever, $[dR/R_{abs}]$	3.208×10^{-10}	Measurement, MEMS strain amplitude, Figure 93
Exerted force amplitude by AFM cantilever, F, N	1.047×10^{-6}	Measurement, Figure 90
Strain to Force relation factor, c_f, N	3263.716	Calculation, Eq. 43
AFM cantilever elasticity, k_{AFM}, N m^{-1}	8.2	Measurement, nano-indenter, Figure 18
Contact point elasticity $k_{interaction}$, N m^{-1}	0.24	Measurement, AFM force distance fit on load region interaction, Figure 90
MEMS strain rate, s^{-1}	1.711×10^{-9}	Measurement, MEMS strain rate fit on load region interaction, Figure 94
Resultant MEMS elasticity, k_{MEMS}, N m^{-1}	0.24	Calculation, springs in series analogy, Eq. 42
Strain rate to elasticity relation factor, c_k, N s m^{-1}	138515488	Calculation, Eq. 44

The complete signal transformation is summarised schematically in Figure 95, showing the measurement input, processing and output stages. This parameter driven signal transformation ensured that the elasticity profiles obtained could be compared with other measurements, independent of instrumentation configuration.

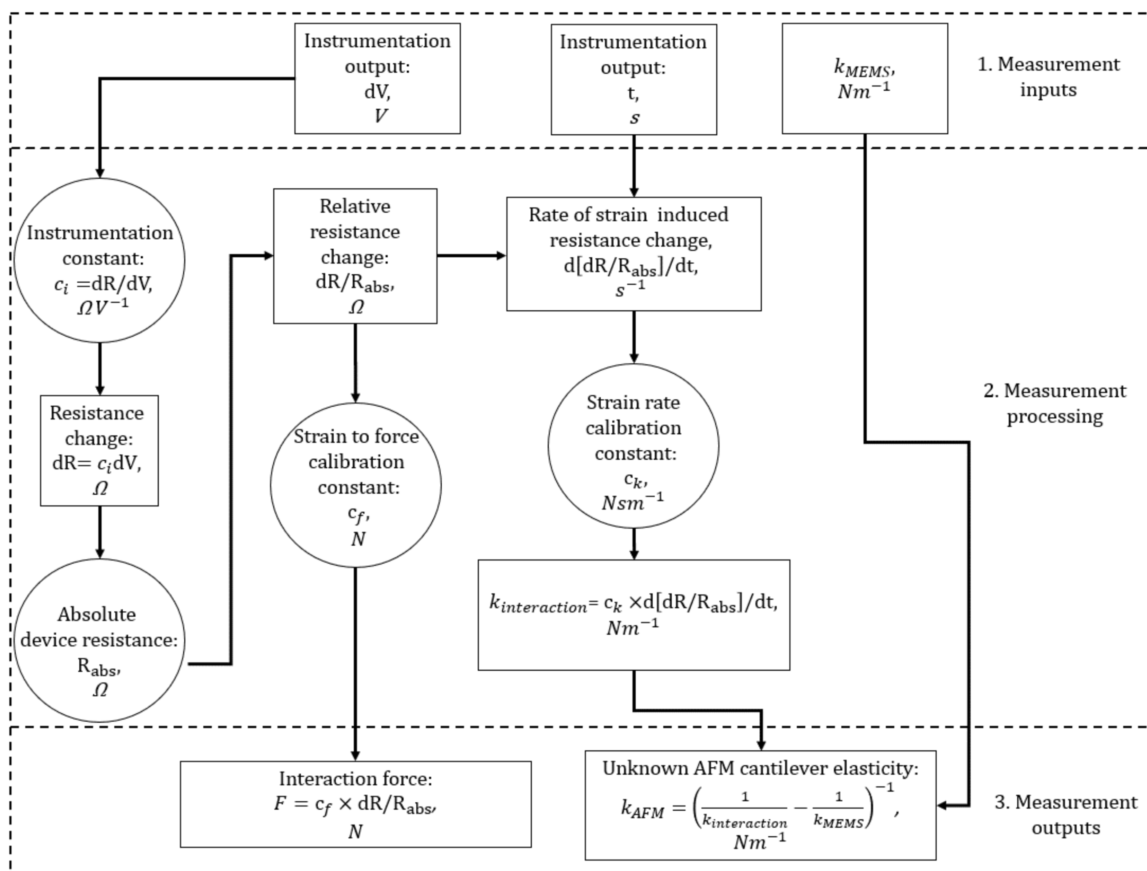

Figure 95. MEMS device instrumentation output interpretation logic for the interaction force and elasticity measurement.

5.5 Conclusion

The data presented in this chapter demonstrated that the complex composition and geometry MEMS devices comply well with the applied analytical and FE method descriptions. This means that any further development could be devised to specification (mechanical compliance and electrical strain sensitivity) solely by theoretical efforts. The attractive performance potential of the metal film sensor was indicated via a survey of its behaviour in a real-life scenario by employing it in-situ AFM laboratory environment. The measurement device exhibited a highly linear relationship during probe interaction loading, as determined by contrasting the signals with the known linear elasticity AFM probe. It demonstrated the capacity for force sensing without requiring extensive load and deformation dependant mapping - which was demonstrably unachievable with the available tools. Most importantly, the proof of concept demonstration of the ability of the MEMS sensor and instrumentation hardware (Figure 96) to transduce AFM relevant mechanical forces as a detectable electrical signal was successfully showcased. The device force calibration is also supportive of alternative approaches that may benefit from accuracy and traceability by the means of identified state of the art indenters and force balances. The MEMS tool can therefore provide a continuous AFM cantilever force and force rate characterisation throughout the interaction in a simple and non-destructive force-distance ramp operation.

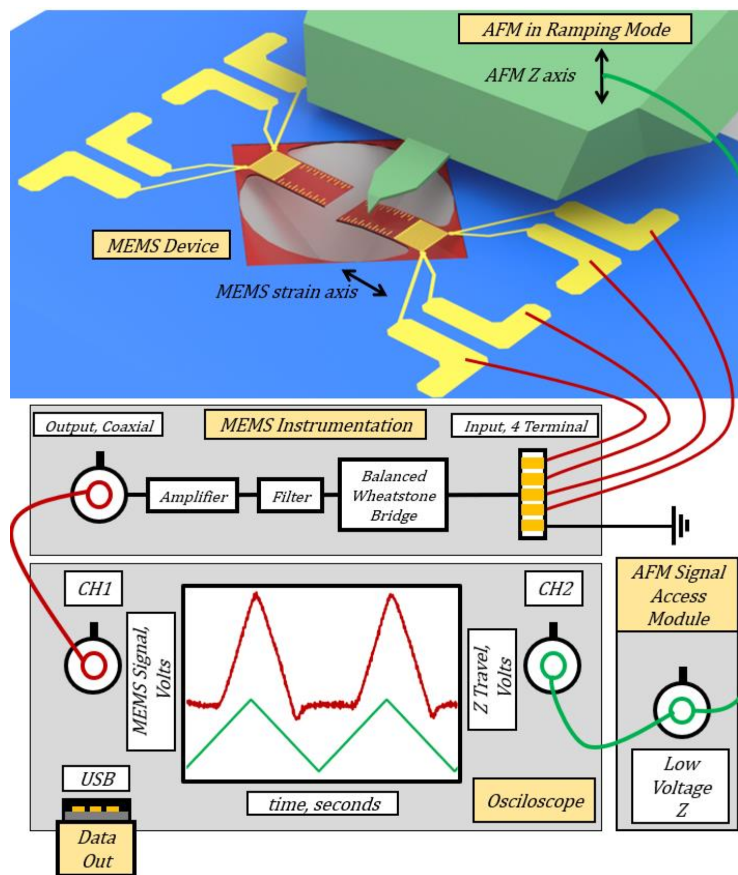

Figure 96. MEMS force measurement setup schematic, showing the vertical (Z-axis) cantilever motion exerting point force load on the strain measuring MEMS device. The purpose designed instrumentation conditions the strain gauge signal form which the elastic interaction behaviour can be interpreted.

Such a feature is often not supported when using alternative methods or is limited when utilising optical lever systems due to the characteristic photodiode detector non-linearities and saturation at large displacements - as evident from a simultaneous capture of both signal sources shown in Figure 97 and elaborated further in section 6.1.4. The clear detection of load-unload and tip-substrate stiction regions was also captured by the sole means of strain measurement which may be utilised in additional AFM probe mechanical behaviour investigations independent of the metrology within the AFM - as explored in the following chapter 6.

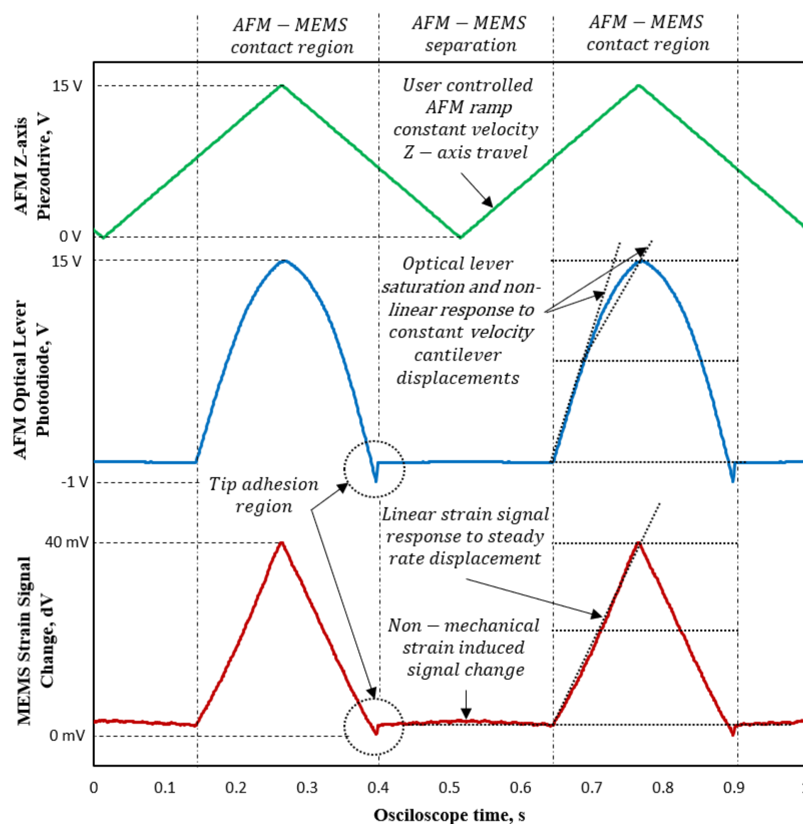

Figure 97. Synchronously captured signals of the user setup 1.99 Hz and 5.795 µm amplitude saw-tooth Z-axis ramping routine (green). The interaction between AFM cantilever and MEMS device is detected by the AFM's own optical lever photodiode readout (blue). The elastic exchange is also independently recorded by the MEMS device produced strain signal (red). The typical to cantilever-sample interaction characteristics are clearly distinguished by both methods, showcasing the idle non-contact separation, progressive displacement during contact and the tip-substrate adhesion regions.

Chapter 6 - MEMS tool application for AFM probe elasticity characterisation

The following chapter describes application of the developed MEMS tool in AFM cantilever elasticity characterisation. The device measurement performance is then compared to conventional elasticity determination techniques, establishing the tools application as an alternative method for quantification of AFM cantilevers with unknown spring constant. The investigation focus is further extended to characterise AFM probes with diverse composition and discontinuous geometry, whose characterisation by conventional methods is otherwise challenging. The demonstrated novelty of a high resolution in-situ force measurement tool and supporting elasticity characterisation methodology is anticipated to be a practical solution for many quantitative measurement focused AFM users and AFM probe manufacturers.

6.1 Complex composition batch produced AFM cantilever elasticity characterisation

It was decided that an appropriate demonstration of the MEMS device being used in a realistic scenario would be to employ it in the characterisation of complex, yet identically batch fabricated AFM probes. The demonstration's purpose was two-fold – first, the practical illustration of the device's ability to obtain an elasticity profile for each structure that could be judged in reference to others. Secondly, to demonstrate the tool's ability to provide the elasticity determining value (spring constant) for each tested structure without additional dimensional knowledge. This could then be further compared against values obtained by established mechanical characterisation methods – dimensional assessment, calibration (reference spring) grid and dynamic or resonance profile-based characterisation.

The investigated AFM probes were 5 pre-internal quality assurance (not for sale) units of KNT-SThM-2an (Figure 98, further referred individually as Probe 1, 2, 3, 4 and 5), obtained from a single production wafer[11] at random. The manufacturer is concerned with consistent control of probe mechanical behaviour and currently employs dimensional and dynamic behaviour-based quality assurance techniques to assess their product, rejecting units that are out of specification. The device composition is depicted in Figure 9 for reader familiarisation purposes only, since accurate dimensional and structural values are proprietary information and not a prerequisite to the MEMS measurement technique used. However, the figure does highlight the features and structural complexity that are essential to the probe's operation. Specifically, SThM probes are used to provide thermal

[11] The probe units were provided by Dr. R. Rajkumar and Dr. Y. Zhang from Kelvin Nanotechnology Ltd, Glasgow, UK [182].

information about the scanned substrate by employing a tip-based metal thermal sensor whilst operating as an ordinary contact mode AFM cantilever. The multitude of features - metallic (palladium, platinum and gold) thermal sensor and mirror, as well as the silicon nitride base with the localised mechanical stiffener (groove section), serve as a great illustration for the structural complexity present in scanning probe microscopy art, together with the production challenges related to ease and clarity of characterisation. The variation in mechanical behaviour of functionalised and complex AFM probes is often difficult to classify or control even when structures undergo identical substrate level processing due to the tolerance stack up in the multi-layer fabrication sequence.

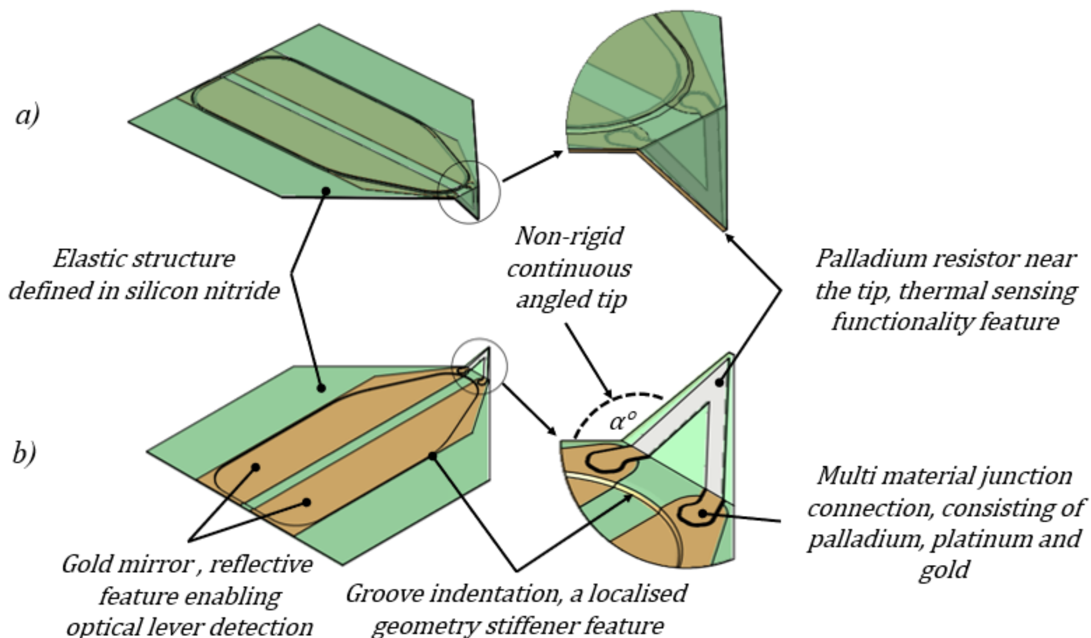

Figure 98. Schematic representation of the KNT-SThM-2an [211] probes, showcasing their structural composition and non-uniformity features in a) top (in-situ AFM placement visible side) and b) bottom (fabrication and ex-situ imaging placement) orientations.

6.1.1 Visual inspection

Prior to mechanical characterisation, the investigated structures were imaged using conventional cleanroom metrology tools that provide a range of dimensional information. Whilst visual inspection does not reveal the mechanical behaviour and elasticity of a cantilever, the relative structural deviations evident between the imaged structures can be useful in explaining any mechanical deviations subsequently measured. The top-down, shared-scale, SEM images (Figure 99) of the five tested structures clearly indicated geometric variance in the stiffener feature (groove) location as well as inconsistencies in the underlying silicon base defined in the release etch step - akin to process described in 4.5. The first observation suggests a potential asymmetry in the cantilever elastic behaviour, whilst the latter may be inferred to mean that Probes 3 and 4 exhibit a shorter effective bend length and could expected to have higher elasticity values.

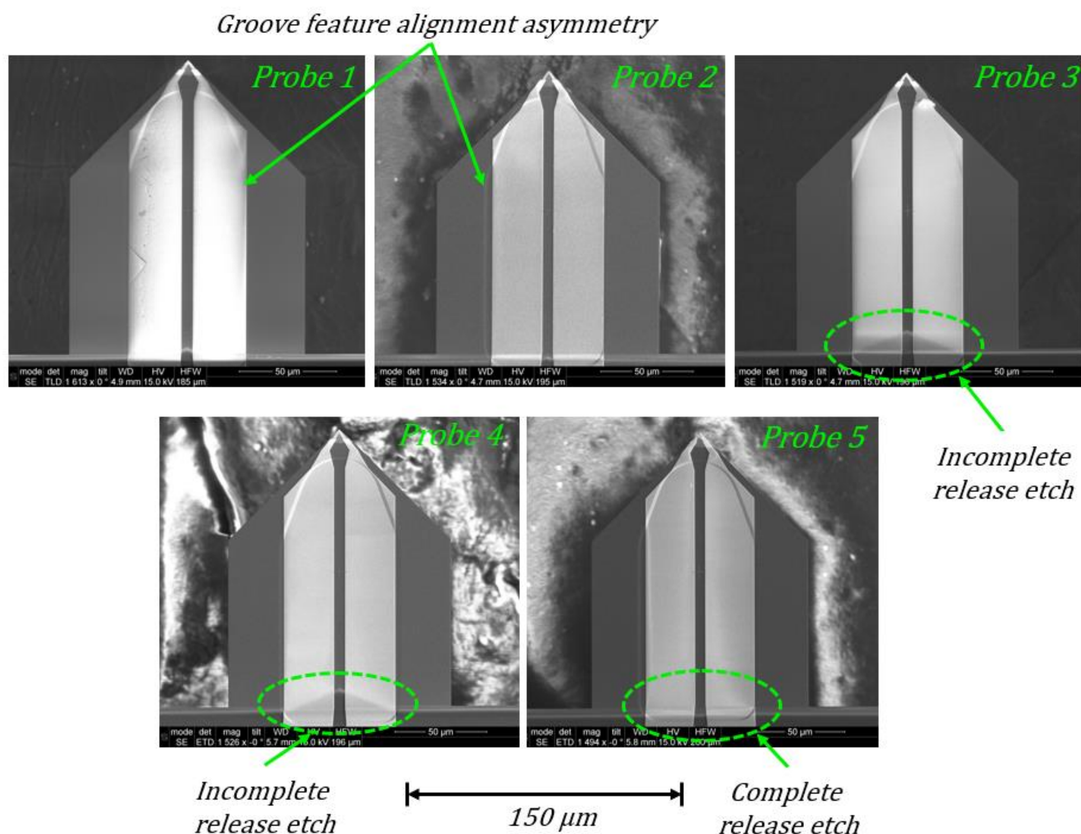

Figure 99. The five tested structures imaged by SEM, highlighting the plainly identifiable variations between the structures – groove alignment in relation to gold mirror and triangular shade at the base indicating an incomplete anisotropic silicon release.

Further non-uniformity can be seen near the functionalised tip region, as shown in Figure 100. This close-up comparison draws attention to two major irregularity types – the vertical position of the curved bend in relation to the tip apex and the inconsistent metallic feature alignment, with suspected leftover fabrication contamination. Unlike the simplest AFM cantilevers (e.g. Figure 28) which have a pyramid shaped tip acting as rigid load transfer point to the cantilever, this kind of probe has a tip formed as an angled 'beak' on the continuous silicon nitride cantilever that may be expected to act as a hinge and introduce its own component into the structure's elastic characteristics. Therefore, the bend location may be a significant contributor to the probe's mechanical behaviour even with the typical (to photolithography) variance – e.g. 2 µm amplitude witnessed in the tested structures.

Furthermore, the inherent variance in multi-level lithography alignment that is necessary for probe fabrication is visible in Probe 1 and Probe 3, where the tip resistors display asymmetry and do not share the consistency shown by the most symmetrical subject - Probe 2. Finally, Probe 4 and Probe 5 exhibit varied degrees of tip contamination either left over from the fabrication processing or unintentionally attached during handling. Such variation at the tip may result in an inconsistent contact point and variance in physical tip mass, possibly affecting the dynamic technique characterisation results.

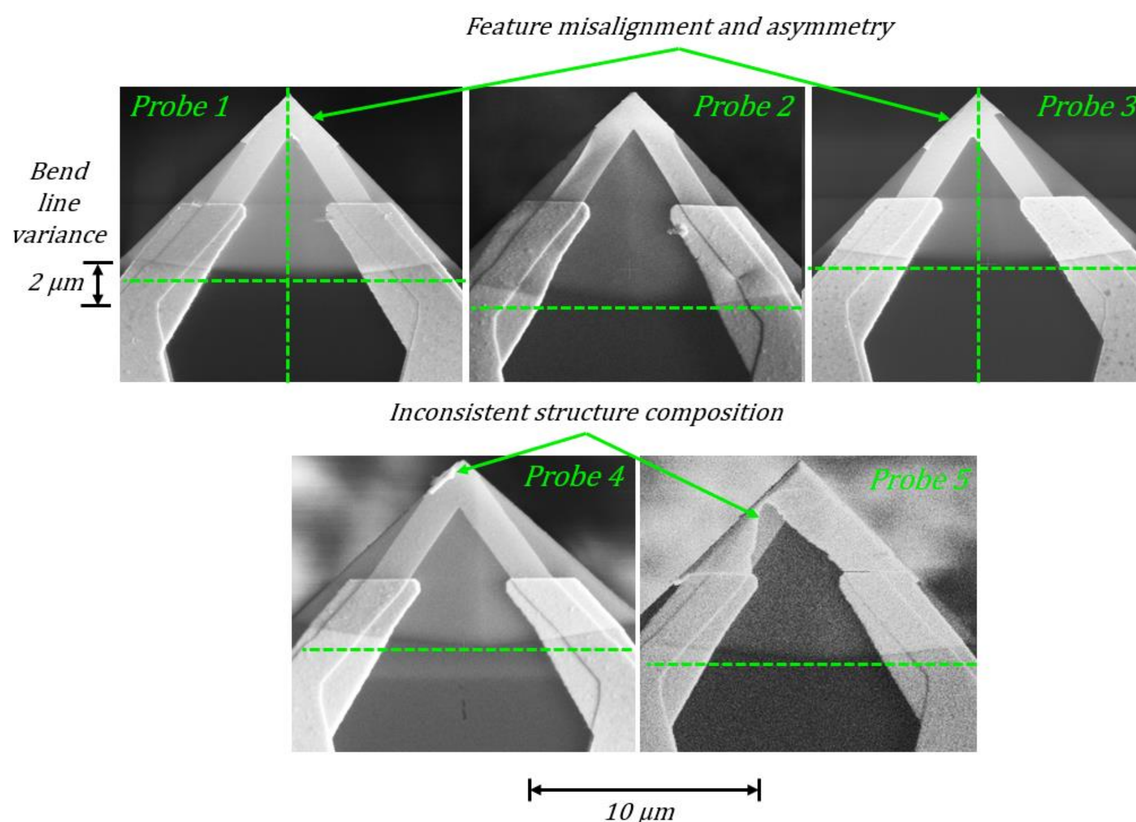

Figure 100. Close-up of the structurally complex region - the tip apex, revealing the composition variation and planar feature asymmetry.

Although effective at identifying global features (lateral dimensions, lithographic defects), this SEM inspection could not easily visualise deviations in the overall flatness of the cantilevers. Since these cantilevers are extremely soft (manufacturer reported nominal elasticity of 0.4 N m^{-1} [211]), surface profiling with a physical tip was not possible due to

contact adhesion/breakage risk. A non-destructive topographical assessment by optical profiling was therefore one of the few characterisation methods suitable for this challenge - procedure previously introduced in 4.5.3. Comparing the scanned topography of the five structures (Figure 101) revealed that Probe 2 and Probe 5 exhibited opposing height gradients (low to high z distance of ~1.2 µm), possibly indicative of internal stress caused free-state deformation. Probe 4 also displayed an upward, albeit lesser magnitude curvature that was in line with the bend axis (low to high z distance of ~0.5 µm). Probes 1 and 3 showed little curvature at the free end perimeter and could therefore be considered as deviating least from nominal design structures. A firm conclusion on the relative impact topological variation has on structure elasticity is difficult to draw since the exact thickness of each layer (silicon nitride, gold, palladium etc.) of the structures was unknown, however, assuming a small variance, it may be anticipated that the largest curvature and thus internal stress magnitude probes (2 and 4) may be stiffer than the rest of the group.

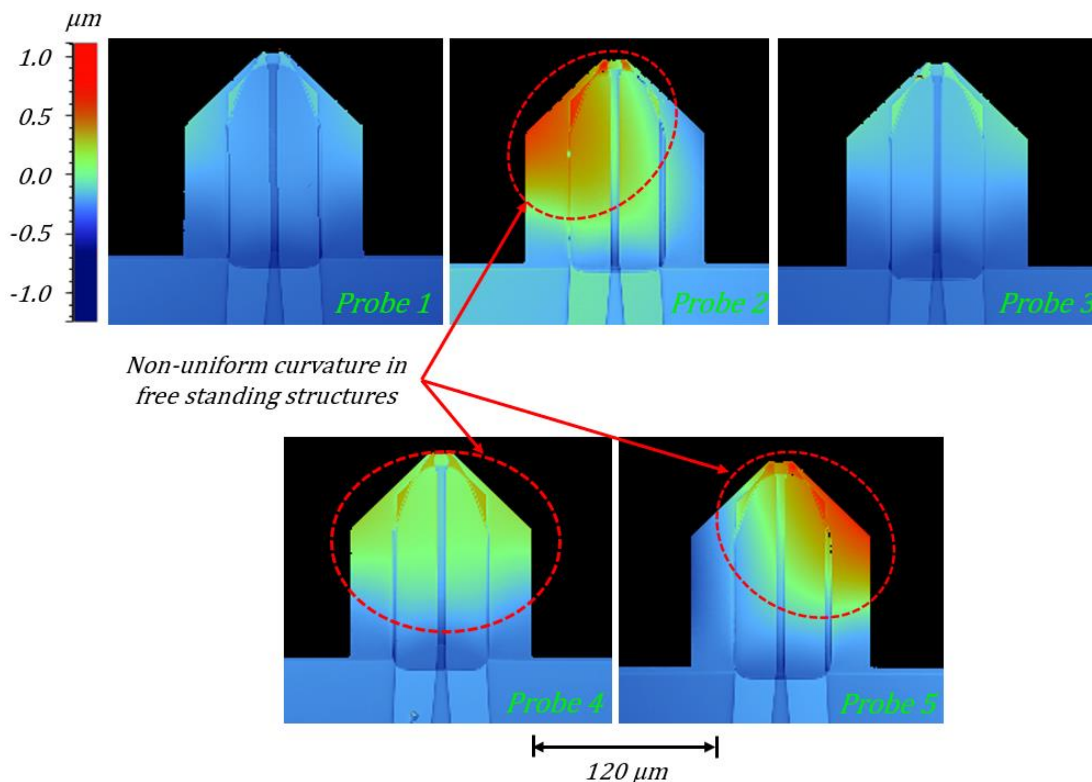

Figure 101. Optical profiler (Bruker Contour GT [212]) obtained surface topology scans, showcasing the non-uniform free-standing structure topology – product of non-intentional fabrication deviations and localised internal stresses.

In summary, inspection of the five nominally identical structures, produced using a common fabrication process, revealed five unique topologies. SEM imaging and topological mapping revealed information about the relative deviations of the investigated group of cantilevers but did not allow definitive conclusions on their structural behaviour to be drawn. This indicated that these structures were likely to exhibit unique mechanical behaviours and return variant elasticity constants, making them ideal candidates for a relative characterisation trial.

6.1.2 Elasticity assessment with the MEMS tool

To employ the MEMS tool for experimental assessment of the AFM probes' mechanical behaviour and determine their cantilever spring constants the five probes were consecutively mounted in the AFM system and brought into contact with the MEMS structure at a determined offset point of known elasticity (Figure 102). Identical parameters were used for each indentation and the instrumentation output was recorded as described previously in 5.4.2. Interaction information was recorded as time and voltage change (Figure 103) but was then subject to the processing schematically described earlier (Figure 95) to obtain relative resistance change. This allowed results to be expressed as time and force magnitude (per calibration conversion in Eq. 43 and Eq. 44), permitting for elasticity modulus determination. Plotting the engagement profile obtained for each structure allowed for elasticity constant extraction in not only the load and unload region, but also for visualisation of tip exerted force behaviour throughout the entire indentation – a feature that can be immensely useful for post fabrication quality assurance purposes.

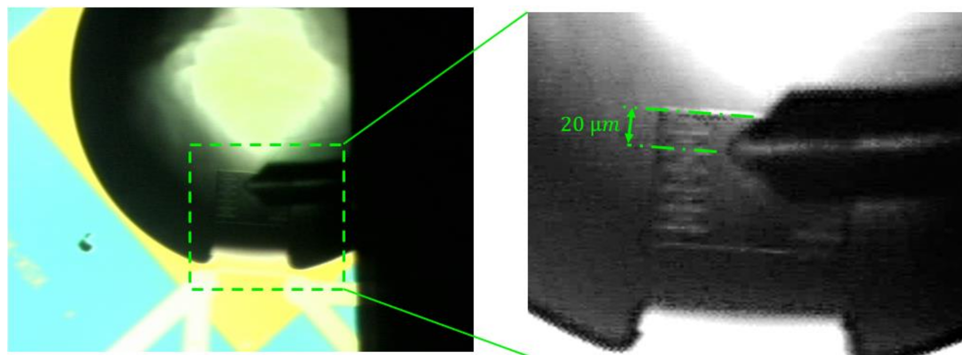

Figure 102. AFM-MEMS contact point determination with the aid of Vernier alignment markings (AFM camera).

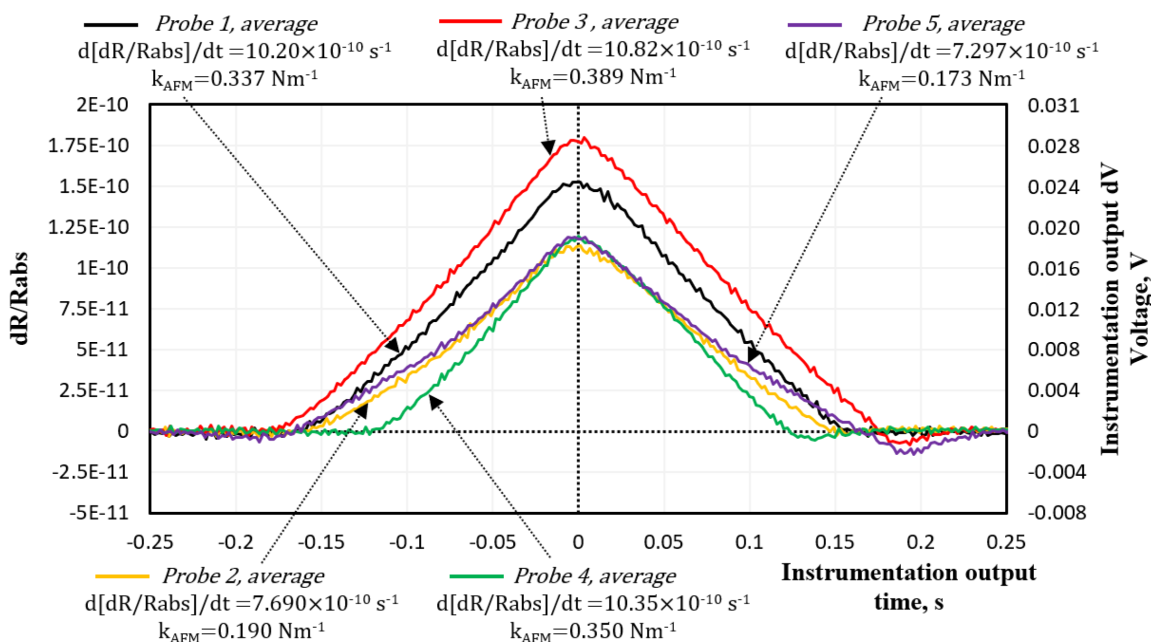

Figure 103. MEMS strain sensor signals for each cantilever. The linear fits over the loading and unloading (approach and retract in AFM terms) regions and their averaging provide characterisation for the measured elasticities in strain (d[dR/Rabs]/dt, s^{-1}) terms, which can be transformed to elasticity units (k_{AFM}, N m^{-1}) by undergoing conversion with a pre-determined calibration constant.

The experiment was designed so that probes came in and out of contact during the indentation, providing an opportunity to capture tip-sample engagement-separation behaviour. Whilst all 5 measurements employed identical parameters, some differences in magnitude and interaction duration remained due to natural variations in the environment and AFM holder positioning as seen in the small variation of engagement duration. The plot of MEMS strain against AFM registered displacement provided information about the interaction in the native relative strain rate units - s^{-1}. When the elastic rate correlation coefficient (c_k) was applied, the rate of change values could then be converted to the N m^{-1} units as used in conventional elasticity expressions. Upon applying the spring-on-spring analogy to extract the probe elasticity component from the measured interaction elasticity, the individual gradients were obtained as summarised (Table 17). These show a

124% deviation in mechanical elasticity between the 5 tested structures over the range 0.173-0.389 Nm^{-1}. For supposedly identical, batch produced structures, aimed at quantitative measurement this is a staggering variation, further illustrating the problematic use of nominal elasticity constant, particularly in multi-layer microfabricated structures. The probes at the upper limit do lie close to the manufacturer indicated nominal value of 0.4 N m^{-1} [211], indicating that the overall design is compatible with the quoted compliance, indicating that Probes 2 and 5 do not meet the manufacturer's tolerances. Additionally, thanks to the previously established linear response of the MEMS device (Figure 94), non-linearities revealed in the data can be directly attributed to the AFM cantilever. Such non-linearities could stem from structural defects, akin to those seen in probes 2 and 5 back in 5.1.1, which also exhibit increases in their elasticity gradient around halfway through the indentation – indicating deflection dependant 'hardening'. Possible explanations for such behaviour could be dual mode bending - e.g., initial elastic deformation of the probe beak that is followed by the more compliant main structure.

Table 17. Summary of the probe elastic interaction gradients expressed as relative strain rate and elasticity figures, interpreted from loading and unloading regions[12].

	Probe 1	**Probe 2**	**Probe 3**	**Probe 4**	**Probe 5**
d[dR/Rabs]/dt, load, $s^{-1}\times10^{-10}$	*9.839*	*7.289*	*10.80*	*10.79*	*7.245*
d[dR/Rabs]/dt, unload, $s^{-1}\times10^{-10}$	*10.56*	*8.090*	*10.84*	*9.903*	*7.348*
d[dR/Rabs]/dt, average, $s^{-1}\times10^{-10}$	*10.20*	*7.690*	*10.82*	*10.35*	*7.297*
$k_{interaction}$, load, N m^{-1}	*0.1363*	*0.1010*	*0.1496*	*0.1495*	*0.1004*
$k_{interaction}$, unload, N m^{-1}	*0.1463*	*0.1121*	*0.1502*	*0.1372*	*0.1018*
$k_{interaction}$, average, N m^{-1}	*0.1413*	*0.1065*	*0.1499*	*0.1433*	*0.1011*
k_{AFM}, load, N m^{-1}	*0.309*	*0.172*	*0.387*	*0.386*	*0.171*
k_{AFM}, unload, N m^{-1}	*0.365*	*0.207*	*0.390*	*0.313*	*0.175*
k_{AFM}, average, N m^{-1}	*0.337*	*0.190*	*0.389*	*0.350*	*0.173*

Furthermore, the high strain sensitivity and sampling rate (1 GHz) allowed for a detailed visualisation of the adhesion region (Figure 104), where the MEMS device displays negative force amplitude, indicating a compression driven reduction in resistance. The clear difference in adhesion force for each individual probe was visible, demonstrating the high resolution (<10 nN) force measurement of the MEMS device. For instance, the highest pull-away force (~40 nN) was shown by Probe 5, which correlates with its differing tip geometry and composition compared to the remainder structures (Figure 100). This result suggests the tool could also be applied to tip contact and adhesion quantification – a highly relevant property for contact mode scanning techniques.

---

[12] The gradient differences in load and unload regions are deemed non-systematic and are suspected due to the not sufficiently rigid mounting setup of the MEMS device on AFM scanning stage - which is simply resting on a copper plate. Strain in connecting wires and mechanical movement due to thermal effects may be attributed to these random errors, therefore permanent device implementation should seek a rigid but serviceable mounting solution with the help of fasteners or clamps.

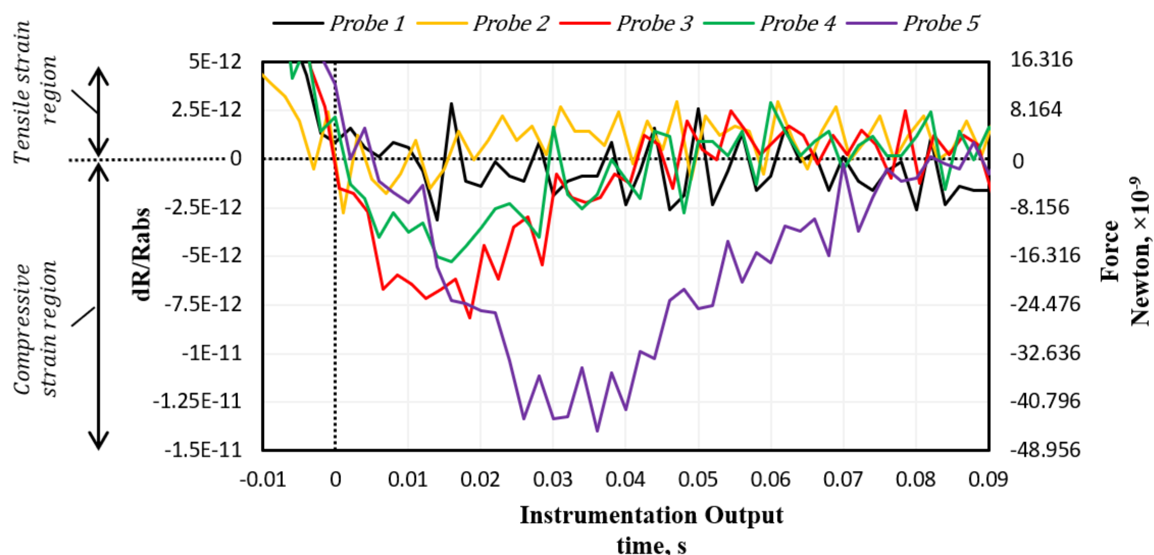

Figure 104. Adhesion region comparison displaying the compressive strain region during the tip-sample adhesion and release caused compressive strain returning to neutral strain plane.

To conclude, the MEMS device assessment of complex AFM probe interactions provided high-resolution characterisation of their elastic profiles – without prior knowledge of the tested structure properties. The information contained inside the uninterrupted interaction profile may therefore be used for extended structural characterisation and fabrication quality assessment – e.g., identifying non-symmetric and non-linear elasticity behaviour in the discrete load-unload and adhesion regions – applications of which are explored in the following text.

6.1.3 Indirect elasticity assessment via dynamic behaviour observation

Techniques that employ probe dynamic behaviour to determine elasticity are popular amongst AFM users due to their speed and operational simplicity - as enabled by their presence in most modern AFM systems. Specifically, motion spectrum analysis can be conducted using most AFM systems supporting the thermal tune method. This approach relies on motion curve interpretation for oscillatory energy dissipation – the theory and application of which was described in 2.3. Additionally, the spectrum also provides easily identifiable natural resonance values that may be used for relative elasticity estimation for structures that undergo Euler-Bernoulli described beam bending – this method was reviewed and demonstrated in sections 3.1.1 and 5.1.3. Therefore, power spectrum analysis of the SThM probe test structures was undertaken using an AFM system with the dynamic characterisation capacity in order to compare the results with those determined using the MEMS device.

The power spectrum density profiles obtained for the 5 structures (Figure 105) show that Probes 1, 3 and 4 displayed similar natural resonance frequencies (f_0) - 6.4% difference between smallest and largest. However, much larger discrepancies were evident between the structures' thermal tune elasticity results (k_{TT}), as obtained via curve integral (area) interpretation, resulting in magnitude variation of 64% within the set of three. Furthermore, the remainder structures - Probes 2 and 5, natural frequency peaks were closely matched (5.1%), however the thermal tune interpretation displayed a several fold difference in the estimated structure elasticity (569%).

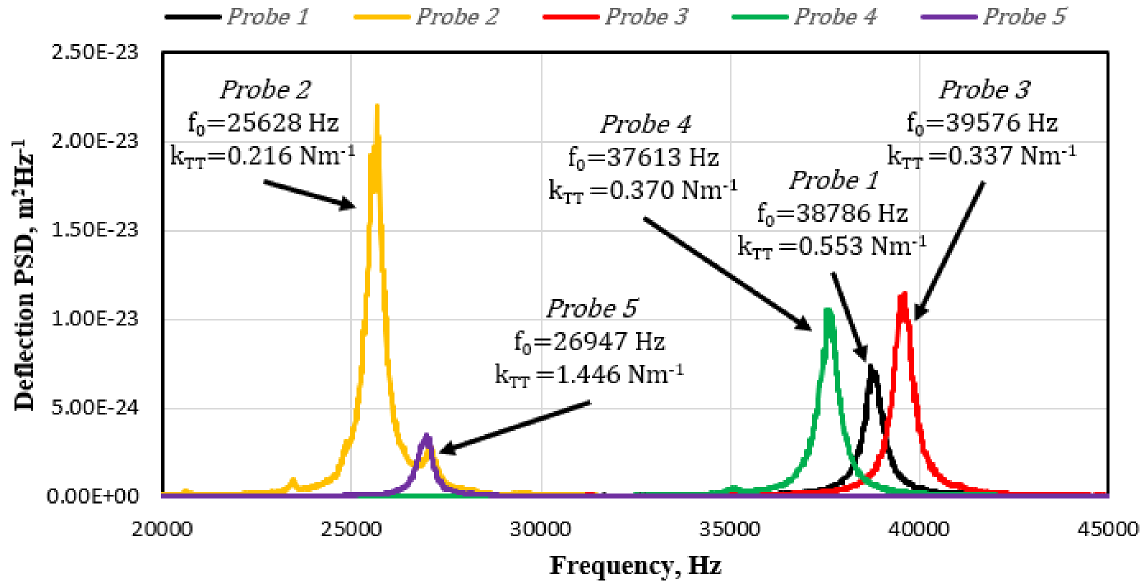

Figure 105. In-situ AFM (Bruker Dimension Icon, USA [25]) motion spectrum analysis of the tested structures, highlighting the natural frequency (f_0) and the determined elasticity by thermal tune method (k_{TT}).

It is reasonable to expect that such drastic differences in mechanical behaviour would result from identifiable structural features that would have been highlighted during the previous visual inspection efforts. This leads to the conclusion that these differences in dynamic response cannot confidently represent the static structural behaviour of these probes. Possible causes of the deviation could be the non-uniform internal stresses or the different tip compositions acting as mass dampener, reducing the idealised thermal energy dissipation modelling used by the approach (further details in section 2.3). The identified outlier highlights the caution required when using the dynamic technique on probes with non-uniform composition. Like the previous visual assessment, conflicting conclusions can be drawn from both dynamic behaviour metrics (frequency and power spectrum integral), however one useful conclusion is the indication that Probes 1, 3 and 4 behave in a dynamically similar fashion, and therefore may be expected to show similar elastic deformation in their static applications.

Table 18. Summarised dynamic behaviour study outcomes.

	Probe 1	**Probe 2**	**Probe 3**	**Probe 4**	**Probe 5**
f_0, Hz	38786	25628	39576	37613	26974
k_{TT}, N m^{-1}	0.553	0.216	0.337	0.370	1.446

6.1.4 Elasticity assessment with a calibrated reference spring

The final elasticity determination technique tested was the spring-on-spring approach employing an off-the-shelf cantilever[13] of known elasticity (Figure 106). This approach employed an experimental setup and interpretation that is analogous to the methodology described previously in 2.4. This method is relatively popular amongst users due to its in-situ characterisation, relative ease of access and the fact that it is indiscriminatory of the AFM cantilever geometry and structural composition - making it suited to the characterisation of complex structures. The technique uses an AFM system to compare the mounted cantilever mechanical response against a rigid surface and then the known elasticity cantilever, providing characterisation of the mechanical loading response that is reliant on the AFM's optical lever.

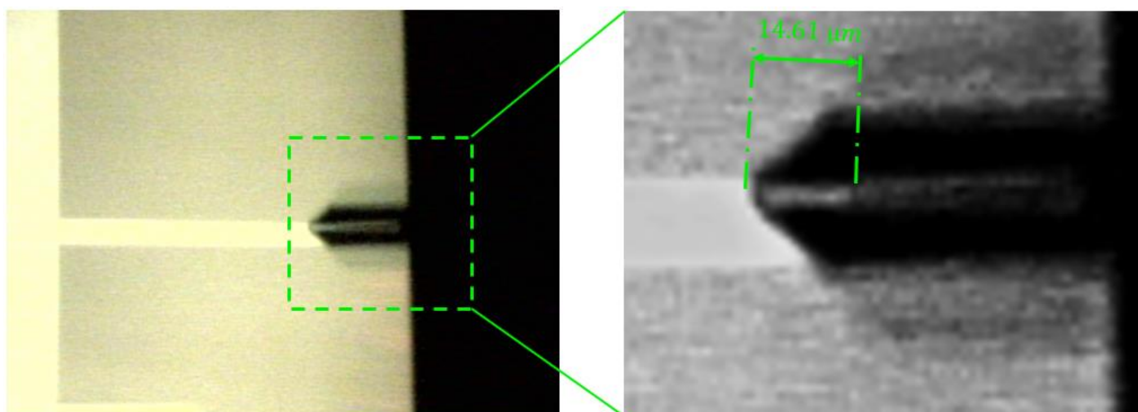

Figure 106. Integrated AFM camera snapshot of the investigated SThM structure and calibration grid cantilever (Bruker CLFC, [116]) contact point during the spring-on-spring experiment interaction.

[13] Bruker CLFC, Wafer No: A002/01 box 5 - Probe 5 [108].

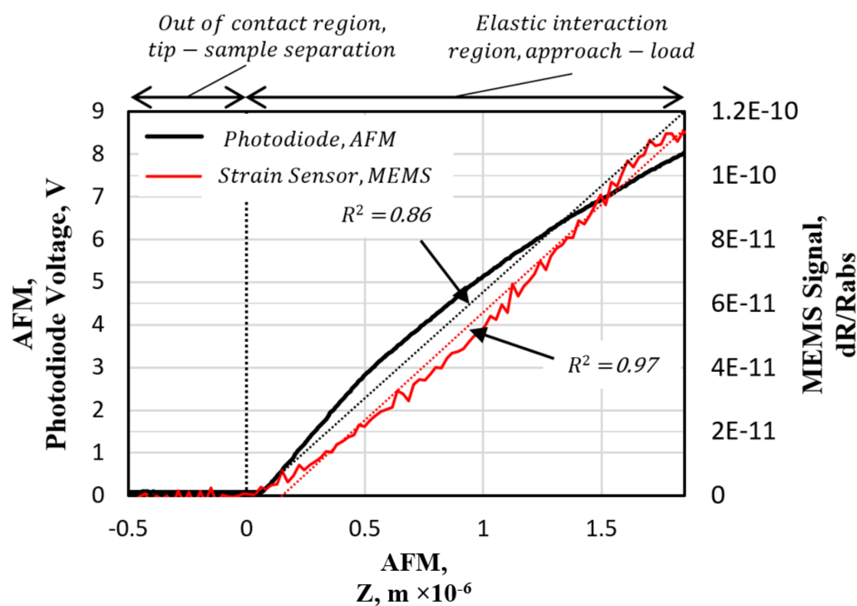

Figure 107. Probe 2 elastic deformation profile and resultant linear fit comparison from two detection methods – approach regions of the AFM optical lever (black) and MEMS strain signal (red).

The assumption of elastic linearity in load and unload gradients for these structures is evidently challenged by the rate of change non-linearity in the interaction plot as seen in the comparison between MEMS and AFM data in Figure 107. It is worth mentioning that all of the interaction gradients obtained contained a notable degree of non-linearity, however for the purpose of clarity the example shown is of the Probe 2 loading region, as it was the most pronounced in the tested set. These non-linearities are naturally less distinct in the stiffer cantilever interactions, that involve much smaller displacements - such as in the case study described in 2.4. However, the cause of the first order non-linearity may not necessarily be a cause of non-linear mechanical behaviour, but an optical lever detection artefact. Split photodetector systems can indeed display such behaviour (e.g. [213]) and the methods of mitigation involve photodiode characterisation against a purpose built linear sensor – necessitating an additional calibration step for high compliance AFM cantilevers.

Table 19. The processed elasticity figures from the complex composition AFM probe characterisation by the calibration reference grid experiment, highlighting the load and unload region output and their averaged values for each structure.

	Probe 1	**Probe 2**	**Probe 3**	**Probe 4**	**Probe 5**
k_{REF}, load, N m^{-1}	0.318	0.155	0.367	0.325	0.171
k_{REF}, unload, N m^{-1}	0.301	0.145	0.360	0.301	0.165
k_{REF}, average, N m^{-1}	0.310	0.150	0.364	0.313	0.168

In conclusion, elasticity of the probes obtained using the reference spring method indicate that Probes 1, 3 and 4 have closely matched magnitudes (within 15.4%), whilst Probes 2 and 5 are the outlier structures with roughly half the elasticity of the first group (Table 18). Notably, an inter-experimental agreement is witnessed - the elasticity figures align with the stiffness trends provided by the MEMS device output as well as by the natural resonance value comparison. Additionally, the optical topology maps obtained earlier (Figure 101) also suggest that the topologically inconsistent structures (Probes 2 and 5) display anomalous elastic behaviour when compared to the rest of the set. This consistency indicates that the reference spring method is a suitable and reliable technique for assessment of probe elastic behaviour, albeit with the potential for non-linearity detection attributed to the optical lever output.

6.1.5 Experimentally obtained elasticity modulus comparison

Whilst all of the methods explored provided unique insights into the complex AFM cantilever composition, the key AFM feature being sought was bend displacement to exerted force quantification - as expressed by the elasticity constant. Therefore, a comparison between the test methods was conducted, contrasting the results in Figure 108 and Table 20. For interpretation simplicity, only the averaged elastic constants are considered where a choice of load/unload (or approach/retract) regions was available.

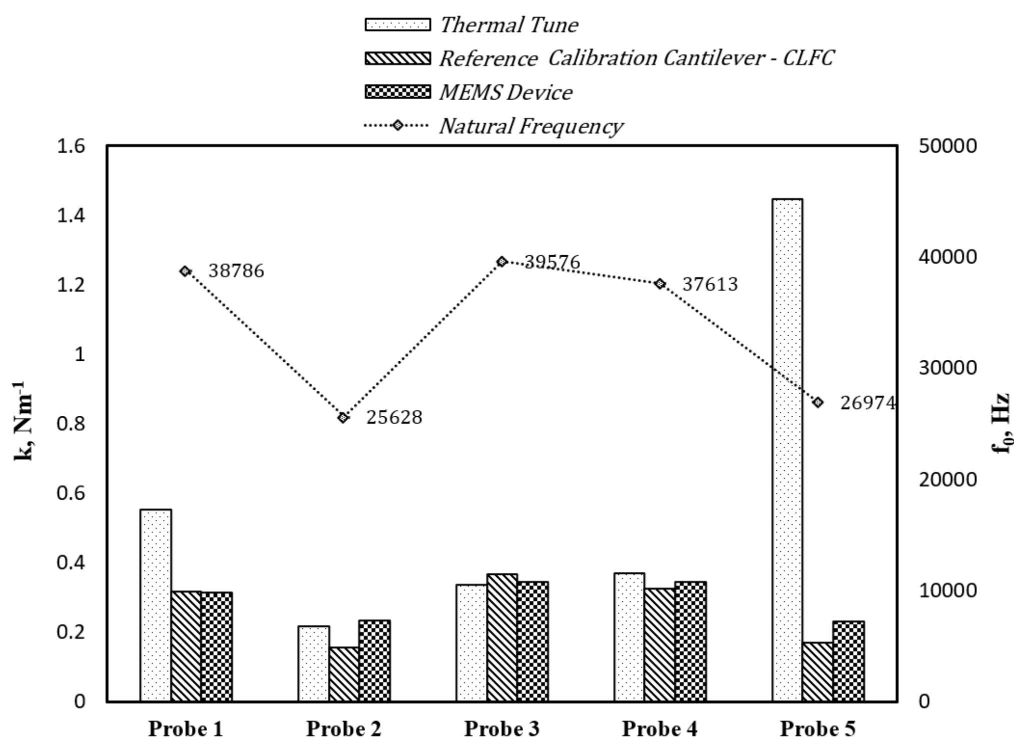

Figure 108. Summarised elasticity assessment results distinguished by characterisation method.

Table 20. The frequency and elasticity result summary corresponding to the five investigated AFM cantilevers, averaged figures used where multiple load and unload gradients were available.

Characterisation method	***Probe 1***	***Probe 2***	***Probe 3***	***Probe 4***	***Probe 5***
f_0, Hz	38786	25628	39576	37613	26974
k_{TT}, N m^{-1}	0.553	0.216	0.337	0.370	1.446
k_{REF}, N m^{-1}	0.310	0.150	0.364	0.313	0.168
k_{MEMS}, N m^{-1}	0.337	0.190	0.389	0.350	0.173

A strong agreement in the measured elasticity is exhibited between the natural frequency, reference spring and MEMS device results. Outlier structures identified by visual inspection and natural frequency trends – Probes 2 and 5, are also accordingly singled out by the physical characterisation methods – MEMS tool and reference spring. The reference spring and MEMS device results are in close agreement about 1, 3 and 4, while returning a consistent offset for Probes 2 and 5. Such amplitude offset with the maintained proportionality trend, may be attributed to the non-linear nature of the photodiode displacement employed by the reference spring method. The thermal tune method provided values for Probes 2, 3 and 4 that are also closely matched to the remaining methods, however the results for Probes 1 and 5 are in disagreement with the physical interaction methods and natural frequency figures. This indicates that the thermal tune method may display limited applicability to complex, but nominally identical structures, as 40% (2 out of 5) of the obtained results are in significant disagreement with the other techniques. The notably simple natural resonance characterisation also proved itself to be a capable technique suited for relative elasticity comparison, where knowledge of absolute elasticity magnitude is not required.

The positive correlation between the three methods inspires confidence in the merits of the MEMS device, while its application can also be extended beyond elastic gradient

determination. Specifically, a single measurement is densely packed with data applicable to discrete mechanical phenomenon permitting a multitude of approaches towards data interpretation - this may compete or provide supporting data to simple visual inspection methods and allow identification of fabrication related process variations and failure modes. Emphasising the above conclusion, the following sections demonstrate possibilities of the MEMS device enabling AFM probe elasticity determination extending beyond the characterisation capabilities provided by conventional solutions.

6.2 MEMS tool application for AFM probe structural modification characterisation

Another potential application of the MEMS device is in exploring changes in mechanical behaviour introduced by probe modification. As an example, the impact of adding a 20 nm thick aluminium coating by physical vapour deposition to the previously studied batch of 5 KNT-SThM-2an [211] probes (Figure 109). This modification is conducted by the AFM probe manufacturer in order to improve the reflective properties of the largely optically transparent silicon nitride cantilever. The result is a functionally improved device when utilised in a conventional optical lever reliant AFM system, where the top cantilever face is utilised as a mirror. It is expected that this alteration will affect the probe's elastic behaviour and the MEMS measurement tool could be employed to detect any changes in the pre and post deposition elasticity gradients – summarised in Table 21.

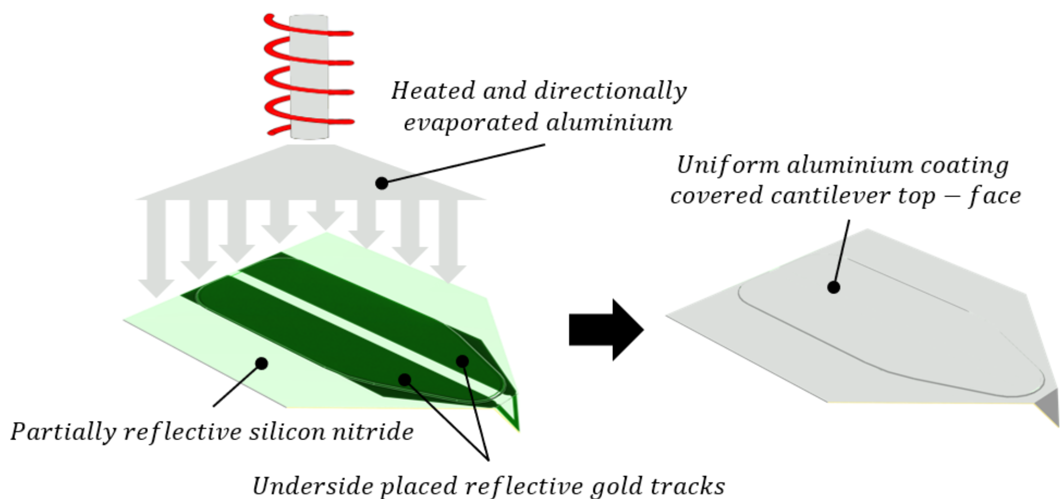

Figure 109. Schematic representation of the directionally coated cantilever by physical aluminium vapour deposition process.

Table 21. Investigated modified AFM cantilever probe elastic interaction gradients in instrumentation native relative strain expression and the approximated SI unit expression. The percentage change is the result of elasticity magnitude comparison against unmodified structures characterised in previous section.

	Probe 1	**Probe 2**	**Probe 3**	**Probe 4**	**Probe 5**
d[dR/Rabs]/dt, load, $s^{-1}\times10^{-10}$	11.18	7.636	11.15	11.01	8.238
d[dR/Rabs]/dt, unload, $s^{-1}\times10^{-10}$	10.91	8.393	11.16	10.48	8.140
d[dR/Rabs]/dt, average, $s^{-1}\times10^{-10}$	11.05	8.015	11.16	10.75	8.189
$k_{interaction}$, load, N m^{-1}	0.1549	0.1058	0.1544	0.1525	0.1141
$k_{interaction}$, unload, N m^{-1}	0.1511	0.1163	0.1546	0.1452	0.1128
$k_{interaction}$, average, N m^{-1}	0.1530	0.1110	0.1545	0.1488	0.1134
k_{AFM_Al}, load, N m^{-1}	0.424	0.187	0.421	0.407	0.214
k_{AFM_AL}, unload, N m^{-1}	0.397	0.222	0.421	0.358	0.210
k_{AFM_Al}, average, N m^{-1}	0.410	0.204	0.421	0.383	0.212
k_{AFM}, average, N m^{-1} (no al, Table 17)	0.337	0.190	0.389	0.350	0.173
Change: dk_{AFM}, average, %	+21.8	+7.57	+8.31	+9.30	+22.5

A theoretical expression of the anticipated elasticity change may be calculated using the Eulerean cantilever bending expression (Eq. 22) solved with the moment of inertia for a rectangular cross-section (Eq. 22, repeated below for clarity). This dictates that a cubed cross-section thickness (t) to stiffness (k) relationship $(k \sim t^3)$ is present in uniform composition cantilever beams. The unmodified structure thickness is stated in the manufacturer specification sheet (400 nm), allowing for a rough conclusion that the 20 nm addition increases the cross-section thickness to 5%, resulting in a stiffness increase of 15.76%. However, this estimation disregards the geometric non uniformity, stresses and variation in material elastic moduli through the cross-section and is therefore only provided as guidance illustrating that such a change may typically fall outside the advertised tolerance and repeatability of some of the conventional methods reviewed previously [112].

$$I_{rectangle} = \int_{-\frac{t}{2}}^{\frac{t}{2}} wz^2 dz = w\left[\frac{z^3}{3}\right]_{-\frac{t}{2}}^{\frac{t}{2}} = \frac{wt^3}{12}; \qquad Eq.\ 22$$

The MEMS instrumentation provided post aluminium coating values showing a consistent stiffness increase when compared to the pre-deposition structures, a behaviour in alignment with structural mechanics theory - increase in bending resisting cross sectional area. The degree of variation in the relative elasticity increase was large – between 7.57 % and 22.5 %, however it agreed well to the analytically expected increase value – an average of 13.9 % across all structures. It is unlikely that this variation is due to inconsistent deposition parameters since all of the structures were coated simultaneously and any placement effects within the evaporation chamber are considered to be insignificant in comparison - as witnessed previously when employing the tool for analogous process in 4.5.3. It is therefore attributed to positioning errors in the contact point between AFM probe and the MEMS device, something that could be reduced by employing a higher-resolution AFM camera system. Furthermore, the consistent trend of increased elasticity when compared to the pre-modification values reassures the measurement detected the subtle structural changes – e.g. the contrast of Probe 1 load elasticity behaviour change shown in Figure 110. Whilst small AFM elasticity changes may also be detected by the passive calibrated reference spring method, the previously witnessed photodiode artefacts and changed reflection conditions mean that linear fitting and comparison of pre and post data could result in deviations which are similar to or exceed the variation introduced by the modification. Dynamic behaviour ‘before and after’ comparisons may also be obscured by the addition of mass and surface stresses, meaning the demonstrated static physical interaction should be theoretically the best representation of the probe modifications effect on real-world performance.

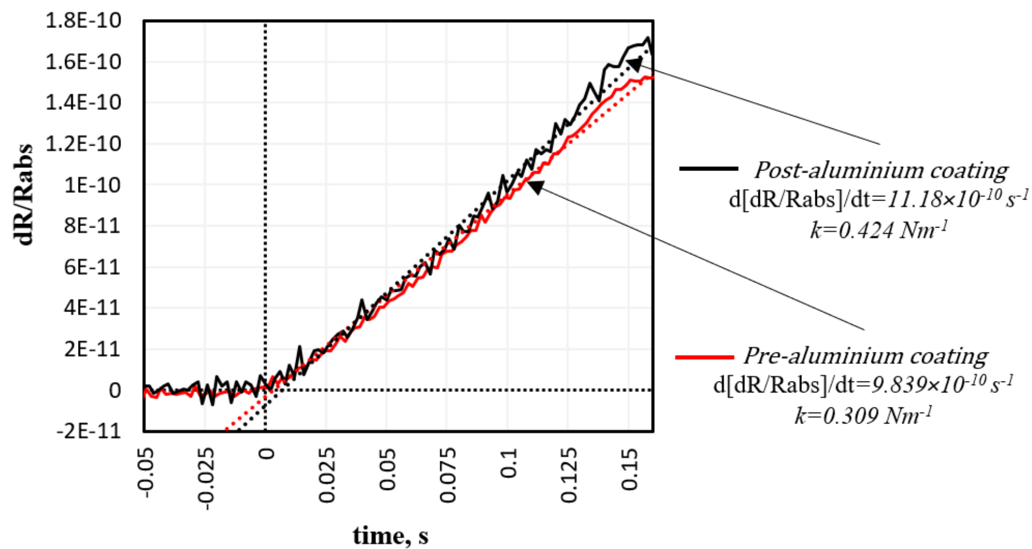

Figure 110. MEMS captured load gradient comparison of the Probe 1 structure before and after structural modification by aluminium thin film deposition.

6.3 Complex AFM probe characterisation

The exploration of MEMS device application was then extended to assessing the spring constant of some conventional AFM probes and obtaining elastic characterisation profiles of some complex and non-linear elasticity structures that cannot be sufficiently described by the conventionally used single scalar value elasticity modulus expressions.

6.3.1 Non-linear elasticity AFM probe characterisation

Continuing efforts to develop AFM based functionalised sensing often result in structurally complex probes that challenge conventional elasticity and force measurement techniques. To illustrate this, the MEMS device was employed to characterise a highly specialised and unorthodox prototype AFM cantilever structures[14]. This probe was designed to have two isolated tips, one acting as a heat source, the other a thermometer which could be used to probe thermal conductivity at the nanoscale [214]. This probe was expected to show non-linear elastic behaviour due to the presence of two, vastly differing cantilever beams (Figure 111). Currently, no conventional, optical lever equipped AFM system supports in-situ elasticity characterisation of this probe. This is because optical lever systems rely in displacement detection through cantilever movement, from which the force exerted at the tip is inferred.

[14] Structure supplied and investigated by permission from Y. Zhang, P. S. Dobson and J. M. R. Weaver from the AFM and Hyperlithoraphy group at Glasgow University.

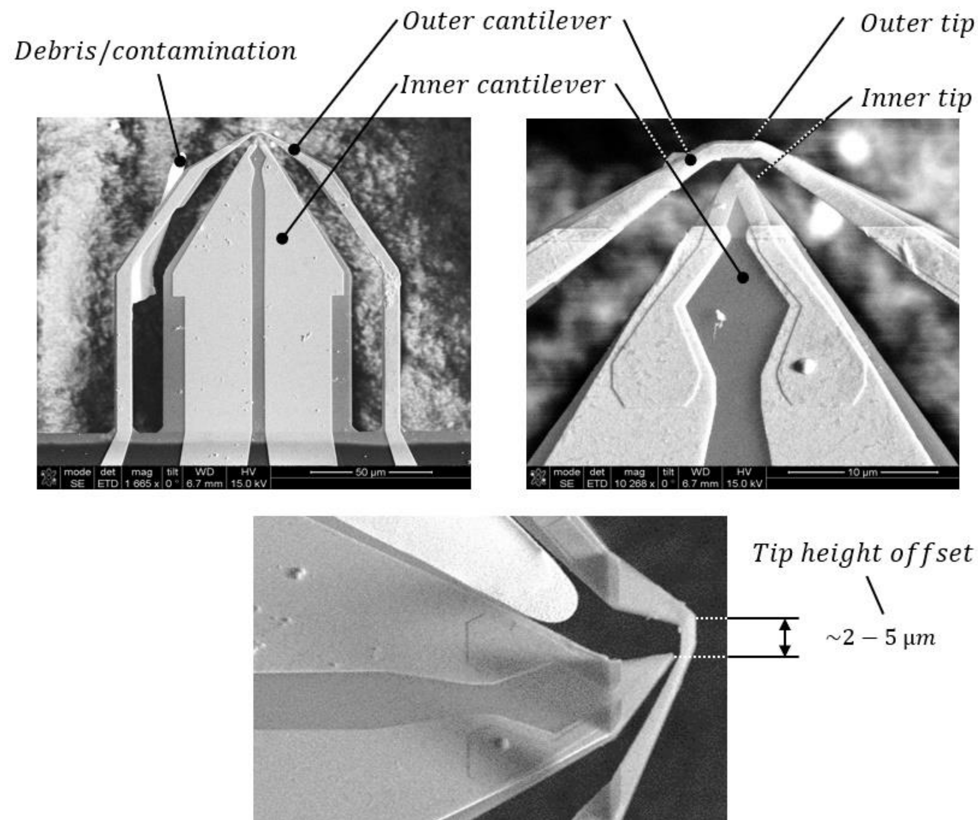

Figure 111. The dual cantilever functionalised AFM probe equipped with two individual tip located sensors (SEM) - an example of non-uniform elastic behaviour exhibiting AFM cantilever. The highlighted offset between relative tip heights results in distinct, vertical displacement dependant engagement properties.

Conventional single point detection methods are unsuited to this multi-cantilever probe, since the planar surface area offered by the thin outer beam is insufficient for a detectable laser reflection. To study this probe, a cyclic indentation sequence was performed on the MEMS device loading site and the resultant strain/force versus time plot shown in Figure 112. The resultant interaction profile displays a distinct and repeated step change in gradient visible at the halfway point in both load and unload directions, indicating the anticipated change in elastic behaviour. This sudden increase in elasticity can be attributed to the second elastic structure contacting the MEMS sensor and exerting an additional load contribution. This occurs at the same displacement rate as the first cantilever due to the

shared vertical actuation. The resultant interaction may be understood using springs in parallel analogy as shown in Figure 113 and Eq. 45, where the combined elastic component is the sum of each individual spring elasticity. This two-variable relationship may be resolved with knowledge of the outer and combined elasticity magnitudes provided by the single MEMS device measurement.

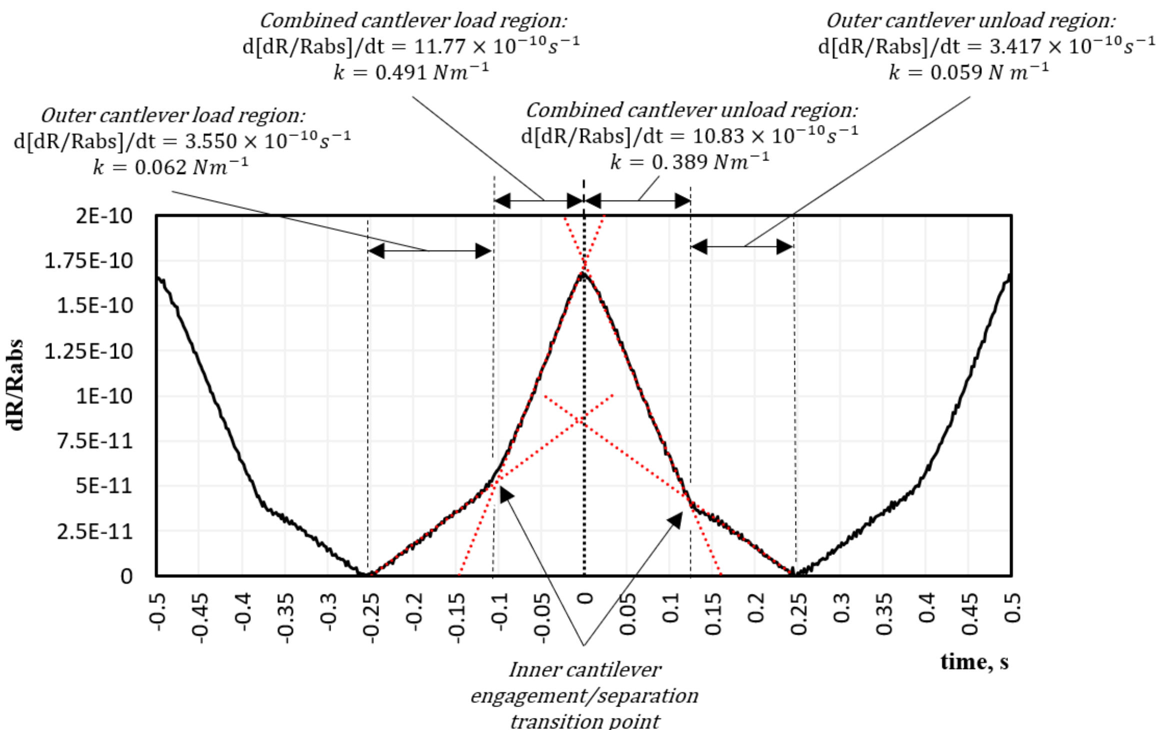

Figure 112. MEMS captured elasticity characterisation plot, displaying the discrete elasticity gradient change throughout the interaction, caused by load transfer via second engaged tip. NB. the outer cantilever does not separate from the MEMS device in the presented interaction, therefore its adhesion properties are not visible.

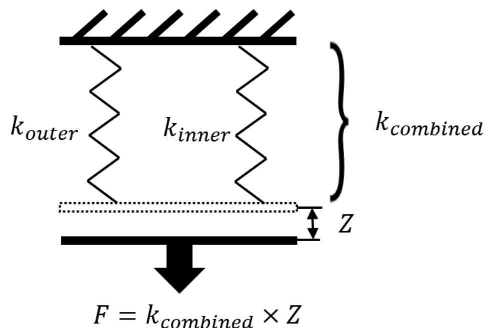

Figure 113. Springs in parallel analogy used to represent the two varied elasticity structures (k_{outer} and k_{inner} cantilever), which act as a compound system with its own elasticity constant ($k_{combined}$), when exposed to system wide force and displacement.

$$k_{combined} = k_{outer} + k_{inner} \qquad \textit{Eq. 45}$$

A single indentation cycle of the in-situ interaction provides further insight into the elasticity exchange parameters between the structures. The plot of the first order rate of change profile – expressed as the interaction elasticity (Figure 114), clearly shows the displacement dependant elasticity magnitude, as well as the engagement and disengagement rates. For example, the loading region elasticity change has a gradual transition to the seven-fold elasticity increase, as compared to the more abrupt transition of the unload region. Such behaviour is attributed to the differing modes of contact formation and breaking – the gradual approach caused repulsive engagement in loading versus a sudden, snap-out separation that occurs in unloading. This is analogous to the commonly witnessed tip-sample adhesion/separation profile differences in conventionally observed AFM cantilever force-distance curves.

Finally, the individual elasticities of each cantilever beam could be resolved and are summarised in Table 22. An elasticity magnitude of 0.376 N m^{-1} for the inner (wider) beam is within expectations due to its geometrical and composition similarity to the previously investigated SThM probe structures. The elasticity of the outer beam of 0.06 N m^{-1} is also

within expectations due to its much smaller cross-sectional area when compared to the stiffer structure. Additionally, elasticity magnitude of the latter structure is at or near the compliance limit of commercially available AFM cantilevers (to be introduced in 6.3.3), indicating that the MEMS tool is capable of characterising an extremely wide range of elasticities making it suitable for the characterisation of most AFM probes.

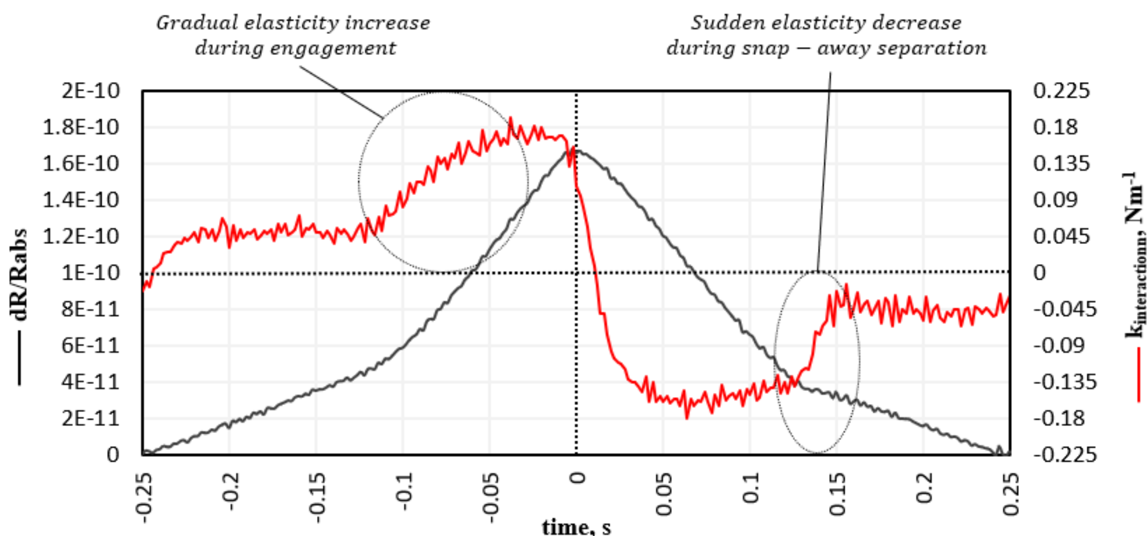

Figure 114. The elasticity profile plotted with the rate of change gradient – or displacement specific elasticity. Differences in rates of elasticity value change is distinct in load and unload regions. The elasticity sign change corresponds the loading direction – positive for load/approach, negative for unload/retract.

Table 22. Elasticity gradient summary, detailing the measured outer and mutual (both) cantilever elasticities. A subtraction operation allows to apply springs in parallel analogy and determine the inner elasticity gradient and constant.

	Combined	Outer	Inner Cantilever = Combined – Outer
d[dR/Rabs]/dt, load, $s^{-1}\times10^{-10}$	11.77	3.550	8.220
d[dR/Rabs]/dt, unload, $s^{-1}\times10^{-10}$	10.83	3.417	7.413
d[dR/Rabs]/dt, average, $s^{-1}\times10^{-10}$	11.30	3.484	7.817
$k_{interaction}$, load, N m^{-1}	0.1630	0.0492	0.1139
$k_{interaction}$, unload, N m^{-1}	0.1500	0.0473	0.1027
$k_{interaction}$, average, N m^{-1}	0.1565	0.0483	0.1083
k_{AFM}, load, N m^{-1}	0.4913	0.0616	0.4297
k_{AFM}, unload, N m^{-1}	0.3894	0.0587	0.3307
k_{AFM}, average, N m^{-1}	0.437	0.060	0.376

6.3.2 Additional complex composition probe characterisation

Some other prototype SThM probe structures with suspected non-linear properties were also characterised using the MEMS tool.

A set of two investigated structures were in-development thermal microscopy AFM probes with different geometry near tip cut-outs, designed for thermal mass reduction and heat dissipation optimisation (detailed in [163]). The through-cuts in the silicon nitride tip/cantilever result in a truss-like structure connecting the sensor to the remainder of the cantilever (Figure 115). The anticipated elastic behaviour is that the major carrier structure is more rigid and the tip region - is less, therefore the tips may ‘collapse’ or adhere to the scanned surface, thus exhibiting non-linear engagement and disengagement elastic behaviour. Nonetheless, the actual elasticity profiles obtained using the MEMS device exhibited highly linear behaviour, with differences in magnitude attributed to fabrication variations - e.g. the unintentionally present silicon support at the cantilever underside. This suggests that the tip area is in fact much more rigid than the remainder of the cantilever. This is supported by a simple, yet not necessarily instantly obvious conclusion - the inverse cube length to elasticity relationship ($k \sim L^{-3}$, detailed earlier in 5.1.3), meaning the much shorter tip can indeed be stiffer than the remainder of the cantilever, even with the drastically reduced cross-section volume.

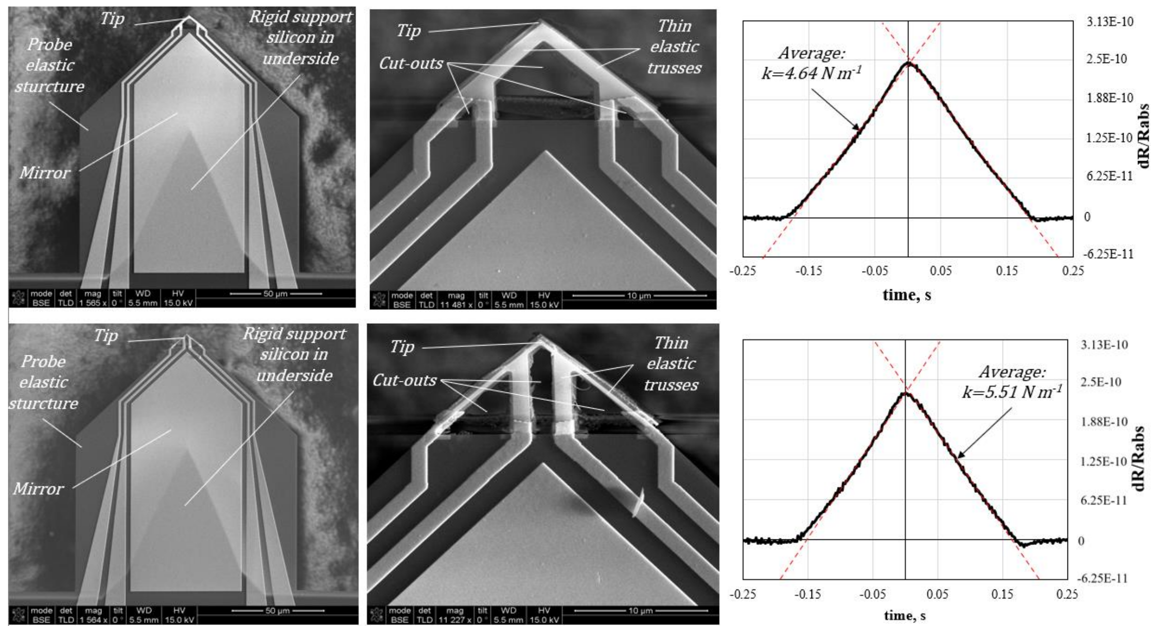

Figure 115. Prototype thermal AFM (SThM) probes with two different style cut-outs (top and bottom) - structures provided by Dr. Rory Lambert, AFM and Hyperlithography Group, Glasgow [53].

Another curious structure was investigated in supplement to the earlier study - a triple-cantilever SThM probe. The structure was equipped with three discrete complex composition cantilevers (Figure 116) – one major structure at the centre and thinner members placed symmetrically outside the main structure. The tips of each are at offset width wise but are of equal height, if compared to the structure described in Figure 111. This composition yielded a unique indentation behaviour, where a distinctly two-step engagement occured (k_1 and k_2) and a singular (constant) disengagement ($k_3 \sim k_2$). This may be challenging to predict, since a three-step engagement and disengagement may make the most sense. However, it appears that the thin members engage almost simultaneously and are only then followed by the major member engagement, while their combined elasticity is maintained until a complete separation from MEMS device occurs. The separation region behaviour is also interesting, as it displays a two-step interaction, likely the result of external and internal members disengaging at separate times. Therefore, the

full interaction elasticity characterisation is once more proven as a useful feature that can define complex AFM probe behaviour beyond the singular elasticity modulus.

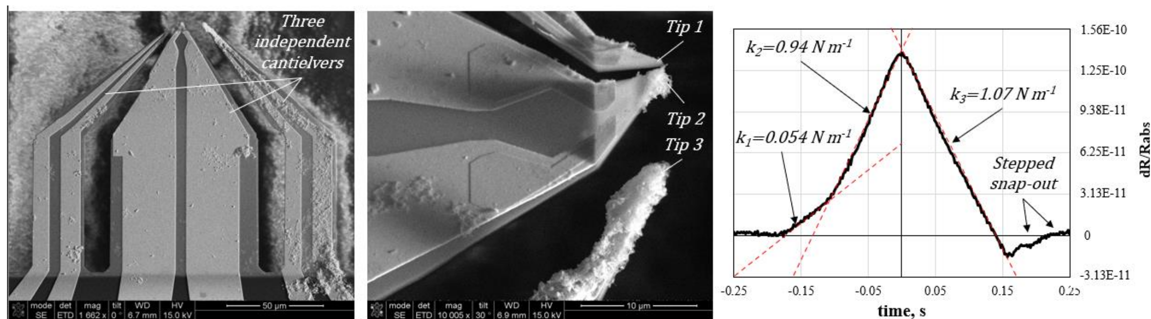

Figure 116. Triple cantilever prototype AFM (SThM) probe with its elasticity profile, showcasing asymmetric engagement and disengagement behaviour. Structures provided by Dr. Yuan Zhang, AFM and Hyperlithography Group, Glasgow [53].

Chapter 7 - Conclusions and future work

7.1 Conclusions

In its most common manifestations, AFM provides users with a highly sensitive tool for monitoring the interaction between a nano-scale tip and a surface by using beam deflection and a simple and inexpensive optical system. As a result - it can produce remarkably high-resolution topography imaging. However, that excellent sensitivity is not matched by AFM's accuracy in force measurements. This is due to the fact that interpretation of the cantilever's deflection as a direct measure of applied force relies on understanding the AFM probe's elastic behaviour. Elasticity characterisation of a complex AFM probe is a challenging endeavour. Existing techniques have been demonstrated to produce good estimates for probes made from a single material having a simple shape, however those that deviate strongly from idealised models are poorly represented. This is combined with the fact that the complexity of SPM probes and their functionalisation by compositional or structural modification is constantly increasing. These developments present a need for an accessible, in-situ elasticity determination method, which can support the complex composition AFM probes. The work in this thesis uncovered the invested research effort into a suitable solution in the form of of a microfabricated MEMS device. The device consisted of a high-resolution, e-beam lithography defined, metal wire strained conductor that was fabricated on a load strained beam appropriately sized for in-operation interaction within an AFM. The instrumentation's simplicity, potential for operational sensitivity and consistent wafer scale manufacturability of the device compared favourably to capacitive

and piezoresistive alternatives, combined with the fact that it could be realised using standard cleanroom procedures.

The successful fabrication of a highly strained sensing device with a low spring constant was the result of design and processing optimisations in several crucial areas. Confidence in finite element methods developed by comparisons with experimental observations allowed the design of the device to deviate from idealised and simplistic cantilever structures and the use of geometrical optimisations in response to the observed fabrication limitations. These included rotated fixed-end boundaries for wet etching and stress raiser mitigating radii, which were adopted whilst maintaining a complete picture of the anticipated structural behaviour. An optimised polymer-only etch mask was demonstrated to be satisfactory for the through-silicon nitride film etch, without the metal masking traditionally employed, resulting in reduced fabrication complexity. Significant effort was focused on addressing the causes of failure witnessed in-processing. Two particularly significant causes were metal stress and collapse of structures due to capillary forces on drying. These were remedied through the development of a low stress PVD metal deposition process and refining the drying practices used for these fragile structures.

The importance of considering complex structures at the system level and in the context of their operating environment was highlighted in the observation of device thermal behaviour. Metal film strain sensors have the beneficial property of linear variation of resistance with temperature. This relationship was characterised on rigid and flexible surfaces, capturing the drastically different behaviour in these two cases. Characterisation of the mode relevant to the operation of the sensor, that of conductor placed on a flexible

surface, allowed the identification and quantification of the effects and artefacts caused by stray light from the AFM laser and optical microscope illumination source.

The interaction of the MEMS device within an AFM environment with a probe having known characteristics proved the ability of the device to perform rapid, high-resolution force and force rate measurements, allowing for capture of the probe elastic character. In this work, it was also used as a demonstration of a convenient and readily transferrable calibration procedure. The device force calibration procedure is also supportive of alternative approaches that may benefit from improved accuracy and traceability such as calibration against indenters and force balances. The MEMS device was then utilised to scrutinise a broad range of AFM probes of extreme complexity, providing continuous resolution of their mechanical behaviour throughout the force-distance ramp interaction. The demonstrated ability of the system to characterise structures in the 0.06 - 8.18 N m^{-1} range at sub 10 nN resolution captures the broad application range of this tool configuration. Finally, the novel insights provided into the behaviour of multi-cantilever sensing probes may be considered as the ultimate demonstration of the tool’s indiscriminate functionality for probe mechanical assessment.

It can therefore be concluded that the objective of this work, that of the mechanical behaviour characterisation of complex AFM probes, was achieved by the demonstrated MEMS device in relative probe elasticity measurements. However, the goal of absolute force or elasticity measurements, traceable to a metrological standard was not achieved due to sensitivity limitations in the available equipment and lack of access to alternative calibration options, although this does not represent a fundamental limitation of the hardware developed. Nevertheless, the demonstrated precision, range and resolution of the

system, combined with the low-cost batch friendly production methods used to fabricate the sensor form an attractive proposition for AFM probe characterisation to AFM probe manufacturers and users alike. In terms of metrological integrity, the system may be placed somewhere between the convenient in-situ calibrated spring grid and the metrologically more competent but inconvenient ex-situ force meters and nano-indenters. As the tool incorporates an independent force sensor which is not reliant on the AFM beam deflection system and is sensibly independent of its influence it may be used freely in any AFM, regardless of the force sensing mechanism or environment.

7.2 Future work

As is normal in a PhD project, many more relevant research and development venues could have been explored beyond those described. In order to make the most of the developed system the focus of this work was placed on demonstrating the capability of the tool in real-world applications. This resulted in comparative neglect of work in determination of the measurement uncertainty. Further work on uncertainty characterisation could develop the described MEMS technology from a relative to an absolute force measurement instrument, giving it metrological credibility. This would require access to a compatible tool within the SI measurement chain and would most likely necessitate collaborative effort with a national measurement institute. While the effects of environmental thermal changes were characterised, experimental quantification of other anticipated sources of uncertainty was cut short by the 2020s pandemic. These sources, including variance in electronic instrumentation, data capture and fitting procedures, transduction constants and contact point positioning errors could be accounted for in full with the current setup, if provided with additional experimental time.

A simple application modification to the current device would transform it into a tribological AFM tip-sample study tool. The MEMS device is quite insensitive to lateral load location, estimated by FE methods to be 0.12 % sensitivity change in elasticity over a 10 µm scan line, as shown in Figure 117. Therefore, a matrix array of tribologically interesting films could be deposited in a segmented fashion shown in Figure 118. The adhesion properties of exposed materials, which are directly related to the change of strain during lateral contact mode scanning could therefore be investigated with the MEMS

device. An electrically active resistive sensor device (SThM probe) having similar composition to the current device has been recently demonstrated [164] to operate under aqueous solution, introducing another potential class of surface science studies under varied media that could be enabled by this easy to use tool.

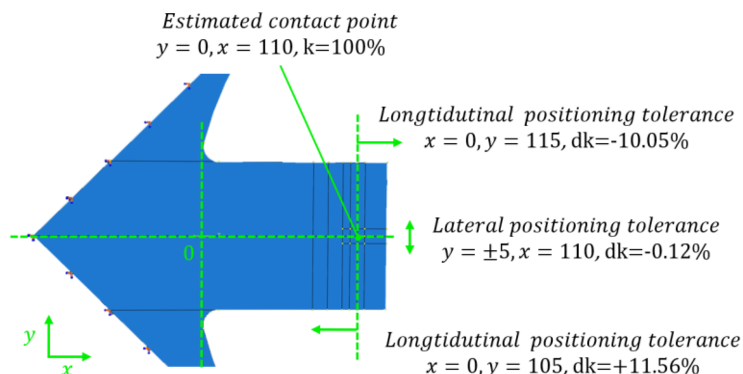

Figure 117. FEA contact point study results highlighting the ±5 µm positionality effect on the relative elasticity (k) at and around the perceived contact point.

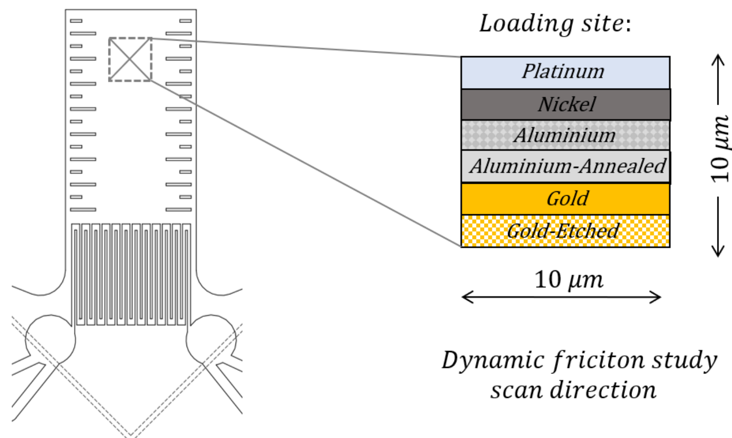

Figure 118. Lateral friction force investigation configuration of the MEMS force device.

A double side clamped beam arrangement for AFM elasticity measurement should also be explored. For the current sensor, the biggest sources of error are believed to arise from the significant longitudinal positioning errors, also shown in Figure 117 , which directly affect the interpretation accuracy of the point load on the measured beam displacement. Whilst guiding markers and good optics on an AFM system help mitigate some of this variance, its existence prevents achievement of the highest possible accuracy. A possible solution

would be careful scanning of the MEMS sensor by the AFM probe under test to locate the ideal position for measurement, which runs counter to the requirement for a quick and easy to use solution. A double end clamped beam, theoretically, would be highly insensitive to load positioning at its centre location. FE trials indicate that a 10 by 10 μm landing pad at the centre of the beam experiences a 0.4 % sensitivity caused by uncertainty in the location of the load within the plane, which is far superior to that of an equivalent cantilever (~ 20% or 50 times worse, per Figure 118). Additionally, the strained sensor quantity may be doubled – by placing one sensor at each side, increasing the sensitivity without additional fabrication complexity and allowing the use of a double bridge which would also confer linearity of bridge measurement of resistance change. The strain response to load is significantly reduced, however, amounting to about $1/11^{th}$ of the value provided by the single end cantilever (8.8%, as determined by study in chapter 3, Figure 24), but this may be compensated in part by employing higher density (but more fragile) strain gauges. Furthermore, such a beam could be made much thinner to increase sensitivity, without suffering the differential expansion bending and stiction failures described in 4.5.3. Fabrication of such device is the same as that used for the introduced MEMS tool - simply involving joining the dual opposing cantilevers in the dry etch step masking, as shown in the preliminary experiment shown in Figure 119.

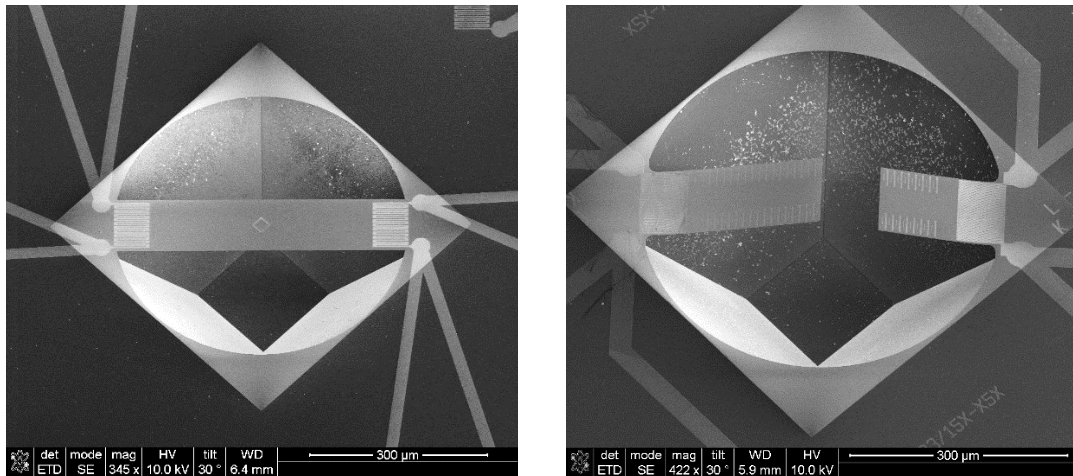

Figure 119. Double clamped beam configuration, next to the analogously fabricated single clamped dual cantilevers.

While a fabricated prototype following this concept was able to detect forces exerted by stiffer AFM probes (>1 μN range), it did not receive further investigation since its strain (and hence resistance) response to load was no longer linear with applied load. As a result, the output of the sensor was impossible to quantify without suitable characterisation involving high-resolution signal to load-displacement mapping. As suitable indentation equipment and/or calibration path was not identified during this project, further investigations related to the double clamped structure application were not undertaken. The author anticipates that, subject to sufficient calibration and development efforts, this configuration would provide significantly improved positional insensitivity in measurements of elasticity and force.

If more removed opportunities are to be discussed, the demonstrated high density metal film strain gauge sensor should be considered for integration on an actual AFM cantilever. This could enable non-silicon based self-sensing probes that would provide desirable design freedom (such as insensitivity to optical illumination or temperature) and a reduced cost solution, when compared to existing conventional self-sensing piezoresistive

cantilevers. Such features may prove extremely desirable in SThM and microfluidic probes, where the independent, high resolution and thermally unobtrusive monitoring of contact force would be of great significance and in the production of extremely compact AFM-based microscopes where the lack of any need for a large optical system and its alignment would be compelling.

Appendix A - MEMS Instrumentation Schematic

The resistance bridge circuit was designed to filter and amplify the output from a high impedance 4-terminal resistive MEMS sensor having large lead resistances. The instrumentation assembly contained the signal processing board (Figure A-1) and the power supply unit (Figure A-2) which were designed and developed by Prof. Jonathan M. R. Weaver of AFM and Hyperlithography Group. The key component functions are described as follows:

Constant current biasing of the balance resistor (A4 and A3/2) and the MEMS sensor using A3/1 and A2, along with active establishment of ground potential at the low end of the sensor by A1/2 allows for 4-terminal measurement without the need for explicit matching of lead resistances. A6/1 and A6/2 have low input bias current and are used to buffer the input of instrumentation amplifier A5 since the MEMS device has a high resistance (100 kΩ- 1 MΩ range). A1/1 sets the equal currents going through sensor and the MEMS device, and A5 amplifies the difference between the voltages across the balance resistor and MEMS sensor. A7/1 suppresses the ground loops when connecting the output of A5 to the rest of the system. A7/2 buffers the output of the passive 50 Hz twin-T notch filter.

The instrumentation is powered by a low noise power circuit supplied by two 12 V lead acid batteries, and all components are contained in a screened metal enclosure.

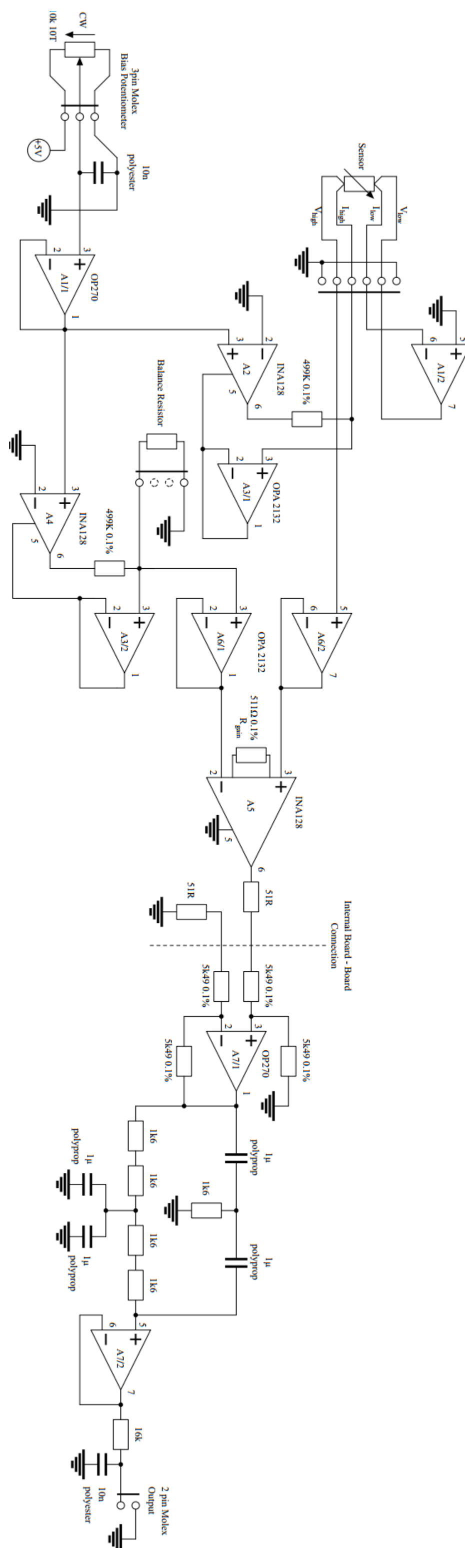

Figure A-1. Instrumentation schematic, showcasing the four-terminal sensor input and amplified and filtered bridge output (designed and drawn by J.M.R Weaver).

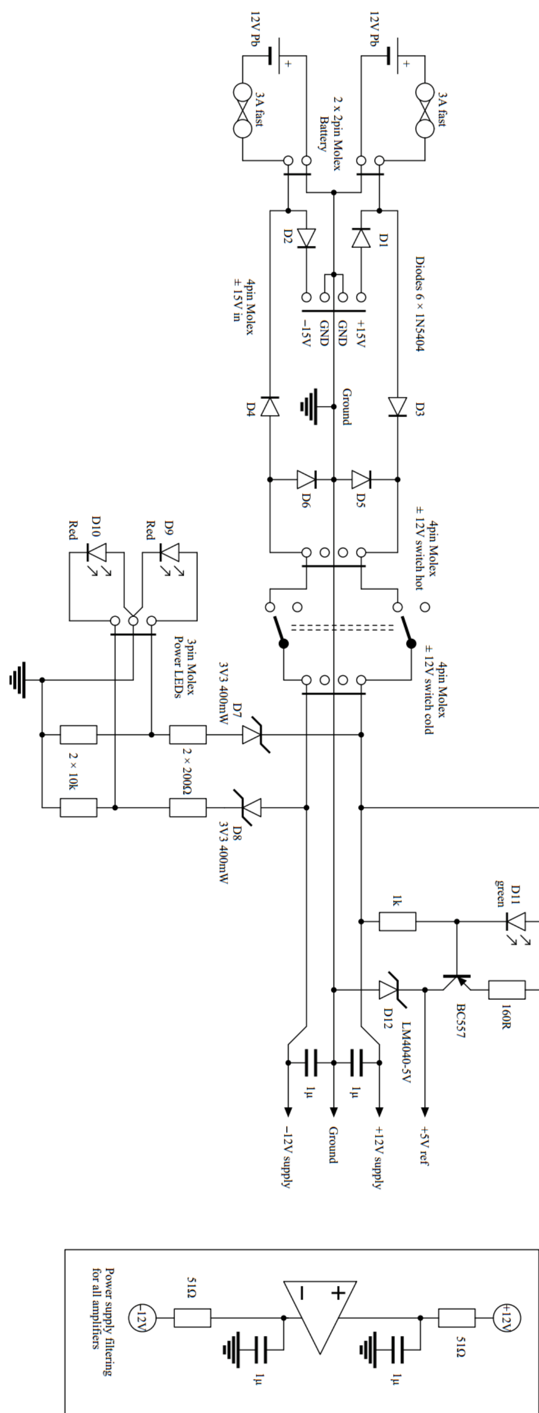

Figure A-2. Instrumentation power supply circuit for the 2x12V lead-acid battery supply, contained in the enclosure (designed and drawn by J.M.R Weaver).

Appendix B - MEMS Device Fabrication Process Details

The microfabrication of the conceived MEMS system consists of 10 distinct steps, grouped into two lithography and metallisation layers for alignment marker and sensor definition, followed by lithography and dry etching layer for elastic structure definition and completed by the wet etching step releasing the instrumented cantilever from underlying substrate.

Process Table 1. Marker layer fabrication.

1. Mask creation:
   - 1.1. Mask material deposition no. 1: Allresist PMMA, AR-P 632.06, thickness: 100 nm, mol. weight: 50 kg mol^{-1}, 60 s spin at 4000 rpm; Oven bake at 180 °C, 30 mins.
   - 1.2. Mask material deposition no. 2: PMMA, AR-P 679.01, thickness 30 nm, mol. weight: 950 kg mol^{-1}, 30 s spin at 5000 rpm. Oven bake at 180 °C, 30 mins.
   - 1.3. Mask pattern writing: electron-beam vector job, Vistec VB6.
   - 1.4. Mask development: Development in MIBK and IPA solution (2.5:1), 25 s, 23 °C, stopped in IPA, rinsed in RO water and dried with Nitrogen.
2. Metal deposition with PVD tool (Plassys):
   - 2.1. Nichrome evaporated on substrate, at 0.4 nm s^{-1} rate for 10 nm total thickness.
   - 2.2. Gold evaporated on substrate, at 0.4 nm s^{-1} rate for 75 nm thickness.
3. Lift off: metallised pattern reveal by dissolving the underlying mask in acetone, 30 minutes at 50 °C.

Process Table 2. Sensor layer fabrication.

1. Mask creation (PMMA and VB6):
   1.1. Mask material deposition no. 1: Allresist PMMA AR-P 632.06, thickness: 100 nm, mol. weight: 50 kg mol^{-1}, 60 s spin at 4000 rpm; Oven bake at 180 °C, 30 mins.
   1.2. Mask material deposition no. 2: Allresist PMMA AR-P 679.01, thickness 30 nm, mol. weight: 950 kg mol^{-1}, 30 s spin at 5000 rpm. Oven bake at 180 °C, 30 mins.
   1.3. Mask pattern writing: electron-beam vector job, Vistec VB6.
   1.4. Mask development: Development in MIBK and IPA solution (2.5:1), 25 s, 23 °C, stopped in IPA, rinsed in RO water and dried with Nitrogen.
2. Metal deposition with PVD tool (Plassys):
   2.1. Titanium evaporation with blanked substrate for 60 seconds to decrease chamber pressure.
   2.2. Nichrome evaporation with blanked substrate for 60 seconds to condition crucible and remove oxidation and foreign contaminants before depositing on substrate.
   2.3. Nichrome evaporated on substrate, at 0.04 nm s^{-1} rate for 30 nm thickness.
3. Lift off: metallised pattern revealed by dissolving the underlying mask in acetone, 120 minutes at 50 °C.

Process Table 3. Beam and etch pit mask definition on Silicon Nitride.

4. Mask creation:
   4.1. Mask material deposition: Allresist PMMA AR-P 642.15, thickness: 1260 nm, mol. weight: 200 kg mol^{-1}, 60 s spin at 4000 rpm; Oven bake at 180 °C, 30 min.
   4.2. Mask pattern writing: electron-beam vector job, Vistec VB6.
   4.3. Mask development: Development in MIBK and IPA solution (2.5:1), 25 s, 23 °C, stopped in IPA, rinsed in RO water and dried with Nitrogen.
5. Plasma etch:
   5.1. Oxygen plasma clean. Oxford RIE 80 Plus. Gas – O_2 (Oxygen) at 6.5 Pa, 20 °C and 50 W plasma power. A 30 second etch to remove surface contaminants.
   5.2. Masked Silicon Nitride etch. Oxford RIE 80 Plus. Gas - C_2F_6 (Halocarbon R116) at 2.0 Pa, 20 °C and 125 W plasma power. Experimentally obtained Allresist mask etch rate of 40-43 nms^{-1} and Silicon Nitride etch rate of 19-21 nm s^{-1}. A 21-minute run to clear the nitride in the supplied substrate.
   5.3. Solvent clean (acetone, methanol, IPA), rinsed in RO water and dried with Nitrogen.

Process Table 4. Elastic structure release.

6. Etching in temperature-controlled solution: 29% Water-KOH (Potassium Hydroxide) at 105 °C for 70 minutes (solution etch rate for silicon - 4-4.2 µm per minute).
7. Drying:
   7.1. Acid (partial) neutralisation - in still RO water for 15 minutes, then wetted transfer to methanol, where the sample is removed from holder jig and remain submerged for 10 minutes.
   7.2. Drying - very gentle and slow Nitrogen drying for 10-15 minutes until all etch pits cleared of liquid (5 minutes).

List of Figures

Figure 1. AFM system photograph, highlighting external composition, Bruker Dimension Icon AFM [25]. 12

Figure 2. Photograph highlighting components composing the core of the AFM system, Bruker Dimension Icon AFM [25]........ 13

Figure 3. Representation of the AFM tip and sample interaction arrangement, highlighting the common AFM cantilever displacement detection options and interacting components........ 17

Figure 4. Software reconstructed plot of the scanned topography. The z-axis is proportional to cantilever deflection. Topography data courtesy of Hao Xu [53] of AFM and Hyperlithography Group, University of Glasgow. 17

Figure 5. Force-distance curve obtained by optical lever AFM plotting retracting cantilever bend versus its z-axis displacement, noting the distinct probe-sample interaction and force exchange regions........ 18

Figure 6. Publication volume of the AFM sub-fields by keyword phrases, according to Web of Science index [66]........ 21

Figure 7. Batch produced Veeco MPP-21100-W probes, wafer no 2149 (left) and close-up, highlighting of the ‘pop-out’ style probe retention and release features on the microfabricated probe wafer (right). 33

Figure 8. The schematic representation of the investigated AFM cantilever geometrical composition........ 33

Figure 9. The full range (1-100 kHz, bandwidth - 7.63 Hz) acquired Thermal Tune Power Spectrum Density capture for the Veeco MPP-21100-W cantilever........ 37

Figure 10. Lorentzian fit (solid line) over the raw signal (dotted line) of the cantilever natural resonance shape over the investigated frequency span. 38

Figure 11. Thermal tune obtained <z^2> integral variation density, indicating a natural distribution. 39

Figure 12. Spring on spring experimental schematic, depicting the soft interaction (S_{soft}) force-distance ramp and variable, figure inspired by Gates et al. [96] description. 44

Figure 13. Tested cantilever positioned to interact in ramp mode with the bulk silicon surface (left) and reference spring (right), obtaining the S_{soft} and S_{hard} values. 45

Figure 14. Veeco RFESPW probe f-d ramp engagement approach region on solid ($Shard$) and CLFC calibrated spring ($Ssoft$). The difference in curve steepness allows to relate curve gradient ratios to the known interaction elasticity of the calibrated spring. 46

Figure 15. The nanoindenter with mounted sample (AFM probe not pictured). 50

Figure 16. The nanoindenter tip displacing the AFM cantilever, captured at maximal indenter displacement. 52

Figure 17. Indenter registered force-distance signals for the 9 tested contact positions. The offset specific elasticities (indicated in microns in k bracket value) resolved by derivation of the linear fit of the interaction region in N m^{-1} units. 53

Figure 18. Offset to inverse elasticity, indicating the resistance to bend relationship plot, showing the third power fit line and the extrapolated calculation point at the tip offset value (k^{-1} expressed in units of m N^{-1}). 55

Figure 19. An ellipse shaped solid body (a) subjected to external loads (b) that result in body deformations. 60

Figure 20. External forces applied on a solid body are distributed internally as normal and shear stress vectors (σ), marked with their indicated directions, which form the tensor element description. 61

Figure 21. Force induced elastic uniaxial deformation of a solid structure allowing for the corresponding lateral and longitudinal strain resolution. 62

Figure 22. Stress and strain relationship example. For isotropic, elastically deforming structure, the relationship between directional stress and strain is described in elastic deformation region governed by the proportionality limit. 64

Figure 23. Perpendicular load induced deformation of a cantilever beam.......... 64

Figure 24. Deformable mechanical structures in red and displayed fixed planes in blue. The load point (black arrow) is responsible for the induced deformation response of the showcased structures: a) single fixed end beam (cantilever); b) double fixed end beam; c) three end fixed beam; d) four end fixed beam (membrane). 65

Figure 25. Unit load applied at maximal strain inducing locations (see Figure 24) comparing the surface strains of different degree of freedom beams (FEA, Abaqus). The structures have a width and length ratio of 1:1, and length to thickness ratio of 100:1. Graph scaled to 100% in vertical axis – as determined by value of maximal strain on a single clamped cantilever under unit load. The arrow values indicate comparative percentage of maximal surface strain, as compared to single end clamped beam -cantilever. 66

Figure 26. Cross-sectional representation of force directions as induced by orthogonal concentrated force in a rectangular cantilever (left) and of second moment of inertia defining variables and neutral axes y and z (right).......... 67

Figure 27. Depiction of cantilever beam structural variables. 68

Figure 28. Cantilever dimensions summarised on an isometric capture of the investigated AFM cantilever (dimensions are angle compensated, SEM). 70

Figure 29. Planar image showing the two distinct width boundaries resulting from the tapered cross-section (optical microscope). 71

Figure 30. Finite Element Analysis representation of the loaded AFM cantilever. NB: 1) Geometry dimensions in micrometres. 2) Part symmetrical along its length. 3) The deformed model visualization scale is hyperbolized by a factor of 150. 78

Figure 31. Capacitive MEMS load sensor cross-sectioned examples – a) pressure sensors (diaphragm configuration), b) microphone acoustic structures (open surfaces) and c) accelerometers (suspended stages).. 81

Figure 32. Strained conductor geometry affecting electrical resistance. 83

Figure 33. Composition of a quarter Wheatstone bridge where one of the resistors is sensitive to strain R_{sensor} and passive resistors (R_{1-3}) are not. 87

Figure 34. Resistive strain resistor connected by a four-terminal arrangement, where current is passed through two wires and instrumentation measures the voltage across two terminals, negating the total wire resistances up to the terminal junction. The strain gauge arrangement contains multiple wire passes in-line with the strain direction, increasing the strained wire length and thus the relative change in resistance, for increased sensitivity. 88

Figure 35. Power spectral density analysis of the AFM Group Laboratory (Rankine Building, School of Engineering, University of Glasgow) where an AFM system was being run (capture by Agilent 35670A spectrum analyser, bandwidth - 0.5 Hz)... 89

Figure 36. Fabrication sequence and material choice outline for the conceptualised strained resistor equipped cantilever force sensor... 91

Figure 37. Visualisation of an elastic cantilever with integrated resistive strain sensor near the fixed end.. 93

Figure 38. 1-2) The marker layer mask pattern is written by CAD data driven electron beam machine on a layer of sacrificial polymer resist layer applied on the substrate by a spin-coat method. 3) Changes in polymer cross-linking under exposure to the electron beam allows a suitable developer liquid to selectively remove material exposed to it. 4) The substrate with the revealed pattern is then uniformly coated by evaporated metal in a physical vapour deposition apparatus, where the metal layer sticks to the revealed silicon nitride surface and the surrounding resist mask. 5-6) The mask is then dissolved in a suitable solvent (e.g. acetone), causing a separation or lifting

of the metal from the substrate that is adhered to it and thus only the mask formed features remain coated in the chosen metal. 95

Figure 39. Registration feature with origin cross and square location markers: a) CAD file for pattern; b-c) Secondary electron scanned origin points and cell marker; d) Optical image after final metalisation steps, indicating the previously exposed areas. 96

Figure 40. a) and b) metallisation layer pattern pictured in CAD and c) optical image of the fabricated metal layer. 97

Figure 41. Showcase of the variation of tested devices described in Table 6, where lift-off quality, directionality variations and repeatability were assessed. 99

Figure 42. Fabricated sensors stitched into a single scale image. 100

Figure 43. Strained sensor (serpentine)geometry parameters. 100

Figure 44. Highlights of the strained wire packaging density variation in the chosen envelope – e.g. the 1.8 mm achieved by the least miniaturised '2XX-2XX' serpentine geometry, versus the highest density successfully fabricated 'X1X-X1X' design with a total length of 28.8 mm. N.B. the 'X' symbol replaces '0' in order to remove closed contours and aid lift-off clarity. 103

Figure 45. Common failure modes: a) a poorly developed (overexposed) pattern containing thick wires and small offset gaps, illustrating a lift-off failure mode and the chosen additive deposition limitations. b) poor lift-off mask quality, resulting in excess metal not 'lifting' from the substrate. c) failed strain sensor geometry definition caused by insufficient mask exposure resulting in localised undercuts at the overpass – common failure for sub 250 nm width wires. 103

Figure 46. 1) A thick mask is patterned by an e-beam., 2) Substrate is bombarded by a charged halocarbon gas that reacts and removes the silicon nitride, as well as the patterned resist layer. 3) Leftover resist is cleaned in solvent, revealing the mask pattern on the silicon nitride and exposing the underlying silicon substrate. 105

Figure 47. The etch pattern on the test substrate (quarter of the LPCVD nitride coated 3" wafer) showcasing the (left) post-plasma etch revealed etched features on silicon and the non-uniform

PMMA thickness caused by the plasma base etch. Right - the cleaned and scribed wafer with the desired silicon nitride features. The colour gradient non-uniformity is due to the LPCVD film variation and not related to dry etch. 106

Figure 48. Wet etching process showcasing how the silicon nitride structure can be released by under etching silicon substrate through taking advantage of the selective etch planes. 107

Figure 49. The MEMS device a) planar and b) tilted views highlighting the anisotropic removed pyramid. Silicon etch planes named per Miller Index convention. The selective etch method allows for different plane etch rates along the crystal planes - ratios of 1:100 are achieved in slow:fast planes with selected KOH concentration [181], enabling consistent regular pyramid feature formation. 109

Figure 50. Post wet-etch failure mode where cantilever adheres to the nearby underlying etch pit. The consistently downward direction and lack displacement form the failure site suggest a common interaction between the wall and cantilever - e.g. a drying liquid presence. 110

Figure 51. The presence of crystal-like particles - believed to be potassium salts, after a non-complete post wet-etch solution neutralisation in water. 111

Figure 52. MEMS wet etch pattern in a) CAD file, b) optical image before submersion and c) SEM image the after selective KOH etch, releasing the device with a directionally formed boundary in the underlying silicon substrate. 111

Figure 53. a) Test beam structure experiencing two failure modes simultaneously under-etch failure caused incomplete edge formation and long cantilever stiction to the shallow etch pit (SEM). b) Inconsistent cantilever boundary revealing a shifted silicon plane during release, due to possible deposition and/or masking contamination. 113

Figure 54. a) planar and b) isometric SEM images of the microfabricated test cantilevers, showcasing the formed free-standing features. Post release cantilever adhesion to etch pit, if etch pit to cantilever length ratio exceeds ~ 1.5:1. 114

Figure 55. Circular boundary cantilevers form a consistent and scalable boundary formation as well as increased cantilever length before stiction to bottom pit. 115

Figure 56. a) and b) SEM images of failed devices and stress raiser induced crack in silicon nitride; c) and d) SEM images of the devices with stress relieving fillet at the stress raiser point; e) and f) FEA stress analysis of surface stress magnitude at the cantilever corner. 117

Figure 57. Images taken at angle to the device planar surface, showcasing the a) presence of bend on the complex structure and b) absence of curvature with the metal layer removed. 118

Figure 58. Physical vapour deposition tool (Plassys Bestek) schematic. 119

Figure 59. Planar images of the (a) non-metallised beams with no visible bend and (b) metallised structures, portraying a pronounced upward arch. 120

Figure 60. Reconstructed 3D image and profile cross-sectioning line (Optical Profiler - Contour XT, Bruker) from which the deflection profiles are obtained. 122

Figure 61. Overlaid bend profiles deflection towards the free cantilever end captured by the optical profiler system (Contour XT, Bruker). Dotted line represents polynomial fit line. NB. The near end non uniformities are due to edge reflection artefacts displayed by the optical profiling technique. 122

Figure 62. MEMS devices with varied length elastic structures, providing a range of mechanical compliances. The isometric view displays the presence of nichrome film resistor caused bend. 125

Figure 63. Top (left) and isometric (right) view of the MEMS device, highlighting the key components and composition (CAD visualisation). 126

Figure 64. SEM picture (left) and CAD drawing (right) of the prototype MEMS device, highlighting cantilever structure and strained resistor dimensions. 126

Figure 65. The complete fabrication mask design for the wafer scale production of the MEMS device, packaging 88 unit dices on a 3-inch (diameter) fabrication wafer. 127

Figure 66. Silicon nitride cantilever t=0.389 µm, w=100 µm indented by the Hysitron PI85. The indentations can only be performed near the fixed end (L< 60 µm), where the structure is most resilient to static charging effects.. 133

Figure 67. Silicon nitride cantilever indentation near the fixed end position 1, 23.94 µm, highlighting the clear engagement region, the near-linear force and displacement relationship and high measurement signal to baseline noise ratio. N.B.: The initial downward slope before engagement is likely caused by the repulsive interaction between indenter tip and nitride cantilever. 133

Figure 68. SEM captures of the scanning beam static charging affecting the cantilever mechanical behaviour - by a) bending, b) twisting and c) sticking to the indenter probe, thus preventing its free-state property characterisation. An example of the captured interaction is provided in Figure 69. 134

Figure 69. Load-displacement curve of an interaction at a 60 µm, offset, where the low stiffness results in high engagement noise and low measurement to noise ratio due to the small magnitude forces measured during the interaction. 134

Figure 70. MEMS device characterised by the Hysitron PI85 [119] Nano Indenter – a) pre-indentation live capture, b) end indentation, live capture (SEM at 5 kV). 136

Figure 71. MEMS indentation data at position 1, showcasing the poor linearity of the force measurement during the engagement – downsides associated with low mechanical resistance in the structure causing the maximal force registered to be at 7.8 µN at the maximal displacement range, value - which is below the engagement noise. The lack of post-engagement linearity in this region concludes that a reliable spring consant approximation (from the rate of change dy/dx fit) may not be obtained. 137

Figure 72. Dynamically assessed free standing structures spanning a range of geometrical variations, summarised in Table 12 - a) full scale MEMS devices of varied lengths and resultant end point stiffness and b) stitched and scaled SEM images of the fabricated test structures. 140

Figure 73. The Laser Doppler Vibrometer system - Polytec MSA-100-3D, for analysing the MEMS cantilever frequency and motion spectrum. 141

Figure 74. Measured natural resonance frequency to estimated end-point stiffness (k) relationship following the power law fit, distinguished by planar geometry and boundary fixation type. NB. The BFX circular boundary fit has an outlier structure at 27 kHz, with stiffness twice as high as the one expected – possible cause of an otherwise undetected structural defect. 142

Figure 75. Left - capture of the 250 μm long MEMS device cantilever used in the electrical characterisation sequence; Right - the device envelope, mostly occupied by the millimetre sized four terminal connection leads required for handling. 144

Figure 76. a) batch fabricated MEMS devices on a substrate quarter wafer, b) individually cleaved, bonded and connected to copper film PCB tracks with conductive paint, to allow for c) soldering a handling-friendly MOLEX type connector for connection to instrumentation. 145

Figure 77. The ‘150-050’ strain resistor with geometrical property describing symbols. 146

Figure 78. Power spectrum analysis of the MEMS device signal and environment in the 1-100 Hz range (Agilent 35670A, bandwidth - 0.125 Hz). 150

Figure 79. Frequency and signal amplitude comparison of the background and MEMS signal spectrum analysis (Agilent 35670A, bandwidth - 62.5 Hz) contrasted with mechanical (Brownian) motion spectrum of the MEMS beam, captured by laser doppler vibrometer system (Polytec MSA-100-3D, bandwidth ~ 100 Hz). 151

Figure 80. Two MEMS configurations used to determine mechanically de-coupled strain gauge TCR (a) and a released MEMS system TCR that contains a product of bi-material beam mechanical behaviour (b). 153

Figure 81. TCR experiment setup with a temperature-controlled enclosure. 153

Figure 82. Experimentally obtained data points showcasing the TCR relationships for the strain gauge and MEMS device, highlighting the radical change in slope gradient once the mechanical response to thermal effects is included. Linear fit gradient shown in red. 154

Figure 83. A single fixed end cantilever of bi-material composition - containing two different CTE values, will respond to temperature change in different rates of expansion that cause non-uniform stress the cross section that manifest in a curvature. 155

Figure 84. (a) AFM optical lever laser spot aimed away and (b) aimed at the MEMS device strain gauge, introducing localised heating to the low thermal mass cantilever. N.B.: MEMS device not visible completely in the capture due to the curvature falling outside the AFM camera depth of field range. 157

Figure 85. AFM camera capture of the laser aimed at the reflective cantilever surface and the visible laser overspill. 159

Figure 86. Thermal intensity heatmap overlaid with the MEMS device contour, highlighting the intensity and location from the optical lever cantilever laser overspill. 159

Figure 87. Illustration (CAD) of the different elasticity AFM and MEMS device interaction, resulting in an equal opposite direction force exchange at a contact point. 162

Figure 88. Springs in series analogy used to represent the two distinct elasticity structures (k_{MEMS} and k_{AFM} cantilevers), which act as a compound system with its own resistance to acting force (F), expressed as common elasticity constant ($k_{interaction}$) and displacement (Z). 162

Figure 89. MEMS-AFM probe interaction at the elasticity characterised loading point illustration (left) and the AFM camera capture of the interaction (right). 163

Figure 90. The AFM obtained indentation data from the known elasticity AFM cantilever indentation of the MEMS device, allowing to express the resultant loading and unloading region gradients in elasticity terms by fitting a linear gradient. 164

Figure 91. The MEMS sensor positioned in the AFM system (Left), permitting user control of the interaction parameters through the AFM ramping mode interface (Right). 166

Figure 92. Snapshot of the two-channel oscilloscope interface showcasing the MEMS signal (yellow) and the low voltage Z axis piezo (green). Both channels synchronised (triggered) on the

rising AFM Z-signal sawtooth wave allowing for obtaining multiple samples through averaging function. 167

Figure 93. The MEMS instrumentation output from the AFM indentation, displaying a single cycle of the load and unload displacement, centred at the direction change point. The secondary axis displays the relative resistance change value, as obtained by the linear mathematical conversion described in Figure 95. 168

Figure 94. The independently and simultaneously captured AFM-MEMS interaction plots, highlighting the relationship between the vertical amplitude axis and the shared displacement capture. 168

Figure 95. MEMS device instrumentation output interpretation logic for the interaction force and elasticity measurement. 171

Figure 96. MEMS force measurement setup schematic, showing the vertical (Z-axis) cantilever motion exerting point force load on the strain measuring MEMS device. The purpose designed instrumentation conditions the strain gauge signal form which the elastic interaction behaviour can be interpreted. 173

Figure 97. Synchronously captured signals of the user setup 1.99 Hz and 5.795 µm amplitude saw-tooth Z-axis ramping routine (green). The interaction between AFM cantilever and MEMS device is detected by the AFM's own optical lever photodiode readout (blue). The elastic exchange is also independently recorded by the MEMS device produced strain signal (red). The typical to cantilever-sample interaction characteristics are clearly distinguished by both methods, showcasing the idle non-contact separation, progressive displacement during contact and the tip-substrate adhesion regions. 174

Figure 98. Schematic representation of the KNT-SThM-2an [211] probes, showcasing their structural composition and non-uniformity features in a) top (in-situ AFM placement visible side) and b) bottom (fabrication and ex-situ imaging placement) orientations. 177

Figure 99. The five tested structures imaged by SEM, highlighting the plainly identifiable variations between the structures – groove alignment in relation to gold mirror and triangular shade at the base indicating an incomplete anisotropic silicon release.. 179

Figure 100. Close-up of the structurally complex region - the tip apex, revealing the composition variation and planar feature asymmetry. 180

Figure 101. Optical profiler (Bruker Contour GT [212]) obtained surface topology scans, showcasing the non-uniform free-standing structure topology – product of non-intentional fabrication deviations and localised internal stresses.. 182

Figure 102. AFM-MEMS contact point determination with the aid of Vernier alignment markings (AFM camera).. 183

Figure 103. MEMS strain sensor signals for each cantilever. The linear fits over the loading and unloading (approach and retract in AFM terms) regions and their averaging provide characterisation for the measured elasticities in strain (d[dR/Rabs]/dt, s^{-1}) terms, which can be transformed to elasticity units (k_{AFM}, N m^{-1}) by undergoing conversion with a pre-determined calibration constant. 184

Figure 104. Adhesion region comparison displaying the compressive strain region during the tip-sample adhesion and release caused compressive strain returning to neutral strain plane. 187

Figure 105. In-situ AFM (Bruker Dimension Icon, USA [25]) motion spectrum analysis of the tested structures, highlighting the natural frequency (f_0) and the determined elasticity by thermal tune method (k_{TT}). 189

Figure 106. Integrated AFM camera snapshot of the investigated SThM structure and calibration grid cantilever (Bruker CLFC, [116]) contact point during the spring-on-spring experiment interaction. 191

Figure 107. Probe 2 elastic deformation profile and resultant linear fit comparison from two detection methods – approach regions of the AFM optical lever (black) and MEMS strain signal (red)... 192

Figure 108. Summarised elasticity assessment results distinguished by characterisation method. 194

Figure 109. Schematic representation of the directionally coated cantilever by physical aluminium vapour deposition process. 197

Figure 110. MEMS captured load gradient comparison of the Probe 1 structure before and after structural modification by aluminium thin film deposition. 200

Figure 111. The dual cantilever functionalised AFM probe equipped with two individual tip located sensors (SEM) - an example of non-uniform elastic behaviour exhibiting AFM cantilever. The highlighted offset between relative tip heights results in distinct, vertical displacement dependant engagement properties. 202

Figure 112. MEMS captured elasticity characterisation plot, displaying the discrete elasticity gradient change throughout the interaction, caused by load transfer via second engaged tip. NB. the outer cantilever does not separate from the MEMS device in the presented interaction, therefore its adhesion properties are not visible. 203

Figure 113. Springs in parallel analogy used to represent the two varied elasticity structures (k_{outer} and k_{inner} cantilever), which act as a compound system with its own elasticity constant ($k_{combined}$), when exposed to system wide force and displacement. 204

Figure 114. The elasticity profile plotted with the rate of change gradient – or displacement specific elasticity. Differences in rates of elasticity value change is distinct in load and unload regions. The elasticity sign change corresponds the loading direction – positive for load/approach, negative for unload/retract. 205

Figure 115. Prototype thermal AFM (SThM) probes with two different style cut-outs (top and bottom) - structures provided by Dr. Rory Lambert, AFM and Hyperlithography Group, Glasgow [53]. 207

Figure 116. Triple cantilever prototype AFM (SThM) probe with its elasticity profile, showcasing asymmetric engagement and disengagement behaviour. Structures provided by Dr. Yuan Zhang, AFM and Hyperlithography Group, Glasgow [53]. 208

Figure 117. FEA contact point study results highlighting the ±5 μm positionality effect on the relative elasticity (k) at and around the perceived contact point. 214

Figure 118. Lateral friction force investigation configuration of the MEMS force device. 214

Figure 119. Double clamped beam configuration, next to the analogously fabricated single clamped dual cantilevers. 216

List of Tables

Table 1. Veeco MPP-21100-W Cantilever manufacturer provided specifications. 32

Table 2. Thermal tune $<z^2>$ statistical component summary. 39

Table 3. Spring on spring measurement interaction gradient summary. 47

Table 4. Veeco MPP-21100-W, mechanical property assessment necessary for analytical and FE modelling exercises. 71

Table 5. Study of Abaqus 3D continuum hexahedral element mesh configuration and quantity effect in comparison to the analytical solution. 76

Table 6. The 36 trialled strain gauge configurations design to fit a 100 by 60 μm envelope, representing the strain sensor occupied region on the MEMS cantilever. NB: Strike-out numbers had not been successfully fabricated. 101

Table 7. Recipe iteration dependant cantilever profile polynomial curve fit variables, $yx = c1x2 + c2x + c3$. 123

Table 8. Metallisation run summary, highlighting the process parameters and resultant film thickness (AFM, Bruker Dimension Icon) and curvature (Optical Profiler, Contour XT). 124

Table 9. Indentation obtained position specific interactions allowing for analytical solution for elastic modulus (E). Note the relationship to SEM beam voltage. 135

Table 10. SEM beam acceleration voltage dependant experimental elastic modulus (E) figures for the Silicon Nitride film used as the structural layer for the MEMS device. 135

Table 11. The 5 indentations at different offsets returning similar spring constant (k) values instead of following the third order analytical relationship – a product of poor measurement. 138

Table 12. Tested cantilever structures, summarising the dimensions, estimated spring constant and measured natural resonance values. 141

Table 13. Instrumentation conversion constant. 145

Table 14. The '150-050' configuration strain sensor geometry and measured resistivity. 148

Table 15. Statistical summary of the TCR experimental determination. 154

Table 16. Strain to force determination by a measured force exchange with an AFM probe...... 170

Table 17. Summary of the probe elastic interaction gradients expressed as relative strain rate and elasticity figures, interpreted from loading and unloading regions. 186

Table 18. Summarised dynamic behaviour study outcomes. 190

Table 19. The processed elasticity figures from the complex composition AFM probe characterisation by the calibration reference grid experiment, highlighting the load and unload region output and their averaged values for each structure. 193

Table 20. The frequency and elasticity result summary corresponding to the five investigated AFM cantilevers, averaged figures used where multiple load and unload gradients were available. ... 195

Table 21. Investigated modified AFM cantilever probe elastic interaction gradients in instrumentation native relative strain expression and the approximated SI unit expression. The percentage change is the result of elasticity magnitude comparison against unmodified structures characterised in previous section. 198

Table 22. Elasticity gradient summary, detailing the measured outer and mutual (both) cantilever elasticities. A subtraction operation allows to apply springs in parallel analogy and determine the inner elasticity gradient and constant. 205

References

[1] Y. M. Efremov, W.-H. Wang, S. D. Hardy, R. L. Geahlen and A. Raman, “Measuring nanoscale viscoelastic parameters of cells directly from AFM force-displacement curves,” *Scientific Reports,* vol. 7, p. 1541, 2017.

[2] M. Lekka, “Discrimination Between Normal and Cancerous Cells Using AFM,” *Bionanoscience,* vol. 6, pp. 65-80, 2016.

[3] K. Iwata, S. Yamazaki, P. Mutombo, P. Hapala, M. Ondráček, P. Jelínek and Y. Sugimoto, “Chemical structure imaging of a single molecule by atomic force microscopy at room temperature,” *Nature Communications,* vol. 6, p. 7766, 2015.

[4] M. Grandbois, M. Beyer, M. Rief, H. Clausen-Schaumann and H. E. Gaub, “How strong is a covalent bond?,” *Science,* vol. 283, no. 5408, pp. 1727-1730, 1999.

[5] J. Suk, R. Piner, J. An and R. Ruoff, “Mechanical Properties of Mono layer Graphene Oxide,” *ACS Nano,* vol. 4, no. 11, pp. 6557-6564, 2010.

[6] J. Salvetat, J. Bonard, N. Thomson, A. Kulik, L. Forro, W. Benoit and L. Zuppiroli, “Mechanical properties of carbon nanotubes,” *Applied Physics A - Materials Science and Processing,* vol. 69, no. 3, pp. 255-260, 1999.

[7] J. Hafner, C. Cheung, T. Oosterkamp and C. Lieber, “High-yield assembly of individual single-walled carbon nanotube tips for scanning probe microscopies,” *Journal of Physical Chemistry B,* vol. 105, no. 4, pp. 743-746, 2001.

[8] S. Lyonnais, M. Hénaut, A. Neyret, P. Merida, C. Cazevieille, N. Gros, C. Chable-Bessia and D. Muiriaux, “Atomic force microscopy analysis of native infectious and inactivated SARS-CoV-2 virions,” *Scientific Reports,* vol. 11, p. 11885, 2021.

[9] R. P. Feynman, “"There's Plenty of Room at the Bottom" - talk at the Amercian Physical Society annual meeting,” Caltech, California, 1959.

[10] H. Hermann and H. Fripp, “On the Limits of the Optical Capacity of the Microscope,” *Journal of Microscopy,* vol. 16, no. 1, pp. 15-39, 1876.

[11] K. Yuliya, N. Alexander and B. S.R.J., “Imaging interferometric microscopy – approaching the linear systems limits of optical resolution,” *Optics Express,* vol. 15, no. 11, pp. 6651-6663, 2007.

[12] E. A. F. Ruska, “Beitrag zur übermikroskopischen Abbildung bei höheren Drucken (Making of photographs with the supermicroscope at high pressures),” *Kolloid-Zeitschrift,* vol. 100, no. 2, pp. 212-219, 1942.

[13] M. Ardenne, “Das Elektronen-Rastermikroskop (The Scanninc Electron Microscope),” *Zeitschrift für Physik A Hadrons and nuclei,* vol. 109, pp. 553-572, 1938.

[14] G. Binnig and H. Rohrer, "Scanning Tunneling Micrsocopy," *Surface Science,* vol. 126, pp. 236-244, 1983.

[15] G. Binnig, C. Quate and C. Gerber, "Atomic Force Microscope," *Physical Review Letters,* vol. 56, no. 9, pp. 930-933, 1986.

[16] J. Xu, K. Lauger, K. Dransfeld and I. Wilson, "Thermal sensors for investigation of heat transfer in scanning probe microscopy," *Review of Scientific Instruments,* vol. 65, no. 7, pp. 2262-2266, 1994.

[17] J. R. Weaver and D. W. Abraham, "High resolution atomic force microscopy potentiometry," *Journal of Vacuum Science & Technology B: Microelectronics and Nanometer Structures Processing, Measurement, and Phenomena,* vol. 9, no. 3, pp. 1559-1561, 1991.

[18] U. Hartmann, "Magnetic force microscopy: Some remarks from the micromagnetic point of view," *Journal of Applied Physics,* vol. 64, no. 3, pp. 1561-1564, 1988.

[19] A. Bard, F. Fan, J. Kwak and O. Lev, "Scanning Electrochemical Microscopy - Introduction and Principles," *Analytical Chemistry,* vol. 61, pp. 132-138, 1989.

[20] E. Betzig, A. Lewis, A. Harootunian, M. Isaacson and E. Kratschmer, "Near-Field Scanning Optical Micrsocopy (NSOM)," *Biophys J,* vol. 49, no. 1, pp. 269-279, 1986.

[21] L. J. Balk, E. Kubalek and E. Menzel, "Microcharacterization of electroluminescent diodes with the scanning electron microscope (SEM)," *IEEE TRANSACTIONS ON ELECTRON DEVICES,* vol. 22, no. 9, pp. 707-712, 1975.

[22] W. Bröcker, G. Hauck and G. Pfefferkorn, "Lock-in technique applied to cathodoluminescence of biomedical specimens in the SEM," *IEEE: SCANNING,* vol. 4, pp. 165-168, 1981.

[23] J. Schaffert, M. Cottin, A. Sonntag, H. Karacuban, D. Utzat, C. Bobisch and R. Möller, "Scanning noise microscopy," *Review of Scientific Instruments,* vol. 84, no. 16, p. 043702, 2013.

[24] R. Hamers, R. Tromp and J. Demuth, "Surface Electronic Structure of Si (111)-(7×7) Resolved in Real Space," *Physical Review Letters,* vol. 56, no. 18, 1986.

[25] Bruker, "Dimension Icon," [Online]. Available: bruker.com. [Accessed 05 03 2020].

[26] E. Green, "Review of Surface Texture Measurement and the Associated Metrological Problems," *Proceedings of the IMechE,* vol. 182, no. 11, pp. 330-343, 1967.

[27] H. J. Butt, P. Siedle, K. Seifert, K. Fendler, T. Seeger, E. Bamberg, A. L. Weisenhorn, K. Goldie and A. Engel, "Scan speed limit in atomic force microscopy," *Journal of Microscopy,* vol. 169, no. 1, pp. 75-84, 1993.

[28] O. D. Payton, L. Picco and T. B. Scott, "High-speed atomic force microscopy for materials science," *International Materials Reviews,* vol. 61, no. 8, pp. 473-494, 2016.

[29] O. D. Payton, L. Pico, A. Raman, M. E. Homer, A. R. Champneys and M. J. Miles, “High-speed atomic force microscopy in slow motion - understanding cantilever behaviour at high scan velocities,” *Nanotechnology,* vol. 23, no. 20, p. 205704, 2012.

[30] R. Garcia and R. Perez, “Dynamic atomic force microscopy methods,” *Surface Science Reports,* vol. 47, pp. 197-301, 2002.

[31] Y. Wang, X. Hu, L. Xu and X. Hu, “Improving the scanning speed of atomic force microscopy at the scanning range of several tens of micrometers,” *Ultramicroscopy,* vol. 124, pp. 102-107, 2013.

[32] R. Van Den Braber, T. Van Den Dool, H. Sadeghian Marnani and N. Rijnveld, “High throughput microscopy device”. Patent US9476908B2, 2013.

[33] A. Humphris, “Probe system with multiple actuation locations”. Patent US20170016932A1, 2014.

[34] R. Proksch, J. Cleveland, D. Bocek, T. Day, M. Viani and C. Cllahan, “Fully digital controller for cantilever-based instruments”. Patent US7234342B2, 2004.

[35] L. Wangxu, Y. Wang, H. Zhang and Q. You, “High-speed scanning atomic-force microscopy micro-nano sample image detecting method, involves fixing micro-probe to sample unit along X-direction, and performing atomic force microscopy image independent interference eliminating process”. Patent CN104849499, 2015.

[36] W. Han, J. Mou, J. Sheng, J. Yang and Z. Shao, “Cryo Atomic-Force Microscopy - A new for biological imaging at high-resolution,” *Biochemistry,* vol. 34, no. 26, pp. 8215-8220, 1995.

[37] K. Hansen, Y. Wu, M. Mogensen and L. Theil Kuhn, “Improved controlled atmosphere high temperature scanning probe microscope,” *Review of Scientific Instruments,* vol. 84, p. 073701, 2013.

[38] W. Allers, A. Schwarz, U. Schwarz and R. Wiesendanger, “Scanning force microscope with atomic resolution in ultrahigh vacuum and at low temperatures,” *Review of Scientific Instruments,* vol. 69, no. 1, pp. 221-225, 1998.

[39] P. Hansma, J. Cleveland and et al., “Tapping mode Atomic-Force microscopy in liquids”.

[40] Bruker Corporation, *NanoScope Analysis,* 2017.

[41] Semilab GmbH, Semilab DME, 2019. [Online]. Available: https://dme-spm.com/scantool.html. [Accessed 06 05 2020].

[42] M. Abramoff, P. Magalhaes and S. Ram, “Image Processing with ImageJ,” *Biophotonics International,* vol. 11, no. 7, pp. 36-42, 2004.

[43] D. Necas and P. Klapetek, “Gwyddion: an open-source software for SPM data analysis,” *Central European Journal of Physics,* vol. 10, no. 1, pp. 181-188, 2012.

[44] H. Butt, B. Cappella and M. Kappl, “Force measurements with the atomic force microscope: Technique, interpretation and applications,” *Surface Science Reports,* vol. 59, no. 1-6, pp. 1-1152, 2005.

[45] G. Binning, H. Rohrer, C. Gerber and E. Weibel, “Surface Studies by Scanning Tunneling Microscopy,” *Physical Review Letters,* vol. 49, no. 1, pp. 57-61, 1982.

[46] R. Erlandsson, G. McClelland, C. Mate and S. Chiang, “Atomic Force Microscopy using optical interferometry,” *Journal of Vacuum Science & Technology A-Vacuum Surfaces and Films,* vol. 6, no. 2, pp. 266-270, 1988.

[47] S. Alexander, L. Hellemans, O. Marti, J. Schneir, V. Elings, P. Hansma, M. Longmire and J. Gurley, “An atomic-resolution atomic-force microscope Implemented using an optical-lever,” *Journal of Applied Physics,* vol. 65, no. 1, pp. 164-167, 1989.

[48] M. Tortonese, R. Barrett and C. Quate, “Atomic resolution with an Atomic Force Microscope using piezoresistive detection,” *Applied Physics Letters,* vol. 62, no. 8, pp. 834-836, 1993.

[49] G. Meyer and N. Amer, “Novel optical approach to atomic force microscopy,” *Applied Physics Letters,* vol. 53, no. 12, pp. 1045-1047, 1998.

[50] O. Marti, A. Ruf, M. Hipp, H. Bielefeldt, J. Colchero and J. Mlynek, “Mechanical and Thermal Effects of Laser Irradiation on Force Microscopy Cantilevers,” *Ultramicroscopy,* vol. 42, pp. 345-350, 1992.

[51] B. Cappella and G. Dietler, “Force-distance curves by atomic force microscopy,” *Surface Science Reports,* vol. 34, no. 1-3, pp. 1-104, 1999.

[52] S. Fujisawa, M. Ohta, T. Konishi, Y. Sugawara and S. Morita, “Difference between the forces measured by an optical lever deflection and by an optical interferometer in an atomic force microscope,” *Review of Scientific Instruments,* vol. 65, no. 3, pp. 944-947, 1994.

[53] J. M. R. Weaver and P. S. Dobson, “AFM & Hyperlithography Group,” University of Glasgow, [Online]. Available: http://web.eng.gla.ac.uk/groups/nano/afm/AfmPage.html.

[54] T. Thundat, X. Zheng, G. Chen and R. Warmack, “Role of relative humidity in atomic force microscopy imaging,” *Surface Science Letters,* vol. 294, no. 1-2, pp. 939-943, 1993.

[55] J. Hutter and J. Bechhoefer, “Measurement and manipulation of van der Waals forces in atomic-force microscopy,” *Journal of Vacuum Science & Technology B,* vol. 12, p. 2251, 1994.

[56] H. Butt, “Measuring electrostatic, van der Waals, and hydration forces in electrolyte solutions with an atomic force microscope,” *Biophysical Journal,* vol. 60, pp. 1438-1444, 1991.

[57] H. Hertz, “Ueber die Berührung fester elastischer Körper,” *Journal für die reine und angewandte Mathematik,* vol. 1882, no. 92, pp. 156-171, 1881.

[58] B. Derjaguin, V. Muller and Y. Toporov, “Effect of contact deformations on the adhesion of particles,” *Journal of Colloid and Interface Science,* vol. 53, no. 2, pp. 314-326, 1975.

[59] K. Johnson, K. Kendall and A. Roberts, “Surface energy and the contact of elastic solids,” *Proceedings of the Royal Society A,* vol. 324, pp. 301-313, 1971.

[60] The International Bureau of Weights and Measures (BIPM), “2.3.4 Derived units,” in *The International System of Units (SI)*, 2019, p. 138.

[61] CIPM MRA-D-04, “Calibration and Measurement Capabilities in the context of the CIPM Mutual Recognition of Measurements,” International Committee for Weights and Measures (CIPM), March 2017. [Online]. Available: http://www.bipm.org/utils/common/CIPM_MRA/CIPM_MRA-D-04.pdf.

[62] N. Khelifa, P. Averlant and M. Himbert, “Traceability of small force measurements and the future international system of units (SI),” *International Journal of Metrology and Quality Engineering,* vol. 7, no. 306, pp. 1-8, 2016.

[63] U. Brand, P. Fiala, B. Reischl and K. Hiller, “Traceable measurement of mechanical properties of nanoobjects,” *European Metrology Research Programme by EURAMET,* no. V1.0, 2016.

[64] Y. Song, S. Wu, L. Xu and X. Fu, “Accurate Calibration and Uncertainty Estimation of the Normal Spring Constant of Various AFM Cantilevers,” *Sensors,* vol. 15, pp. 5865-5883, 2015.

[65] D. M. Stefanescu, Handbook of Force Transducers, Springer Berlin Heidelberg, 2011.

[66] Clarivate Analytics, “Web of Science,” [Online]. Available: https://clarivate.com/webofsciencegroup/solutions/web-of-science/.

[67] J. Pratt, J. Kramar, D. Newell and D. Smith, “Review of SI traceable force metrology for instrumented indentation and atomic force microscopy,” *Measurement Science and Technology,* vol. 16, no. 11, pp. 2129-2137, 2005.

[68] “The NIST microforce realisation and measurement project,” *IEEE Transactions on Instrumentation and Measurement,* vol. 52, no. 2, pp. 508-511, 2003.

[69] J. Kramar, R. Dixson and N. Orji, “Scanning probe microscope dimensional metrology at NIST,” *Measurement Science and Technology,* vol. 22, no. 2, 2010.

[70] C. Jones, J. Kramar, S. Davidson, R. Leach and J. Pratt, “Comparison of NIST SI Force Scale to NPL SI Mass Scale,” National Physical Laboratory, Teddington, 2008.

[71] EURAMET, “Traceable small force metrology - EMRP Call 2012,” National Physical Laboratory, Teddington, 2012.

[72] P. J. Cumpson and J. Hedley, “Accurate analytical measurements in the atomic force microscope: a microfabricated spring constant standard potentially traceable to the SI,” *Nanotechnology,* vol. 14, pp. 1279-1288, 2003.

[73] Y. Song, S. Wu, L. Xu and X. Fu, “Accurate Calibration and Uncertainty Estimation of the Normal Spring Constant of Various AFM Cantilevers,” *Sensors,* vol. 15, pp. 5865-5883, 2015.

[74] C. Diethold and F. Hilbrunner, “Force measurement of low forces in combination with high dead loads by the use of electromagnetic force compensation,” *Measurement Science and Technology,* vol. 23, no. 074017, 2012.

[75] N. Khelifa and M. Himbert, “Sensitivity of Miniaturized Photo-elastic Transducer for Small Force Sensing,” *Sensors and Transducers,* vol. 184, no. 1, pp. 19-25, 2015.

[76] E. A-Hassan, W. Heinz, J. Hog and e. al., “Relative Microelastic Mapping of Living Cells by Atomic Force Microscopy,” *Biophysical Journal,* vol. 74, pp. 1564-1578, 1998.

[77] H. Marchman and N. Dunham, “AFM: a valid reference tool?,” in *23rd Annual International Symposium on Microlithography*, Santa Clara, 1998.

[78] H. Schmidt, J. Heil, J. Wesner and W. Grill, “Atomic force sensors constructed from carbon and quartz fibers,” *Journal of Vacuum Science & Technology A,* vol. 8, pp. 388-390, 1989.

[79] T. Albrecht, S. Akamine, T. Carver and C. Quate, “Microfabrication of cantilever styli for the atomic force microscope,” *Journal of Vacuum Science & Technology A,* vol. 8, pp. 3386-3396, 1990.

[80] Y. Zhang, P. S. Dobson and J. M. R. Weaver, “High temperature imaging using a thermally compensated cantilever resistive probe for scanning thermal microscopy,” *Journal of Vacuum Science & Technology,* vol. 30, no. 1, 2012.

[81] Y. Kawai, T. Ono, E. Meyers, C. Gerber and M. Esashi, “Piezoelectric Actuator Integrated Cantilever with Tunable Spring Constant For Atom Probe,” in *19th IEEE International Conference on Micro Electro Mechanical Systems*, Istanbul, Turkey, 2006.

[82] H. Muramatsu, N. Chiba, M. Fujihira and e. al., “Multi-functional SNOM/AFM probe with accurately controlled low spring constant,” *Ultramicroscopy,* vol. 71, pp. 73-79, 1998.

[83] P. J. Cumpson, C. A. Clifford and J. Hedley, “Quantitative analytical atomic force microscopy: a cantilever reference device for easy and accurate AFM spring-constant calibration,” *Measurement Science and Technology,* vol. 15, pp. 1337-1346, 2004.

[84] P. J. Cumpson, P. Zhdan and J. Hedley, “Calibration of AFM cantilever stiffness: a microfabricated array of reflective spring,” *Ultramicroscopy,* vol. 100, no. 3-4, pp. 241-251, 2004.

[85] J. P. Cleveland, S. Manne, D. Bocek and P. K. Hansma, “Nondestructive method for determining the spring constant of cantilevers for scanning force microscopy,” *Review of Scientific Instruments,* vol. 64, no. 2, pp. 403-405, 1993.

[86] B. Ohler, “Cantilever spring constant calibration using laser Doppler vibrometry,” *Review of Scientific Instruments,* vol. 78, no. 063701, 2007.

[87] J. Hutter and J. Bechhoefer, “Calibration of atomic-force microscope tips,” *Review of Scientific Instruments,* vol. 64, no. 7, pp. 1868-1873, 1993.

[88] R. Levy and M. Maaloum, “Measuring the spring constant of atomic force microscope cantilever: thermal fluctuations and other methods,” *Nanotechnology,* vol. 13, pp. 33-37, 2002.

[89] R. W. Stark, T. Drobek and W. M. Heckl, “Thermomechanical noise of a free v-shaped cantilever for atomic-force microscopy,” *Ultramicroscopy,* vol. 86, pp. 207-215, 2001.

[90] T. E. Schaffer, “Calculation of thermal noise in an atomic force microscope with a finite optical spot size,” *Nanotechnology,* vol. 16, pp. 664-670, 2005.

[91] U. Brand, “Comparing AFM cantilever stiffness measured using the thermal vibration and the improved thermal vibration methods with that of an SI traceable method on MEMS,” *Measurement Science and Technology,* vol. 28, no. 0.34010, 2017.

[92] J. Sader, I. Larson, P. Mulvaney and L. White, “Method for the calibration of atomic force microscope cantilevers,” *Review of Scientific Instruments,* vol. 66, pp. 3789-3798, 1995.

[93] J. E. Sader, “Frequency response of cantilever beams immersed in viscous fluids with applications to the atomic force microscope,” *Journal of Applied Physics,* vol. 84, no. 1, pp. 64-76, 1998.

[94] J. Sader, R. Borgani, C. Gibson, D. Havilan and e. al., “A virtual instrument to standardise the calibration of atomic force microscope cantilevers,” *Review of Scientific Instruments,* vol. 87, p. 093711, 2016.

[95] A. Torii, M. Sasaki, K. Hane and S. Okuma, “A method for determining the spring constant of cantilevers for atomic force microscopy,” *Measurement Science and Technology,* vol. 7, pp. 179-184, 1996.

[96] R. S. Gates and M. G. Reitsma, “Precise atomic force microscope cantilever spring constant calibration using a reference cantilever array,” *Review Of Scientific Instruments,* vol. 78, p. 086101, 2007.

[97] M. Tortonese, R. Barret and C. Quate, “Atomic resolution with an atomic force microscope using piezoresistive detection,” *Applied Physics Letters,* vol. 62, pp. 834-836, 1993.

[98] Y. Su, A. Evans, A. Brunnschweiler, G. Ensell and M. Koch, “Fabrication of improved piezoresistive silicon cantilever probes for the atomic force microscope,” *Sensors and Actuators A,* vol. 60, pp. 163-167, 1997.

[99] S. Jarvis, A. Oral, T. Wihs and J. Pethica, “A novel force microscope and point contact probe,” *Review of Scientific Instruments,* vol. 64, pp. 3515-3520, 1993.

[100] D. Scholl, M. P. Everson and R. C. Jaklevic, “In situ force calibration of high force constant atomic force microscope cantilevers,” *Review of Scientific Instruments,* vol. 65, pp. 2255-2257, 1994.

[101] C. Lee, T. Itoh and T. Suga, “Self-excited piezoelectric PZT microcantilevers for dynamic SFM - with,” *Sensors and Actuators A,* vol. 72, pp. 179-188, 1999.

[102] T. Senden and W. Ducker, “Experimental Determinaiton of Spring Constants in Atomic Force Microscopy,” *Langmuir,* vol. 10, pp. 1003-1004, 1994.

[103] P. Cumpson, J. Hedley, C. Clifford, X. Chen and S. Allen, “Microelectromechanical system device for calibration of atomic force microscope cantilever spring constants between 0.01 and 4 N/m,” *Juornal of Vacuum Science & Technology,* vol. 22, pp. 1444-1449, 2004.

[104] S. Gao, Z. Zhang, Y. Wu and K. Herrmann, “Towards quantitative determination of the spring constant of a scanning force microscope cantilever with a microelectromechanical nano-force actuator,” *Measurement Science and Tehcnology,* vol. 21, p. 015103, 2009.

[105] M.-S. Kim, J.-H. Choi and Y.-K. Park, “Accurate determination of spring constant of AFM cantilever and comparison with other methods,” in *XVIII IMEKO WORLD CONGRESS*, Brazil, 2006.

[106] E. Oñate, “Slender Plane Beams. Euler-Bernoulli Theory,” in *Structural Analysis with the Finite Element Method Linear Statics. Lecture Notes on Numerical Methods in Engineering and Sciences*, Dordrecht., Springer, 2013, pp. 1-36.

[107] Bruker, “RFESPW-75,” [Online]. Available: https://www.brukerafmprobes.com/p-3918-rfespw-75.aspx. [Accessed 05 03 2020].

[108] Bruker, “MPP-21100-W,” [Online]. Available: https://www.brukerafmprobes.com/p-3338-mpp-21100-w.aspx. [Accessed 05 03 2020].

[109] H. J. Butt and M. Jaschke, “Calculation of thermal noise in atomic force microscopy,” *Nanotechnology,* vol. 6, no. 1, p. 5, 1995.

[110] S. Naeem, Y. Liu, H.-Y. Nie, W. M. Lau and J. Yang, “Revisiting atomic force microscopy force spectroscopy sensitivity for single molecule studies,” *Journal of Applied Physics,* vol. 104, pp. 114504-5, 2008.

[111] B. Ohler, “Practical Advice on the Determination of Cantilever Spring Constants, Application note 94, Revision A0,” Veeco instruments Inc., 2007.

[112] C. A. Clifford and M. P. Seah, "The determination of atomic force microscope cantilever spring constants via dimensional methods for nanomechanical analysis," *Nanotechnology,* vol. 16, pp. 1666-1680, 2005.

[113] B. Ohler, "Cantilever spring constant calibration using laser Doppler vibrometry," *Review of Scientific Instruments,* vol. 78, no. 063701, 2007.

[114] S. B. Aksu and J. A. Turner, "Calibration of atomic force microscope cantilevers using piezolevers," *Review of Scientific Instruments,* vol. 78, no. 043704, 2007.

[115] W. L. Bonin and M. Guthold, "Easy and direct method for calibrating atomic force microscopy lateral force measurements," *Review of Scientific Instruments,* vol. 78, no. 6, p. 063707, 2007.

[116] Bruker CLFC, "brukerafmprobes.com," [Online]. Available: https://www.brukerafmprobes.com/p-3242-clfc-nobo.aspx. [Accessed 09 03 2020].

[117] Bruker AFM Probes: Force Calibration Cantilevers , "Support Note 013-000-000," [Online]. Available: https://www.brukerafmprobes.com/images/product/specPDF/3242.pdf.

[118] C. A. Schuh, "Nanoindentation studies of materials," *Materials Today,* vol. 9, no. 5, pp. 32-40, 2006.

[119] Bruker, "Hysitron PI 85 SEM PicoIndenter," Bruker, [Online]. Available: https://www.bruker.com/products/surface-and-dimensional-analysis/nanomechanical-test-instruments/nanomechanical-test-instruments-for-microscopes/pi-85l-sem-picoindenter/overview.html. [Accessed 18 03 2020].

[120] Zeiss, "Zeiss Sigma Field Emission SEM," Zeiss, [Online]. Available: https://www.zeiss.com/microscopy/int/products/scanning-electron-microscopes/sigma.html. [Accessed 18 03 2020].

[121] C. A. Clifford and M. P. Seah, "Improved methods and uncertainty analysis in the calibration of the spring constant of an atomic force microscope cantilever using static experimental methods," *Measurement Science and Technology,* vol. 20, p. 125501, 2009.

[122] Z. C. Ying., M. G. Reitsma and R. S. Gates, "Direct measurement of cantilever spring constants and correction for cantilever irregularities using an instrumented indenter," *Review of Scientific Instruments,* vol. 78, p. 063708, 2007.

[123] J. Menčík, "Nanoindentation in Materials Science," in *Uncertainties and Errors in Nanoindentation*, DOI: 10.5772/50002, IntechOpen, 2012.

[124] W. C. Young and R. G. Budynas, "Shear, moment, slope, and deflection formulas for elastic straight beams," in *Roark's Formulas for Stress and Strain*, New York, McGraw-Hill Professional, 2001, p. 189.

[125] N. Yu, A. Polycarpou and W. Bonin, “High-resolution capacitive load-displacement transducer and its application in nanoindentation and adhesion force measurements,” *Review of Scientific Instruments,* vol. 76, no. 4, p. 045109, 2005.

[126] P. Regtien, Instrumentation Electronics: Basic Electronic Theory and Techniques, New York: Prentice-Hall, 1992.

[127] The Center for Engineering Design, University of Utah, “A Proposal for the Development of Micro Electro-Mechanical Systems (MEMS),” Salt Lake City, 1986.

[128] D. Green, “Semiconductor safari - Exotic materials beyond silicon,” *Defence Advanced Research Projects Agency 1958-2018,* p. 55, 2018.

[129] M. E. Gurtin and I. Murdoch, “A continuum theory of elastic material surfaces,” *Archive for Rational Mechanics and Analysis,* vol. 57, pp. 291-323, 1975.

[130] W. C. Young and R. G. Budynas, “Shear, moment, slope, and deflection formulas for elastic straight beams,” in *Roark’s Formulas for Stress and Strain*, New York, McGraw-Hill Professional, 2001, p. 189.

[131] J. A. Woollam, B. D. Johs, D. W. Doerr and R. A. Christenson, “Ellipsometer”. Nebraska, USA Patent 5373359, 13 12 1994.

[132] S. A. Chalmers and R. S. Geels, “Thin-film metrology using spectral reflectance with an intermediate in-line reference”. California, US Patent 7502119 B2, 10 03 2009.

[133] B. Bhushan and X. Li, “Micromechanical and tribological characterization of doped single-crystal silicon and polysilicon films for microelectromechanical systems devices,” *Journal of Materials Research,* vol. 12, no. 1, p. 59, 1997.

[134] FEI Company, Nova NanoSEM, “fei.co.jp,” [Online]. Available: http://www.fei.co.jp/_documents/NovaNanoSEMDatasheet.pdf. [Accessed 05 03 2020].

[135] Nikon Eclipse L200N Series, “nikonmetrology.com,” Nikon, [Online]. Available: https://www.nikonmetrology.com/en-gb/product/eclipse-l200n-series. [Accessed 09 03 2020].

[136] B. Bhushan, “2.3.3 AFM Probe Construction,” in *Nanotribology and Nanomechanics* , Berlin, Springer, 2005, p. 65.

[137] J. J. Wortman and R. A. Evans, “Young's Modulus, Shear Modulus, and Poisson's Ratio in Silicon and Germanium,” *Journal of Applied Physics,* vol. 36, p. 154, 1994.

[138] Dassault Systemes , “Abaqus/CAE,” Simulia, [Online]. Available: https://www.3ds.com/products-services/simulia/products/abaqus/abaquscae/.

[139] R. Puers, “Capacitive sensors: when and how to use them,” *Sensors and Actuators A,* Vols. 37-38, pp. 93-105, 1993.

[140] W. P. Eaton and J. H. Smith, “Micromachined pressure sensors: review and recent developments,” *Smart Materials and Structures,* vol. 6, p. 531, 1997.

[141] A. Beliveau, G. T. Spencer, K. A. Thomas and S. L. Roberson, “Evaluation of MEMS capacitive accelerometers,” *IEEE Design and Test of Computers,* vol. 16, no. 4, pp. 48-56, 1999.

[142] D. Scholl, M. P. Everson and R. C. Jaklevic, “In situ force calibration of high force constant atomic force microscope cantilevers,” *Review of Scientific Instruments ,* vol. 65, no. 2255, 1994.

[143] P. Eswaran and S. Malarvizhi, “MEMS Capacitive Pressure Sensors: A Review on Recent Development and Prospective,” *International Journal of Engineering and Technology,* vol. 5, no. 3, p. 2739, 2013.

[144] S. Gao and U. Brand, “In-situ nondestructive characterization of the normal spring constant of AFM cantilevers,” *Measurement Science and Technology,* vol. 25, p. 044014, 2014.

[145] J. Wooldridge, J. Blackburn, A. Muniz-Piniella, M. Stewart, T. Shean, P. Weaver and M. Cain, “Finite Element Analysis of the Vertical Levitation Force in an Electrostatic MEMS Comb Drive Actuator,” *Journal of Physics: Conference Series,* vol. 012002, p. 2013, 472.

[146] A. Dec and K. Suyama, “A 1.9-GHz CMOS VCO with Micromachined Electromechanically Tunable Capacitors,” *IEEE JOURNAL OF SOLID-STATE CIRCUITS,* vol. 35, no. 8, pp. 1231-1238, 2000.

[147] G. Y. Yang, V. J. Bailey, G. Lin, W. C. Tang and J. H. Keyak, “Design of microfabricated strain gauge array to monitor bone deformation in vitro and in vivo,” in *EEE Symposium on Bioinformatics and Bioengineering (BIBE)* , Taichung, Taiwan, 2004.

[148] H. Onishi, M. Sohgawa, H. Tachibana, Y. M. Huang, T. Kanashima, M. Okuyama, K. Yamashita, M. Noda and H. Noma, “Stability Improvement of Tactile Sensor of Normal and Shear Stresses Using Ni-Cr Thin Film Gauge,” *IEEJ Transactions on Sensors and Micromachines,* vol. 129, no. 11, pp. 411-416, 2009.

[149] N. D. Arora, J. R. Hauser and D. J. Roulston, “Electron and Hole Mobilities in Silicon as a Function of Concentration and Temperature,” *IEEE Transactions on Electron Devices,* vol. 29, no. 2, pp. 292-295, 1982.

[150] M. V. Fischetti and S. E. Laux, “Band structure, deformation potentials, and carrier mobility in strained Si, Ge, and SiGe alloys,” *Journal of Applied Physics,* vol. 80, p. 2234, 1996.

[151] J. Thaysen, A. Boisen, O. Hansen and S. Bouwstra, “Atomic force microscopy probe with piezoresistive read-out and a highly symmetrical Wheatstone bridge arrangement,” *Sensors and Actuators,* vol. 83, p. 49, 2000.

[152] I. H. Kazi, P. M. Wild, T. N. Moore and M. Sayer, “Characterization of sputtered nichrome (Ni–Cr 80/20 wt.%) films for strain gauge applications,” *Thin Solid Films,* vol. 515, p. 2604, 2006.

[153] A. K. Ghosh, C. Fishamn and T. Feng, “Theory of the electrical and photovoltaic properties of polycrystalline silicon,” *Journal of Applied Physics,* vol. 551, p. 449, 1980.

[154] F. D. King, J. Shewchun, H. D. Barber and W. A. Pieczonka, “Polycrystalline silicon resistors for integrated circuits,” *Solid-State Electronics,* vol. 16, no. 6, pp. 701-708, 1973.

[155] J. Rölke, “Nichrome thin tilm technology and its application,” *Electrocomponent Science and Technology,* vol. 9, pp. 51-57, 1981.

[156] G. G. Stoney and C. A. Parsons, “The tension of metallic films deposited by electrolysis,” *Proceedings of the Royal Society A,* vol. 82, pp. 172-175, 1909.

[157] G. S. Nadvi, D. P. Butler, Z. Celik-Butler and I. E. Gonenli, “Micromachined force sensors using thin film nickel–chromium piezoresistors,” *Journal of Micromechanics and Microengineering,* vol. 22, p. 065002, 2012.

[158] S. Ekelof, “The Genesis of the Wheatstone Bridge,” *Engineering Science and Education Journal,* vol. 10, no. 1, pp. 37-40, 2001.

[159] A. Boisen, J. Thaysen, H. Jensenius and O. Hansen, “Environmental sensors based on micromachined cantilevers with integrated read-out,” *Ultramicroscopy,* vol. 82, pp. 11-16, 2000.

[160] A. Midha, Batch-fabrication of novel nanoprobes for SPM. PhD Thesis, University of Glasgow, 1999.

[161] G. B. Mills, Scanning thermal microscopy using nanofabricated probes. PhD Thesis, University of Glasgow, 1999.

[162] P. S. Dobson, J. M. R. Weaver, D. P. Burt, M. N. Holder, N. R. Wilson, P. R. Unwin and J. V. MacPherson, “Electron beam lithographically-defined scanning electrochemical-atomic force microscopy probes: fabrication method and application to high resolution imaging on heterogeneously active surfaces,” *Physical Chemistry Chemical Physics,* vol. 8, pp. 3909-3914, 2006.

[163] R. Lambert, Design, fabrication and characterisation of thermally optimised novel SThM probes. PhD thesis, University of Glasgow, 2020.

[164] F. Tofani, Thermal-AFM under aqueous environment. PhD thesis, University of Glasgow, 2020.

[165] K. Rudnicki, MOSFET transistor fabrication on AFM tip, University of Glasgow, 2014.

[166] Y. Ge, Quantitative Measurement Using Scanning Thermal Microscopy. PhD Thesis, University of Glasgow, 2016.

[167] Z. Umatova, A sensitive device for SThM quantifiation, University of Glasgow, 2018.

[168] Chalmers University of Technology, *Department of Microtechnology and Nanoscience, Nanofabrication Laboratory,* SE-412 96 Gothenburg, Sweden.

[169] Bruker AFM Probes International, "MLCT," [Online]. Available: https://www.brukerafmprobes.com/p-3444-mlct.aspx.

[170] Bruker AFM Probes International, "SNL-10," [Online]. Available: https://www.brukerafmprobes.com/p-3693-snl-10.aspx.

[171] NanoAndMore GbmH, "ARROW-TL1," [Online]. Available: https://www.nanoandmore.com/AFM-Probe-ARROW-TL1.

[172] Plassys Bestek, "Evaporation HV/UHV Products," [Online]. Available: https://plassys.com/evaporation-hv-uhv/.

[173] K. E. Docherty, K. A. Lister, J. Romijn and J. M. R. Weaver, "High robustness of correlation-based alignment with Penrose patterns to marker damage in electron beam lithography," *Microelectronic Engineering,* vol. 86, pp. 532-534, 2009.

[174] P. S. Ho and T. Kwok, "Electromigration in metals," *Reports on Progress in Physics,* vol. 52, no. 321, 1989.

[175] Oxford Instruments Plasma Technology, "Reactive Ion Etching (RIE) Systems," Oxford Instruments Group, 2020. [Online]. Available: https://plasma.oxinst.com/products/rie/.

[176] C. Zhang, C. Yang and D. Ding, "Deep reactive ion etching of PMMA," *Applied Surface Science,* vol. 227, no. 1-4, pp. 139-143, 2004.

[177] A. R. Wind and M. A. Hines, "Macroscopic etch anisotropies and microscopic reaction mechanisms: a micromachined structure for the rapid assay of etchant anisotropy," *Surface Science,* vol. 460, no. 1-3, pp. 21-38, 2000.

[178] J. R. Dwyer and M. Harb, "Through a Window, Brightly: A Review of Selected Nanofarbicated Thin-Film Platforms for Spectroscopy, Imaging, and Detection," *Applied Spectroscopy,* vol. 71, no. 9, p. 2054, 2017.

[179] P. Pal and K. Sato, "A comprehensive review on convex and concavecorners in silicon bulk micromachining basedon anisotropic wet chemical etching," *Micro and Nano Systems Letters,* vol. 3, no. 6, 2015.

[180] Brigham Young University, "KOH Ething Notes," [Online]. Available: https://cleanroom.byu.edu/KOH. [Accessed 13 09 2020].

[181] H. Seidel, L. Csepregi, A. Heuberger and H. Baumgärtel, "Anisotropic Etching of Crystalline Silicon in Alkaline Solutions," *Journal of The Electrochemical Society,* vol. 137, no. 11, pp. 3612-3632, 1990.

[182] J. J. Jasper, “The Surface Tension of Pure LiquidCompounds,” *Journal of Physical and Chemical Reference Data 1,* vol. 841, 1972.

[183] P. M. Dunlap and S. R. Faris, “Surface Tension of Aqueous Solutions of Potassium Hydroxide,” *Nature,* vol. 196, p. 1313, 1962.

[184] K. E. Petersen and C. R. Guarnieri, “Young's modulus measurements of thin films using micromechanics,” *Journal of Applied Physics,* vol. 50, p. 6761, 1979.

[185] Transene Company Inc., “Chromium Etchants 1020,” [Online]. Available: transene.com/cr/.

[186] X. W. Zhou, R. A. Johnson and H. N. G. Wadley, “A molecular dynamics study of nickel vapor deposition: temperature, incident angle, and adatom energy effects,” *Acta materiala,* vol. 45, no. 4, pp. 1513-1524, 1997.

[187] J. X. J. Zhang and K. Hoshino, “Chapter 6 - Mechanical transducers: Cantilevers, acoustic wave sensors, and thermal sensors,” in *Molecular Sensors and Nanodevices (Second Edition)*, Elsevier Inc., 2019, p. 322.

[188] G. Abadias, E. Chason, J. Keckes, M. Senastiani, G. B. Thompson, E. Barthel, G. L. Doll, C. E. Murray, C. H. Stoessel and L. Martinu, “Stress in thin films and coatings: Current status, challenges, and prospects,” *Juornal of Vacuum Science & Technology A,* vol. 36, no. 2, p. 020801, 2018.

[189] J. M. R. Weaver, Interviewee, *"Thin-film stress investigation - vacuum increase in metal evaporator".* [Interview]. 05 06 2019.

[190] L. D. Hall, J. C. Helmer and R. L. Jepsen, “Electrical vacuum pump apparatus and method”. Patent US2993638A, 24 07 1957.

[191] “KNT Nano,” Kelvin Nanotechnology, 2020. [Online]. Available: www.kntnano.com.

[192] M. Hopcroft, W. Nix and T. Kenny, “What is the Young’s Modulus of Silicon?,” *Journal of Microelectromechanical Systems,* vol. 19, no. 2, pp. 229-238, 2010.

[193] F. Zhang, S. Krishnaswamy and C. Lilley, “Bulk-wave and guided-wave photoacoustic evaluation of the mechanical properties of aluminum/silicon nitride double-layer thin films,” *Ultrasonics,* vol. 45, no. 1-4, pp. 66-76, 2006.

[194] T. Yoshioka, T. Ando, M. Shikida and K. Sato, “Tensile testing of SiO2 and Si3N4 films carried out on a silicon chip,” *Sensors and Actuators A: Physical,* vol. 82, no. 1-3, pp. 291-296, 2000.

[195] K. B. Gavan, H. J. Wstra, E. W. J. M. van der Drift, W. J. Venstra and H. S. J. van der Zant, “Size-dependent effective Young’s modulus of silicon nitride cantilevers,” *Applied Physics Letters,* vol. 94, p. 233108, 2009.

[196] M.-F. Yu, O. Lourie, M. J. Dyer, K. Moloni, T. F. Kelly and R. S. Ruoff, “Strength and Breaking Mechanism of Multiwalled Carbon Nanotubes Under Tensile Load,” *Science,* vol. 287, no. 5453, pp. 637-640, 2000.

[197] R. A. Serway, Principles of physics, Forth Worth: Saunders College Pub., 1998.

[198] J. Zhou, T. Ohno and C. A. Wolden, “High-temperature stability of nichrome in reactive environments,” *Journal of Vacuum Science & Technology A Vacuum Surfaces and Films,* vol. 21, no. 3, 2003.

[199] I. H. Kazi, P. M. Wild, T. N. Moore and M. Sayer, “The electromechanical behaviour of nichrome (80/20 wt.%) film,” *Thin Solid Films,* vol. 433, p. 339, 2003.

[200] G. S. Moschytz, “Two-step precision tuning of twin-T notch filter,” *Proceedings of the IEEE,* vol. 54, no. 5, p. 811, 1966.

[201] F2 Chemicals Ltd., “FLUTEC PP3.FH11,” [Online]. Available: f2chemicals.com/pdf/data_sheets/flutec_pp3.

[202] N. Chuang, J. T. Lin and H. R. Chen, “TCR control of Ni–Cr resistive film deposited by DC magnetron sputtering,” *Vacuum,* vol. 119, pp. 200-203, 2015.

[203] J. R. Davis, “Electrical Applications,” in *ASM Specialty Handbook: Copper and copper alloys*, Ohio, ASM International, 2001, p. 158.

[204] S. Timoshenko, “Analysis of Bi-Metal Thermostats,” *Journal of the Optical Society of America,* vol. 11, no. 33, p. 233, 1925.

[205] S. Sumita, “Calculation of Thermal Expansion of Ni-Cr Thin Film by High Temperature X-ray Diffraction Spectroscopy,” *International Journal of the Society of Materials Engineering for Resources,* vol. 2, no. 1, pp. 86-92, 1994.

[206] A. Kaushik, H. Kahn and A. H. Heuer, “Wafer-Level Mechanical Characterization of Silicon Nitride MEMS,” *Journal of Microelectromechanical Systems,* vol. 14, no. 2, p. 366, 2005.

[207] W. Wang, C. Li, Y. Wang, G. Yang and K. Sonoya, “Tensile deformation behavior of plasma-sprayed Ni-45Cr coatings,” *Surface & Coatings Technology,* vol. 201, pp. 842-847, 2006.

[208] G. Sureshkannan and M. Velliangiri, “RAMAN analysis and experimental investigation of Nichrome and Aluminium Nitride microtubular coil heaters: a 2D approach,” *International Journal of Mechanical Engineering and Robotics Research.*

[209] L. Ramiandrisoa, A. Allard, Y. Joumani, B. Hay and S. Gomés, “A dark mode in scanning thermal microscopy,” *Review of Scientific Instruments,* vol. 88, no. 125115, 2017.

[210] Bruker AFM Probes, “SCANASYST-AIR-HPI Specification,” [Online]. Available: https://www.brukerafmprobes.com/p-3967-scanasyst-air-hpi.aspx.

[211] “AFM Probes, KNT-SThM-2an,” Nano and More GmbH, 2020. [Online]. Available: www.nanoandmore.com/AFM-Probe-KNT-SThM-2an.

[212] Bruker, “ContourGT-X 3D Optical Profiler,” Bruker 3D Optical Microscopes, [Online]. Available: www.bruker.com/products/surface-and-dimensional-analysis/3d-optical-microscopes/contourgt-x/overview.html.

[213] H. Xie, J. Vitard, S. D. Haliyo and S. Régnier, “Enhanced Accuracy of Force Application for AFM Nanomanipulation Using Nonlinear Calibration of Optical Levers,” *2008,* vol. 8, no. 8, pp. 1478-1485, IEEE Sensors Journal.

[214] Y. Zhang, P. S. Dobson and J. M. R. Weaver, “Batch Fabricated Dual Cantilever Resistive Probe for Scanning Thermal Microscopy,” *Microelectronic Engineering,* vol. 88, no. 8, pp. 2435-2438, 2011.

[215] H. Dingle, “Angstrom (A) or Ångström (Å)?,” *Nature,* vol. 167, p. 908, 1951.

[216] PI-KEM Limited, “Silicon Wafer 3" (76.2mm) N(Phos) Prime - WAFER-SILI-0347W25,” [Online]. Available: https://www.pi-kem.co.uk/shop/product/silicon-wafer-3-inch-762mm-nphos-prime-25-pack-wafer-sili-0347w25. [Accessed 30 09 2020].

[217] S. Tönnberg, “Optimisation and characterisation of LPCVD silicon nitride thin film growth, Master of Science Thesis,” 2006. [Online]. Available: http://publications.lib.chalmers.se/records/fulltext/18906.pdf. [Accessed 30 09 2020].

[218] Bruker AFM Probes International, “SCANASYST-AIR-HPI,” [Online]. Available: https://www.brukerafmprobes.com/p-3967-scanasyst-air-hpi.aspx.